



5-2010

# The Lipid Acyl-Chain Dynamics in Giant Liposomes and Characterization of Domain 4 of the Wilson Disease Protein

Wilson Okumu  
*Western Michigan University*

Follow this and additional works at: <http://scholarworks.wmich.edu/dissertations>

 Part of the [Chemistry Commons](#)

## Recommended Citation

Okumu, Wilson, "The Lipid Acyl-Chain Dynamics in Giant Liposomes and Characterization of Domain 4 of the Wilson Disease Protein" (2010). *Dissertations*. 615.  
<http://scholarworks.wmich.edu/dissertations/615>

This Dissertation-Open Access is brought to you for free and open access by the Graduate College at ScholarWorks at WMU. It has been accepted for inclusion in Dissertations by an authorized administrator of ScholarWorks at WMU. For more information, please contact [maira.bundza@wmich.edu](mailto:maira.bundza@wmich.edu).



THE LIPID ACYL-CHAIN DYNAMICS IN GIANT LIPOSOMES AND  
CHARACTERIZATION OF DOMAIN 4 OF THE WILSON  
DISEASE PROTEIN

by

Wilson Okumu

A Dissertation  
Submitted to the  
Faculty of the Graduate College  
in partial fulfillment of the  
requirements for the  
Degree of Doctor of Philosophy  
Department of Chemistry  
Advisor: David Huffman, Ph.D.

Western Michigan University  
Kalamazoo, Michigan  
May 2010

UMI Number: 3410415

All rights reserved

**INFORMATION TO ALL USERS**

The quality of this reproduction is dependent upon the quality of the copy submitted.

In the unlikely event that the author did not send a complete manuscript and there are missing pages, these will be noted. Also, if material had to be removed, a note will indicate the deletion.



UMI 3410415

Copyright 2010 by ProQuest LLC.

All rights reserved. This edition of the work is protected against unauthorized copying under Title 17, United States Code.



ProQuest LLC  
789 East Eisenhower Parkway  
P.O. Box 1346  
Ann Arbor, MI 48106-1346

THE LIPID ACYL-CHAIN DYNAMICS IN GIANT LIPOSOMES AND  
CHARACTERIZATION OF DOMAIN 4 OF THE WILSON  
DISEASE PROTEIN

Wilson Okumu, Ph.D.

Western Michigan University, 2010

Steady-state and nanosecond time-resolved fluorescence of the nitro-2, 1, 3-benzoxadiazol-4-yl (NBD) probe and line tension force were determined in phospholipids acyl-chain dynamics in giant liposomes made from a homologous series of phosphatidylcholines (PC). The fluorescence spectroscopy of a NBD probe attached to the headgroup (NBD PE) or the tail (NBD PC) of the phospholipid were used to determine the rate of dithionite quenching in a homologous series of phospholipids. Similar experiments were performed in the gel and the fluid phases of the 1,2-dimyristoyl-*sn*-glycero-3-phosphocholine (DMPC). Nanosecond time scale lifetimes and anisotropy measurements were obtained by a 470 nm LED pulse laser diode and time correlated single photon counting detection.

The fluorescence lifetime and intensity of NBD PE and NBD PC in acyl-chain lengths from 12:0 PC to 20:0 PC were determined. The half life of dithionite quenching of NBD varied with both phospholipid chain length and the position of the fluorescent probes and of quenching in the gel, fluid and phase transition phases. Line tensions measured by laser ablation method in a homologous series of lipids, revealed acyl-chain length and phase state dependence.

Studies were conducted on human Wilson disease protein. This is a copper transporting ATPase found in the copper secretory pathway. It possesses six cytosolic metal binding domains in the N-terminus. These domains are involved in the acquisition of copper(I) from the metallochaperone HAH1. Insight into the stability of metal-binding domain four will be presented.

Copyright by  
Wilson Okumu  
© 2010

## ACKNOWLEDGEMENTS

This work is a product of hard work, patience and support from people that I want to acknowledge. I want to recognize their great help, blessings and patience especially from my family, relatives and friends. I want to convey genuine gratitude for their assistance throughout the course of my education.

I feel deeply indebted to my supervisor, Professor David Huffman, a humble and dedicated mentor. His continuous guidance enabled me to develop understanding of the project and to learn how to critically evaluate the data. His patience and support and insightful comments ensured success in completing the work described in this dissertation. His acceptance of my views in the discussion saved me confidence and greatly enriched my ideas that I humbly present in this dissertation.

I am grateful to my former supervisor Professor Subra Muralidharan for his guidance and patience. His mentorship provided a strong foundation for gaining fundamental knowledge in chemistry. Although his decision to move to Washington State University at Pullman, Washington was distressful, I believe it was an opportunity for me to gain a wider experience as a graduate student.

I sincerely extend my special thanks and gratitude to the members of my doctoral committee for their invaluable support. The support offered by Professor Ekkehard Sinn who is also the Chair to the Department is greatly acknowledged. The comments provided by Dr. Reinhold are immensely appreciated. I am greatly

### Acknowledgments—continued

indebted to Dr. Tripp. He played a great role in the project design and constantly availed himself in the weekly discussions that determined the direction of this project. Gratitude is the fairest blossom which spring from the soul. My heartily gratitude goes to Dr. Sherine Obare who was my greatest inspiration to the end of this project. She was a constant source of encouragement, help and guidance. These virtues were critical to my graduate studies. I am grateful for her critical readings and comments that created the present form of this work.

I want to thank the following for their support and patience. Mildred my wife and to each of our two girls Jeddy and Jillian, my mother Margaret for her devotion to her children and constant love, my brother Michael who laid a firm foundation for my knowledge in science, all my dear friends and colleagues for encouragement and suggestions in the course of my education, the memory of my father Elly, and the Department of Chemistry staff at Western Michigan University for their personal sacrifice and help over many years when needed in the department.

This research was supported by grants obtained from the W. M. Keck Foundation, Department of Defense, Western Michigan University President's Innovation Fund and an NSF CARREER Award to Prof. David Huffman.

Wilson Okumu



## TABLE OF CONTENTS

ACKNOWLEDGMENTS .....	ii
LIST OF TABLES .....	xii
LIST OF FIGURES .....	xiii
LIST OF ABBREVIATIONS.....	xix
CHAPTER	
1. GIANT LIPOSOMES FOR CELL MEMBRANE STUDIES.....	1
1.1 Introduction.....	1
1.1.1 Giant Liposomes .....	1
1.1.2 The Plasma Membrane of the Cell .....	9
1.2 Phospholipid .....	10
1.2.1 Structure .....	10
1.2.2 Composition and Shape .....	11
1.3 Lipid Bilayer Region .....	13
1.4 The Thickness of a Lipid Bilayer .....	16
1.5 Phase Transition .....	18
1.6 Dielectric Constant of the Bilayer .....	20
1.7 Fluorescence Spectroscopy .....	22
1.8 Membrane Probes .....	27
1.8.1 NBD Membrane Fluorescent Probe.....	28
1.9 Dithionite Quenching of NBD .....	30

## Table of Contents-Continued

### CHAPTER

1.10 Lipid Bilayer Dynamics .....	32
1.10.1 Membrane Fluidity .....	32
1.10.2 Membrane Dynamics .....	33
1.11 Dynamics of Pore Formation and Line Tension in Giant Vesicles .....	35
1.12 Conclusion .....	36
1.13 References.....	38
2. EXPERIMENTAL METHODS AND PROCEDURES .....	54
2.1 Reagents.....	54
2.1.1 Phospholipids .....	54
2.1.2 Fluorescent Lipids .....	54
2.1.3 Chemicals .....	58
2.2 Apparatus .....	58
2.2.1 UV-VIS Spectrometer .....	58
2.2.2 Fluorescence Spectrometer .....	59
2.2.3 Nikon Eclipse TE2000U Microscope .....	59
2.2.4 Confocal Microscopy .....	61
2.2.5 Darkfield Microscopy .....	61
2.2.6 Pore Formation and Line Tension Force .....	62
2.3 Methods .....	63
2.3.1 Preparation of Liposomes .....	63

## Table of Contents-Continued

CHAPTER		
	2.3.2 Lamellarity of Liposomes .....	64
	2.3.3 Fluorescence Anisotropy .....	65
	2.3.4 Fluorescence Quenching .....	66
	2.3.5 Lifetime and Time-Resolved Anisotropy .....	67
	2.3.6 Bulk Solution Measurement in Edinburgh Instrument .....	70
	2.4 References .....	72
3. GIANT LIPOSOMES FROM A BINARY MIXTURE OF LIPIDS.....		74
	3.1 Introduction.....	74
	3.2 Imaging .....	77
	3.3 NBD Assay .....	79
	3.4 Lamellarity of Liposome from a Mixture of DLPC and DPPC.....	85
	3.5 Lamellarity of Egg PC Liposomes.....	87
	3.6 Darkfield Images.....	88
	3.7 Confocal Fluorescence Images .....	90
	3.8 Discussion.....	94
	3.9 Conclusion .....	97
	3.10 References .....	99
4. GIANT LIPOSOMES FROM HOMOLOGOUS SERIES OF LIPIDS .....		104
	4.1 Introduction.....	104
	4.2 Fluorescence Quenching Experiments.....	106

## Table of Contents-Continued

### CHAPTER

4.3	Fluorescence Intensity Measurements .....	118
4.4	Lifetime Measurement .....	122
4.5	Percent of NBD Quenched by Dithionite .....	124
4.6	Conclusion .....	129
4.7	References .....	132
5.	TIME-RESOLVED MEASUREMENTS IN SINGLE LIPOSOME.....	136
5.1	Introduction.....	136
5.2	Fluorescence Lifetime of NBD Moiety .....	141
5.2.1	Microscope Slide .....	141
5.2.2	Edinburgh Fluorimeter .....	144
5.3	Time-Resolved Measurements on a Single Liposome .....	147
5.3.1	Egg PC .....	147
5.3.2	DMPC .....	150
5.3.3	Carboxyfluorescein.....	156
5.4	Bulk Solution Measurements in Edinburgh Fluorimeter.....	158
5.5	Activation Energy .....	162
5.6	Discussion .....	168
5.7	Conclusion .....	171
5.8	References .....	174

## Table of Contents-Continued

### CHAPTER

6. LINE TENSION FORCE AND PORE FORMATION DYNAMICS.....	178
6.1 Introduction.....	178
6.2 Line Tension .....	180
6.3 Pore Size and Vesicle Radius .....	183
6.4 Pore Formation in Giant Vesicle by Laser Ablation.....	186
6.4.1 Protocol.....	186
6.4.2 Membrane Deformation in Giant Vesicles .....	189
6.5 Results.....	189
6.5.1 Line Tension.....	189
6.6 Discussion.....	194
6.7 Conclusion .....	197
6.8 References .....	199
7. CHARACTERIZATION OF THE N-TERMINAL HUMAN WILSON PROTEIN DOMAIN 4.....	204
7.1 Introduction.....	204
7.1.1 Importance of Copper and Wilson Disease .....	204
7.1.2 Wilson Disease.....	205
7.1.3 P-Type ATPases.....	206
7.1.4 Structure of ATP7B .....	210
7.1.5 Copper Trafficking in Cells .....	212
7.1.6 Metallochaperone and Copper Transport in Cells.....	215

## Table of Contents-Continued

### CHAPTER

7.1.7	Metal Coordination Chemistry .....	216
7.1.8	Copper Transfer from HAH1 to ATPase .....	218
7.1.9	HAH1 and Human Wilson Domain 4 (WLN4) .....	219
7.1.10	Domain-Domain Interaction and Copper Transfer .....	221
7.1.11	Significance of this Study .....	224
7.1.12	Objectives of the Study .....	225
7.2	References .....	226
8.	EXPERIMENTAL METHODS AND PROCEDURES .....	236
8.1	Reagents .....	236
8.1.1	Plasmid Vector and Bacterial Cells .....	236
8.1.2	Chemicals and Apparatus .....	237
8.1.3	Components of pET-32Xa/LIC Plasmid Vector .....	238
8.2	Transformation of pET-32Xa/LIC/WLN4 .....	239
8.2.1	Agarose Gel Electrophoresis .....	240
8.3	WLN4 Protein Expression .....	241
8.3.1	Transformation .....	241
8.3.2	Induction and Expression of WLN4 Protein .....	241
8.3.3	Extraction of Protein WLN4 .....	243

## Table of Contents-Continued

### CHAPTER

8.4	Protein Purification .....	244
8.4.1	Factor Xa Protease Cleavage .....	245
8.4.2	Protein Concentration .....	246
8.5	Static and Dynamic Light Scattering .....	246
8.6	Circular Dichroism Measurements .....	247
8.6.1	Chemical and Thermal Denaturation .....	248
8.6.2	Free Energy of Unfolding .....	250
8.7	References.....	251
9.	RESULTS AND DISCUSSIONS.....	253
9.1	Recovery of the Plasmid Vector .....	253
9.2	Protein Induction and Expression .....	255
9.3	Purification of WLN4 Fusion Protein.....	256
9.3.1	HisPrep Purification .....	256
9.3.2	Factor Xa Protease Cleavage .....	260
9.3.3	Protein Concentration .....	263
9.4	Determination of Protein Size by Light Scattering.....	263
9.4.1	Static Light Scattering .....	263
9.4.2	Dynamic Light Scattering.....	265
9.5	Circular Dichroism .....	271
9.6	References .....	284

Table of Contents-Continued

CHAPTER

10. CONCLUSIONS AND FUTURE DIRECTIONS.....	289
10.1 Success in Giant Liposomes .....	289
10.2 Single Molecule Fluorescence Studies of Wilson Protein and HAH1 .....	291
10.3 Significance and Conclusion .....	294
10.4 References .....	296



## LIST OF TABLES

2.1. List of phospholipids.....	55
2.2. Structure and phase transition temperature of phospholipids .....	57
3.1. Lamellarity of liposome from pure and mixed lipids.....	86
3.2. Lamellarity values calculated for egg PC liposomes .....	87
4.1. Gel phase temperature of phosphatidylcholines.....	111
4.2. Half life calculated for the different chain lengths.....	116
5.1. Fluorescence lifetime of NBD PE in solvents of varying polarity.....	144
5.2. Long component lifetime for NBD PE in dioxane.....	147
5.3. Arrhenius activation barriers for the long and short lifetime components in DMPC and egg PC vesicles .....	167
6.1. Line tension force in homologous series and egg PC liposomes at 24°C .....	193
9.1. Summary HPLC-Gel filtration and light scattering .....	269
9.2. Summary free energy of unfolding of WLN4 .....	281
9.3. Free energy of unfolding extrapolated to zero denaturant concentration .....	281
9.4. Chemical unfolding parameters for WLN4 protein .....	282

## LIST OF FIGURES

1.1	Sequence of vesicle fission of DMPC: cholesterol vesicles.....	4
1.2	Shape transformations of giant vesicles as a function of temperature showing formation of endocytic vesicle .....	4
1.3	Exit of a small vesicle through transient pore .....	8
1.4	Structure of a phosphatidylcholine .....	11
1.5	Polymorphic phases and corresponding dynamic molecular shapes of component lipids .....	15
1.6	A cartoon drawing of the lipid double layer.....	16
1.7	A modern picture of a membrane .....	17
1.8	Schematic diagram representing an endothermic peak in calorimetry.....	19
1.9	Dielectric constant profile of the lipid bilayer .....	21
1.10	Schematic representation of Jablonski diagram .....	23
1.11	Time-domain lifetime measurement .....	24
1.12	Frequency domain lifetime measurement .....	25
2.1	Structure of NBD PE .....	56
2.2	Structure of NBD PC .....	56
2.3	Structure of DPPG .....	58
2.4	Nikon eclipse TE2000U microscope .....	60
2.5	Change in fluorescence intensity of NBD on addition of dithionite and Triton X-100 .....	65
2.6	Focused laser beam on an isolated liposome .....	68

## List of Figures-Continued

2.7	The IRF and sample decay signal .....	69
3.1	Brightfield image of DPPC liposome.....	77
3.2	Brightfield image of DLPC liposome .....	78
3.3	Brightfield image of DLPC / DPPC mixture (1:1).....	78
3.4	Brightfield image of DLPC / DPPC mixture (3:2).....	79
3.5	NBD assay profile of liposomes of DPPC / DLPC mixture (1:1) .....	80
3.6	NBD assay profile of DPPC liposome .....	81
3.7	NBD assay in liposomes composed of DPPC / DPPG ( 9:1) and DLPC / DPPG ( 9:1) .....	83
3.8	Brightfield images of liposomes from DPPC / DPPG mixture (9:1) .....	83
3.9	Brightfield images of liposomes composed of DLPC and DPPG mixture (9:1) .....	84
3.10	Brightfield images of liposomes composed of egg PC and DPPG mixture (9:1) .....	84
3.11	Brightfield images of DLPC liposomes .....	85
3.12	Brightfield images of egg PC liposomes.....	88
3.13	Darkfield images of liposomes composed of DLPC / DPPC (1:1).....	89
3.14	Darkfield images of liposomes composed of DLPC / DPPC (1:1) in a dark background.....	90
3.15	Structure of FM1-43 dye .....	91
3.16	Confocal images of DLPC / DPPC (1:1).....	93
4.1	UV-Vis absorbance of NBD PE .....	107

## List of Figures-Continued

4.2	NBD PE and NBD PC orientation in lipid bilayer .....	108
4.3	Exponential decay of dithionite quenching of the NBD PC .....	114
4.4	Half life of dithionite quenching of NBD fluorescence in acyl chain of variable chain lengths .....	115
4.5	Measurements of initial fluorescence intensity of NBD PE and NBD PC in lipids of different chain lengths .....	120
4.6	Fluorescence intensity measurements in DMPC liposomes .....	121
4.7	Lifetime of NBD PE and NBD PC in acyl-chain of varying lengths .....	123
4.8	Preferred headgroup conformation in bilayer .....	124
4.9	Exponential decay plots of dithionite quenching of NBD in acyl-chain of varying lengths .....	125
4.10	Percentage of NBD quenched in the DMPC lipid bilayer as a function of temperature .....	127
4.11	Temperature-dependence steady-state anisotropy of NBD in DMPC bilayer .....	128
4.12	Looping back of the NBD of NBD PC as a function of phase state of the host lipid .....	130
5.1	Fluorescence intensity decay signal after excitation with a pulsed light.....	137
5.2	Photo-selection of fluorophores oriented parallel to the electric vector of the exciting light.....	139
5.3	Fluorescence lifetimes of the NBD PE and NBD PC dissolved in a mixture of dioxane and water ( % w/w).....	146
5.4	Fluorescence lifetime of NBD PE in egg PC liposome .....	148

## List of Figures-Continued

5.5 Time-resolved anisotropy of NBD PE in egg PC liposomes.....	149
5.6 Long component lifetime of NBD group in DMPC liposomes .....	151
5.7 Short component lifetime of NBD group in DMPC liposomes.....	152
5.8 Time-resolved anisotropy of NBD group in DMPC as a function of temperature .....	153
5.9 Time-resolved anisotropy of the NBD group in the DMPC with a fixed lifetime measured as a function of temperature.....	156
5.10 Lifetime of 5-Carboxyfluorescein as a function of temperature .....	157
5.11 Edinburgh lifetime measurements of concentrated sample of DMPC .....	159
5.12 Edinburgh lifetime measurements of diluted DMPC (14:0) sample .....	160
5.13 Arrhenius plot for the long component lifetime of the NBD PE in egg PC.....	163
5.14 Arrhenius plot of long and short lifetime components for the NBD PE in DMPC .....	164
5.15 Arrhenius plot of the long and short lifetime components for the NBD PC in DMPC.....	165
6.1 Time evolution of pore and vesicle radius .....	182
6.2 Traverse view of a pore with radius $r$ .....	184
6.3 Time course event for coumarin laser ablation of a giant vesicle .....	187
6.4 Time course event (video frames from 1-105 sec) of a 20 $\mu\text{m}$ diameter egg PC liposome undergoing deformation without laser ablation.....	188
6.5 A plot of $R^2 \ln r_{\text{pore}}$ as a function of time $t$ for egg PC with 10% dihydrocholesterol .....	191

## List of Figures-Continued

7.1	Hydrolysis of ATP upon copper binding to Cu-ATPase .....	208
7.2	Cycling of Menkes protein between the trans-Golgi network and plasma membrane in excess of copper.....	210
7.3	The structure of Wilson disease protein .....	212
7.4	Copper trafficking pathways in a cell .....	214
7.5	Coordination chemistry for Cu(I) ions in metal binding sites showing possible 2, 3 and 4 coordination sites in HAH1 .....	217
7.6	Proposed model of copper transfer from Atox1 to ATPase.....	222
8.1	Map of plasmid vector pET32XaLIC .....	238
8.2	A cartoon drawing showing the various parts of a vector .....	242
9.1	Agarose gel of plasmid vector pET-32Xa/LIC/WLN4.....	254
9.2	SDS-PAGE analysis of protein induction and expression of WLN4 .....	255
9.3	The WLN4 fusion protein elution from HisPrep FF 16/10 Sepharose column .....	258
9.4	SDS-PAGE gel showing progress of Factor Xa cleavage of WLN4-Trx-His-tag protein .....	259
9.5	HiLoad Superdex 75 26/60 gel filtration chromatogram.....	261
9.6	SDS-PAGE analysis of purified WLN4 .....	262
9.7	Molar mass versus time for the WLN4 protein .....	265
9.8	Autocorrelation function .....	266
9.9	Hydrodynamic radius distributions.....	269
9.10	CD spectrum of WLN4.....	273

## List of Figures-Continued

9.11	Thermal unfolding of WLN4 measured between 190 and 260 nm .....	274
9.12	A two-state model of thermal unfolding of WLN4 taken at 222 nm.....	275
9.13	Chemical unfolding with GnHCl.....	277
9.14	Equilibrium curves for chemical unfolding .....	278
9.15	Concentration dependence of the chemical unfolding and change in free energy .....	280
9.16	Structure of WLN4 (B) and Third domain (A) of Wilson protein .....	283
10.1	Single molecule diffusing in a focused laser beam .....	292
10.2	Immobilization of liposome on a surface by avidin biotin conjugation.....	294

## LIST OF ABBREVIATIONS

ABD.....	Amino-2,1,3-benzoxadiazol-4-yl
Egg PC.....	L- $\alpha$ -phosphatidylcholine (Egg, Chicken)
DLPC (12:0).....	1,2-dilauroyl- <i>sn</i> -glycero-3-phosphocholine
DLS.....	Dynamic Light Scattering
DMPC (14:0) .....	1, 2-dimyristoyl- <i>sn</i> -glycero-3-phosphocholine
DNA.....	Deoxyribonucleic acid
DPH.....	Diphenylhexatriene
DPPC (16:0).....	Dipalmitoylglycerophosphocholine
DOPC (18:0) .....	1,2-dioleoyl- <i>sn</i> -glycero-3-phosphocholine
DPPG.....	1, 2-dipalmitoyl- <i>sn</i> -glycero-3-phospho-(1'- <i>rac</i> -glycerol) (sodium salt)
GUV.....	Giant Unilamellar Vesicles
HAH1.....	human homologue of a copper binding protein
HEPES.....	N-2-Hydroxyethylpiperazine-N'-2-ethanesulfonic acid
IRF.....	Instrument Response Function
$k_1$ .....	Rate coefficient for the fast reduction
LED.....	Light emitting diode
MALS .....	Multi-angle Laser Light Scattering
MLV.....	Multi-lamellar Vesicles



## List of Abbreviations-Continued

MKNK1.....	First domain of Menkes Disease Protein
MNK2.....	Second domain of Menkes Disease Protein
NBD .....	Nitro-2,1,3-benzoxadiazol-4-yl
NBD PE (16:0).....	(1, 2-dipalmitoyl- <i>sn</i> -glycero-3-phosphoethanolamine-N-(.....7-nitro-2-1, 3-benzoxadiazol-4-yl) (ammonium salt)
NBD PC (16:0-12:0)...	1-palmitoyl-2-[12-[(7-nitro-2-1, 3-benzoxadiazol-4-yl) amino].....dodecanoyl]- <i>sn</i> -glycero-3-phosphocholine
DPPN.....	1,2-dipalmitoyl- <i>sn</i> -glycero-3-phospho-[ <i>N</i> -(4-nitrobenz-2-oxa-1,3-diazole)-ethanolamine]
PC.....	Phosphatidylcholine
PG.....	Phosphatidylglycerol
POPC.....	1-palmitoyl 2-oleoyl phosphatidylcholine
POPG.....	1-Palmitoyl-2-oleoyl- <i>sn</i> -glycero-3-phospho-(1'- <i>sn</i> -glycerol) (sodium salt)
QEL.....	Quasi Elastic Light Scattering
RNA.....	Ribonucleic acid
RO.....	Reverse Osmosis
SUV.....	Small Unilamellar Vesicles
TCSPC.....	Time-Correlated Single Photon Counting
WD.....	Wilson Disease
WLN4.....	Fourth Domain Wilson Disease protein

## CHAPTER 1

### GIANT LIPOSOMES FOR CELL MEMBRANE STUDIES

#### 1.1 Introduction

##### 1.1.1 Giant Liposomes

A liposome is a tiny spherical vesicle with a bilayer membrane composed of phospholipid. “Giant” refers to its size compared to a diameter between 5 and 200  $\mu\text{m}$  [1]. It has size and the curvature that are similar to those of the living cell [1, 2]. It has been used extensively as a model membrane system because of the structure and the large size that allows for the direct observation by optical microscopy [3]. The liposomes are simple and well defined model systems that can be isolated, controlled and be modulated to simulate some cellular characteristics.

A prominent example of the application of giant liposomes to simulate cellular membranes was reported by Roux, who showed the formation of tubules using purified motor proteins [4]. Koster further measured forces involving the formation of the tube using a laser tweezer [5]. A laser tweezer uses a laser beam focused through a high numerical aperture objective lens and provides a piconewton force that can trap and move a tiny object. These findings when put together, provided the basic understanding of the mechanisms involved in cellular transport. Furthermore, the membrane elastic property of a lipid bilayer is involved in critical cellular processes that include budding, fission, fusion and membrane poration. The

giant liposomes with diameters greater than 10  $\mu\text{m}$  have been used to extensively study the elastic properties of phospholipid membranes [6, 7]. In addition, mechanical properties of the cell membranes have been studied using model membranes presented by giant unilamellar vesicles [8-10]. Studies have demonstrated that deformation of a single lipid component depends on its membrane environment [11]. The membrane deformation can be characterized by the bending and area compression modulus [12]. These properties determine membrane function, like the ability of proteins to insert into a lipid bilayer [13].

Giant liposomes can in principle, be used as a proto-cell for the expression of the basic functions of a living cell. This was demonstrated by acquiring DNA from the external environment using the proto-cells [14, 15].

A giant liposome has a thin phospholipid bilayer that encloses an extremely small volume at the center. Reaction in an extremely small enclosed volume of the size between  $10^{-12}$  and  $10^{-21}$  liters and in soft matter has been desired by many scientists [16-18]. The chemical reactions inside the cell are complex and take place in small volumes that involve a small number of molecules [1, 19]. The chemical reactions inside a giant liposome can be observed using an optical microscope because of the advantage of the giant sizes of vesicle. Studies have shown that lipid bilayer permeability to certain molecules is potentially applicable to certain biochemical reactions. For example, the membrane permeability was shown by DNA or RNA substrate in the lumen of a vesicle from a specific nuclease in the external surface environment of the giant liposomes generated by electroformation [20]. A

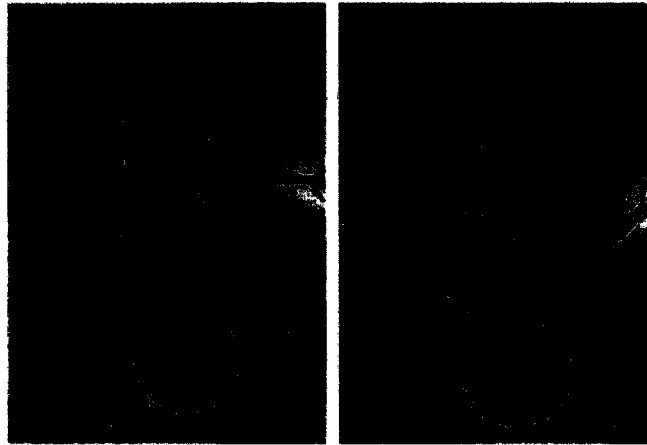
compartmentalized biochemical reaction has been shown by the protein expression and polymerase chain reaction in giant liposome [21, 22]. These reactions are not possible with the conventional small sized liposomes. These findings further demonstrate importance of the membrane size and the curvature in affecting the physical and chemical properties of lipid bilayers.

Cellular membrane components are mobile in a wide range of time and length scales. The movements of the lipid bilayer components form the core of the many molecular processes taking place in the cell membrane. While the models for the cell membranes developed over time, the molecular dynamics of the membrane have been classified into three main motions: lateral, rotational and the transverse diffusion. These motions contribute to membrane fluidity and maintain the integrity and function of the living cell. The membrane fluidity concept of Nicholson and Singer [23] is largely due to the hydrophobic proteins and lipids in the bilayer. Lateral diffusion is the spontaneous movement of these components across the monolayer of the lipid bilayer. This movement has been reported by recovery after photobleaching experiments. Studies using the giant vesicles and supported phospholipid bilayer models, have shown that lateral diffusion is two times higher in giant liposomes than in the supported bilayer [24].

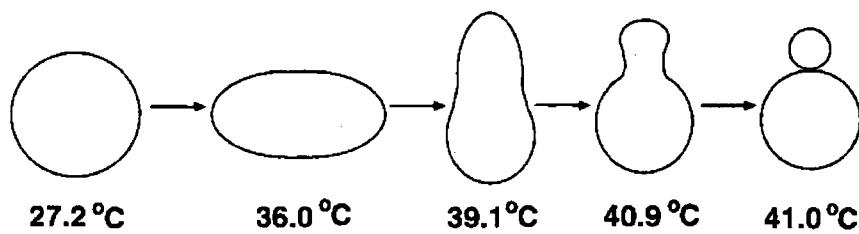
Budding and the fission events are very important physical processes observed by the optical microscopy in the cell membranes [25]. They are a direct consequence of lipid membrane heterogeneity and formation of lipid domains. These domains

freely diffuse within the bilayer. The vesicle fission process is captured in Figure 1.1.

One single vesicle divides to form two separate vesicles.



**Figure 1.1** Sequence of vesicles fission of DMPC: cholesterol vesicles [25].



**Figure 1.2** Shape transformations of giant vesicles as a function of temperature showing formation of endocytic vesicle [2].

A model that demonstrates shape transformation induced by temperature leading to the budding events in a giant liposome is shown in Figure 1.2. The fission of a membrane or division of membrane into two leads to the formation of endocytic vesicles in cells. The fission vesicles are used as carriers in transport and trafficking endoplasmic reticulum and the Golgi apparatus complex products to different cell organelles [26]. The formation of giant vesicles was shown using phospholipase A<sub>2</sub> in raft and non-raft forming vesicles [27] and in detergents in liquid-disordered phase domains [28].

Fluorescently labeled giant liposomes from multiple lipid compositions have been used to demonstrate the presence of lipid rafts in model membranes [29]. Multiple lipid components have a tendency to laterally segregate into co-existing liquid phases or into domains with distinct composition. Raft formation in cell membranes has an important biological implication in the signal transduction [30] and membrane trafficking [31]. Since it is possible to visualize giant liposomes under the microscope, it is possible to observe micron scale domains by fluorescence microscopy and study liquid phase immiscibility in a controlled environment.

To be considered a good cell model, a giant liposome should be prepared under physiological conditions and must be unilamellar. It is desirable to have a rapid method that can generate giant liposomes from non-destructive conditions in order to protect labile and reactive biomolecules [32]. Different methods have been proposed and implemented to produce the giant liposomes with the aforementioned qualities. The formation of giant liposomes by a gentle hydration method in the presence of 100

mM KCl and 1 mM CaCl<sub>2</sub> was reported by Akashi [33]. In the gentle hydration method, a dried phospholipid film consisting of a stack of lamellar layers is hydrated and rehydrated with aqueous solutions [3]. The aqueous liquid seeps in between the lipid bilayers and the film begins to swell. As it swells, it detaches from the surface and eventually forms a liposome that buds off and forms in the solution above the film. This is difficult with lipids that have a net charge of zero, termed neutral. This is because of lack of electrostatic repulsion in separating lipid membranes [33]. In this case, the divalent ions such as Mg<sup>2+</sup> and Ca<sup>2+</sup> bind to phospholipids and provide positive charges on the membrane surface resulting in electrostatic repulsion. In this way, giant liposomes were formed from neutral phospholipids in the presence of divalent ions as reported by Akashi [34]. Another method that gives a high yield of giant liposomes was reported by Zare and his co-workers [32].

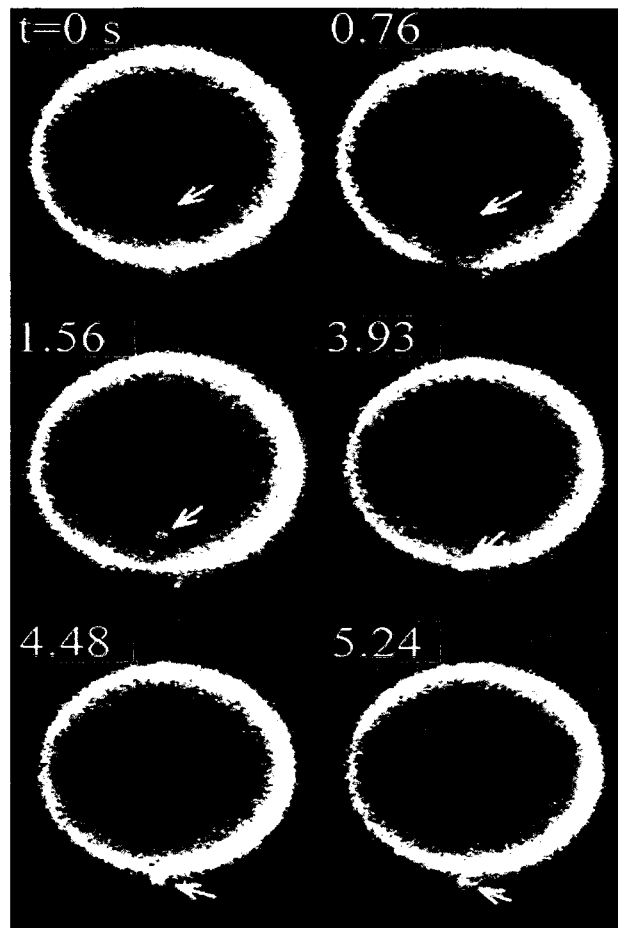
Hydration of lipid films in the presence of electric fields, generate giant vesicles by an electroformation mechanism [35]. In this method, it is possible to produce giant unilamellar liposomes with different membrane compositions in a variety of electrolytes [36]. The first step in the electroformation method involves separation of bilayers in the multi-layered film of lipids on an electrode such as ITO (Indium tin oxide) electrode [37]. This method is only possible when the ionic strength is less than 50 mM [37, 38]. A flow chamber in the electroformation method was employed to show the possibility of producing giant unilamellar vesicles under higher ionic strengths comparable to physiological conditions [39]. The

electroformation results in giant vesicles which are predominantly unilamellar and devoid of defects as opposed to gentle hydration [3].

The bilayer structure in giant liposomes is identical to the lipid portion of natural plasma membranes. Therefore, they can be used as model systems of biological membranes. In living cells, transport of solutes occurs through transient pores and transmembrane proteins. The study of giant liposomes has shown that lipid redistribution is prompted by inserting conic-shaped fluorescent lipids and forced adhesion of functionalized lipids can lead to submicroscopic transient pores [40]. Brochard-Wyart used a theoretical analysis in giant liposomes and calculated the dynamic growth of pores driven by the surface tension. The closure of pores driven by line tension [41]. Brochard-Wyart showed that it is possible to visualize the dynamics of transient pores in real time using fluorescent probes [42]. They demonstrated transport across the transient pores by using both a small vesicle and a giant vesicle as shown in Figure 1.3.

Nicolas Rodriguez showed that the lifetime of these micron-sized transient pores in the giant vesicles can be extended to 2 min [43]. This was realized by introducing the fluorescent dye nitrobenzodiazole (NBD) and dithionite quenching dynamics to the giant liposome and making observations by epifluorescence microscopy. These results provide adequate evidence that the lipid bilayer membrane is permeable and can be precisely triggered to open pores that can be used for controlled experiments such as transport across the vesicles.





**Figure 1.3** Exit of a small vesicle through transient pore [42].

### **1.1.2 The Plasma Membrane of the Cell**

The cell plasma membrane has been studied for over a century [44]. It is a thin membrane enclosing a cell. It acts as a physical barrier separating cell cytoplasm and its surrounding environment. It is a double-layered oily lipid assemblage containing integral and peripheral membrane proteins. The membrane proteins account for about 20-25% of the entire protein content of the living cell [45]. The lipids and the membrane proteins together constitute biological membranes that are essential for living organisms. Proteins perform the basic transport of small molecules and participate in the signaling pathways. Phospholipids are the structural building block of the membrane bilayer. Although the structure of a cell membrane was proposed several years ago, it is an incredibly active and exponentially expanding field in the last decade due to importance attached to lipid bilayer. The knowledge of the membrane dynamics have benefited a great deal from modeling studies using liposomes.

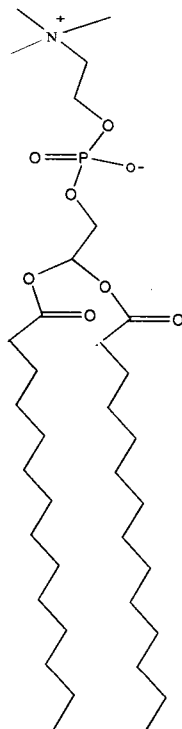
Understanding the complex nature of cell membranes requires the study of a simple model system. These models have been developed from vesicle-like structures called liposomes. Liposomes are enclosed lipid bilayers. Studies on liposomes were pioneered by Hotani in 1984 [46]. Since then, studies have been conducted in the multilamellar, small unilamellar (30-100 nm in diameter) and recently in the large unilamellar vesicles (100-200 nm). However, reports have focused on giant unilamellar vesicles that have sizes ranging from 50 to 500  $\mu\text{m}$  [47]. This because

large sizes of liposomes provide the advantage of real time observation using optical microscopy [48].

## **1.2 Phospholipid**

### **1.2.1 Structure**

Phospholipids form the structural component of cell membranes and liposomes. The structure of a phospholipid has a glycerol-backbone in which the phosphate containing headgroup is attached via an ester linkage and one or two acyl-chains attached by ester or ether linkages (see Figure 1.4). Therefore, the structure has a hydrophilic polar headgroup and a hydrophobic non-polar tail. Consequently, a phospholipid headgroup is soluble in water and the tail is sparingly soluble in water. The hydrophobic has low water solubility and thus drives the self assembly process because of the hydrophobic effect [49]. Hydrocarbon chain forms the primary barrier for the movement of charged species across the membrane. A study of a lipid bilayer dynamics and properties in model systems provides a good opportunity to understand the cell membrane organization and dynamics that is critical to the cell viability.



**Figure 1.4** Structure of a phosphatidylcholine.

### 1.2.2 Composition and Shape

Lipids are classified into three main classes: phospholipids, glycosphingolipids, and cholesterol with a molar ratio in most cells on the order of 75%: 5%: 20% [50-53]. These lipids are distributed asymmetrically in the inner and outer leaflets of plasma membranes [54]. Phospholipid molecules have lengths that vary from 14 to 24 carbon atoms with 18 to 20 being very common in nature while 15 to 22 are rich in polymorphism [55]. Lipid polymorphism refers to the long range order of lipid aggregates. These aggregates include micellar, lamellar and hexagonal

II phases. Depending on the prevailing conditions, these aggregates can undergo geometric rearrangements from one form to another. The nature of the packing of phospholipids in the bilayer depends to a large extent on hydrocarbon tails, and the length and degree of saturation. The headgroup region differs in charge, polarity and also in reactivity. This contributes to the diversity observed in phospholipids.

There are four classes of primary phospholipids that are found in eukaryotic cell membranes. These are phosphatidylcholine (PC), phosphatidylethanolamine (PE), phosphatidylserine (PS) and sphingomyelin (SM) [56]. These phospholipids are distributed in the cell membrane asymmetrically between inner and outer leaflets of membrane. PCs are widely distributed in eukaryotic organisms and are major constituents of human lung surfactant, serum lipoproteins, and bile [55]. PC has a hydrophilic headgroup which is zwitterionic at a neutral pH. The PC interfacial region has only the hydrogen bond-accepting groups as opposed to the SM which possesses both hydrogen donating and accepting groups [53]. The PC is distributed in the outer leaflets of plasma membrane [54, 57]. PC represents 56% of all the records found in LIPIDAT 2.0.

The above classes of phospholipids can either adopt vesicle (lamellar) type or non-lamellar (hexagonal, cubic, inverted micelle, micelle) structures. These are the polymorphic structures commonly found in lipids. The structures formed are important in cellular processes such as cell fusion. The headgroup structure, degree of unsaturation and hydration of the lipid itself influence the stability of the structure formed [55]. These structures have been elucidated by X-ray and differential scanning

colorimetry experiments [58, 59]. The results have shown lamellar-hexagonal structural transitions depending on the external stimuli. The PC head-group is prone to more lamellar organization than PE. Hexagonal  $H_{II}$  structures (Figure 1.5) are formed predominantly by PE phospholipid head-group that account for 35% of the total membrane lipids [60]. Diacylglycerol can promote the formation of PC-based hexagonal and cubic phase structures that depend on the temperature [61, 62].

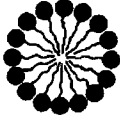

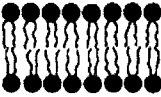

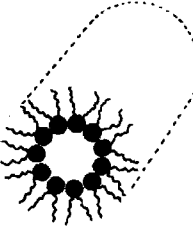

### **1.3 Lipid Bilayer Region**

A lipid bilayer membrane is formed as result of the hydrophobic effect. Lipids are insoluble in water. However, they are soluble in non-polar solvents. The hydrophobic effect is due the inability of hydrocarbons of phospholipids to hydrogen bond with the water molecules. The hydrophobic effect and the properties of water of hydration influence stability of lipid bilayers [63]. It is energetically favorable for a hydrocarbon to associate with other hydrocarbons to minimize the surface area of contact with water. This is responsible for the mechanism behind the self assembly of phospholipids.

The lipid bilayer is a double layer that is constructed such that two lipid layers form with the polar headgroup pointing towards the aqueous environment. It has been studied widely since its discovery in red blood cell membranes in 1925 by Gorter and Grendel [64]. Figure 1.6 shows the model proposed by Groter and Grendel. In this model, a monolayer area was formed and calculated. The area was found to be twice that of the surface area of red blood cells. The model contributed to our understanding

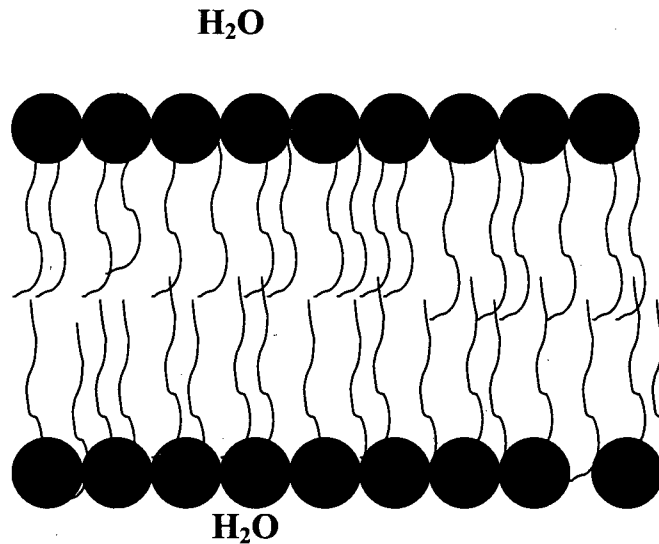
of the double layer leaflet for the cell membranes but failed to account for the many functions that were displayed by the cell membranes. Therefore, several studies were conducted to elucidate the correct structure of the bilayer that could account for observations made from cell membranes. Many of these observations were acquired by electron microscopy.

In 1972, a more accurate model was established by Singer and Nicolson [23]. In this model, the components of the membrane float freely within a matrix of lipid and proteins. Proteins found in the matrix were divided into peripheral and integral proteins. The peripheral proteins were loosely attached to the membrane surface and could easily be detached from the surface. Integral proteins could not easily be separated from the lipid bilayer. Mouritsen and Bloom in 1984 made a significant improvement to the Singer and Nicolson model. A mattress model was established that suggested proteins and lipids display interactions with a positive energy content as a result of the variations in the hydrophobic length of the molecule (see Figure 1.7) [65].

LIPID	PHASE	MOLECULAR SHAPE
LYSOPHOSPHOLIPIDS DETERGENTS	 MICELLAR	 INVERTED CONE
PHOSPHATIDYLCHOLINE SPHINGOMYELIN PHOSPHATIDYLSERINE PHOPHATIDYLINOSITOL PHOSPHATIDYLGLYCEROL PHOSPHATIDIC ACID CARDIOLIPIN DIGALACTOSYLDIGLYCERIDE	 BILAYER	 CYLINDRICAL
PHOSPHATIDYLETHANOLAMINE (UNSATURATED) CARDIOLIPIN - $\text{Ca}^{2+}$ PHOSPHATIDIC ACID - $\text{Ca}^{2+}$ (pH < 6.0) PHOSPHATIDIC ACID (pH < 3.0) PHOSPHATIDYLSERINE (pH < 4.0) MONOGALACTOSYLDIGLYCERIDE	 HEXAGANOL (H <sub>II</sub> )	 CONE

**Figure 1.5** Polymorphic phases and corresponding dynamic molecular shapes of component lipids [66].



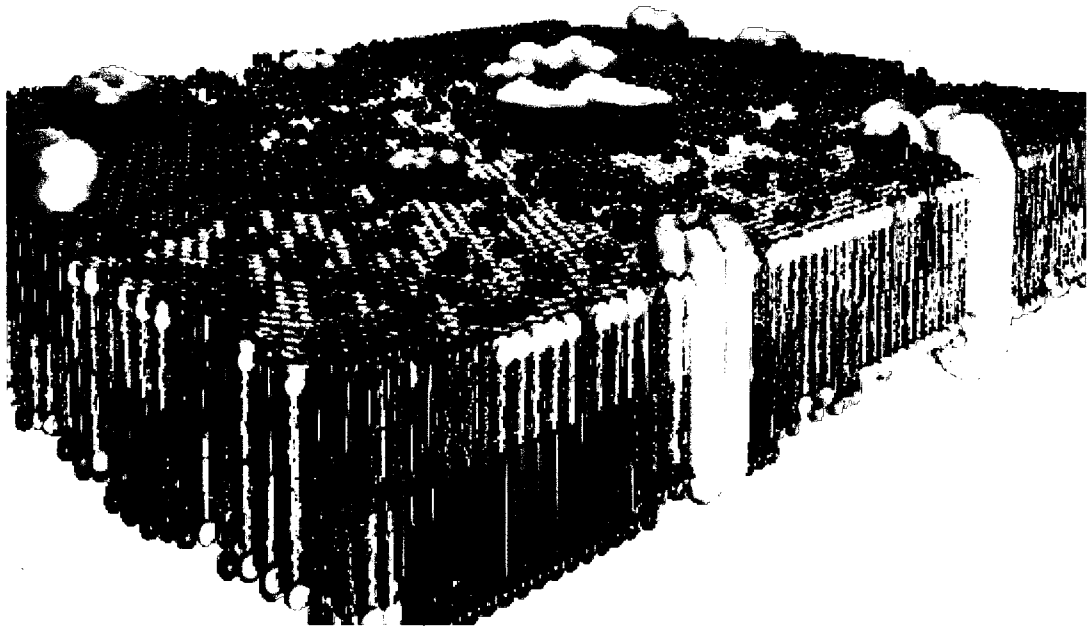


**Figure 1.6** A cartoon drawing of the lipid double layer. This was the picture projected by Groter and Grendel.

#### **1.4 The Thickness of a Lipid Bilayer**

The majority of the studies on the lipid bilayer structure have been conducted in multilamellar and unilamellar model membranes system. A study using the DMPC vesicles showed a lipid bilayer thickness of  $44.5 \pm 0.3 \text{ \AA}$  and surface area of  $58.9 \pm 0.8 \text{ \AA}$  [67]. The thickness depends on the length and degree of saturation of the fatty acyl chains of the lipids [68]. It also depends on the degree of hydration. The less hydrated, the thicker the bilayer will be. Dehydration causes the headgroup and the fatty acyl chains to get closer together and stretch out. Cholesterol also has a tendency to stretch out and order the fatty acid chains of phospholipids. Higher temperature makes the bilayer thinner. The thickness of a lipid bilayer affects lipid and protein

interactions. If the hydrophobic core of the membrane protein is longer than this value of the thickness, the hydrophobic core will be exposed to water and lipids have to compensate for the unfavorable hydrophobic interactions by deformation that lead to membrane tensions [65]. This is the hydrophobic matching as proposed by Mouritsen and Bloom [65]. This property modulates activity of the pure proteins such as cytochrome c oxidase and Ca-ATPase when they are reconstituted in phospholipid bilayers as previously reported [69].



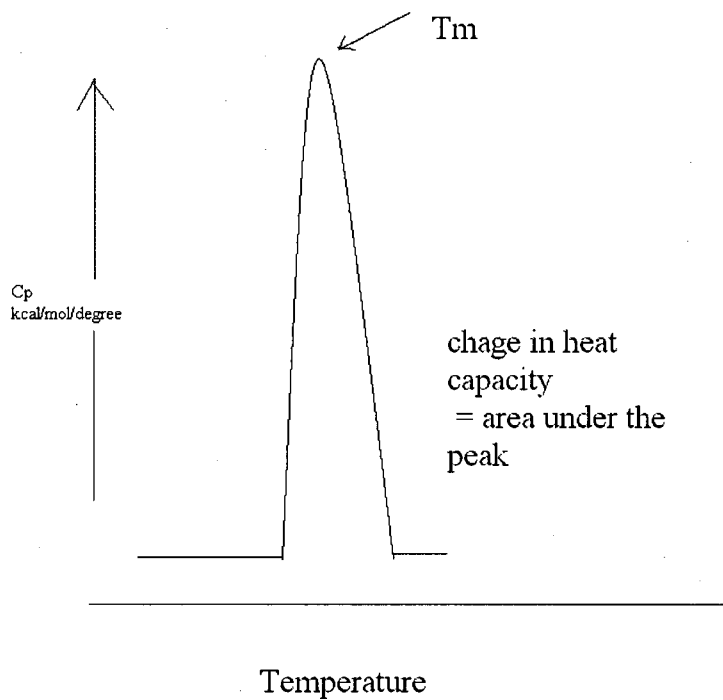
**Figure 1.7** A modern picture of a membrane [70]. This displays membrane lateral heterogeneities, cluster and domain formation within the membrane plain. Protein penetrates through the membrane or is bound to surface.

## 1.5 Phase Transition

Lipids, like other compounds undergo changes in the physical state. The phase transition of phospholipids has been widely studied as a result of their biological significance in living cells [71]. The change in physical state is known as phase transition. In the membranes, composed of synthetic lipids, the phase transition from liquid to solid state occur at a critical temperature that depends on the structure of the phospholipids. In homogenous membranes this is called the melting temperature ( $T_m$ ). The transition temperature of membrane depends on the length and saturation of the acyl chain in hydrophobic region. The  $T_m$  can be affected by properties of the headgroup region and charge screening at higher salt concentrations.

Above  $T_m$  regions, the membrane is fluidic and the lipids diffuse freely inside the lipid bilayer. Below the  $T_m$  is the gel phase of the lipid or the liquid crystalline phase. In this region, the membrane is immobile and the lipids are packed in an ordered trans-configuration. At the phase transition temperature, two phases coexist that result in properties that neither fluid nor gel. Pure lipids have a sharp and well defined transition temperature with a more significant cooperativity in the melting process [55]. This is displayed in differential scanning calorimetry as a sharp and conspicuous peak. The transition phase behavior of phospholipids is determined to a large extent by hydrocarbon chains [58]. The bilayer transition temperature increases with effective chain length and degree of unsaturation of the lipids [72]. The polar headgroup influences the phase transition [73] by affecting the lipid chain packing. This is observed in the pre-transition as depicted in the calorimetry diagram in Figure

1.8. The changes are observed from the lamellar to the non lamellar phases [74]. For example, the PE headgroup protonation leads to the change from a lamellar to a non-lamellar transition. The biological significance of this behavior is observed in membrane fusion processes.

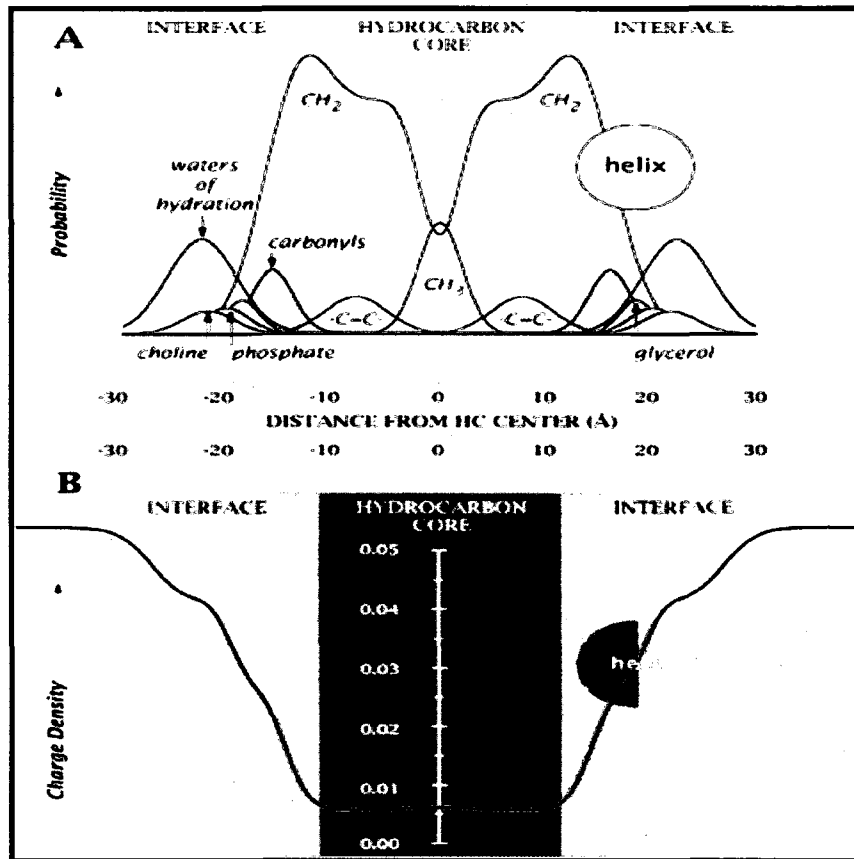


**Figure 1.8** Schematic diagram representing an endothermic peak in calorimetry.

## 1.6 Dielectric Constant of the Bilayer

Individual water molecules can penetrate the lipid bilayer below the surface. Using electron spin resonance spin-labeling measurements, the hydrocarbon region of the saturated phospholipid membranes is hydrated and this level of water is reduced by the presence of cholesterol and lipid unsaturation [75, 76]. The penetration of water into the interior of the lipid bilayer leads to membrane polarity and hydration profiles across the lipid bilayer. This is important for the maintenance of the structure and for transport across the bilayer.

A gradient of polarity exists that is high at the bilayer-water interface and low at the bilayer centre (Figure 1.9). Consequently, an electric field gradient is formed across the lipid bilayer [77]. These fields contribute to the surface and dipole potentials [78, 79]. The dielectric constant increases from two to eighty from the hydrophobic core to bulk water respectively. However, these values depend on the methods used to acquire the data. Using a theoretical approach, Levitt and Huang [80] obtained a value of 2.06 at the hydrocarbons core of the bilayer. Cametti and Di Biasio [81] obtained a value same as above. The dielectric constant of the polar headgroup was estimated between 10 and 45 units by Toccane and Teissie [82]. The interfacial region has a strong dipole moment. It can attract the counter ions from bulk medium. The first layer of water molecules bound by hydrogen bonds to the membrane is polarized while second layer has no preferred orientations that significantly influence the permeability of the polar compounds [83-85].

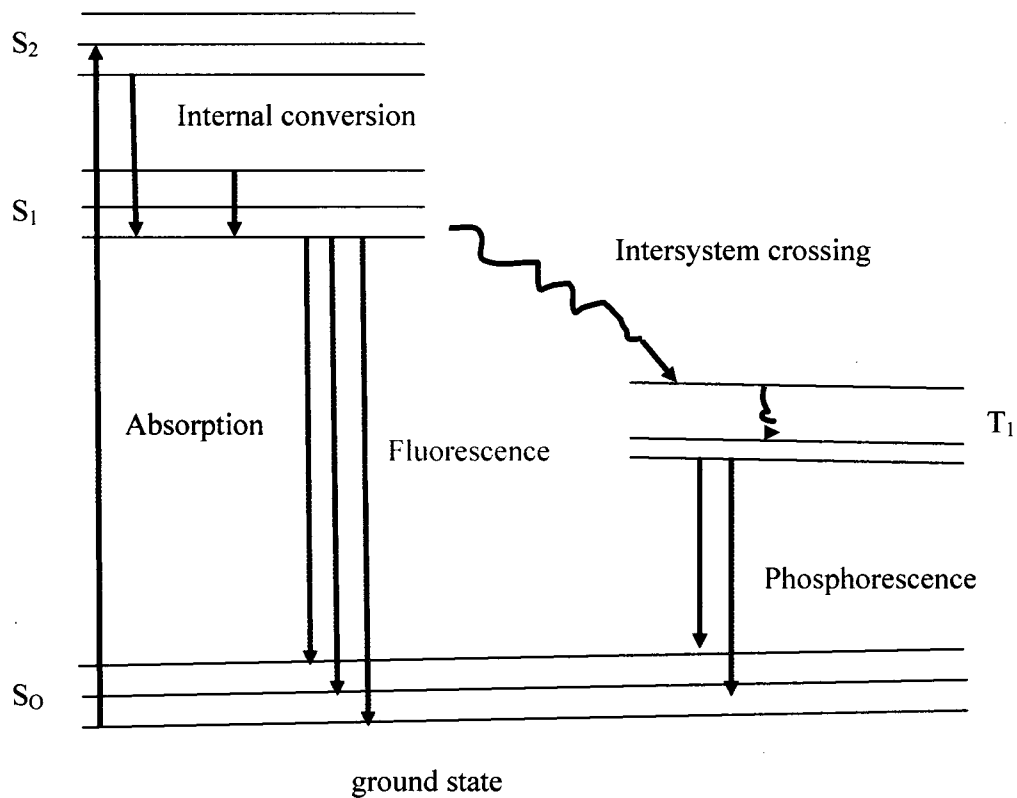


**Figure 1.9** Dielectric constant profile of the lipid bilayer. The figure shows the thickness of the hydrocarbons core and the interface regions. Part B is a representation of the variations in the dielectric constant within a lipid bilayer [68].

## 1.7 Fluorescence Spectroscopy

Structures and dynamics of the lipid bilayer have been determined largely from fluorescence spectroscopy studies. Fluorescence is the emission of light from the electronically excited states. Fluorescence emission is best understood from the diagram proposed by Jablonski [86]. Figure 1.10 is a representation of Jablonski diagram. In this diagram a process of light absorption and emission is illustrated by vertical lines that show energy levels. The horizontal lines represent spin multiplicity. Radiative transitions are shown by straight lines while nonradiative transitions by squiggly arrows.

In this diagram, the singlet excited state, the electron in the excited state is opposite in spin to original partner in the ground state orbital. Consequently, return to the ground state is spin allowed and occurs rapidly with the emission of a photon. The fluorescence lifetime  $\tau$ , is determined from the decay of fluorescence intensity of a fluorophore after excitation. Immediately after excitation, the fluorescence intensity  $I_0$ , will be at maximum and then decreases exponentially according to equation 1.1

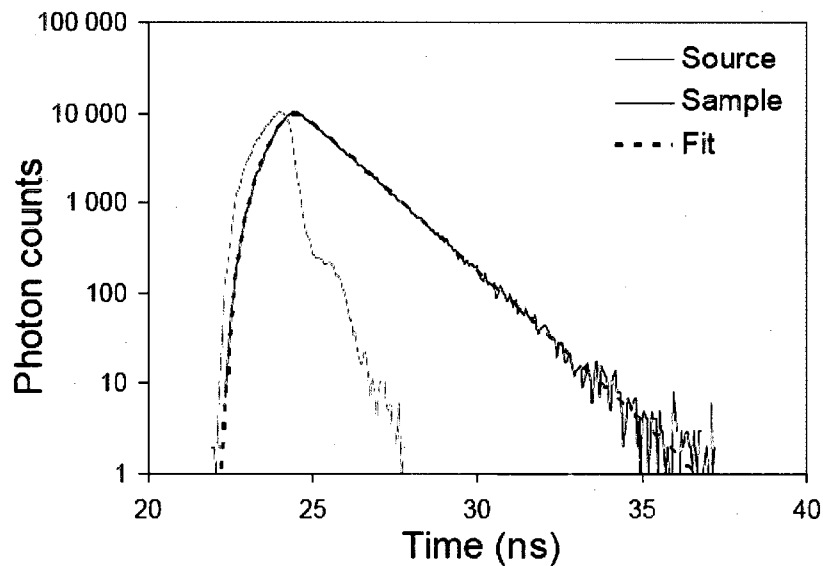


**Figure 1.10** Schematic representation of Jablonski diagram. The diagram illustrates electronic states of molecule and the transition between them.  $S_0$  and  $S_1$  and  $S_2$  are singlet ground, first and second electronic states respectively.  $T_1$  is the triplet state.



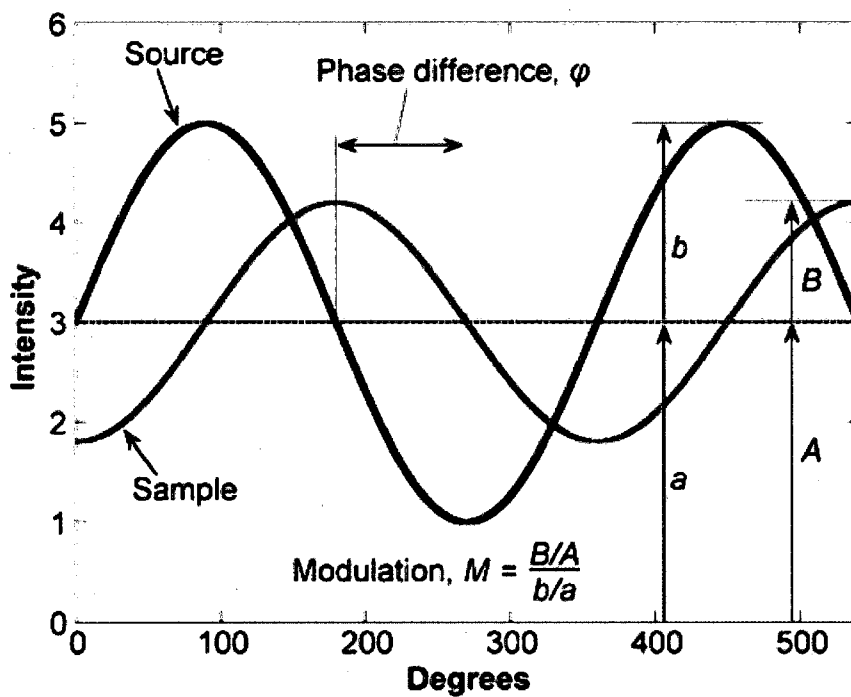
$$I(t) = I_0 e^{-t/\tau} \quad [1.1]$$

Fluorescence lifetime can be measured based on time (Figure 1.11) or frequency domain (Figure 1.12). In the time domain, a short pulse of light excites the sample. The fluorescence emission from the sample is recorded as a function of time on a nanosecond time scale. Time-domain can be recorded by camera, integrators and the more superior time correlated single-photon counting (TCSPC).



**Figure 1.11** Time-domain lifetime measurement. The gray is the pulsed light source (instrument response function, IRF) and the dark color is the sample response. A single exponential fit yields lifetime [86].

In frequency domain, the sample is excited by a modulated source of light. The fluorescence emitted by the sample has a similar waveform and is phase shifted from the excitation curve. Both the modulation and the phase shift are determined by the lifetime and therefore one can determine the lifetime based on the observed modulation and phase shift.



**Figure 1.12** Frequency domain lifetime measurement. Excitation source in black and the sample response in gray illustrating the phase angle shift ( $\phi$ ) and the demodulation ratio ( $M$ ) [86].

Fluorescence studies can discern the environment of a fluorophore in the lipid bilayer. The following parameters can be obtained from fluorescence studies: viscosity, pH, temperature, polarity and solvation dynamics and fluorescence anisotropy. In fluorescence anisotropy, the fluorophore is excited with plane polarized light. The light is emitted in the same polarized plane, provided the molecule remains stationary throughout the excited state. But in most cases the molecule rotates and tumbles out of this plane during the excited state and light is emitted in a different plane relative to the excited light.

When vertically polarized light is exciting the fluorophore, then the intensity of emitted light can be monitored either in the vertical or the horizontal planes (perpendicular or parallel). If the molecule is small, then rotation and tumbling are faster and the emitted light is depolarized relative to the excitation plane. Fluorescence anisotropies  $\langle r \rangle$  can be calculated from fluorescence intensities measured in directions parallel ( $I_{\parallel}$ ) and perpendicular ( $I_{\perp}$ ) to the electric vector of the exciting light from the following equation 1.2.

$$r = \frac{I_{\parallel} - G * I_{\perp}}{I_{\parallel} + 2 * G * I_{\perp}} \quad [1.2]$$

In this equation  $r$  refers to the anisotropy value and  $G$  is grating correction factor which measures instrument sensitivity or the detection efficiencies determined by wavelength. Fluorescence anisotropy can act as an indicator of the mobility of a fluorophore and hence viscosity in the membranes where the fluorophore is embedded.

### **1.8 Membrane Probes**

Fluorescence spectroscopy can detect extremely low probe concentrations in the lipid membrane. Consequently, there is little interference with the membrane properties that is accessed by the fluorescent probes. A fluorescent lipid probe must be similar to the native lipids to reduce the effects on the membrane properties that are under investigation. It should also respond to the polarity of the microenvironment and be randomly distributed in the host lipids. The depth and location within the membrane must be known for a good and sensitive probe.

Solvatochromic fluorescence membrane probes have been used to determine the polarity and hydration of the lipid bilayer [77]. These probes include dansyl, laurdan, 7-nitrobenz-2-oxa-1,3-diazol-4-yl (NBD), and anthroyloxy derivatives [16, 87-92]. Anthroyloxy fatty acid fluorescent probes have shown a Stokes shift and mean relaxation times that are strongly dependent on the position of the probe in small unilamellar vesicles [93]. This probe is more sensitive to solvent dynamics at variable membrane depths [94]. A diphenylhexatriene membrane probe has been used to investigate fluidity, order and membrane depth and structure relationship [95-97].

The pyrene probe localizes to the hydrophobic region of the bilayer. It forms excited state dimers (excimer) in a diffusion limited reaction that is sensitive to the temperature fluctuations and can monitor diffusion processes in membranes [98, 99]. The phase state of phospholipid membranes has been determined by the fluorescent probe Laurdan [100], based on its ability to sense membrane polarity and dynamics from the dipolar relaxation processes in the immediate environment. Laurdan is a molecule that has lauric acid tail that strongly interacts with the lipid alkyl tail. The fluorescent moiety is located in the glycerol region of phospholipid molecule.

### **1.8.1 NBD Membrane Fluorescent Probe**

A membrane probe can be from either non-lipid origin or fluorophores attached to a lipid moiety. Membrane probes from a non-lipid origin include pyrene and diphenylhexatriene. Fluorophores attached to a lipid skeleton include the 7-nitrobenz-2-oxa-1,3-diazol-4-yl (NBD). NBD can be attached to one of the acyl-chains of phospholipids [101] or linked to the headgroup region of the same [102]. This fluorophore was discovered in 1968 [103] and showed potent photophysical properties [101, 102, 104]. NBD fluorescent probe fluoresces weakly in water and strongly in solvents of low dielectric constant [102, 105]. This has been helpful in the study of membranes [17]. It can be used to estimate the depth of water penetration in a lipid bilayer based on the Red Edge Excitation Shift. It is also used for both spectroscopic and microscopic investigations of membranes [106]. The NBD probe was used to determine membrane asymmetry [107], bilayer defects, and permeability

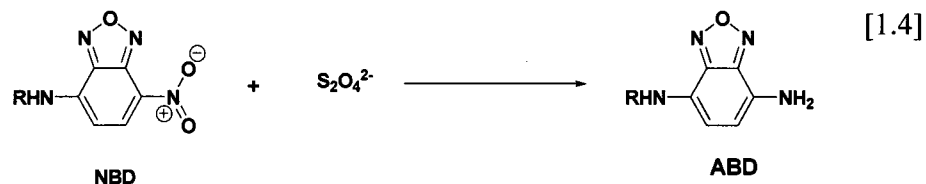
[108]. The NBD prefers a more polar environment in the membrane [109]. The maximum absorption wavelength of NBD-labeled liposome dispersions occur in a narrow range around a central value of 335 nm for the  $\pi, \pi^*$  band and 470 nm for the charge transfer band [17], with a fluorescence emission spectrum at around 541 nm. With the increasing polarity of the environment, the absorptivity of the charge transfer (470 nm) increases strongly whereas the  $\pi, \pi^*$  transition remains constant [110]. Probe populations residing in different environmental polarities can therefore be estimated by selecting the excitation wavelength of either 470 or 335 nm [16]. The charge transfer between the electron-donating amino group and the electron-accepting nitro group is a unique photophysical property that varies with the polarity of the surrounding environment. In a non-polar medium, the NBD group absorption maximum occurs between 420 and 450 nm [111]. In polar media such as water, this value covers a narrow range near 470 nm. The fluorescence emission maximum shifts from 490-519 nm to 566-571 nm when the dielectric constant increases from that of hydrocarbon to water [104]. Therefore, the NBD moiety is a good indicator of the polarity of the environment where it is located. NBD embedded in vesicles experiences motional restriction. This was shown by the polarization values of NBD in dioleoylphosphatidylcholine (DOPC) vesicles [112]. This study showed that the NBD PC has a higher polarization values than NBD PE. This was attributed to the looping back of the NBD attached to the acyl chain. The lifetime of NBD PE was reported at 7.71 ns and that of NBD PC was slightly lower at 6 ns [112, 113].

Nichols and co-workers used resonance energy transfer that show that NBD-labeled lipids can be transferred between vesicles [114]. Calculations of the thermodynamics and kinetics of phospholipid and vesicle interaction showed that the NBD PC dissociation from and association with the lipid bilayer passes through a high energy state that has higher enthalpic contribution [115]. Vaz recently determined the rates of desorption and insertion for the association of NBD-labeled lipids in large unilamellar vesicles. The thermodynamics and kinetics involved in exchanging chemicals between membranes of a cell were determined [116, 117].

### **1.9 Dithionite Quenching of NBD**

Sodium dithionite was originally shown to reduce nitrophenols to aminophenols in alkaline solution through a radical ion intermediate  $SO_2^-$  (Equation 1.3) [118]. The reduction resulted in irreversible quenching of NBD fluorescence as well as elimination of the absorbance peak at 468 nm (see Equation 1.4).





The fluorescence-quenching property has been used to measure dithionite ion permeability through multilamellar and unilamellar vesicles [108, 119]. 1 mol % of NBD PE probe was added to large unilamellar liposomes resulting in a slightly asymmetrical labeled bilayer [120]. Addition of dithionite to the outside of the liposomes results in an immediate reaction with NBD molecules in the outer leaflets within 10 to 20 seconds. Studies have indicated that  $\text{S}_2\text{O}_4^{2-}$  ion or  $\text{SO}_2^-$  radicals permeate through the lipid bilayer leading to subsequent reaction with NBD in the inner monolayer [107]. Addition of dithionite reagent causes the emission to drop quickly. It was found that any subsequent decay is due to permeation of the dithionite ion through the lipid membrane and reaction with the NBD in the inner leaflets. The addition of Triton X-100 destroys all the vesicles, allowing dithionite to react with all the NBD molecules. The absorbance signal never reaches zero due to some residual absorbance.

The rate of dithionite quenching of the NBD in liposomes is dependent on the dipole potential [121]. The dipole potential is one of the electrostatic interactions in and near the membrane. Other potentials are the surface and transmembrane



potentials. The dipole potential of the interface arises as a result of the orientation of the carbonyls, phosphate, choline, ethanolamine and the organization of water dipoles in the hydration sphere. The dipole potential decreases abruptly at the phase transition of the bilayer. The properties of NBD can have potential applications in discerning membrane phase transition [16].

## **1.10 Lipid Bilayer Dynamics**

### **1.10.1 Membrane Fluidity**

The dynamics of biological membranes are best understood by considering membrane fluidity and lateral organization. The fluidity of the membrane is highly regulated by both the headgroup and acyl chain of phospholipids [122], temperatures, and presence of cholesterol. Hydrocarbon tails of lipids pack closely at low temperature to form an ordered and rigid gel phase state. When the temperature increases, the lipid molecules vibrate more rapidly. The bilayer melts into a disordered and more fluid phase state. At a higher temperature or in the presence of short or double bonds in the hydrocarbon chain, the bilayer is fluid. Short chains have fewer interactions with the neighboring chains. This leads to a low melting temperature. The presence of a double bond causes lipid chains to bend and not to pack together, thereby increasing membrane fluidity. Cholesterol has a hydroxyl group that aligns close to the headgroup of phospholipids. The hydrophobic rings and the side chains of cholesterol are buried within the fatty acyl chains of the bilayer.

The rigid steroid ring interacts with the tails and stiffens them. This leads to less fluidity of the bilayer.

### 1.10.2 Membrane Dynamics

Lipid membrane dynamic studies have relied primarily on electron paramagnetic resonance. A nitroxide free radical moiety has been used as a monitoring group. This moiety can be located at various depths and domains in membranes [123, 124]. The spin-lattice relaxation time of spin labels has yielded biomolecular rate constants due to collisions between paramagnetic molecules and nitroxide spin labels [125-127]. The relaxation time is much longer ( $10^{-6}$ - $10^{-5}$ s) than the rotational times ( $10^{-10}$ - $10^{-9}$ s). Thus, it is possible to study membrane dynamics in longer time scales [128].

The  $^1\text{H}$  magic angle spinning nuclear Overhauser enhancement spectroscopy ( $^1\text{H}$  MAS NOESY) was recently used to study the dynamics and location of NBD covalently attached to the short (C6) or the long (C12) *sn2* acyl chain of phosphatidylcholine molecule [109]. The study showed that the long chain analog was more accessible to dithionite present in the aqueous phase compared to the short-chain one and both showed a broad distribution in the upper acyl chain glycerol region of the phospholipid bilayer. A study conducted by Huster and his co-workers using the  $^1\text{H}$  MAS NOESY method showed that the NBD attached to phosphatidylserine was folded back to the lipid-water inter and zwitterionic phosphatidylcholine membranes [129]. They observed that showed a broader

distribution of NBD in phosphatidylserine than in phosphatidylcholine. They reported that the fluorophore position was affected by the lipid packing. This was confirmed by studies using monolayers [111]. The localization of the NBD towards the interfacial region is stabilized by both electrostatic and non-polar forces that are balanced in a complex manner [109] but more towards electrostatic forces. These forces develop from the strong dipole moment of aromatic NBD. The distribution of the molecule is broad since it has been found in both the lower acyl-chain as well as the headgroup region in the lipid bilayer [109]. This can be attributed to disorder and structural reorientation of the probe in phospholipid membranes determined by X-ray studies [130].

The NBD group attached to cholesterol was found localized deeper in the hydrocarbon region of the membrane between 5 and 6 Å from the centre of the bilayer [131, 132]. Here, the NBD in cholesterol does not loop back probably due to the rigidity of the sterol ring [101]. On the other side, NBD PC has a tendency to segregate into micro-domains in the gel state membranes. It partitions into the fluid domains in fluid-gel coexistence regions which is not observed in headgroup labeled NBD [133]. The headgroup labeled NBD in the DPPN fluorophore is located in an hydrophobic environment which result in changes in the rate constant and relative fluorescence intensity [16]. This reduces the accessibility NBD to dithionite at the transition region where the lateral compressibility of the bilayer is maximum [134, 135]. The change in organization and dynamics of Triton X-100 micelles was studied in the presence of urea. The results showed that fluorescence emission maximum,

anisotropy, lifetime and quenching were increased with increase in polarity around the NBD group as a result of water penetration in the micelle [136].

### **1.11 Dynamics of Pore Formation and Line Tension in Giant Vesicles**

A cell is enclosed with a phospholipid bilayer. This bilayer controls transport of molecules and ions across the cell. This is essential for cellular viability and function. Understanding the mechanism involved in transmembrane transport is important because of its wider application in therapeutics, nonviral gene therapy and target drug delivery in liposomes. Pores allow transport across membranes. Pore-mediated cellular processes such as endocytosis, exocytosis, cell fusion and cell division are poorly understood. Fundamental mechanism involved in pore formation is still lacking despite several research in this area.

Giant vesicles are useful models for studying pore formation dynamics in cell membranes. Transient pores have been generated in model membranes using different methods. These techniques include proteins [137, 138], electroporation [139-141], micropipette aspiration [142] and visible light radiation [42]. An important step in understanding pore formation dynamics is to visualize pore formation by laser ablation in a giant vesicle in an optical microscope. Pore opening is driven by surface tension while pore closure by line tension [41, 143, 144]. Line tension is a weak one-dimensional force measured in piconewton (pN). Line tension opposes surface tension.

Direct measurement of line tension is difficult because it is small. Using pore dynamics, it has been shown that the line tension can be modified by addition of cholesterol and surfactant [145]. The line tension estimates range from 0.1 to 10 pN [146, 147]. Measurements of line tension in a phase coexistence membrane domains have resulted in a very small value of 1 pN [29, 148]. The values of line tension obtained depend on several parameters of the vesicle. Among others are hydrophobic mismatch in phase segregated domains [149] and impurities [42]. Pore opening is a function of the balance forces between forces driving the opening (or closing) of the pore and those damping the opening. The latter depends on the viscosity.

### **1.12 Conclusion**

In this chapter, a survey of the literature on giant vesicles as models for cell membranes studies is presented. Giant vesicles have become model systems for understanding natural cell membranes. These liposomes have advantage over the small conventional liposomes. They can be visualized in an optical microscope, manipulated by micropipette and in a laser tweezer. They have been used as microreactors to perform certain chemical reactions in a small confined volume in femtolitres. Giant vesicles have been used to study cell mechanical properties such as elasticity and bending modulus. Opening pores in a giant liposome is a step toward inserting small molecules into the lumen of the liposome. This step is important in drug delivery and in understanding transmembrane transport in cellular membranes.

In this chapter, methods used in generating giant liposomes under physiological conditions are highlighted. Liposomes are derived from phospholipids. The structures of phospholipids are presented. The dynamics of lipid bilayer is presented. The methods used to discern the dynamics of lipid bilayer are presented in detail. The application of fluorescent probes to discern the bilayer region of lipid membrane is enumerated. The dynamics of NBD probe located in the headgroup region and acyl chain of a phospholipid is discussed with respect to dielectric constant and the polarity of the membrane in different phospholipid bilayers. Finally, the dynamics of the pore formation and measurement of line tension in giant vesicles are discussed and the importance outlined in detail.

This thesis is in two parts divided into 10 Chapters. The experimental procedures and methods are presented in Chapter 2. Chapter 3 is a discussion of giant vesicles made from a two-component lipid system that displays gel and fluid co-existence. The excited state lifetime measurements of the NBD in lipid acyl-chain of variable lengths will be presented in Chapter 4. The time-resolved measurement of the NBD probe in DMPC and egg PC liposomes is presented in Chapter 5. The laser ablation technique and pore dynamics to measure the line tension from the pore closing dynamics is summarized in Chapter 6. Part two covers Chapters 7 to 9 of this thesis. It presents studies that were conducted on human Wilson disease protein. Conclusion and future research are summarized in Chapter 10.

### 1.13 References

- 1 Menger, F. M., Keiper, J. S. (1998) Chemistry and physics of giant vesicles as biomembrane models. *Curr Opin Chem Biol* **2**, 726-732
- 2 Menger, F. M., Angelova, M. I. (1998) Giant vesicles: imitating the cytological processes of cell membranes. *Acc Chem Res* **31**, 789-797
- 3 Rodriguez, N., Pincet, F., Cribier, S. (2005) Giant vesicles formed by gentle hydration and electroformation: A comparison by fluorescence microscopy. *Colloids Surf B Biointerfaces* **42**, 125-130
- 4 Roux, A., Cappello, G., Cartaud, J., Prost, J., Goud, B., Bassereau, P. (2002) A minimal system allowing tubulation with molecular motors pulling on giant liposomes. *Proc Natl Acad Sci U S A* **99**, 5394-5399
- 5 Koster, G., VanDuijn, M., Hofs, B., Dogterom, M. (2003) Membrane tube formation from giant vesicles by dynamic association of motor proteins. *Proc Natl Acad Sci U S A* **100**, 15583-15588
- 6 Evans, E., Heinrich, V., Ludwig, F., Rawicz, W. (2003) Dynamic tension spectroscopy and strength of biomembranes. *Biophys J* **85**, 2342-2350
- 7 Rawicz, W., Smith, B. A., McIntosh, T. J., Simon, S. A., Evans, E. (2008) Elasticity, strength, and water permeability of bilayers that contain raft microdomain-forming lipids. *Biophys J* **94**, 4725-4736
- 8 Sackmann, E. (1994) The seventh Datta Lecture. Membrane bending energy concept of vesicle- and cell-shapes and shape-transitions. *FEBS Lett* **346**, 3-16
- 9 Kwok, R., Evans, E. (1981) Thermoelasticity of large lecithin bilayer vesicles. *Biophys J* **35**, 637-652

- 10 Rawicz, W., Olbrich, K. C., McIntosh, T., Needham, D., Evans, E. (2000) Effect of chain length and unsaturation on elasticity of lipid bilayers. *Biophys J* **79**, 328-339
- 11 Meleard, P., Gerbeaud, C., Bardusco, P., Jeandaine, N., Mitov, M. D. and Fernandez-Puente, L. (1998) Mechanical properties of model membranes studied from shape transformations of giant vesicles. *Biochimie* **80**, 401-413
- 12 Baoukina, S., Monticelli, L., Risselada, H. J., Marrink, S. J. and Tieleman, D. P. (2008) The molecular mechanism of lipid monolayer collapse. *Proc Natl Acad Sci U S A* **105**, 10803-10808
- 13 Zuckermann, M. J. and Heimburg, T. (2001) Insertion and pore formation driven by adsorption of proteins onto lipid bilayer membrane-water interfaces. *Biophys J* **81**, 2458-2472
- 14 Nomura, S. M., Yoshikawa, Y., Yoshikawa, K., Dannenmuller, O., Chasserot-Golaz, S., Ourisson, G., Nakatani, Y. (2001) Towards proto-cells: "primitive" lipid vesicles encapsulating giant DNA and its histone complex. *Chembiochem* **2**, 457-459
- 15 Nomura, S. M., Tsumoto, K., Yoshikawa, K., Ourisson, G., Nakatani, Y. (2002) Towards proto-cells: "primitive" lipid vesicles encapsulating giant DNA and its histone complex. *Cell Mol Biol Lett* **7**, 245-246
- 16 Alakoskela, J. M. I., Kinnunen, P. K. J. (2001) Probing phospholipid main phase transition by fluorescence and a surface redox reaction. *J Phys Chem B* **105**, 11294-11301
- 17 Mazeres, S., Schram, V., Tocanne, J. F. and Lopez, A. (1996) 7-nitrobenz-2-oxa-1,3-diazole-4-yl-labeled phospholipids in lipid membranes: differences in fluorescence behavior. *Biophys J* **71**, 327-335
- 18 Schram, V. and Thompson, T. E. (1995) Interdigitation does not affect translational diffusion of lipids in liquid crystalline bilayers. *Biophys J* **69**, 2517-2520



- 19 Angelova, M. I., Tsoneva, I. (1999) Interactions of DNA with giant liposomes. *Chem Phys Lipids* **101**, 123-137
- 20 Fischer, A., Oberholzer, T., Luisi, P. L. (2000) Giant vesicles as models to study the interactions between membranes and proteins. *Biochim Biophys Acta* **1467**, 177-188
- 21 Oberholzer, T., Nierhaus, K. H., Luisi, P. L. (1999) Protein expression in liposomes. *Biochem Biophys Res Commun* **261**, 238-241
- 22 Oberholzer, T., Albrizio, M., Luisi, P. L. (1995) Polymerase chain reaction in liposomes. *Chem Biol* **2**, 677-682
- 23 Singer, S. J., Nicolson, G. L. (1972) The fluid mosaic model of the structure of cell membranes. *Science* **175**, 720-731
- 24 Przybylo, M., Sykora, J., Humpolickova, J., Benda, A., Zan, A., Hof, M. (2006) Lipid diffusion in giant unilamellar vesicles is more than 2 times faster than in supported phospholipid bilayers under identical conditions. *Langmuir* **22**, 9096-9099
- 25 Dobereiner, H. G., Kas, J., Noppl, D., Sprenger, I., Sackmann, E. (1993) Budding and fission of vesicles. *Biophys J* **65**, 1396-1403
- 26 Mironov, A. A., Weidman, P., Luini, A. (1997) Variations on the intracellular transport theme: maturing cisternae and trafficking tubules. *J Cell Biol* **138**, 481-484
- 27 Staneva, G., Angelova, M. I., Koumanov, K. (2004) Phospholipase A2 promotes raft budding and fission from giant liposomes. *Chem Phys Lipids* **129**, 53-62
- 28 Staneva, G., Seigneuret, M., Koumanov, K., Trugnan, G., Angelova, M. I. (2005) Detergents induce raft-like domains budding and fission from giant unilamellar heterogeneous vesicles: a direct microscopy observation. *Chem Phys Lipids* **136**, 55-66

- 29 Baumgart, T., Hess, S. T., Webb, W. W. (2003) Imaging coexisting fluid domains in biomembrane models coupling curvature and line tension. *Nature* **425**, 821-824
- 30 Cinek, T., Horejsi, V. (1992) The nature of large noncovalent complexes containing glycosyl-phosphatidylinositol-anchored membrane glycoproteins and protein tyrosine kinases. *J Immunol* **149**, 2262-2270
- 31 Brown, D. A., Rose, J. K. (1992) Sorting of GPI-anchored proteins to glycolipid-enriched membrane subdomains during transport to the apical cell surface. *Cell* **68**, 533-544
- 32 Moscho, A., Orwar, O., Chiu, D. T., Modi, B. P., Zare, R. N. (1996) Rapid preparation of giant unilamellar vesicles. *Proc Natl Acad Sci USA* **93**, 11443-11447
- 33 Akashi, K., Miyata, H., Itoh, H., Kinoshita, K. Jr. (1996) Preparation of giant liposomes in physiological conditions and their characterization under optical microscope. *Biophys J* **71**, 3242-3250
- 34 Akashi, K., Miyata, H., Itoh, H., Kinoshita, K. Jr. (1998) Formation of Giant Liposomes Promoted by Divalent Cations: Critical Role of Electrostatic Repulsion. *Biophys J* **74**, 2973-2982
- 35 Angelova, M., Dimitrov, D. (1986) Liposome electroformation. *Discuss Faraday Soc* **81**, 303-311
- 36 Pott, T., Bouvrais, H., Meleard, P. (2008) Giant unilamellar vesicle formation under physiologically relevant conditions. *Chem Phys Lipids* **154**, 115-119
- 37 Bagatolli, L. A., Parasassi, T., Gratton, E. (2000) Giant phospholipid vesicles: comparison among the whole lipid sample characteristics using different preparation methods. A two photon fluorescence microscopy study. *Chem Phys Lipids* **105**, 135-147

- 38 Mathivet, L., Cribier, S., Devaux, P. F. (1996) Shape change and physical properties of giant phospholipid vesicles prepared in the presence of an AC electric field. *Biophys J* **70**, 1112-1121
- 39 Estes, D. J., Mayer, M. (2005) Giant liposomes in physiological buffer using electroformation in a flow chamber. *Biochim Biophys Acta* **1712**, 152-160
- 40 Rodriguez, N., Heuvingh, J., Pincet, F., Cribier, S. (2005) Indirect evidence of submicroscopic pores in giant unilamellar [correction of unilamellar] vesicles. *Biochim Biophys Acta* **1724**, 281-287
- 41 Brochard-Wyart, F., Gennes de, G. P., Sandre, O. (2000) Transient pores in stretched vesicles: role of leak-out. *Physica A* **278**, 32-51
- 42 Karatekin, E., Sandre, O., Guitouni, H., Borghi, N., Puech, P. H., Brochard-Wyart, F. (2003) Cascades of transient pores in giant vesicles: line tension and transport. *Biophys J* **84**, 1734-1749
- 43 Rodriguez, N., Cribier, S., Pincet, F. (2006) Transition from long- to short-lived transient pores in giant vesicles in an aqueous medium. *Phys Rev E Stat Nonlin Soft Matter Phys* **74**, 061902
- 44 De Weer, P. (2000) A century of thinking about cell membranes. *Annu Rev Physiol* **62**, 919-926
- 45 Nielsen, N., Malmendal, A., Vosegaard, T. (2004) Techniques and applications of NMR to membrane proteins. *Mol Membr Biol* **21**, 129-141
- 46 Hotani, H., Nomura, F., Suzuki, Y. (1999) Giant liposomes: from membrane dynamics to cell morphogenesis. *Curr Opin Coll Int Sci* **4**, 358-368
- 47 Paavo, K. (2000) Giant liposomes as model biomembranes for roles of lipids in cellular signalling. *Perspectives in supramolecular chemistry* **6**, 273-284

- 48 Akashi, K., Kinoshita, K. Jr., Miyata, H., Itoh, H. (2000) Observation of a variety of giant vesicles under optical microscope. *Supramol Chem* **6**, 135-136
- 49 Tanford, C. (1978) The hydrophobic effect and the organization of living matter. *Science* **200**, 1012-1018
- 50 Meer, G., Holthuis M. C. J. (2000) Sphingolipid transport in eukaryotic cells. *Biochim Biophys Acta* **1486**, 145-170
- 51 Simmons, K., Ikonen, E. (2000) How cells Handle Cholesterol. *Science* **290**, 1721-1726
- 52 Ohvo-Rekila, H., Ramstedt, B., Leppimaki, P., Slotte, P. J. (2002) Cholesterol interactions with phospholipids in membranes. *Prog Lipid Res* **41**, 66-97
- 53 Brown, E. R. (1998) Sphingolipid organization in biomembranes: what physical studies of model membranes reveal. *J Cell Sci* **111**, 1-9
- 54 Devaux, F. P. (1991) Static and Dynamic Lipid Assymetry in Cell Membranes. *Biochemistry* **30**, 1163-1173
- 55 Koynova, R., Caffrey, M. (1998) Phases and phase transitions of the phosphatidylcholines. *Biochim Biophys Acta* **1376**, 91-145
- 56 Op den kamp, J. A. F. (1979) Lipid asymmetry in membranes. *Ann Rev Biochem* **48**, 47-71
- 57 Janmey, P. A., Kinnunen, J. K. P. (2006) Biophysical properties of lipids and dynamic membranes. *Trends Cell Biol* **16**, 538-546
- 58 Rand, P. R., Chapman, D., Larsson, K. (1975) Tilted Hydrocarbon Chains of Dipalmitoyl Lecithin Become Perpendicular to the Bilayer Before Melting. *Biophys J* **15**, 1117-1124

- 59 Tristram-Nagle, S., Isaacson, Y., Lyatskaya, Y., Liu, Y., Brummond, K., Katsaras, J., Nagle, F. J. (1999) Polymorphism in Myristoylpalmitoylphosphatidylcholine. *Chem Phys Lipids* **100**, 101-113
- 60 Jean, E. V. (1996) *Biochemistry of Lipids, Lipoproteins and Membranes*. Elsevier, Amsterdam; New York
- 61 Heimburg, T., Wurz, U., Marsh, D. (1992) Binary phase diagram of hydrated dimyristoylglycerol-dimyristoylphosphatidylcholine mixtures. *Biophys J* **63**, 1369-1378
- 62 Goni, M. F., Alonso, A. (1999) Structure and functional properties of diacylglycerol in membranes. *Prog Lipid Res* **38**, 1-48
- 63 Finer, E. G., Darke, A. (1974) Phospholipid hydration studied by deuterium magnetic resonance spectroscopy. *Chem Phys Lipids* **12**, 1-16
- 64 Gorter, E., Grendel, J. (1925) On bimolecular layers of lipids on the chromocytes of blood. *J Exp Med* **41**, 439-443
- 65 Mouritsen, O. G., Bloom, M. (1984) Mattress Model of Lipid-Protein Interactions in Membranes. *Biophys J* **46**, 141-153
- 66 Cullis, P. R., Hope, M. J., Tillock, C. P. S. (2006) Lipid Polymorphism. *Ann N Y Acad of Sci* **492**, 88-102
- 67 Kucerka, N., Kiselev, A. M., Balgavy, P. (2004) Determination of bilayer thickness and lipid surface area in unilamellar dimyristoylphosphatidylcholine vesicles from small-angle neutron scattering curves: a comparison of evaluation methods. *Eur Biophys J* **33**, 328-334
- 68 Mouritsen, O. G. (2005) *Life- As a Matter of Fat: The emerging Science of Lipidomics*. Springer-Verlag, Berlin Heidelberg New York

- 69 Mitra, K., Ubarretxena-Belandia, I., Taguchi, T., Warren, G., Engelman, M. D. (2004) Modulation of the bilayer thickness of the exocytic pathway membranes by membrane proteins rather than cholesterol. *Proc Natl Acad Sci U S A* **101**, 4083-4088
- 70 Heimburg, T. (2007) *Thermal Biophysics of Membranes*. Wiley-VCH
- 71 Chapman, D. (1975) Phase transitions and fluidity characteristics of lipids and cell membranes. *Q Rev Biophys* **8**, 185-235
- 72 Chapman, D., Williams, M. R., Ladbroke, D. B. (1967) Physical studies of phospholipids. VI. Thermotropic and lyotropic mesomorphism of some 1, 2-diacyl-phosphatidylcholines (lecithins). *Chem Phys Lipids* **1**, 445
- 73 Chapman, D., Urbina, J., Keough, M. K. (1974) Biomembrane phase transitions. Studies of lipid-water systems using differential scanning calorimetry. *J Biol Chem* **249**, 2512
- 74 Cullis, P. R., Hope, M. J., Tilock, C. P. S. (1986) Lipid polymorphism and the roles of lipids in membranes. *Chem Phys Lipids* **40**, 127-144
- 75 Subczynski, W. K., Wisniewska, A., Yin, J. J., Hyde, J. S., Kusumi, A. (1994) Hydrophobic barriers of lipid bilayer membranes formed by reduction of water penetration by alkyl chain unsaturation and cholesterol. *Biochemistry* **33**, 7670-7681
- 76 Tokutake, N., Jing, B., Regen, S. L. (2004) Probing the hydration of lipid bilayers using a solvent isotope effect on phospholipid mixing. *Langmuir* **20**, 8958-8960
- 77 Klymchenko, A. S., Mely, Y., Demchenko, A. P., Duportail, G. (2004) Simultaneous probing of hydration and polarity of lipid bilayers with 3-hydroxyflavone fluorescent dyes. *Biochim Biophys Acta* **1665**, 6-19

- 78 Gawrisch, K., Ruston, D., Zimmerberg, J., Parsegian, V. A., Rand, R. P., Fuller, N. (1992) Membrane dipole potentials, hydration forces, and the ordering of water at membrane surfaces. *Biophys J* **61**, 1213-1223
- 79 Zheng, C., Vanderkooi, G. (1992) Molecular origin of the internal dipole potential in lipid bilayers: calculation of the electrostatic potential. *Biophys J* **63**, 935-941
- 80 Huang, W. and Levitt, D. G. (1977) Theoretical calculation of the dielectric constant of a bilayer membrane. *Biophys J* **17**, 111-128
- 81 Di Biasio, A., Cametti, C. (2007) Dielectric properties of aqueous zwitterionic liposome suspensions. *Bioelectrochemistry* **70**, 328-334
- 82 Tocanne, J. F. and Teissie, J. (1990) Ionization of phospholipids and phospholipid-supported interfacial lateral diffusion of protons in membrane model systems. *Biochim Biophys Acta* **1031**, 111-142
- 83 Shepherd, J. C. and Buldt, G. (1978) Zwitterionic dipoles as a dielectric probe for investigating head group mobility in phospholipid membranes. *Biochim Biophys Acta* **514**, 83-94
- 84 Raudino, A. and Mauzerall, D. (1986) Dielectric properties of the polar head group region of zwitterionic lipid bilayers. *Biophys J* **50**, 441-449
- 85 Bernik, D. L., Zubiri, D., Tymczynsyn, E., Disalvo, E. A. (2001) Polarity and packing at the carbonyl and phosphate regions of lipid bilayers. *Langmuir* **17**, 6438-6442
- 86 Lackowicz, R. L. (1999) *Principles of Fluorescence Spectroscopy*. Plenum Publishers, New York, N. Y.
- 87 Krasnowska, G., E., Parasassi, T. (1998) Prodan as a membrane surface fluorescent probe: partitioning between water and phospholipid phases. *Biophys J* **74**, 1984-1993

- 88 Parasassi, T., De Stasio, G., d'Ubaldo, A., Gratton, E. (1990) Phase fluctuation in phospholipid membranes revealed by Laurdan fluorescence. *Biophys J* **57**, 1179-1186
- 89 Parasassi, T., Stefano, D. M., Loiero, M., Ravagnan, G., Gratton, E. (1994) Cholesterol modifies water concentration and dynamics in phospholipid bilayers: a fluorescence study using Laurdan probe. *Biophys J* **66**, 763-768
- 90 Ho, C., Slater, S. J., Stubbs, C. D. (1995) Hydration and order in lipid bilayers. *Biochemistry* **34**, 6188-6195
- 91 Chattopadhyay, A., Mukherjee, S. (1999) Red Edge Excitation Shift of a Deeply Embedded Membrane Probe: Implication in Water Penetration in the Bilayer. *J Phys Chem B* **103**, 8180-8185
- 92 Asuncion-Punzalan, E., Kachel, K., London, E. (1998) Groups with polar characteristics can locate at both shallow and deep locations in membranes: the behavior of dansyl and related probes. *Biochemistry* **37**, 4603-4611
- 93 Hutterer, R., Schneider, F. W., Lanig, H., Hof, M. (1997) Solvent relaxation behaviour of n-anthroyloxy fatty acids in PC-vesicles and paraffin oil: a time-resolved emission spectra study. *Biochim Biophys Acta* **1323**, 195-207
- 94 Sykora, J., Slavicek, P., Jungwirth, P., Barucha, J., Hof, M. (2007) Time-dependent Stokes shifts of fluorescent dyes in the hydrophobic backbone region of a phospholipid bilayer: combination of fluorescence spectroscopy and ab initio calculations. *J Phys Chem B* **111**, 5869-5877
- 95 Pebay-Peyroula, E., Dufourc, E. J., Szabo, A. G. (1994) Location of diphenyl-hexatriene and trimethylammonium-diphenyl-hexatriene in dipalmitoylphosphatidylcholine bilayers by neutron diffraction. *Biophys Chem* **53**, 45-56
- 96 Mely-Goubert, B., Freedman, M. H. (1980) Lipid fluidity and membrane protein monitoring using 1,6-diphenyl-1,3,5-hexatriene. *Biochim Biophys Acta* **601**, 315-327



- 97 Kaiser, R. D., London, E. (1999) Location of diphenylhexatriene (DPH) and its derivatives within membranes: comparison of different fluorescence quenching analyses of membrane depth. *Biochemistry* **38**, 2610
- 98 Vanderkooi, J. M., Callis, J. B. (1974) Pyrene. A probe of lateral diffusion in the hydrophobic region of membranes. *Biochemistry* **13**, 4000-4006
- 99 Fischkoff, S., Vanderkooi, J. M. (1975) Oxygen diffusion in biological and artificial membranes determined by the fluorochrome pyrene. *J Gen Physiol* **65**, 663-676
- 100 Mukherjee, S., Kalipatnapu, S., Pucadyil, T. J., Chattopadhyay, A. (2006) Monitoring the organization and dynamics of bovine hippocampal membranes utilizing differentially localized fluorescent membrane probes. *Mol Membr Biol* **23**, 430-441
- 101 Chattopadhyay, A. (1990) Chemistry and biology of N-(7-nitrobenz-2-oxa-1,3-diazo-4-yl): fluorescent probes of biological and model membranes. *Chem Phys Lipids* **53**, 1-15
- 102 Shaw, A. W., Christian, T. S., Monti, A. J. (1978) Synthesis and properties of highly fluorescent derivative of phosphatidylethanolamine. *J Lipid Res* **19**, 222-228
- 103 Ghosh, P. B., Whitehouse, W. M. (1968) 7-Chloro-4-nitrobenzo-2-1, 3-diazole: a new fluorogenic reagent for amino acids and other amines. *Biochem J* **108**, 155-163
- 104 Chattopadhyay, A., London, E. (1988) Spectroscopic and ionisation properties of N-(7-nitrobenz-2-oxa-1, 3-diazol-4-yl)-labeled lipids in model membranes. *Biochim Biophys Acta* **938**, 24-34
- 105 Mukherjee, S., Chattopadhyay, A., Samata, A., Soujanya, T. (1994) Dipole moment changes of NBD group upon excitation studied using solvatochromic and quantum chemical approaches; implications in membrane research. *J Phys Chem* **98**, 2809-2812

- 106 Pucadyil, T. J., Mukherjee, S., Chattopadhyay, A. (2007) Organization and dynamics of NBD-labeled lipids in membranes analyzed by fluorescence recovery after photobleaching. *J Phys Chem B* **111**, 1975-1983
- 107 McIntyre, J. C., Sleight, R. G. (1991) Fluorescent Assay for Phospholipid Membrane Assymetry. *Biochemistry* **30**, 11819-11827
- 108 Langer, M., Hui, S. W. (1993) Dithionite penetration through phospholipid bilayers as a measure of defects in lipid molecular packing. *Chem Phys Lipids* **65**, 23-30
- 109 Huster, D., Muller, P., Arnold, K., Hermann, A. (2001) Dynamics of membrane penetration of the fluorescent 7-nitrobenz-2-oxa-1,3-diazol-4-yl (NBD) group attached to an acyl chain of phosphatidylcholine. *Biophys J* **80**, 822-831
- 110 Fery-Forgues, S., Fayet, P. J., Lopez, A. (1993) Drastic changes in the fluorescence properties of NBD probes with polarity of the medium: involvement of TICT state? *J Photochem Photobiol A Chem* **70**, 229-243
- 111 Tsukanova, V., Grainger, W. D., Salessse, C. (2002) Monolayer Behavior of NBD-Labeled Phospholipids at the Air/Water Interface. *Langmuir* **18**, 5539-5550
- 112 Mukherjee, S., Raghuraman, H., Dasgupta, S., Chattopadhyay, A. (2004) Organization and dynamics of N-(7-nitrobenz-2-oxa-1,3-diazol-4-yl)-labeled lipids: a fluorescence approach. *Chem Phys Lipids* **127**, 91-101
- 113 Chattopadhyay, A., Mukherjee, S. (1993) Fluorophore environments in membrane-bound probes: A red edge excitation shift study. *Biochemistry* **32**, 3804-3811
- 114 Nichols, W. J., Pagano E. R. (1982) Use of resonance energy transfer to study the kinetics of amphiphile transfer between vesicles. *Biochemistry* **21**, 1720-1726

- 115 Nichols, W. J. (1985) Thermodynamics and Kinetics of Phospholipid Monomer-Vesicle Interaction. *Biochemistry* **24**, 6390-6398
- 116 Abreu, M. S., Moreno, M. J., Vaz, W. L. (2004) Kinetics and thermodynamics of association of a phospholipid derivative with lipid bilayers in liquid-disordered and liquid-ordered phases. *Biophys J* **87**, 353-365
- 117 Sampaio, J. L., Moreno, M. J., Vaz, W. L. (2005) Kinetics and thermodynamics of association of a fluorescent lysophospholipid derivative with lipid bilayers in liquid-ordered and liquid-disordered phases. *Biophys J* **88**, 4064-4071
- 118 Wasmuth, C. R., Edwards, C., Hutcherson, R. (1964) Participation of the SO Radical Ion in the Reduction of p-Nitrophenol by Sodium Dithionite. *J Phys Chem* **68**, 423-425
- 119 Langer, M., Hui, S. W. (2000) Effect of free fatty acids on the permeability of 1,2-dimyristoyl-sn-glycero-3-phosphocholine bilayer at main phase transition. *Biochim Biophys Acta* **1463**, 439-447
- 120 Balch, R., Morris, R., Sleight, G. R. (1994) The use of N-(7-nitrobenz-2-oxa-1,3-diazole-4-yl)-labeled lipids in determining transmembrane lipid distribution. *Chem Phys Lipids* **70**, 205-212
- 121 Alakoskela, J.-M. I., Kinnunen, P. K. J. (2001) Control of a redox reaction on lipid bilayer surfaces by membrane dipole potential. *Biophys J* **80**, 294-304
- 122 Seu, K. J., Cambrea, L. R., Everly, R. M., Hovis, J. S. (2006) Influence of lipid chemistry on membrane fluidity: tail and headgroup interactions. *Biophys J* **91**, 3727-3735
- 123 Kusumi, A., Subczynski, W. K., Pasenkiewicz-Gierula, M., Hyde, J. S., Merkle, H. (1986) Spin-label studies on phosphatidylcholine-cholesterol membranes: effects of alkyl chain length and unsaturation in the fluid phase. *Biochim Biophys Acta* **854**, 307-317

- 124 Subczynski, W. K., Markowska, E., Siewiewsiuk, J. (1993) Spin-label studies on phosphatidylcholine-polar carotenoid membranes: effects of alkyl-chain length and unsaturation. *Biochim Biophys Acta* **1150**, 173-181
- 125 Kusumi, A., Subczynski, W. K., Hyde, J. S. (1982) Oxygen transport parameter in membranes as deduced by saturation recovery measurements of spin-lattice relaxation times of spin labels. *Proc Natl Acad Sci U S A* **79**, 1854-1858
- 126 Subczynski, W. K., Hyde, J. S., Kusumi, A. (1989) Oxygen permeability of phosphatidylcholine--cholesterol membranes. *Proc Natl Acad Sci U S A* **86**, 4474-4478
- 127 Subczynski, W. K., Antholine, W. E., Hyde, J. S., Kusumi, A. (1990) Microimmiscibility and three-dimensional dynamic structures of phosphatidylcholine-cholesterol membranes: translational diffusion of a copper complex in the membrane. *Biochemistry* **29**, 7936-7945
- 128 Subczynski, W. K., Wisniewska, A. (2000) Physical properties of lipid bilayer membranes: relevance to membrane biological functions. *Acta Biochim Pol* **47**, 613-625
- 129 Huster, D., Muller, P., Arnold, K. (2003) Dynamics of lipid chain attached fluorophore 7-nitrobenz-2-oxa-1, 3-diazol-4-yl (NBD) in negatively charged membranes determined by NMR spectroscopy. *Eur Biophys J* **32**, 47-54
- 130 Wiener, M. C., White, H. S. (1992) Structure of a fluid dioleoylphosphatidylcholine bilayer determined by joint refinement of x-ray and neutron diffraction data III. Complete structure. *Biophys J* **61**, 434-447
- 131 Chattopadhyay, A., London, E. (1987) Parallax method for direct measurement of membrane penetration depth utilizing fluorescence quenching by spin-labeled phospholipids. *Biochemistry* **26**, 39-45
- 132 Mukherjee, S., Chattopadhyay, A. (1996) Membrane Organization at Low Cholesterols: A study Using 7-Nitrobenz-2-oxa-1,3-diazol-4-yl-Labeled Cholesterol. *Biochemistry* **35**, 1311-1322

- 133 Weis, R. M. (1991) Fluorescence microscopy of phospholipid monolayer phase transitions. *Chem Phys Lipids* **57**, 227-239
- 134 Evans, E., Kwok, R. (1982) Mechanical calorimetry of large dimyristoylphosphatidylcholine vesicles in the phase transition region. *Biochemistry* **21**, 4874-4879
- 135 Nagle, J. F., Scott, L. H. (1978) Lateral compressibility of lipid mono and bilayers. Theory of membrane permeability. *Biochim Biophys Acta* **513**, 236-243
- 136 Raghuraman, H., Pradhan, K. S., Chattopadhyay, A. (2004) Effect of Urea on the organization and Dynamics of Triton X-100 Micelles: A Fluorescence Approach. *J Phys Chem B* **108**, 2489-2496
- 137 Ladokhin, A. S., Selsted, M. E., White, S. H. (1997) Sizing membrane pores in lipid vesicles by leakage of co-encapsulated markers: pore formation by melittin. *Biophys J* **72**, 1762-1766
- 138 Hanke, W., Methfessel, C., Wilmsen, H. U., Katz, E., Jung, G. and Boehm, G. (1983) Melittin and a chemically modified trichotoxin form alamethicin-type multi-state pores. *Biochim Biophys Acta* **727**, 108-114
- 139 Ho, S. Y., Mittal, G. S. (1996) Electroporation of cell membranes: a review. *Crit Rev Biotechnol* **16**, 349-362
- 140 Vernier, P. T., Ziegler, M. J. (2007) Nanosecond field alignment of head group and water dipoles in electroporating phospholipid bilayers. *J Phys Chem B* **111**, 12993-12996
- 141 Riske, K. A., Dimova, R. (2005) Electro-deformation and poration of giant vesicles viewed with high temporal resolution. *Biophys J* **88**, 1143-1155
- 142 Evans, E., Heinrich, V., Ludwig, F., Rawicz, W. (2003) Dynamic tension spectroscopy and strength of biomembranes. *Biophys J* **85**, 2342-2350

- 143 Taupin, C., Dvolaitzky, M., Sauterey, C. (1975) Osmotic pressure induced pores in phospholipid vesicles. *Biochemistry* **14**, 4771-4775
- 144 Sandre, O., Moreaux, L., Brochard-Wyart, F. (1999) Dynamics of transient pores in stretched vesicles. *Proc Natl Acad Sci U S A* **96**, 10591-10596
- 145 Karatekin, E., Sandre, O., Brochard-Wyart, F. (2003) Transient pores in vesicles. *Polym Int* **52**, 486-493
- 146 Towles, K. B., Dan, N. (2007) Line tension and coalescence in heterogeneous membranes. *Langmuir* **23**, 13053-13058
- 147 Akimov, S. A., Kuzmin, P. I., Zimmerberg, J., Cohen, F. S. (2007) Lateral tension increases the line tension between two domains in a lipid bilayer membrane. *Phys Rev E Stat Nonlin Soft Matter Phys* **75**, 011919
- 148 Baumgart, T., Das, S., Webb, W. W., Jenkins, J. T. (2005) Membrane elasticity in giant vesicles with fluid phase coexistence. *Biophys J* **89**, 1067-1080
- 149 Blanchette, C. D., Lin, W. C., Orme, C. A., Ratto, T. V., Longo, M. L. (2007) Using nucleation rates to determine the interfacial line tension of symmetric and asymmetric lipid bilayer domains. *Langmuir* **23**, 5875-5877

## CHAPTER 2

### EXPERIMENTAL METHODS AND PROCEDURES

#### 2.1 Reagents

##### 2.1.1 Phospholipids

The following saturated phospholipids were purchased from Avanti Polar Lipids (Alabaster, AL), used as received without any further purification and stored at -20°C freezer. A list of phospholipids used is displayed in Table 2.1. The molecular structures and phase transition temperature ( $T_m$ ) are summarized in Table 2.2.

##### 2.1.2 Fluorescent Lipids

1,2-dipalmitoyl-*sn*-glycero-3-phosphoethanolamine-N-(7-nitro-2-1,3 benzoxadizol-4-yl) (ammonium salt) (16:0) NBD PE, (Figure 2.1 ) (Cat.# 810144).

1-palmitoyl-2-[12-[(7-nitro-2-1,3-benzoxadiazol-4-yl)amino]dodecanoyl]-*sn*-glycero-3-phosphocholine 16:0-12:0 NBD PC ( Cat. # 810131).

The NBD PE and the NBD PC fluorescent probes have NBD moiety attached differently in the phospholipid structure. The lipid structure of the NBD PE is displayed in Figure 2.1. The NBD is attached to a phosphatidylethanolamine headgroup [1, 2]. In NBD PC shown in Figure 2.2, the NBD fluorescent group is attached to the *sn*-2-acyl chain of a phosphatidylcholine head-group [3].

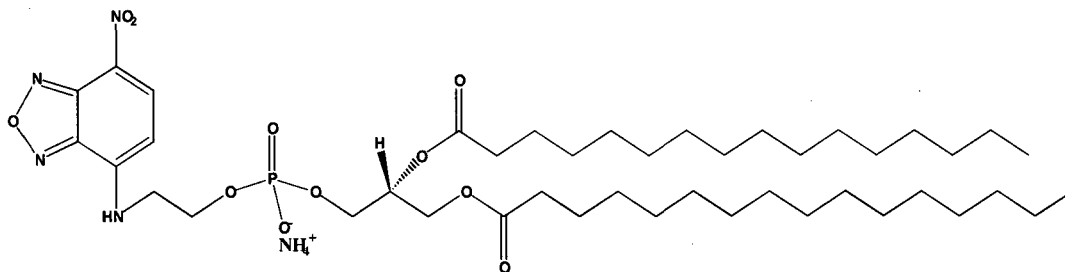
**Table 2.1** List of phospholipids<sup>1</sup>.

<b>Lipid</b>	<b>Common Name</b>	<b>Cat. Number</b>
1,2-dilauroyl- <i>sn</i> -glycero-phosphatidylcholine,	DLPC (12:0)	850335C
1,2-ditridecanoyl- <i>sn</i> -Glycero-3-Phosphocholine,	13:0 PC	850340C
1, 2-dimyristoyl- <i>sn</i> -glycero-3-phosphocholine	DMPC (14:0 PC)	850345C
1,2-dipentadecanoyl- <i>sn</i> -Glycero-3-Phosphocholine	15:0 PC	850350C
1,2-dipalmitoyl- <i>sn</i> -Glycero-3-Phosphocholine	DPPC (16:0 PC)	850355C
1,2-diheptadecanoyl- <i>sn</i> -Glycero-3-Phosphocholine	17:0 PC	850360C
1,2-distearoyl- <i>sn</i> -Glycero-3-Phosphocholine	DSPC (18:0 PC)	850365C
1,2-diarachidoyl- <i>sn</i> -Glycero-3-Phosphocholine	(20:0 PC)	850368C
L- $\alpha$ -phosphatidylcholine (Egg, Chicken)	Egg PC	241601C

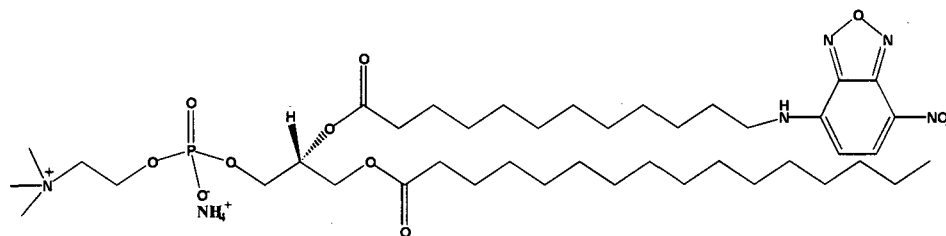
---

<sup>1</sup> Avanti Lipids



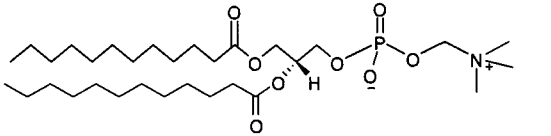
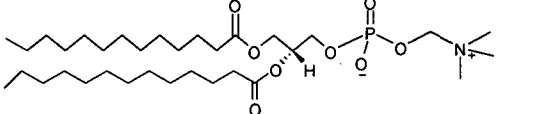
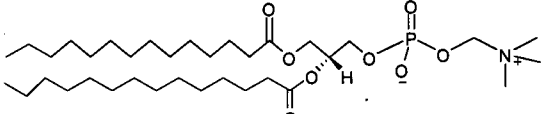
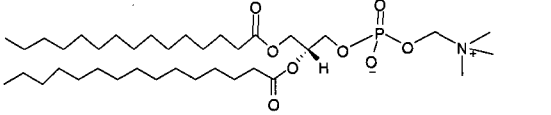
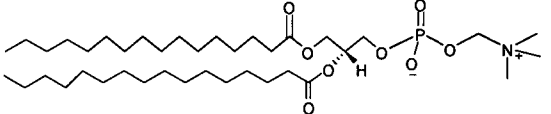
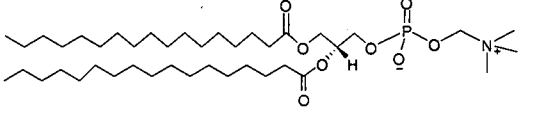
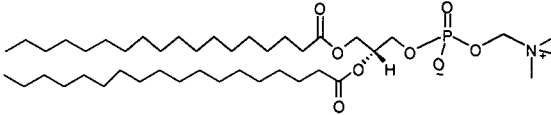
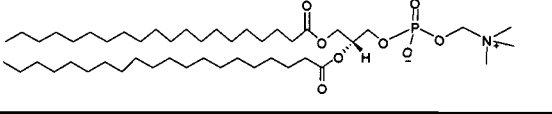


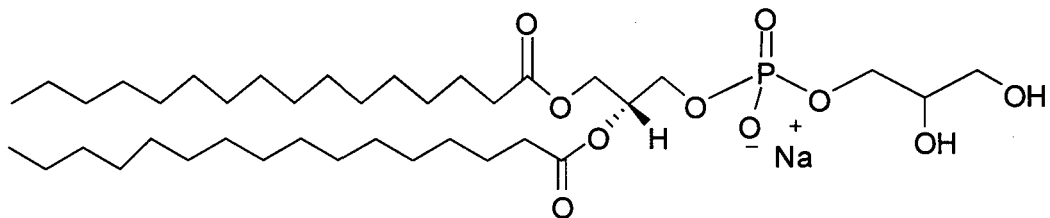
**Figure 2.1** Structure of NBD PE.



**Figure 2.2** Structure of NBD PC.

**Table 2.2** Structure and phase transition temperature ( $T_m$ ) of phospholipids.

Name	Molecular Structure	$T_m$ (°C)
<b>DLPC</b> <b>(12:0 PC)</b>		<b>-1</b>
<b>13:0 PC</b>		<b>14</b>
<b>14:0 PC</b> <b>(DMPC)</b>		<b>23</b>
<b>15:0 PC</b>		<b>33</b>
<b>16:0 PC</b>		<b>41</b>
<b>17:0 PC</b>		<b>48</b>
<b>18:0 PC</b>		<b>55</b>
<b>20:0 PC</b>		<b>66</b>



**Figure 2.3** Structure of DPPG.

### 2.1.3 Chemicals

Sodium dithionite (S310-500), Chloroform (C606SK-4), Methanol (A452N1-19) and Ethanol (A995-4) were purchased from Fischer scientific. They were of analytical grade. Triton X-100 was obtained from Fluka Chemicals (T9284), while Magnesium chloride hexahydrate OmniPur<sup>®</sup> (EM5980) was purchased from VWR. 5-carboxyfluoresceine (single isomer, C-1359) was purchased from Molecular probes. Trizma base (T1503) chemical was purchased from Sigma Aldrich. Barnstead NANOpure Diamond water purification system was used to generate Nanopure water. This water was used in all the experimental procedures as detailed in the experimental section.

## 2.2 Apparatus

### 2.2.1 UV-VIS Spectrometer

UV-Vis absorption spectroscopy of the NBD PE and NBD PC in liposomes was recorded with Shimadzu UV-VIS1650PC spectrophotometer. The data was acquired and processed by UVProbe software. This instrument was equipped with a

tungsten iodide lamp in the visible region and a deuterium arc lamp for the ultraviolet region.

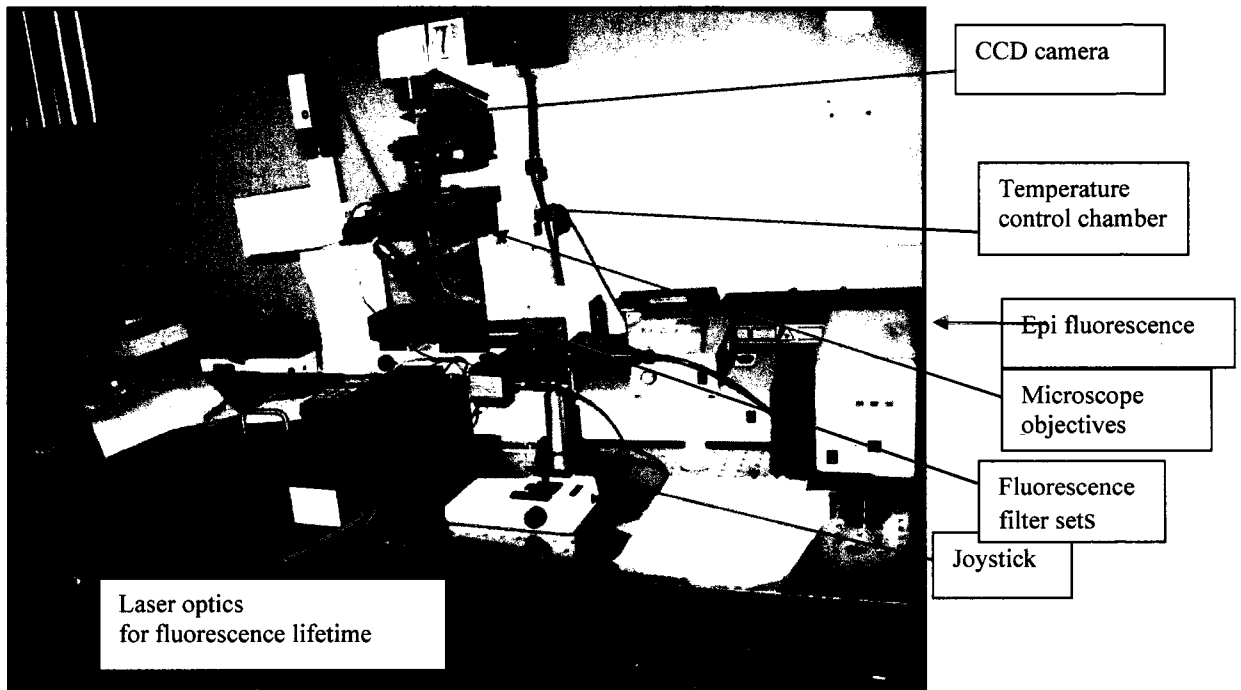
### **2.2.2 Fluorescence Spectrometer**

Excitation and emission spectral data were acquired and recorded with a Shimadzu RF-5301 spectrofluorometer. This instrument was equipped with a temperature-controlled chamber, detachable polarization and magnetic stirrer accessories. The instrument was also equipped with a 150 W Xenon lamp. Fluorescence quartz cuvette, 1 cm, 3.5 mL (CVFL-Q-10) from VWR was used. The emission was observed orthogonal to the direction of exciting beam.

### **2.2.3. Nikon Eclipse TE2000U Microscope**

The morphology and size of the liposomes was determined using Nikon eclipse TE2000U inverted microscope. The instrument had multiple ports design and a cooled CCD color camera to capture image and record video. It was designed and assembled by Arryx, Inc. Chicago, IL. The microscope was mounted and operated on a vibration-free table as shown in Figure 2.4. This instrument had the capability to capture fluorescence, phase contrast, and bright field images. It was equipped with a detachable temperature stage that consisted of a peltier thermoelectric device and a water circulating bath with a temperature probe. Water condensation at temperatures below 10°C was avoided by blowing air under pressure from the bench top through the temperature controlled chamber. In the temperature controlled experiments, the

chamber was equilibrated and checked with a thermocouple for at least five minutes before measurement was initiated.



**Figure 2.4** Nikon eclipse TE2000U microscope.

The microscope in Figure 2.4 was equipped with a time-correlated single-photon counting (TCSPC) instrument, joystick and mercury fiber optic illumination for epifluorescence microscopy. In a TCSPC, data is collected under multiple cycles with periodic excitations [4]. The cycles can be reconstructed to a single decay cycle from single photon events that are collected after the cycles. The TCSPC instrument

had a number of reflecting mirrors that directed a 470 nm LED laser beam from a pulsed laser diode (PDL800-B Picoquant GmbH, Germany) operating at 20 MHz with a rise time of 35 picoseconds. The beam was directed through a beam splitter to the microscope objectives (60X, 1.4 NA, oil immersion). The microscope was equipped with an iris and neutral density filters that were used to adjust light intensities. The epifluorescence beam was conveyed from mercury lamp source through fiber optic cable to neutral density filters. The images of liposomes were acquired at room temperature unless otherwise stated. In the time-correlated anisotropy experiments, a movable arm was used to control movement of the polarizer in and out of the plane of the optics.

#### **2.2.4 Confocal Microscopy**

Confocal images were acquired using an inverted scanning microscope (LSM 510, Carl Zeiss Germany) using the 488 line of Krypton/Argon laser at full power at 25°C. A 50  $\mu$ L specimen was placed in a single depression well slide (VWR 48324-001) and mounted onto a microscope stage.

#### **2.2.5 Darkfield Microscopy**

The dark field images were observed at 25°C with a dark field microscope (Nikon Eclipse E600). The images were acquired with a digital camera (QImaging QICAM) and processed with imaging software.

### 2.2.6 Pore Formation and Line Tension Force

Nikon TE200U inverted microscope was used to image and capture video. This microscope was attached to a homemade apparatus as displayed in Figure 2.4. A fast digital Sentech STC630 CCD camera was mounted on the microscope and connected to a personal computer. This camera was capable of capturing video images at 30 frames/s. The microscope is equipped with a spatial light modulator and light from a 1064 nm CW Nd:YAG laser. The light passed through the spatial light modulator (SLM) to generate a holographic optical tweezer (Arryx Inc.) that was used for optical trapping.

The tweezer can generate up to 200 optical traps with the same light intensity. The large diameter vesicles (20  $\mu\text{m}$ ) were studied without trapping while the smaller diameter sized ones were trapped by the holographic tweezer. The Nitrogen pumped dye laser was directed through one of the microscope ports to the 50  $\mu\text{L}$  sample on a depression slide. This laser was directed onto a single liposome for ablation and deformation of the bilayer region of the liposome. A Coumarin dye laser line was used to obtain 440 nm laser emission and Rhodamine 610 dye was used to obtain 626 nm laser emission. The peak laser energy in each case was 100  $\mu\text{J}$ . The 440 nm laser was employed for ablation experiments, and the 626 nm laser was used for the deformation experiments. The video images obtained from the experiment were analyzed by Videomatch 4.0.4 software to obtain the line tension force. Liposomes made from the homologous series of acyl chain and egg PC phospholipids were used determine line tension force.

## 2.3 Methods

### 2.3.1 Preparation of Liposomes

A modification of Zare's procedure for giant liposome preparation was used to generate liposomes [5]. The method reported by Zare resulted in giant vesicles and the liposomes could be reproduced in different solvent media and under reduced pressure. This method was found suitable for labile and highly reactive compounds that were meant to be encapsulated by liposomes. Here, a rotatory evaporator (Buchi Rotavapor<sup>®</sup>) was used to supply heat and generate liposomes in 11 mM magnesium chloride. A 4 mg/mL lipid concentration was prepared for samples analyzed in subsequent sections except where indicated. Phospholipids were purchased either as solid or solutions in chloroform.

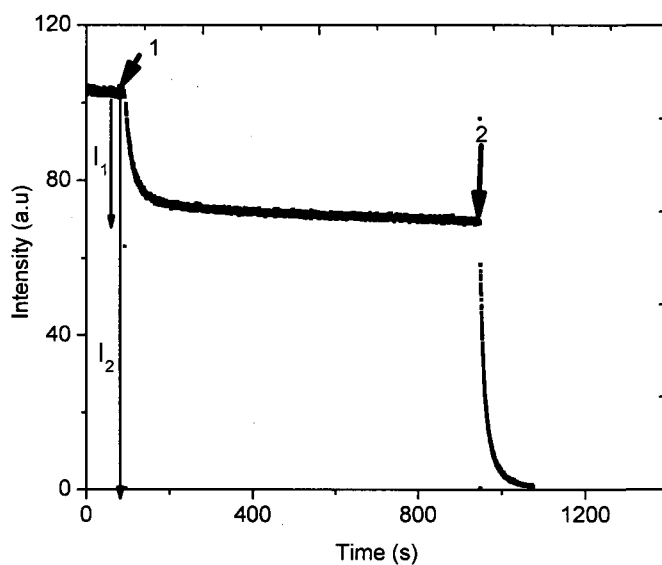
To prepare a 4 mg/mL solution, a 160  $\mu$ L of 25 mg/mL egg PC (molecular weight, 770.12) in chloroform was transferred to a 50 mL round bottomed flask previously baked in an oven at 260°C. Approximately 26  $\mu$ L of 1 mg/mL NBD PE (molecular weight, 872.09) [6] or the NBD PC (molecular weight, 856.04) [6] fluorescent dye was added to the mixture to obtain a 0.5% (mol/mol) with respect to egg PC. Approximately 814  $\mu$ L of chloroform and methanol (2:1) was added to the flask to bring to a total of 1 mL organic solvent and phospholipids. A 1 mL 11 mM magnesium chloride hexahydrate ( $\text{MgCl}_2 \cdot 6\text{H}_2\text{O}$ ) (filtered through 200 nm polycarbonate membrane) aqueous solution was gently added to the organic layer along the side of the flask. The flask was immersed in a water bath at 65°C. A stream of nitrogen gas was gently passed through the flask to drive off the organic layer. The



process took approximately 5 minutes. The flask was left on the water bath to cool to room temperature for a further 10 minutes. Approximately 850  $\mu\text{L}$  of a solution rich in giant vesicles was obtained from the procedure. The sample was characterized by microscopy and dithionite quenching.

### 2.3.2 Lamellarity of Liposomes

The lamellarity of liposomes prepared in section 2.3.1 was analyzed following the method reported by Gruber and Schindler [7]. The fluorescence signal of NBD was monitored as a function of time. Dithionite reduces outer leaflet NBD to a non-fluorescent ABD [8-10]. Addition of Triton X-100 to the liposomes resulted in the exposure of inner leaflets to the excess dithionite in solution. The change in fluorescence intensity before and after dithionite addition to liposomes was used to analyze lamellarity of the liposome. A 150  $\mu\text{L}$  of a 4 mg/mL liposome suspension labeled with either 0.5% NBD PE or NBD PC was diluted to 3 mL using HEPES buffer with sodium chloride pH 7.4. The sample was excited at 470 nm and emission monitored at 540 nm. Figure 2.5 shows initial fluorescence intensity before addition of 30  $\mu\text{L}$  of freshly prepared 1 M sodium dithionite as indicated by 1. The change in fluorescence on addition of dithionite reagent was denoted by  $I_1$ . Addition of 150  $\mu\text{L}$  of 20% (w/v) Triton X-100 (see stage 2 in figure 2.4) resulted in the reduction of inner leaflets NBD fluorescence. The overall change ( $I$ ) was a measure of the outer and inner leaflets NBD reduced by dithionite. The ratio of  $I_1$  and  $I_2$  should be 0.5 for or unilamellar liposomes.



**Figure 2.5** Change in fluorescence intensity of NBD on addition of dithionite (1) and Triton X-100 (2).

### 2.3.3. Fluorescence Anisotropy

Steady-state fluorescence anisotropy measurements were acquired by RF-5301 PC fluorimeter from Shimadzu. The instrument was equipped with an L-shaped detachable polarizer accessory. A 150  $\mu\text{L}$  of a 4 mg/mL liposome suspension was transferred to a 3 mL HEPES with sodium chloride buffer pH 7.4 (100 mM NaCl, 10 mM HEPES-NaOH) [7] in a 1 cm path length quartz cuvette. The liposomes were labeled with either a 0.5% (mol/mol) NBD PE or NBD PC. Excitation and emission slit-widths of 5 nm were used for all measurements. The sample was continuously stirred using a magnetic stir bar and equilibrated with temperature before the fluorescence measurements were initiated.

Fluorescence anisotropy was computed from the fluorescence intensities measured in the directions parallel and perpendicular to the electric vector of the exciting light [11]. The sample was irradiated with 470 nm an excitation wavelength and the emission was followed at 540 nm. The measurements were performed as a function of temperature and continuous stirring. The results were analyzed using equation 1.2. All the fluorescence measurements were conducted in a thermally jacketed cell holder with a connection to the adjustable temperature circulating water bath. The sample temperature was measured directly employing a thermocouple.

#### **2.3.4 Fluorescence Quenching**

The dithionite quenching of NBD fluorescence labeled samples were studied partially based on the method reported by Gruber and Schindler [7]. 150  $\mu\text{L}$  of liposome solution were mixed with a 2.85 mL solution of HEPES buffer pH 7.4 containing NaCl (100 mM NaCl, 10 mM HEPES-NaOH) in a 1 cm path quartz cuvette. The fluorescence signal was initiated, after 10 minute wait to equilibrate with the set temperature. The sample was continuously stirred using a controlled magnetic stir bar placed inside the cuvette. The baseline fluorescence was measured for approximately 20 sec before addition of freshly prepared 30  $\mu\text{L}$  of 1 M sodium dithionite directly from 4°C. 1 M sodium dithionite was prepared by dissolving 3.48 g  $\text{Na}_2\text{S}_2\text{O}_4$  and 2.43 g Trizma base in millipore water to a final weight of 21.4 g and pH was adjusted to 10. The sample in the cuvette was irradiated at 470 nm (5 nm slit) and fluorescence studied at 540 nm (5 nm slit) for 10 minutes or less for both NBD PE

and NBD PC labeled samples. A 150  $\mu\text{L}$  solution of a 20% (w/v) Triton X-100 was added to the sample after dithionite reduction. The spectral data from the instrument was analyzed using OriginLab 7.5 software from OriginLab Corporation (Northampton, MA, USA). In all the cases the data was treated to a sum of two exponentials using Equation 2.1.

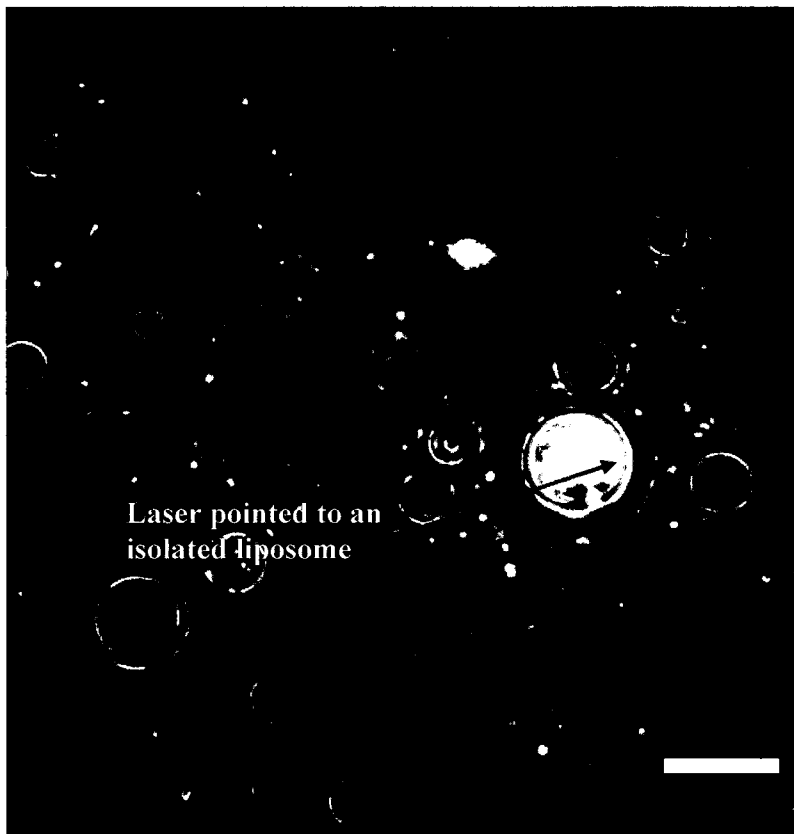
$$S = a_1 e^{-k_1 t} + a_2 e^{-k_2 t} \quad [2.1]$$

In the equation fluorescence intensity was denoted by  $S$ , the fast step by  $k_1$  and the slow step by  $k_2$ . The corresponding contributions for  $k_1$  and  $k_2$  were denoted by  $a_1$  and  $a_2$  respectively.

### 2.3.5 Lifetime and Time-Resolved Anisotropy

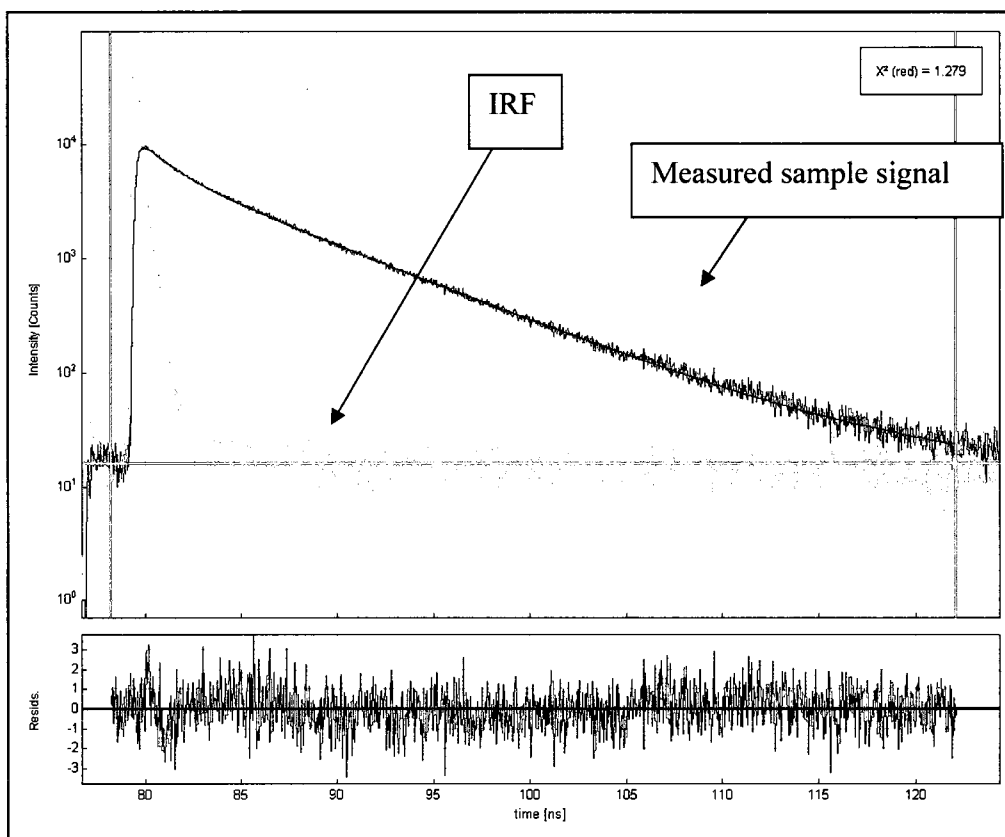
Fluorescence lifetime and time-resolved anisotropy measurements performed on a single vesicle were performed as described in Section 2.2.3. A single liposome was isolated and the dye excited by directing a focused laser beam to induce fluorescence decay as shown in Figure 2.5. 50  $\mu\text{L}$  of a 4 mg/mL labeled with either 0.5% (mol/mol) NBD PE or NBD PC liposome suspension was transferred into a depression slide. The sample was covered with a microscope cover slip and mounted with the cover slip on an oil immersion objective lens (60X, 1.4 NA). A single

liposome trapped on the slide was selected and excited at 470 nm with a LED laser. Emission was collected through the same objective via a high aperture collection optic in the microscope. The signal was detected by a single photon photomultiplier (Becker and Hickl GmbH, Berlin, Germany).



**Figure 2.6** Focused laser beam on an isolated liposome. The picture was taken at 20°C with a 60X objective. The white bar represents 10  $\mu\text{m}$ .

The instrument response function (IRF) is the response of the instrument to a zero lifetime sample. It was determined by scattering the laser beam on a mirror before sample experiments on the stage. The IRF was adjusted by focusing a laser beam on mirror a mounted on the same objective lens. The IRF and sample decay signal functions are as shown in Figure 2.7. The background signal was later deconvoluted from the IRF to obtain fluorescence lifetime and anisotropy data.



**Figure 2.7** The IRF and sample decay signal. The lower panel was the residual fit that was used to gauge the best fit data.

The timing electronics were operated using TimeHarp 200 PC board (PicoQuant GmbH, Germany). Fluorescence signal was processed by FluoroFit software. The software was able to perform the tail fitting and numerical reconvolution that accounted for the IRF signal. The IRF signal width was measured in the range of picoseconds and less than the sample lifetime. The goodness of the fit was determined from the weighted residuals and the reduced chi-square. The goodness of the fit was assumed to be good with a reduced chi-square value less than 1.2. There were two independent observations, single and biexponential, that were attempted to evaluate the goodness of the fit of the data obtained. The lifetime of NBD PE and NBD PC fitted well to a bi-exponential function. The contributions from the long and short components were approximately 67 and 33% respectively. The time-correlated anisotropy was acquired simultaneously with fluorescence lifetime. However, when acquiring fluorescence anisotropy, the polarizer was placed either in perpendicular or parallel position along the path of the signal. The polarizer was manually controlled by a movable arm in and out of the plane of optics and was located outside the box. Analysis of the anisotropy was performed using multiexponential decay of fluorescence fitting using the FluoroFit software.

### **2.3.6 Bulk Solution Measurement in Edinburgh Instrument**

Fluorescence lifetime of the NBD PE and NBD PC in DMPC was measured in solution in quartz cuvette (1 cm, 3.5 mL, CVFL-Q-10, VWR LLC). The data was acquired by the FLS920 Edinburgh instrument. The instrument was equipped with

PCS900 card and F900 operating software for single photon counting data acquisition. The instrument had a PDL800-pulse diode laser driver operating at a frequency of 20 MHz. The IRF measured and fine tuned using aluminum foil to scatter the laser beam. The laser beam was initiated with an excitation wavelength at 450 nm and emission monitored at 540 nm with a slit width of 5 nm. A 1 ml 4 mg/mL liposome suspension tagged with either a 0.5% NBD PE or NBD PC was used. The fluorescence lifetime data was acquired by FAST software. Fluorescence lifetime was also determined using dilute samples. Measurement of fluorescence lifetime was conducted as a function of temperature.



## 2.4 References

- 1 Mazeret, S., Schram, V., Tocanne, J. F. and Lopez, A. (1996) 7-nitrobenz-2-oxa-1,3-diazole-4-yl-labeled phospholipids in lipid membranes: differences in fluorescence behavior. *Biophys J* **71**, 327-335
- 2 Araiso, T., Koyama, T. (1995) Fluidity of glycerol skeletal region in phospholipid bilayers: a time-resolved fluorescence depolarization study. *Jpn J Physiology* **45**, 187-196
- 3 Mukherjee, S., Raghuraman, H., Dasgupta, S., Chattopadhyay, A. (2004) Organization and dynamics of N-(7-nitrobenz-2-oxa-1,3-diazol-4-yl)-labeled lipids: a fluorescence approach. *Chem Phys Lipids* **127**, 91-101
- 4 Wahl, M., GmbH, P. (2009) Time-correlated single photon counting technical note. Retrieved on September 2009, [http://www.picoquant.com/technotes/technote\\_tcspc.pdf](http://www.picoquant.com/technotes/technote_tcspc.pdf)
- 5 Moscho, A., Orwar, O., Chiu, D. T., Modi, B. P., Zare, R. N. (1996) Rapid preparation of giant unilamellar vesicles. *Proc Natl Acad Sci USA* **93**, 11443-11447
- 6 Avanti, P. L. (2009) Phosphatidylcholines. *Avanti Polar Lipids* Retrieved on September 25, 2009 from <http://www.avantilipids.com/>
- 7 Gruber, H. J., Schindler, H. (1994) External surface and lamellarity of lipid vesicles: a practice-oriented set of assay methods. *Biochim Biophys Acta* **1189**, 212-224
- 8 Langer, M., Hui, S. W. (1993) Dithionite penetration through phospholipid bilayers as a measure of defects in lipid molecular packing. *Chem Phys Lipids* **65**, 23-30
- 9 McIntyre, J. C., Sleight, R. G. (1991) Fluorescent Assay for Phospholipid Membrane Assymetry. *Biochemistry* **30**, 11819-11827

- 10 Wasmuth, C. R., Edwards, C., Hutcherson, R. (1964) Participation of the SO Radical Ion in the Reduction of p-Nitrophenol by Sodium Dithionite. *J. Phys. Chem.* **68**, 423-425
- 11 Lackowicz, R. L. (1999) *Principles of Fluorescence Spectroscopy*. Plenum Publishers, New York, N. Y.

## CHAPTER 3

### GIANT LIPOSOMES FROM A BINARY MIXTURE OF LIPIDS

#### 3.1 Introduction

Liposomes are made from a wide range of synthetic and natural phospholipids. Most of these lipids are found in the lipid bilayer of natural cell membranes. They are diverse in their structure and function. Because of this diversity, they display diverse cellular phenomena found in biological cells. A binary mixture of phospholipids provides a simple model system to study fluctuations and dynamics properties in the lipid membrane. These fluctuations observed in model system provide a deeper understanding of the principles underlying the structural organization and functional roles of biological membranes [1].

Studies of the gel / fluid and liquid / ordered phase separation, in giant liposomes from mixture of lipids was shown by a two-photon excitation microscopy [2]. In two-photon fluorescence imaging two low energy photons either of the same or of different frequencies simultaneously interact with a fluorophore resulting in the absorption whose intensity is nonlinear [3]. This eliminates out of point focus, gives higher penetration depth, and reduces damage to the specimen. The gel / fluid phase was observed by fluorescence lifetime imaging technique that provides an image contrast derived from fluorescence lifetimes at each point of the image [2]. A mixture of DLPC and DPPC presents limited miscibility and form two phase regions of

coexisting ordered (rich in DPPC) and fluid (rich in DLPC) phase equilibrium. This mixture has been the subject of extensive studies to understand lipid segregation in model membranes of different composition [4-6]. Confocal fluorescence correlation spectroscopic studies show that lateral lipid mobility in the ordered phase is 250 times below the fluid phase [7]. In this case, images showed regions of co-existing phases able to distinguish between fluid and ordered phases occurring in the bilayer. The phase co-existing domains have also been observed in monolayers and in supported lipid bilayers [8]. A mixture of DPPC and cholesterol analogs phase behavior has been extensively investigated by Keller *et al* [9]. A more recent study using a high resolution imaging secondary-ion mass spectrometry on fluid-gel separated DLPC / DSPC mixtures have shown composition variations within the domains of phospholipid bilayer [10].

In this chapter, a binary mixture from a pure synthetic system and natural egg PC phospholipids was investigated. Microscopy and dithionite quenching of NBD fluorescence were used to explore lipid bilayer region. Lipid composition and the environmental conditions were varied to understand the behavior of a two component lipid bilayer system. Liposomes obtained were evaluated on the basis of size, lamellarity and shape. Giant liposomes were examined directly by fluorescence, bright field, confocal and dark field microscopy. This section detailed studies on the bilayer region of liposomes composed of a binary mixture of the DLPC and DPPC. In all cases presented herein, the liposomes were prepared in 11 mM magnesium chloride following the method discussed in Chapter 2, Section 2.3. The DLPC and

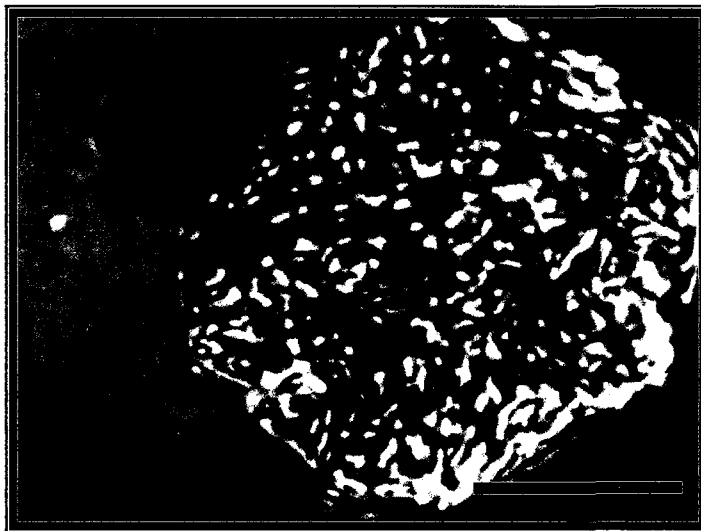
DPPC are zwitterionic. The DPPC and DLPC have phase transitions at 41 and -1 °C respectively. Therefore, the DPPC is in the gel phase and DLPC in the fluid phase at room temperature.

Dithionite induced quenching of NBD was studied as a function of temperature. The quenching curves were evaluated using calculated values of lamellarity. The latter was calculated from the method discussed in Chapter 2, Section 2.3.2. The study also monitored the effect of having a two lipid system with different phase transition temperatures. The effect of adding a negatively charged lipid DPPG phospholipid to DLPC and DPPC were also examined by microscope imaging. The results obtained were compared with those of more complex natural egg PC phospholipids. This system is fluid throughout the temperature range. It has both unsaturated and saturated lipids combine to form a pure natural egg PC system.

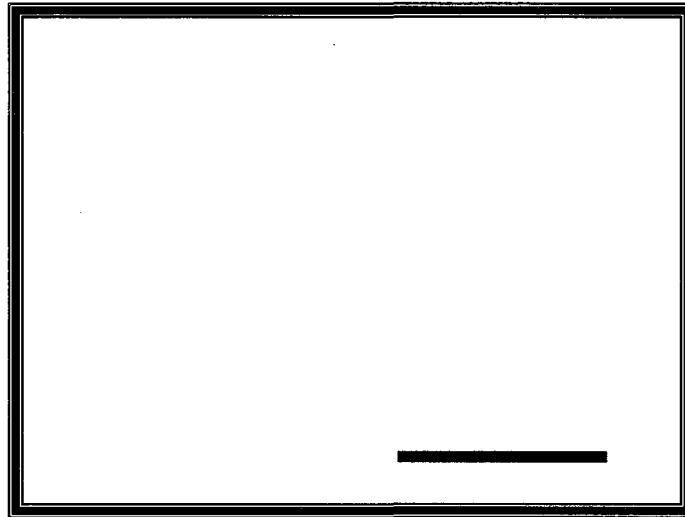
The vesicles were evaluated on the basis of vesicle morphology, lamellarity and size. The DLPC / DPPC system was used to study the existence of lipid domains in a mixed lipid bilayer system [11, 12]. A charged DPPG phospholipid was added at low concentrations either in a mixture or a unitary lipid system. It is known that biological membranes are surrounded by aqueous buffer containing cations and anions. The influence of divalent cations, particularly  $Mg^{2+}$  in charged and zwitterionic lipids were investigated from the images under microscope.

### 3.2 Imaging

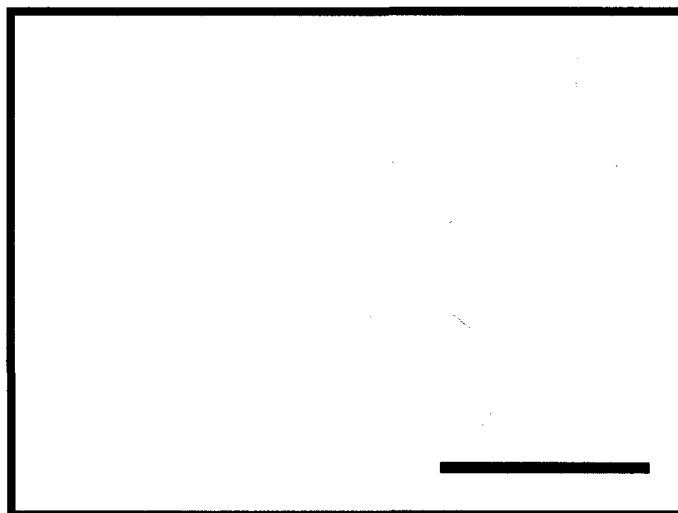
The liposome suspensions were examined by optical brightfield, dark field and confocal fluorescence microscopy methods. Figures 3.1 and 3.2 show images of giant liposomes made from DPPC and DLPC phospholipids respectively. The yield of liposomes prepared from method discussed in Chapter 2 Section 2.3, was abundant. Majority of liposomes of DLPC lipid system appeared circular or spheroidal. The DPPC liposomes displayed a rough surface and were sparsely populated as displayed in Figure 3.1. However, when DPPC was mixed with DLPC in all proportions examined, the roughness disappeared (Figure 3.3 and 3.4).



**Figure 3.1** Brightfield image of a DPPC liposome. The image was acquired with magnification of 40X objective. The bar represents 20  $\mu\text{m}$ .



**Figure 3.2** Brightfield image of DLPC liposome. The liposomes were prepared at 65 °C and a total lipid concentration of 4 mg/mL, acquired with a magnification of 40X. The bar represents 20  $\mu\text{m}$ .



**Figure 3.3** Brightfield image of DLPC / DPPC mixture (1:1). The total concentration of lipid used was 4 mg/mL. The magnification was 40X. The bar represents 20  $\mu\text{m}$ .



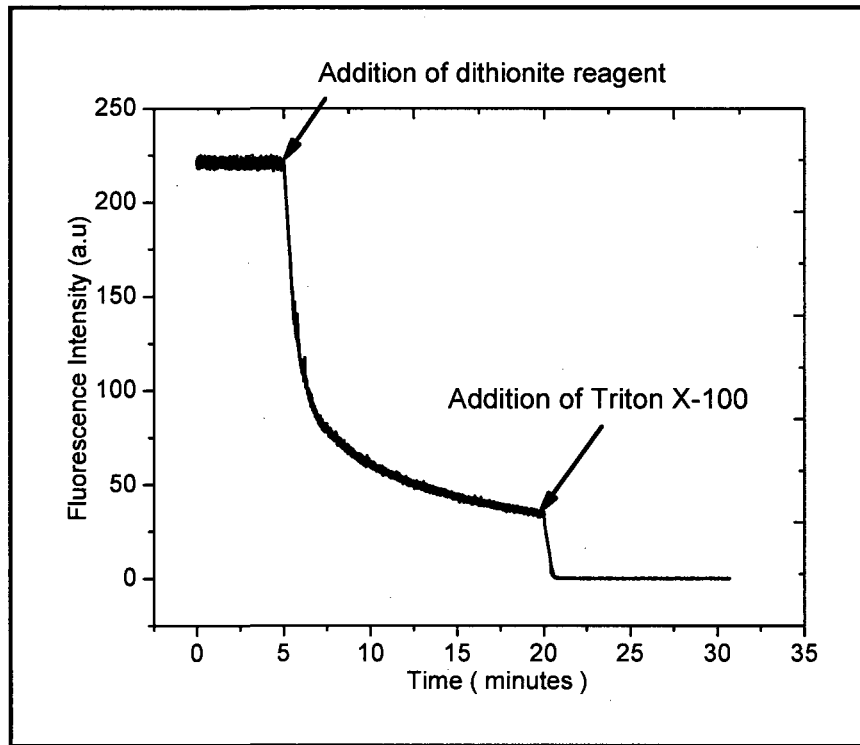
**Figure 3.4** Brightfield image of DLPC / DPPC mixture (3:2). These liposomes were prepared at 65°C. The total lipid concentration was 0.4 mg/mL and a magnification 40X .The bar represents 20  $\mu\text{m}$ .

### 3.3 NBD Assay

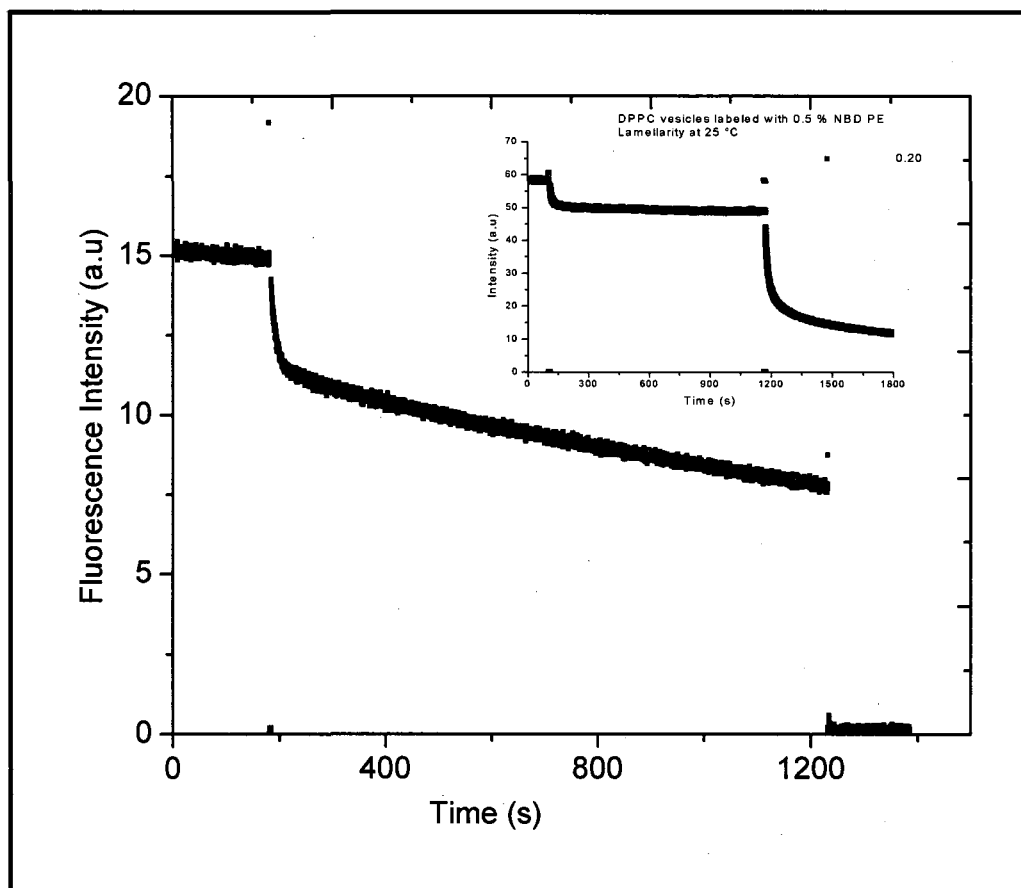
The external surface of the lipid bilayer in a binary mixture of DLPC and DPPC was evaluated based on quenching of NBD fluorescence by dithionite. Time course experiments of the NBD quenching assay is shown in Figure 3.5. The ratio of NBD to dithionite was 1 to 100 (mol/mol). The procedure is detailed in Section 2.3.4. The quenching of the NBD by dithionite in liposomes was rapidly decreased to a near zero fluorescence intensity. This behavior is similar to fluorescence quenching of pure DLPC and DPPC liposomes at the phase transition temperature. The fluorescence decay profile of DPPC liposomes at the phase transition (41°C) is displayed in Figure 3.6. A plot at room temperature (gel phase of DPPC) is displayed in the Figure insert. At the phase transition temperature region, there is a rapid



decrease in the fluorescence intensity observed over a long time. 70% of the original fluorescence was quenched by dithionite reagent on addition of detergent Triton X-100. However, at room temperature conditions, there was no further decrease in fluorescence intensity in excess dithionite reagent (see the Figure insert).



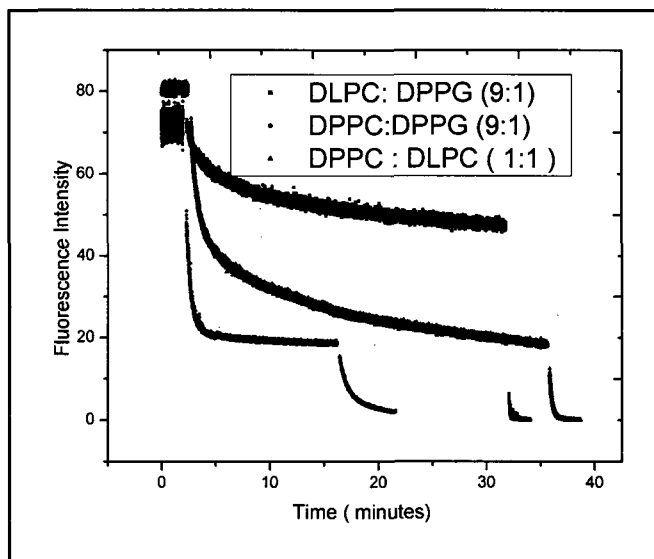
**Figure 3.5** NBD assay profile of liposomes of DPPC / DLPC mixture (1:1). A 0.5% NBD PE was added to a total lipid concentration of 10 mg/mL. The NBD assay was performed at room temperature.



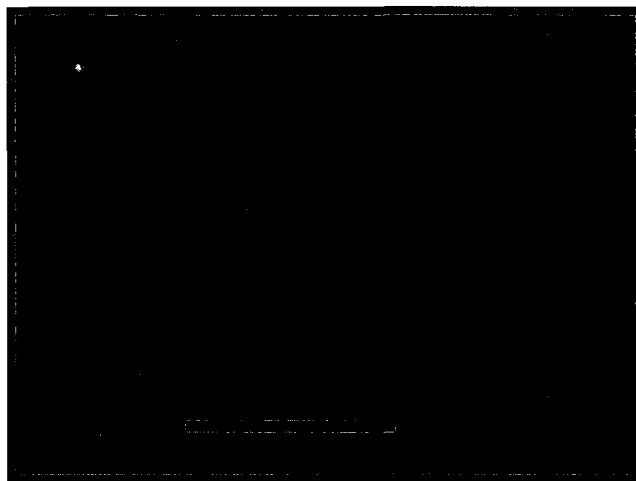
**Figure 3.6** NBD assay profile of DPPC liposome. This figure was obtained at the phase transition temperature (41°C). The figure insert shows a similar study conducted at room temperature (25°C). A 0.5% NBD PE was used in this experiment.

The dithionite experiment was performed in DPPC and DLPC containing DPPG phospholipids. The DPPG phospholipid is a negatively charged phospholipid at pH 7. In general, a very slow reduction of NBD fluorescence by dithionite was observed in DLPC / DPPG and DPPC / DPPG mixture (Figure 3.7). The reduction was greater in DPPC / DPPG than in DLPC / DPPG binary system. A mixture of two or more phospholipids with a large difference in acyl-chain length and headgroup structure can result in immiscible phospholipids bilayer [13]. As expected, the mixing behavior is largely dependent on the chemical structure of the lipid components in the mixture. These include the head group structure, acyl chain length, and degree of unsaturation. The miscibility strongly depends on the physical state of the bilayer, the gel or fluid phase. DPPC at room temperature is in the gel phase state. DLPC at the same temperature is in fluid state. It also expected that the presence of impurity chains that are shorter than the bulk of the chains is less perturbing to the structure than the presence of longer chains. This can possibly explain why the effect of DPPG is more pronounced in DLPC than in DPPC liposomes bilayer.

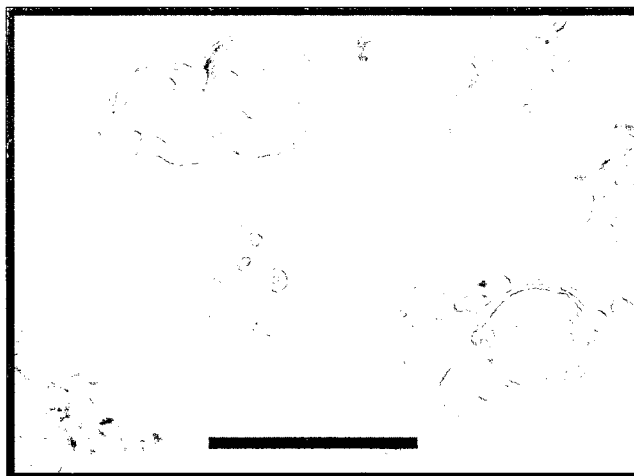
Addition of a 10% (mol/mol) DPPG formed liposomes which appeared aggregated as viewed under the microscope (Figures 3.8, 3.9 and 3.10). The effect of DPPG was greater in DPPC than in DLPC lipid bilayer. The inclusion of DPPG lipids to DPPC formed liposomes that were aggregated and sparsely populated. The DPPC and DPPG phospholipid differ only in the nature of their headgroups.



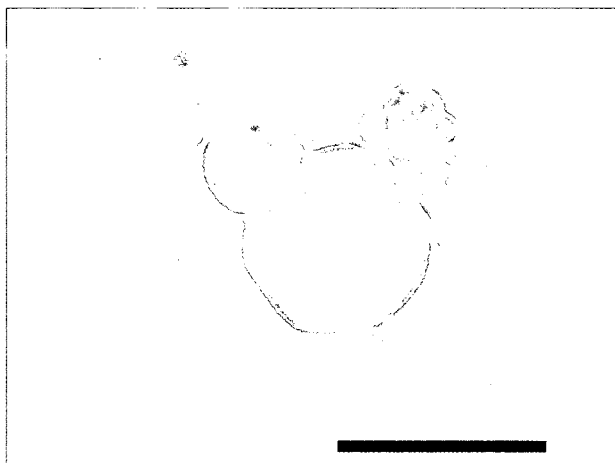
**Figure 3.7** NBD assay in liposomes composed of DPPC / DPPG (9:1) and DLPC / DPPG (9:1).



**Figure 3.8** Brightfield images of liposomes from DPPC / DPPG mixture (9:1). The bar represents a distance of 20  $\mu\text{m}$ .



**Figure 3.9** Brightfield images of liposomes composed of DLPC and DPPG mixture (9:1). Total lipid concentration was 4 mg/mL. The vesicles were observed at magnification of 40X. The bar represents a distance of 20  $\mu$ m.



**Figure 3.10** Brightfield images of liposomes composed of egg PC and DPPG mixture (9:1). Total lipid concentration was 4 mg/mL. The vesicles were observed at magnification of 40X. The bar represents a distance of 20  $\mu$ m.



**Figure 3.11** Brightfield images of DLPC liposomes. Total lipid concentration was 4 mg/mL. The vesicles were observed at magnification of 60X. The bar represents a distance of 20  $\mu$ m.

### **3.4 Lamellarity of Liposome from a Mixture of DLPC and DPPC**

Lamellarity refers to the number of layers forming the liposome membrane. Lamellarity was calculated based on percent reduction of fluorescence signal from the original peak before and after the addition of dithionite reagent as described in Chapter 2. The values of lamellarity were calculated for DLPC / DPPC phospholipid binary mixture. The results were compared to synthetic unitary systems DLPC, DPPC and natural and more complex egg PC. Analysis of the lamellarity parameter is

considered important in determining characteristics of liposomal preparations. A perfect unilamellar vesicle should have a value of 0.5. In Table 3.1 values of lamellarity for DLPC / DPPC mixtures showed about 70% reduction in the fluorescence signal (lamellarity value of 0.7). Pure DLPC and DPPC showed values that were close to expected unilamellar vesicles. Irrespective of the temperature employed in determining lamellarity, this value always remained close to a value of 0.5 for egg PC phospholipids. In the case of DLPC / DPPC binary system, the outer and inner leaflet NBD is quenched by dithionite at considerable higher rate.

**Table 3.1** Lamellarity of liposomes from pure and mixed lipids.

<b>Lipid System</b>	<b>Lamellarity</b>
Pure DLPC	0.5 ± 0.1
Pure DPPC	0.5 ± 0.1
DLPC / DPPC (1:1)	0.7 ± 0.0
DLPC / DPPC (3:1)	0.7 ± 0.2
DLPC / DPPC ( 2:3)	0.8 ± 0.0
Pure egg PC	0.4 ± 0.1

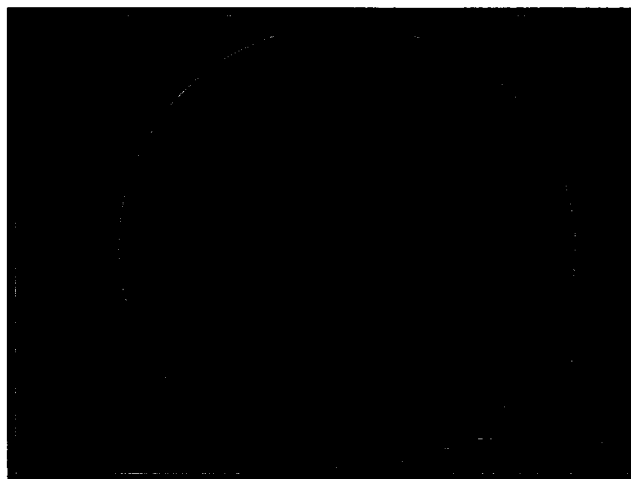
### 3.5 Lamellarity of Egg PC Liposomes

Lamellarity values were calculated for egg PC vesicles. Table 3.2 shows size distribution as a function of the polycarbonate membrane pore size. The membrane was used to extrude liposomes of a particular size distribution. The particle size and distribution was measured by the dynamic light scattering. Lamellarity was calculated for extruded and liposomes without extrusion. The analysis of the results of these measurements revealed that egg PC lipid bilayer was unilamellar and uniform in size distribution. This was conducted in liposomes sizes below 400 nm size. Surprisingly, the values for lamellarity calculated for egg PC was independent of the sizes of liposomes generated. In many cases encountered, liposomes generated from egg PC phospholipids were above 50  $\mu\text{m}$  (Figure 3.12). Egg PC phospholipid is made of different acyl-chain combinations and forms more stable liposomes

**Table 3.2** Lamellarity values calculated for egg PC liposome. Lamellarity values were calculated for variable size distributions estimated by light scattering.

Pore size (nm)	Measured size distribution (nm)	Lamellarity
No-extrusion	sample size were polydisperse	0.5
50	46-70	0.5
100	90	0.5
400	4-360	0.4
1000	n/a	0.4





**Figure 3.12** Brightfield images of egg PC liposomes. The images were acquired at a magnification of 60X. The bar represents a distance of 20  $\mu\text{m}$ .

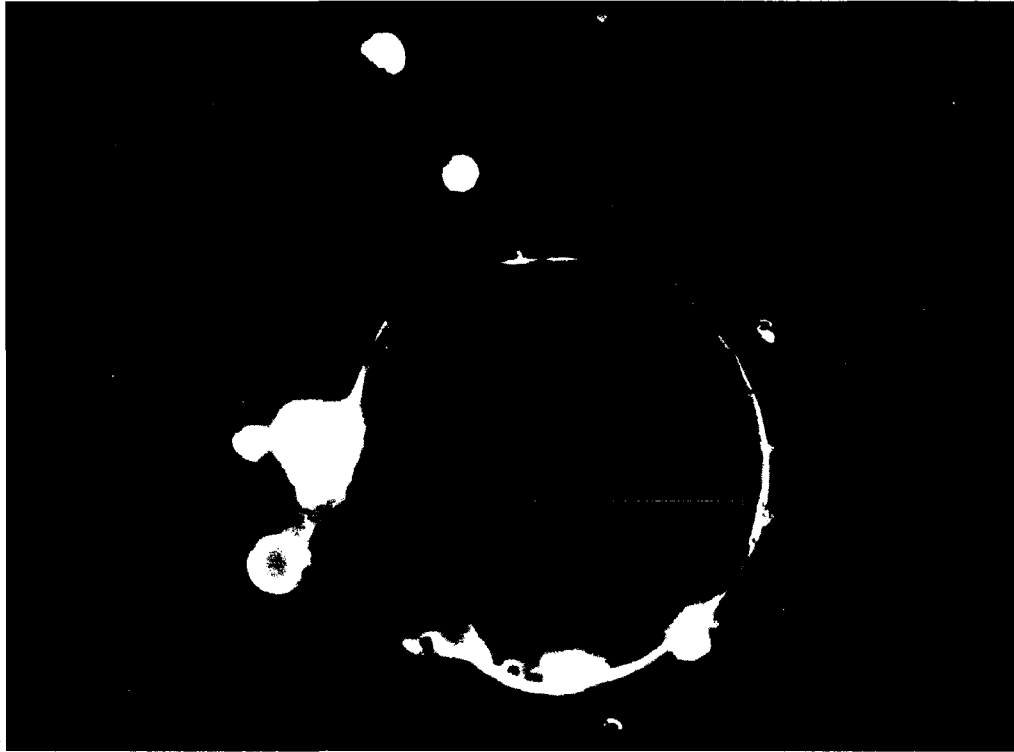
### 3.6 Darkfield Images

Liposomes generated from a binary mixture of DLPC / DPPC was examined by darkfield mode of microscopy. A high-intensity dark-field microscopy provides visualization of the intact three-dimensional morphology and the dynamic behavior under high contrast [14]. Figure 3.13 shows giant liposomes in 8-20  $\mu\text{m}$ . Most liposomes observed appeared spherical or elliptical in shape. The edge of liposomes appeared thick as a result of the objects ability to scatter light. The results of a darkfield microscopy study showed that light intensity scattered from liposome bilayer region reflect its thickness [15]. It has been shown that when unilamellar liposomes transform into multilamellar ones, the line-like images observed in a darkfield microscope becomes 10-fold brighter [16] than unilamellar liposomes. Here, the smaller sized liposomes observed show line-like images with uniform

brightness (Figure 3.13). The brightness in giant liposomes was unevenly distributed (Figure 3.14).



**Figure 3.13** Darkfield images of liposomes composed of DLPC / DPPC (1:1). The red bar represents a distance of 20  $\mu\text{m}$ .



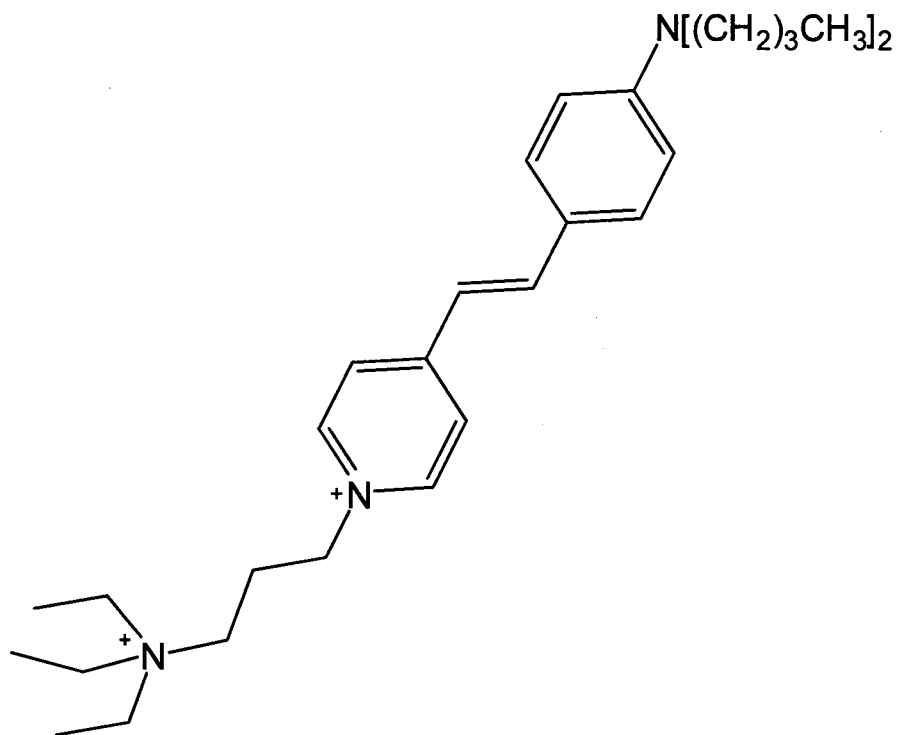
**Figure 3.14** Darkfield images of liposomes composed of DLPC / DPPC (1:1) in a dark background. The red bar represents a distance of 20  $\mu\text{m}$ .

### 3.7 Confocal Fluorescence Images

Confocal images were acquired on a 20X objective (N.A 0.75, Fluor: Nikon) on an inverted microscope (LCM 510: Carl Zeiss, Inc., Tokyo) in fluorescence mode. A 20  $\mu\text{L}$  liposome suspension solution was observed on a depression slide. Room temperature fluorescence images were acquired by exciting the samples at wavelength of 488 nm and studying emission occurring between 505 and 550 nm.

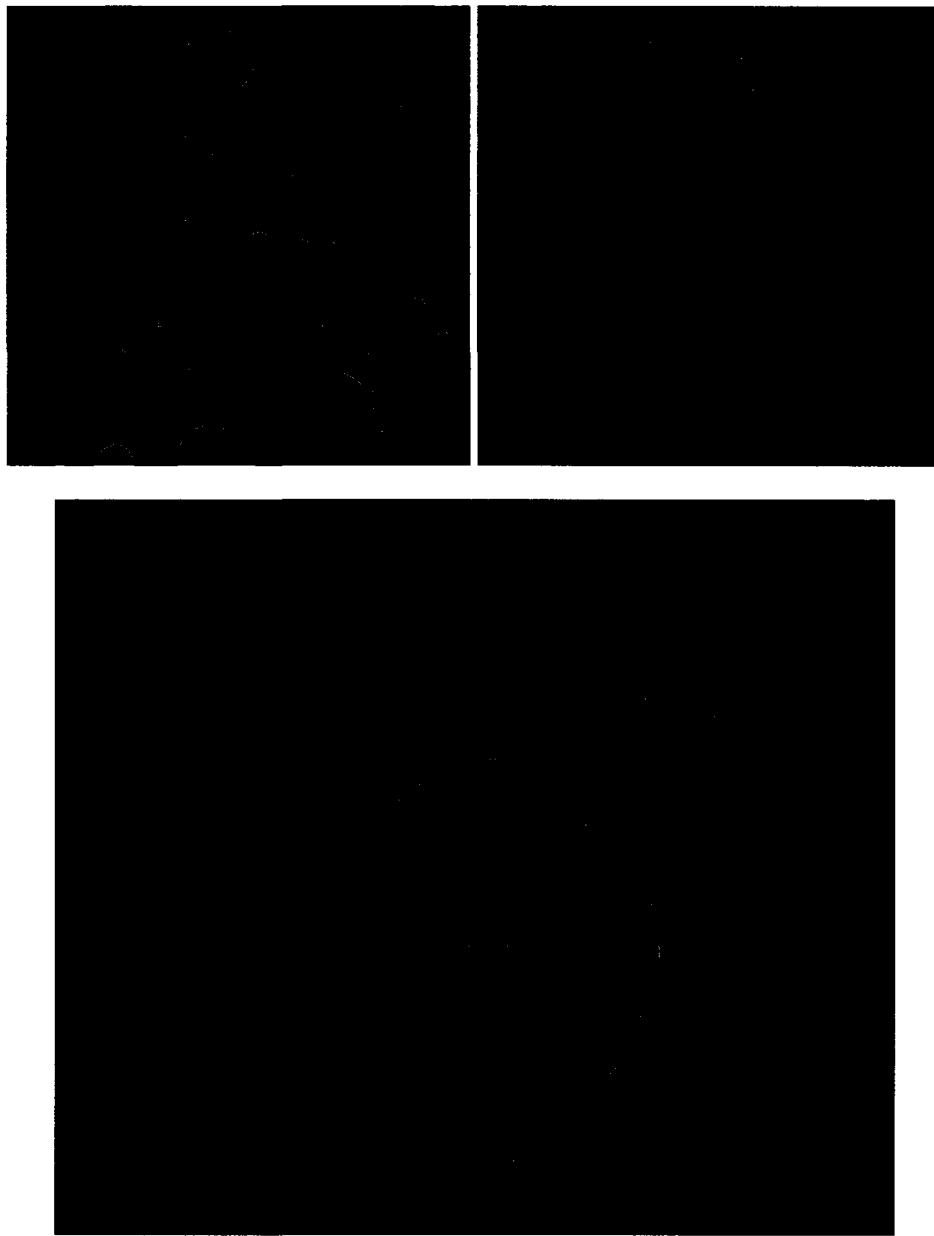
In confocal fluorescence microscopy, a lipophilic FM1-43 fluorescent dye was incorporated into liposomes in the ratio of dye to lipid of 1: 640. FM1-43 is

styrylpyridinium molecule belongs to a family of styryl dye used to monitor exocytosis, endocytosis and endosomal traffic in motor nerve terminals [17, 18]. The hydrophobic tail of the dye allows it to be readily incorporated in the vesicle bilayer even after preparation. The structure of the dye is shown in Figure 3.15.



**Figure 3.15** Structure of FM1-43 dye.

The dye was purchased from Molecular Probes. It stains only the bilayer region of membranes [19]. It has been used in monitoring exocytosis and endocytosis in living cells in real time with the ordinary epifluorescence [20]. Exocytosis is a method of transporting secretory vesicles out of the cell membrane. Endocytosis is the reverse of the exocytosis. These activities can be visualized from live cells by FM1-43 dye fluorescence emission. This dye was used to visualize liposomes obtained from DLPC / DPPC binary mixture. Confocal microscopic sections at the equator of liposomes are displayed in Figure 3.16. Liposomes were imaged by fluorescence emission from the FM1-43 dye. The imaging was done on the DLPC / DPPC binary mixture in equimolar concentrations. Liposomes were observed as a result of the dye strong tendency to localize in the bilayer region.



**Figure 3.16** Confocal images of DLPC / DPPC (1:1). Images were captured at the equator the GUVs through a 20X objective. The lipid vesicles were labeled with FM1-43 dye at 1 dye to 640 lipids molecules. The bar represents a distance of 20  $\mu\text{m}$ .

### 3.8 Discussion

Large compositional heterogeneity of lipids in natural membranes presents an environment where many proteins and enzymes play critical role to ensure membrane functions properly. The complexity of the natural system can best be understood by defining simple model systems. DPPC / DLPC mixture is a simple system with hydrocarbon chain differing by four methylene groups. It presents a non-ideal mixture of saturated hydrocarbons only differing in the acyl chain length. The non-ideality of the mixture has been extensively investigated by colorimetry, fluorescence and by vibrational spectroscopy [4, 21, 22]. Non-ideal behavior of DPPC / DLPC presents a possibility of domain existence [1, 12, 23-25]. A two-color fluorescence microscopy images have shown DPPC / DLPC mixture from domains which are pertinent to the phase behavior of DPPC. It is known that DPPC undergo two thermal transitions at room temperature[26].

A binary system of DLPC and DPPC has been explored by a variety of techniques in the model membranes using different techniques. The results have shown coexisting gel-fluid phases that behave non-ideally. The non-ideality is evidently shown in our case by dithionite quenching and the calculated lamellarity values. The mixture of DLPC / DPPC in our case showed dithionite quenching pattern (Figure 3.5) similar to pure lipids at the phase transition temperature (Figure 3.6). The calculated lamellarity value of a mixture of DPPC / DLPC shown in Table 3.1 showed higher percent NBD quenched compared to pure DLPC or DPPC. Korlach, using confocal imaging techniques showed the existence of fluid and gel

phases in a ternary mixture composed of DLPC, DPPC and cholesterol [7]. Two-photon fluorescence microscopy also demonstrated the existence of these domains in a mixture of DPPC and DLPC [27]. A similar study conducted in vesicles of equimolar mixture of DOPC instead of DLPC and DPPC also showed the presence of a coexisting rigid and fluid phases [26].

Here, a combination of imaging technique and NBD quenching assay was used to investigate the influence of lipid acyl-chain length and charged headgroup in a binary system. The results obtained from a mixture of lipids were compared to those for a pure phospholipid system made from DLPC, DPPC and egg PC. A nearly 50% decrease in fluorescence signal was observed in DLPC and in DPPC (Table 3.1) after addition of dithionite followed by Triton X-100. A 50% value obtained here is characteristic of perfectly unilamellar liposomes as detailed by Gruber and Schindler [28]. This indicates a general even distribution of NBD dye in the inner and outer leaflets of the bilayer. Analysis of the bilayer of a binary system composed of DLPC and DPPC in any combination used, showed 70% decrease in the fluorescence intensity (Table 1, Figure 3.7). Similar studies on egg PC resulted in nearly 40% decrease in fluorescence intensity. DLPC (C-12) and DPPC (C-16) differ on the chain length by four carbon atoms. This can present a possible mismatch in the organization structure in the hydrocarbon region of lipid membrane formed. Lipid bilayers composed of two phospholipids with significant mismatch behave as a non-ideal mixture and result in mismatched packing defects. The higher decrease in fluorescence quenching of the DLPC / DPPC binary mixture can be rationalized



based on the existence of bilayer defects [29]. A change in diameter of the liposome in the transition region could lead to transient pore formation that allow water to transit across the bilayer region [27]. During the cooling process, DPPC passes through the phase transition. This is not observed in DLPC since it has a lower phase transition temperature than DPPC. Bagatolli *et al* using a two-photon fluorescence imaging technique observed that the vesicle diameter can overshoot at the phase transition during cooling cycles [27]. At the phase transition temperature between fluid and gel domains, defects can allow water to pass through the membranes that can lead to change in diameter of the vesicle. This is supported by computer simulations by Mouritsen and Zuckerman in their account of softening of lipid bilayers [30]. In Figure 3.6, there was a continuous decrease in fluorescence intensity on addition of sodium dithionite. This decrease is can be attributed to co-existence of gel / fluid phase occurring at phase transition temperature in DPPC liposomes. This behavior is not observed when DPPC was in the gel phase (at 25°C, Figure 3.6 insert). A similar trend was displayed by the DLPC / DPPC binary mixture.

The brightfield images of DPPC showed rippled appearance on the surface of liposome. This effect did not appear when DLPC phospholipids were added to the DPPC. This effect could be attributed to lipid bilayers of two phospholipids with significant differences in the acyl chain. Such a system forms a non ideal mixture that was reported by fluorescence energy transfer (FRET) [31] and by an atomic force microscopy study by Mouritsen and Jorgensen [32].

### 3.9 Conclusion

A rapid evaporation method developed by Zare *et al* [33] was modified to generate giant liposomes. We were interested in generating giant liposomes from a series of saturated phospholipids. A temperature above the phase transitions of the lipids and 11 mM magnesium chloride solution were used. This concentration of magnesium chloride is consistent with that from physiological conditions. This concentration was successful for generating giant liposomes. Attempts to produce giant liposomes from concentrations above and below this value were not successful in obtaining giant liposomes. Images obtained from brightfield, darkfield and confocal fluorescence modes of microscopy showed giant liposome generated from saturated phosphatidylcholines based on our method.

The formation of liposomes from phospholipids with 10% negatively charged lipid DPPG resulted in aggregated liposomes, Figures 3.9. The divalent cations, in our case  $Mg^{2+}$  cations, possibly induced long range electrostatic repulsion that led to the spontaneous self assembly of phospholipids to form giant liposomes. A similar behavior of magnesium and calcium divalent cations was reported by Akashi [34]. In their case, giant liposomes were produced in the presence of millimolar concentrations of cations that were ranging between 1 and 30. This was reversed by addition of a 10% negatively charged lipid POPG in DOPC. This was attributed to the reversal in surface charge that was dominated by the negatively charged POPG being neutralized upon binding by the divalent cations. Lau *et al* attributed that effect to charge when a negative zeta potential in PG membrane became positive at divalent

ion concentrations between 0.1 and 0.2 M [35]. The liposomes prepared from inclusion of 10% DPPG in DPPC, DLPC or in the mixture are displayed in Figures 3.8 and 3.9 respectively. Inclusion of 10% egg PG in egg PC displayed a similar effect (Figure 3.10). The nature of the headgroup in the phospholipids can result in a dramatic effect upon the characteristics of liposomes [36-38]. Interactions between lipid headgroup that also happens in large molecules occur due to electrostatic, van der Waals and hydration forces [39, 40]. We can rationalize the behavior observed in our system with DPPG to stronger hydrogen bonding presented by DPPG headgroup region. It is also evident that strong electrostatic interactions could play a critical role in the behavior observed in our case with DPPG. Membranes always bear negative charge due to the presence of acidic phospholipids, gangliosides and proteins. Studies have showed that acidic phospholipids behave differently in varied pH conditions, ionic strength and the nature of counterions [41-43]. The association of anionic lipids with metal ions is higher than zwitterionic ones. This is because the net negative charge presented by negative lipids such as DPPG in the mixture of lipids can potentially concentrate cations such as  $Mg^{2+}$  in solution near the lipid-water interface according to Gouy-Chapman theory of electrical double layer double layer [44-46].

### 3.10 References

- 1 Celli, A., Beretta, S., Gratton, E. (2008) Phase fluctuations on the micron-submicron scale in GUVs composed of a binary lipid mixture. *Biophys J* **94**, 104-116
- 2 de Almeida, R. F., Borst, J., Fedorov, A., Prieto, M., Visser, A. J. (2007) Complexity of lipid domains and rafts in giant unilamellar vesicles revealed by combining imaging and microscopic and macroscopic time-resolved fluorescence. *Biophys J* **93**, 539-553
- 3 Denk, W., Strickler, J. H. and Webb, W. W. (1990) Two-photon laser scanning fluorescence microscopy. *Science* **248**, 73-76
- 4 Mabrey, S. and Sturtevant, J. M. (1976) Investigation of phase transitions of lipids and lipid mixtures by sensitivity differential scanning calorimetry. *Proc Natl Acad Sci U S A* **73**, 3862-3866
- 5 von Dreele, P. H. (1978) Estimation of lateral species separation from phase transitions in nonideal two-dimensional lipid mixtures. *Biochemistry* **17**, 3939-3943
- 6 Mukherjee, S., Soe, T. T. and Maxfield, F. R. (1999) Endocytic sorting of lipid analogues differing solely in the chemistry of their hydrophobic tails. *J Cell Biol* **144**, 1271-1284
- 7 Korlach, J., Schwille, P., Webb, W. W. and Feigenson, G. W. (1999) Characterization of lipid bilayer phases by confocal microscopy and fluorescence correlation spectroscopy. *Proc Natl Acad Sci U S A* **96**, 8461-8466
- 8 Keller, S. L. (2002) Co-existing liquid phases in lipid monolayers and bilayers. *J. Phys.: Condens. Matter* **14**, 4763-4766
- 9 Stottrup, L. B., Keller, L. S. (2006) Phase Behavior of Lipid Monolayers Containing DPPC and Cholesterol Analogs. *Biophys J* **90**, 3176-3183

- 10 Kraft, L. M., *et al* (2006) Phase Separation of Lipid Membranes Analyzed with High-Resolution Secondary Ion Mass Spectrometry. *Science* **313**, 1948
- 11 Garidel, P., Johann, C. and Blume, A. (1997) Nonideal mixing and phase separation in phosphatidylcholine-phosphatidic acid mixtures as a function of acyl chain length and pH. *Biophys J* **72**, 2196-2210
- 12 Bagatolli, L. A., Gratton, E. (2000) Two photon fluorescence microscopy of coexisting lipid domains in giant unilamellar vesicles of binary phospholipid mixtures. *Biophys J* **78**, 290-305
- 13 Garidel, P., Johann, C. and Blume, A. (1997) Nonideal mixing and phase separation in phosphatidylcholine-phosphatidic acid mixtures as a function of acyl chain length and pH. *Biophys J* **72**, 2196-2210
- 14 Honda, M., Takiguchi, K., Ishikawa, S., Hotani, H. (1999) Morphogenesis of liposomes Encapsulating Actin Depends on the Type of Actin-crosslinking. *Journal of Molecular Biology* **287**, 293-300
- 15 Nomura, F., Inaba, T., Ishikawa, S., Nagata, M., Takahashi, S., Hotani, H., Takiguchi, K. (2004) Microscopic observations reveal that fusogenic peptides induce liposome shrinkage prior to membrane fusion. *Proc Natl Acad Sci USA* **101**, 3420-3425
- 16 Hotani, H. (1984) Transformation pathways of liposomes. *J Mol Biol* **178**, 113-120
- 17 Betz, W. J. and Bewick, G. S. (1992) Optical analysis of synaptic vesicle recycling at the frog neuromuscular junction. *Science* **255**, 200-203
- 18 Betz, W. J., Mao, F. and Bewick, G. S. (1992) Activity-dependent fluorescent staining and destaining of living vertebrate motor nerve terminals. *J Neurosci* **12**, 363-375
- 19 Wu, Y., Yeh, F. L., Mao, F. and Chapman, E. R. (2009) Biophysical characterization of styryl dye-membrane interactions. *Biophys J* **97**, 101-109

- 20 Angleson, J. K., Cochilla, A. J., Kilic, G., Nussinovitch, I., Betz, W. J. (1999) Regulation of dense core release from neuroendocrine cells revealed by imaging single exocytic events. *Nat. Neurosci.* **2**, 440-446
- 21 van Dijck, P. W., Kaper, A. J., Oonk, H. A. and de Gier, J. (1977) Miscibility properties of binary phosphatidylcholine mixtures. A calorimetric study. *Biochim Biophys Acta* **470**, 58-69
- 22 Parasassi, T., De Stasio, G., d'Ubaldo, A., Gratton, E. (1990) Phase fluctuation in phospholipid membranes revealed by Laurdan fluorescence. *Biophys J* **57**, 1179-1186
- 23 Hui, S. W. (1981) Geometry of phase-separated domains in phospholipid bilayers by diffraction-contrast electron microscopy. *Biophys J* **34**, 383-395
- 24 Tokumasu, F., Hwang, J. and Dvorak, J. A. (2004) Heterogeneous molecular distribution in supported multicomponent lipid bilayers. *Langmuir* **20**, 614-618
- 25 Tokumasu, F., Hwang, J. and Dvorak, J. A. (2004) Heterogeneous molecular distribution in supported multicomponent lipid bilayers. *Langmuir* **20**, 614-618
- 26 Parasassi, T., Gratton, E., Weiming, Y., Paul, W., Moshe, L. (1997) Two-photon fluorescence microscopy of laurdan generalized polarization domains in model and natural membranes. *Biophys J.* **72**, 2413-2429
- 27 Bagatolli, A., Gratton, E. (1999) Two-Photo Fluorescence Microscopy Observation of Shape Changes at the Phase Transition in Phospholipid Giant Unilamellar Vesicles. *Biophys J.* **77**, 1090-2101
- 28 Gruber, H. J., Schindler, H. (1994) External surface and lamellarity of lipid vesicles: a practice-oriented set of assay methods. *Biochim. Biophys. Acta* **1189**, 212-224

- 29 McIntyre, J. C., Sleight, R. G. (1991) Fluorescent Assay for Phospholipid Membrane Assymetry. *Biochemistry* **30**, 11819-11827
- 30 Mouritsen, O. G., Zuckermann, M. J. (1985) Softening of lipid bilayers. *Eur. Biophys. J.* **12**, 75-86
- 31 de Almeida, R. F. M., Loura, L. M. S., Fedorov, A., Prieto, M. (2002) Nonequilibrium Phenomena in the Phase Separation of a Two-Component Lipid Bilayer. *Biophys J* **82**, 823-834
- 32 Mouritsen, O. G., Jorgensen, K. (1994) Dynamical order and disorder in lipid bilayers. *Chem Phys Lipids* **73**, 3-25
- 33 Moscho, A., Orwar, O., Chiu, D. T., Modi, B. P., Zare, R. N. (1996) Rapid preparation of giant unilamellar vesicles. *Proc Natl Acad Sci USA* **93**, 11443-11447
- 34 Akashi, K., Miyata, H., Itoh, H., Kinoshita, K. Jr. (1998) Formation of Giant Liposomes Promoted by Divalent Cations: Critical Role of Electrostatic Repulsion. *Biophys J* **74**, 2973-2982
- 35 Lau, A., McLaughlin, A., McLaughlin, S. (1981) The adsorption of divalent cations to phosphatidylglycerol bilayer membranes. *Biochim. Biophys. Acta.* **645**, 279-292
- 36 Das, S. and Singhal, G. S. (1984) Light scattering studies on interaction of  $Ca^{2+}$  with phosphatidylserine liposomes: triggering action of pH. *Biochem Int* **8**, 669-677
- 37 Hammel, M., Schwarzenbacher, R., Gries, A., Kostner, G. M., Laggner, P. and Prassl, R. (2001) Mechanism of the interaction of beta(2)-glycoprotein I with negatively charged phospholipid membranes. *Biochemistry* **40**, 14173-14181

- 38 Brown, P. M. and Silvius, J. R. (1989) Stability and fusion of lipid vesicles containing headgroup-modified analogues of phosphatidylethanolamine. *Biochim Biophys Acta* **980**, 181-190
- 39 Rand, R. P., Fuller, N., Parsegian, V. A. and Rau, D. C. (1988) Variation in hydration forces between neutral phospholipid bilayers: evidence for hydration attraction. *Biochemistry* **27**, 7711-7722
- 40 Yu, Z. W., Calvert, T. L. and Leckband, D. (1998) Molecular forces between membranes displaying neutral glycosphingolipids: evidence for carbohydrate attraction. *Biochemistry* **37**, 1540-1550
- 41 Marra, J. (1986) Direct measurement of the interaction between phosphatidylglycerol bilayers in aqueous electrolyte solutions. *Biophys J* **50**, 815-825
- 42 Lau, A., McLaughlin, A. and McLaughlin, S. (1981) The adsorption of divalent cations to phosphatidylglycerol bilayer membranes. *Biochim Biophys Acta* **645**, 279-292
- 43 Zidovetzki, R., Atiya, A. W. and De Boeck, H. (1989) Effect of divalent cations on the structure of dipalmitoylphosphatidylcholine and phosphatidylcholine/phosphatidylglycerol bilayers: an <sup>2</sup>H-NMR study. *Membr Biochem* **8**, 177-186
- 44 McLaughlin, S., Mulrine, N., Gresalfi, T., Vaio, G. and McLaughlin, A. (1981) Adsorption of divalent cations to bilayer membranes containing phosphatidylserine. *J Gen Physiol* **77**, 445-473
- 45 McLaughlin, S. G., Szabo, G., Eisenman, G. and Ciani, S. M. (1970) Surface charge and the conductance of phospholipid membranes. *Proc Natl Acad Sci U S A* **67**, 1268-1275
- 46 McLaughlin, S. G., Szabo, G. and Eisenman, G. (1971) Divalent ions and the surface potential of charged phospholipid membranes. *J Gen Physiol* **58**, 667-687



## CHAPTER 4

### GIANT LIPOSOMES FROM HOMOLOGOUS SERIES OF LIPIDS

#### 4.1 Introduction

Biological membranes are composed of different lipid species. These lipids have different headgroup structure and hydrocarbon chain length. These differences show that there is a wide range of structural features that are required to maintain cellular processes. Because biological membranes are more complex, studies using liposomes have provided insight into the organization, dynamics and important roles of each lipid in the bilayer region. In this study, liposomes of mixed size distribution from saturated hydrocarbon chains of varying lengths were characterized by the fluorescent properties of the NBD PE and NBD PC probes. These properties are sensitive to the environment around the NBD fluorescent probe.

Changes in the environment surrounding NBD have proved valuable in evaluating the fate and localization of the lipid and nature of interactions in the lipid bilayer. For example, dithionite quenching of NBD fluorescence in the tail region of the bilayer is a method used to measure phospholipid packing in the membrane [1]. It is also possible with fluorescence to determine the depth that can be penetrated by the fluorescent quenchers in the membrane by changing the length of the chain to which the fluorophore is attached. This is possible with sensitive fluorophores that can be

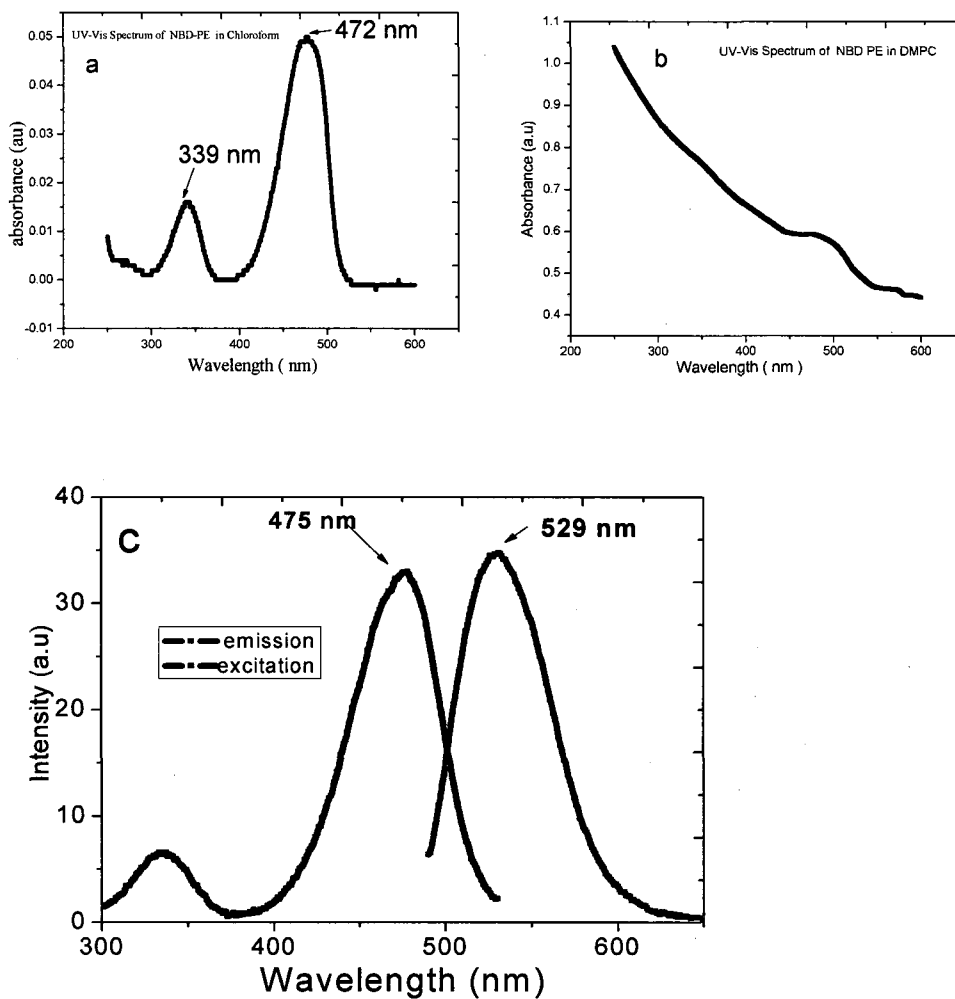
placed in acyl-chain of varying lengths to measure penetration depth. This could also be useful in determining the partitioning parameters of the quenchers in the membranes [2]. In our case, the effect of the acyl-chain on NBD fluorescent properties was studied by placing the NBD probe in membrane of varying acyl-chain length. We studied both the NBD PE and NBD PC fluorescence behavior since they probe different regions of the lipid bilayer.

A 4 mg/mL lipid concentration of was used in all cases presented in this study. The NBD PE or NBD PC fluorescent probe was added to phosphatidylcholines at 0.5% (mol/mol) with respect to the lipid. (See details in Section 2.3.1). We choose 0.5% (mol/mol) with respect to the total lipid concentration in order to minimize artifacts that could possibly be generated by the probe embedded in the bilayer. In the past, the NBD probe at a higher concentration in the membrane was reported to undergo aggregation that can lead to self-quenching in the bilayer [3, 4]. The excitation wavelength was set at 470 nm with a slit width of 5 nm. The emission of NBD moiety was monitored at 540 nm with the similar slit width as the excitation. It has been noted earlier in Chapter 1 that the NBD probe is endowed with fluorescence properties that include lifetime, quantum yield and Stokes shift. These properties are affected by the polarity of the surrounding medium. In Figure 4.1, the UV-Vis spectral data of NBD PE in chloroform and in liposomes is presented. The spectrum of NBD PE in a solvent shows two absorption peaks at 339 and 472 nm. In liposomes the 470 nm absorption peak is stronger than absorption at 339 nm. These peaks are consistent with the absorption maxima discussed in Section 1.8. The wavelength at

339 nm represents the  $\pi$ ,  $\pi^*$  band whereas the 470 nm is for the charge transfer transition band. Excitation using the 470 nm wavelength of the NBD PE in polydisperse DPPC liposomes showed emission maximum at 572 nm as shown in Figure 4.1 (c).

#### **4.2 Fluorescence Quenching Experiments**

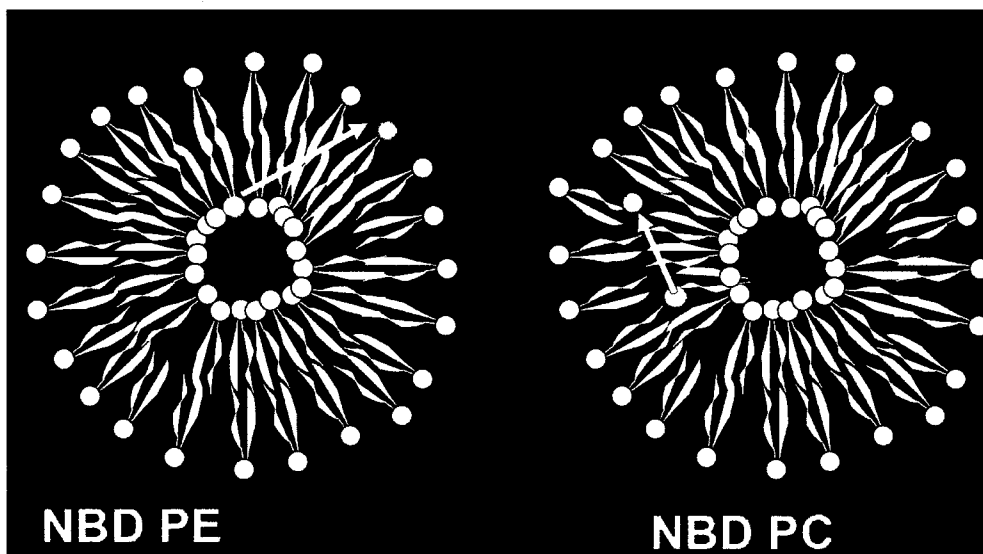
The present study was undertaken to investigate acyl-chain length on the behavior of the fluorescence properties of the NBD PE and NBD PC probes. Liposomes were prepared from a homologous series from 12:0 PC to 20:0 PC. Fluorescence quenching of the NBD moiety was initiated by dithionite. The studies were conducted using a polydisperse size distribution of liposomes obtained from phospholipids of varying acyl-chain lengths. The quenching experiments were measured at temperatures corresponding to the gel phase of each phospholipid. It was assumed that at this temperature, the membrane is solid or compact with minimum density fluctuations. The rate of quenching was calculated from an exponential decay curve shown in Figure 2.5 in Section 2.3.2. The curve fitted well to a sum of two exponentials (Equation 2.2 Section 2.3.4).



**Figure 4.1** UV-Vis absorbance of NBD PE (16:0 PC). The spectra data was obtained in chloroform (a) and in DMPC liposomes (b) and fluorescence excitation emission of NBD PE in DPPC (c).

The correlation to the fit and its chi-square ( $\chi^2$ ) values were computed using Origin software. The model yielding the least  $\chi^2$  was used. The rate coefficient  $k_1$  for the immediate quenching of the NBD by dithionite and the slow step was determined from the biexponential fitting.

The half life of the first-order reaction kinetics was calculated using equation 4.2. It appeared from Figures 4.3 and 4.4 that the NBD PE probe was less efficiently quenched by dithionite than the NBD PC probe.



**Figure 4.2** NBD PE and NBD PC orientation in lipid bilayer.

On the ease of accessibility of the NBD moiety of the NBD PE (see Figure 4.2) to dithionite, one can assume that it is quenched faster than NBD PC probe. The rate coefficients of NBD PE and NBD PC obtained from this study do not support the aforementioned assumption. Even though the lipid bilayer presents an anisotropic phase with the acyl-chain aligned perpendicularly to the membrane surface, it is also a region of high structural heterogeneity. This can potentially affect the photophysical properties of the fluorescent probes embedded within it. The membrane displays a two compartment distribution of NBD, the inner leaflet and the outer leaflets NBD [5-9]. The rate coefficient for the immediate quenching corresponds to a reaction of the dithionite with NBD analogs on the outer leaflets [8]. This is can be described by a single exponential rate equation,  $S_1 = a_1 e^{-k_1 t}$ . Once the outer leaflets NBD are completely quenched, there could be a concentration gradient developing across the bilayer resulting in the transbilayer movement as depicted by the arrows in Figure 4.3. This is a slow step that leads to a second slow rate coefficient  $k_2$  yielding a fluorescent intensity,  $S_2 = a_2 e^{-k_2 t}$ . The concentration of dithionite in solution is 100 times in excess of that of NBD dye in the bilayer. Therefore, the reaction between NBD and dithionite is pseudo-first order with respect to dithionite concentration [10]. The influx of dithionite across the membrane and reduction of the inner leaflets by dithionite or transbilayer movement rate was given by the rate coefficient  $k_2$ . In this chapter, we considered the rate coefficient  $k_1$  to further understand the acyl-chain

dynamics on the behavior of the NBD PE and NBD PC embedded in regions of varying hydrophobic thickness.

$$t_{1/2} = (\ln 2 / k_1) \quad [4.1]$$

The outer leaflets NBD PE or NBD PC were reduced by addition of cold freshly prepared 30  $\mu\text{L}$  of 1 M sodium dithionite ( $\text{N}_2\text{S}_2\text{O}_4$ ) in 1 M Tris buffer pH 10. 150  $\mu\text{L}$  of a total lipid concentration of 4 mg/mL was added to 3 mL HEPES buffer containing sodium chloride at pH 7.4 (100 mM NaCl, 10 mM HEPES-NaOH). The details are available in the experimental Section 2.3.4. The rate constant of dithionite quenching of the NBD fluorescence was calculated using the half-life obtained using Equation 4.1. Half life was plotted as a function of the number of carbon atoms as shown in Figure 4.4. The measurements were conducted at a temperature corresponding to the gel phase of each phospholipid as tabulated in Table 4.1. The structures of these phospholipids and their transition temperatures can be found in Table 2.2 in the experimental section.

**Table 4.1** Gel phase temperature of phosphatidylcholines. This was used for quenching experiments.

<b>Lipid</b>	<b>Temperature ( °C )</b>
DLPC	-5
13:0 PC	5
DMPC	17
15:0 PC	23
DPPC	25
17:0 PC	37
DSPC	25
20:0 PC	25

Saturated phosphatidylcholine lipids were used in all the experiments. The rate co-efficient of the fast step  $k_1$ , was obtained directly from the fittings for each acyl-chain constituting the liposome under investigation. The exponential loss in fluorescence upon addition of dithionite was attributed to the reduction of the nitro group in NBD to amine group by dithionite [8]. The equation leading to the reduction is shown in Equation 1.4, Section 1.9. Inspection of Figure 4.4 which shows the relationship between the length of acyl-chain and rate of quenching of NBD PE

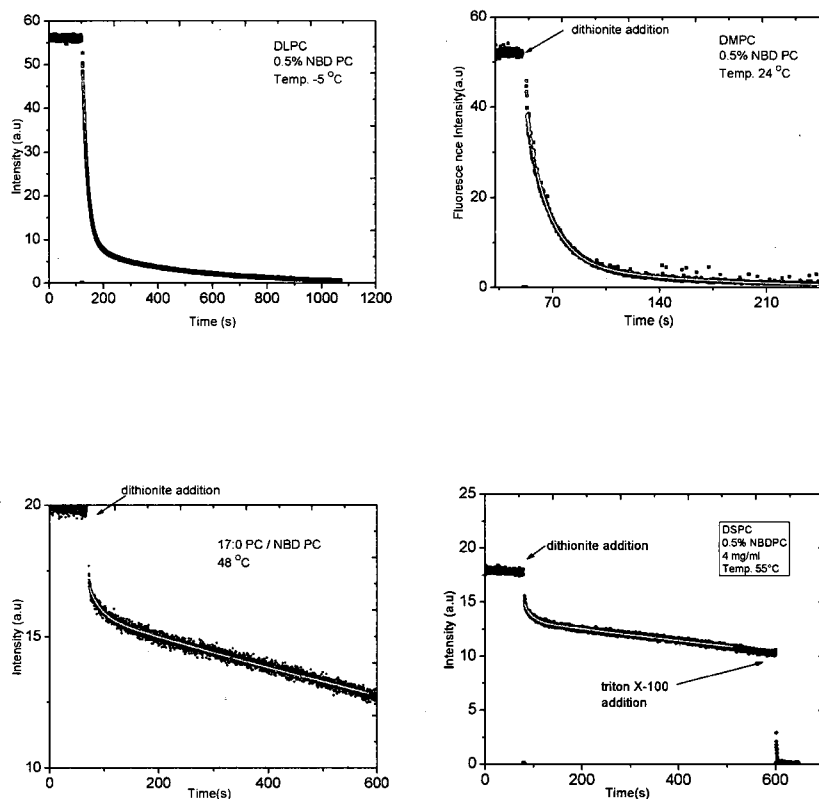


decreases with increasing acyl chain length up to 16:0 PC. In the past, studies in the gel phase of phospholipid bilayer membrane composed of the phosphatidylcholines with asymmetrical acyl-chain length experience static interdigitation of the acyl-chains [11, 12]. This could lead to thinner membranes compared to symmetrical ones [11]. Having a thinner interdigitated bilayer can also lead to the formation of or stabilization of the lipid domains in the gel phase [13]. Mazeres showed that the fluorescence properties of the NBD fluorophore are strongly affected by the chemical structure and the physical state of the host lipids [14]. He further showed that the quantum yield was the most affected among the fluorescence properties considered.

We expect NBD PC to have different fluorescent behavior compared to NBD PE. As expected, the gel phase temperature increases with increase in number of carbon atoms. The bilayers of longer acyl-chains from 17:0 PC to 20:0 PC display a characteristic sub-main transition slightly below the main transition temperature [15]. Sub-main transition is a low-enthalpy highly co-operative phase transition temperature between pre- and main transition of phospholipids [16]. It is the first step in the disordering of the acyl-chain. It is observed a few degrees before the main transition temperature. This follows the interaction of water molecules with the hydrocarbon region of the phospholipid bilayer leading the conformational change of the acyl-chain [17]. Computer simulations have shown that the sub-main transition occurs due to the lattice melting whereas the acyl-chain melting occurs at a higher temperature at the main phase transition [18]. This occurs due to decoupling of the acyl-chain melting from the pseudo-to one-dimensional crystalline lattice [19]. The

heat capacity measurements have shown that the sub-main transition enthalpy is affected by the salt concentration and equilibration time but not the transition temperature [20]. These features have been detected by spectroscopic properties of fluorescent probe in lipid bilayer region [15].

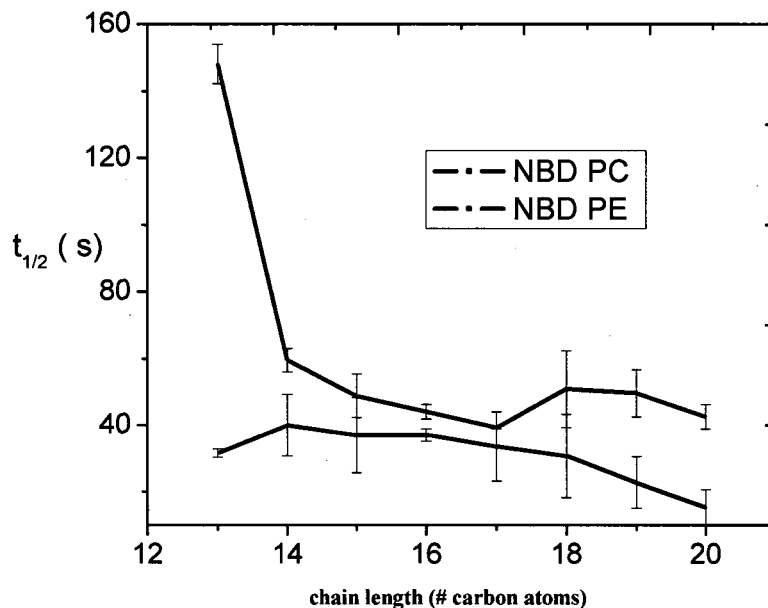
In this section, the spectroscopic changes of the NBD PE and NBD PC in the homologous series were determined with respect to the fluorescence intensity measurements. The fluorescence intensity value decreases gradually to zero after addition of dithionite as shown in Figure 4.3. The longer acyl-chain length liposomes required more reaction time for the complete quenching reaction of dithionite with the NBD than the shorter ones. The rate of dithionite quenching was faster in the phospholipids lipid bilayers with few number of carbon atoms (DLPC and DMPC). The rate of dithionite quenching was of NBD PC was faster than the NBD PE probe.



**Figure 4.3** Exponential decay of dithionite quenching of the NBD PC. The measurements for the DLPC, DMPC, 17:0 PC and DSPC were taken at the temperatures corresponding to the phase transition.

It is clear from Figure 4.4 that kinetic of dithionite quenching of NBD fluorescence and fluorescence intensity in the gel phase of the lipids was negatively correlated to the acyl-chain length between DMPC (14:0) and 20:0 PC for NBD PC. The rate of quenching of NBD group in NBD PE and NBD PC was different at higher acyl chain length. The result of 13:0 PC was anomalous (Figure 4.4). An expanded

portion (without 13:0 PC) showed that with the increasing chain length, the differences between NBD PE and NBD PC become more apparent.



**Figure 4.4** Half life of dithionite quenching of NBD fluorescence in acyl chain of variable chain lengths.

The objective of this study was to investigate the region within the vicinity of the probe. The NBD PE probes interfacial region since NBD moiety of this phospholipid analog is confined to the headgroup region. In NBD PC, the fluorescent moiety is linked to the short chain residue at position 12 in the *sn*2-position while a palmitoyl residue is in the *sn*1-position. In NBD PE, the fluorescent NBD is attached to the negatively charged phosphate in the headgroup region of the phospholipid

analog. The NBD moiety is reduced to a non-fluorescent amino group by the reaction of dithionite. The results displayed in Figures 4.3 and 4.4 were obtained at a temperature corresponding to the gel phase temperature of the lipid. Lateral diffusion is minimal in gel phase. In view of this, the nature of a membrane is only probed by the NBD moiety located in the headgroup or in the hydrocarbon region. Sampling was done in three replicates to ascertain reproducibility of the data. The results were reported and the standard deviation shown as an error bar as tabulated in Table 4.2.

**Table 4.2** Half life calculated for the different chain lengths.

<b>Acyl-chain length (# of carbon atoms)</b>	<b>NBD PC <math>t_{1/2}</math> (s)</b>	<b>NBD PE <math>t_{1/2}</math> (s)</b>
14	39.9 ± 9.3	59.4 ± 3.5
15	36.9 ± 11.3	48.7 ± 6.5
16	37.0 ± 1.9	43.9 ± 2.1
17	33.6 ± 10.5	39.2 ± 0.4
18	30.7 ± 12.5	50.7 ± 11.6
19	22.7 ± 7.7	49.5 ± 7.0
20	15.2 ± 5.4	42.4 ± 3.6

Similar studies conducted by Alakoskela Kinunnen using DPPN instead of NBD PE as fluorescent analog yielded results that are much in agreement with the

findings [15]. The group employed liposomes that were 100 nm in size. They attributed the slow rate of DPPN reduction to the negative charge carried by the phosphate group in DPPN. The slow rate of headgroup NBD PE could possibly be due to the microdomains formation that increases with the acyl-chain length. Previous studies have shown that there is a tendency of the negatively charged NBD PE to be enriched in these transient domains while undergoing phase transition [15]. In such a situation, the surface charge density of transient domains would be higher [21] and the rate of dithionite quenching of NBD PE could be expected to decrease.

The position of NBD probe in the bilayer region has been investigated by different techniques. For example, paramagnetic fluorescence quenching by spin labels and fluorescence properties in a media of varying dielectric constant showed that this moiety has high affinity for polar environment [14, 22]. The NBD on the hydrocarbon tail loops back towards the lipid water interface [22]. It possesses a strong dipole moment that favors the propensity for a more polar environment. In Figure 4.4 the rate of dithionite quenching of NBD is determined by the thickness of the bilayer. The thickness of the bilayer varies linearly with the number of carbons per acyl chain [23]. This change can be associated with thermally induced lateral density fluctuations. The latter is defined as the number of lipid molecules per unit volume along the plane of the bilayer. These fluctuations are derived from the fact that lipid bilayer is a two-dimensional soft system. They behave like liquid crystals and exhibit a very high level of flexibility. This flexibility allows thickness fluctuation motions. These motions can be either the conformation transitions of the

lipid hydrocarbon tails that take place in picoseconds or bending that can take several milliseconds.

A high degree of conformational change is observed in the acyl-chain from a rigid extended conformation in the low temperature gel phase, to a shortened kink-like conformation in the high temperature fluid phase. The lateral density parameter is known to increase as acyl-chain is decreased. It is also strongly enhanced at the phase transition region [24]. As already mentioned elsewhere, the polarity of NBD can influence the location of the bulky NBD in the bilayer. Based on this fact, NBD essentially probes the head-group region of the bilayer at the water-interface region of the bilayer. It is also reasonable to expect the chromophore perturbing local bilayer organization. This can occur for any chromophore concentration. It is this environment that is being sensed by the NBD spectroscopic response. NBD located in the acyl-chain (NBD PC) could possibly contribute to a certain disorder in the lipid bilayer. In the case of NBD PE, the NBD moiety is attached to the headgroup. This restricts its movement. This argument is also supported by the steep decrease in the fluorescence intensity as seen in Figure 4.5. That for a fraction of NBD PC probe, the polarity of the environment decreases sharply at increasing chain length.

### **4.3 Fluorescence Intensity Measurements**

Fluorescence intensity measurements were conducted in the gel phase of the lipid. These measurements were studied as a function of the hydrocarbon chain length. The emission at 540 nm was followed with absorption maximum at 470 nm.

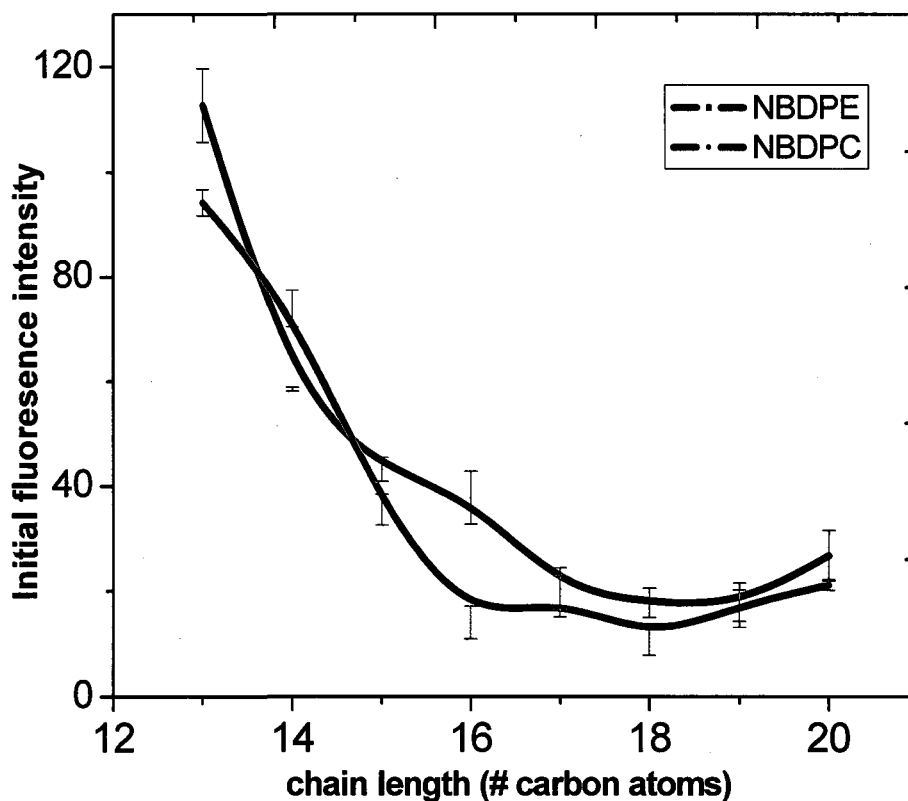
At maximum saturation, the fluorescence is proportional to the quantum yield and absorption maximum of chromophore. Quantum yield is a measure of integrated photon emission over the fluorophore spectral band. The rate of emission is a function of the lifetime of the excited state.

The fluorescence intensity gradually declines with the increasing chain length (Figure 4.5). A decrease of fluorescence intensity is an indication of increased water content within the region surrounding the NBD moiety. In our case the effect is a linear function of the acyl-chain length. A critical level of hydration is required by lipid molecules to achieve lipid bilayer [25]. It is also established that water diffuses across the lipid bilayers and therefore it is found within the hydrophobic region [26]. The penetration of water into the bilayer sets a dielectric constant gradient from a value of about 80 to 5 at the bilayer center as discussed in Chapter 1.

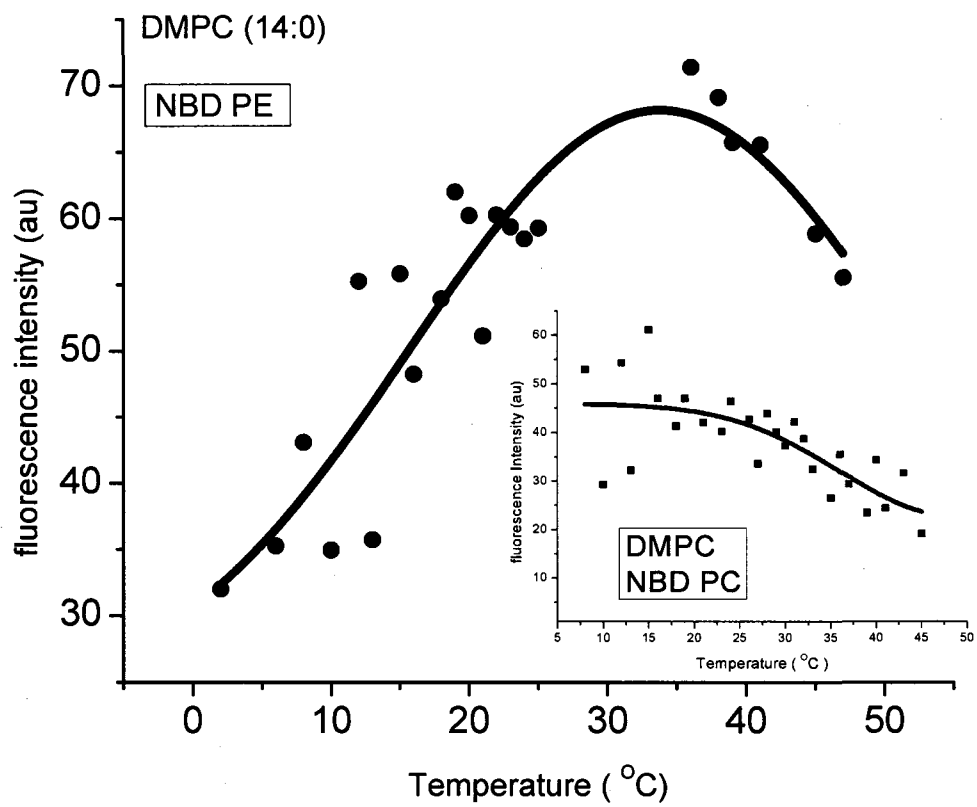
Fluorescence spectroscopy method using solvatochromic fluorophores has reported membrane that is permeable to water [27]. It is also important to note that fluorescence emission intensity is positively correlated to the membrane dipole potential [28]. The change in dipole potential in the bilayer is similar to that of freedom of movement and anisotropy of interface water molecules. The hydration shell provided by these water molecules could also account for the NBD fluorescence in an acyl-chain of varying chain length. It appears that a change in fluorescence intensity from either NBD PE or NBD PC in acyl-chain of varying length is sensitive to polarity of lipid bilayer region. On heating, the fluorescence intensity of the NBD PE and NBD PC increases continuously with the gel phase of DMPC (Figure 4.6). It



begins to increase more steeply at about 10 to 20°C and reaches a maximum at about 23°C for NBD PC and thereafter decreases continuously. The data can be explained as follows. The probes NBD PE or NBD PC are strongly excluded from the gel phase of DMPC. In the gel phase matrix, the probe could possibly segregate into domains leading to increase in the fluorescence intensity [15].



**Figure 4.5** Measurements of initial fluorescence intensity of NBD PE and NBD PC in lipids of different chain lengths. Measurements were taken at 25°C.



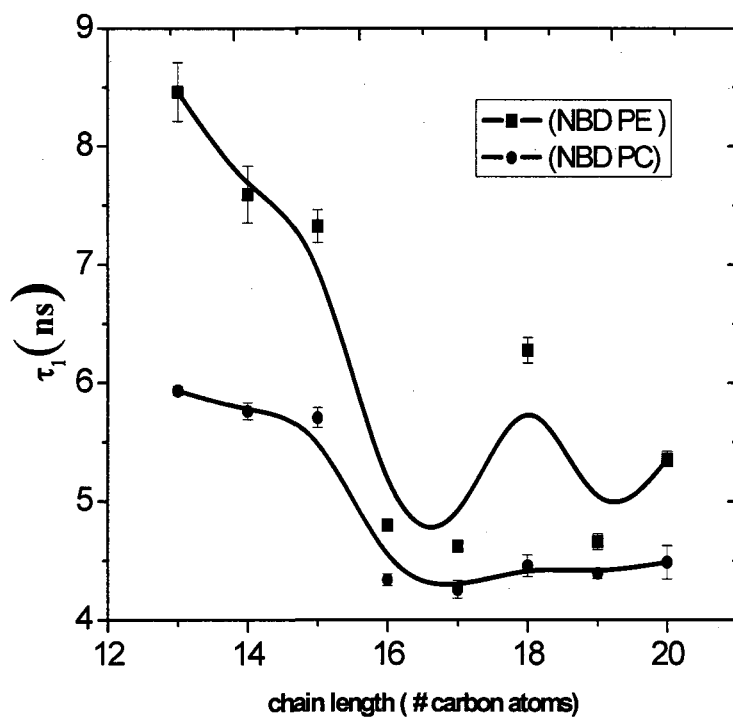
**Figure 4.6** Fluorescence intensity measurements in DMPC liposomes.  $T_m$  is 23°C for DMPC.

#### 4.4 Lifetime Measurement

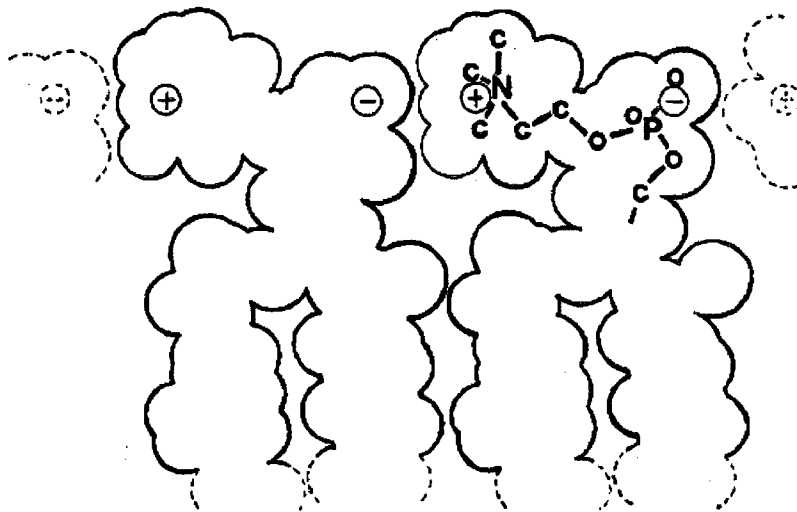
The fluorescence lifetime property of NBD was used to determine the dynamics of the bilayer by headgroup NBD PE and tail-labeled NBD PC fluorescent probes. The lifetimes were calculated from changes in fluorescence intensity. All fluorescence decays were fitted to a bi-exponential. Since we were interested in studying NBD PE and NBD PC in acyl-chains of varying lengths, the shorter lifetime component,  $\tau_1$  was analyzed. This was used to gauge the performance and dynamics of an NBD probe in the bilayer. The excited lifetime of NBD PE and NBD PC as a function of chain length obtained in the gel phase temperature is displayed in Figure 4.7. There is a steady decrease in the lifetime with increasing acyl-chain length of the phospholipids to 16. Such a change is indicative of changes in the microenvironment of the NBD moiety in the acyl chain composition [29]. This could be due to changes in the polarity or location of the fluorescent probe in the liposome bilayer region.

The excited state lifetime reported of NBD PE in membranes is between 6 and 8 nanoseconds [29, 30]. The lifetimes obtained in this study is in agreement with findings by these authors. This value reduces due to the hydrogen bonding between the NBD and the solvent [30]. This is accompanied by an increase in the rate of nonradiative decay leading the de-excitation of the fluorophore [14, 30]. In our case, the NBD PE consistently gave a relatively longer lifetime than NBD PC. This was attributed possibly to packing and geometry arising from the differences in the orientation of NBD moiety. NBD PE lies in the headgroup region of the bilayer. This

region is more restricted in mobility compared to the hydrocarbon [31]. In the past, studies have shown that the phosphatidylcholine headgroup is oriented parallel to the bilayer surface as shown schematically in Figure 4.8. It is reasonable to expect that the headgroup region has a more and stronger intermolecular interaction than the acyl-chain of phospholipids. The phosphatidylethanolamine headgroup with its ammonium group attached to the headgroup in the structure is expected to engage strongly in molecular interactions than the choline headgroup. These interactions can affect the NBD PE headgroup mobility in the lipid bilayer.



**Figure 4.7** Lifetime of NBD PE and NBD PC in acyl-chain of varying lengths.

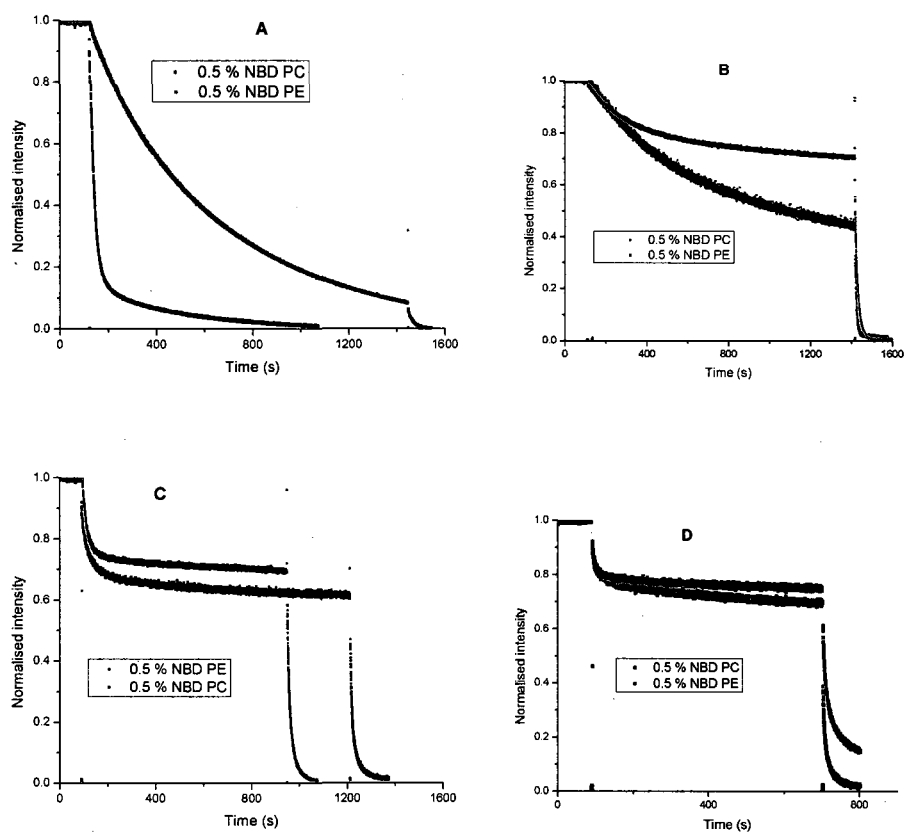


**Figure 4.8** Preferred headgroup conformation in bilayer [31].

#### **4.5 Percent of NBD Quenched by Dithionite**

The extent of dithionite quenching of NBD in acyl-chain of varying length was evaluated. Normalized intensity was used for the data presented. In Figure 4.9, the results of lower and higher acyl-chain length are presented. It was evident in this case that the percentage of NBD fluorescence quenched was relatively less in 16:0 PC and higher hydrocarbon chains. This was true for both NBD PE and NBD PC. The rate of quenching was always higher in NBD PC than NBD PE in all acyl-chain lengths investigated. This behavior was more prominent in the short chain hydrocarbons (DLPC and DMPC). The NBD moiety of NBD PC perhaps suffers the setback of being located in a more hydrophobic environment. This potentially creates

bilayer defects especially due to packing defects between DLPC and NBD PC (16:0-12:0). Such defects could lead to leakage across the bilayer. This is aggravated by the fact that NBD moiety in NBD PC loops back to the interfacial region of the bilayer.

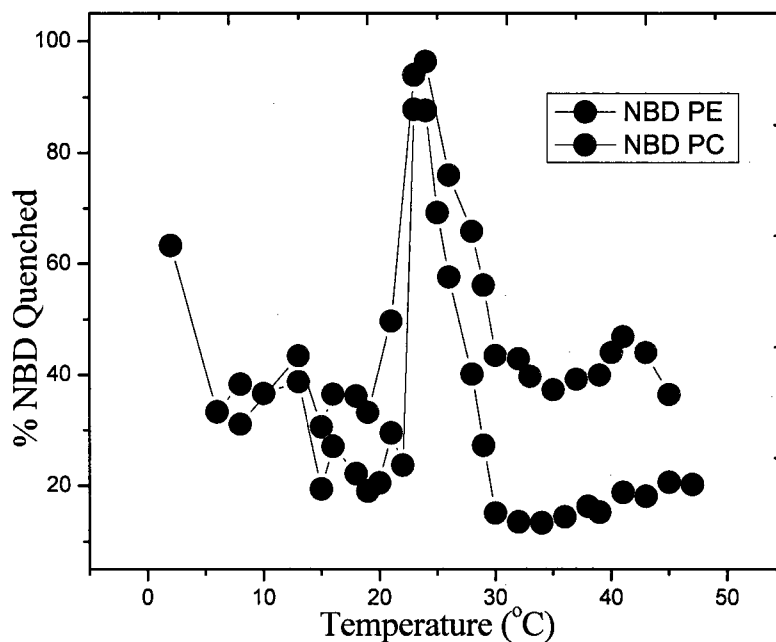


**Figure 4.9** Exponential decay plots of dithionite quenching of NBD in acyl-chain of varying lengths. The figures are as follows and data obtained at the temperature in parenthesis: A is DLPC (-5°C), B, 13:0 PC (5°C), C, 15:0 PC (23°C) and D, 17:0 PC (37°C).

The fluorescence intensity change in NBD PE and NBD PC in DMPC was calculated before and after addition of dithionite reagent. The calculation was based on the lamellarity as discussed in Section 2.3.2. The difference was then expressed as a percentage of the NBD probe quenched. This was plotted as a function of the temperature as shown in Figure 4.10. Results showed that the amount of NBD reduced on addition of 1 M sodium dithionite was different in the gel, fluid and the phase transition regions. This was consistent with DMPC undergoing a gel-fluid transition. At 23°C, nearly 100% dithionite quenching of NBD moiety was observed. This corresponds to the phase transitions of DMPC [32]. A slight hump was observed below phase transition region. Above the phase transition there was a relatively smaller increase in the amount of the NBD quenched. The NBD fluorescence in NBD PC was completely quenched at the phase transition.

The percentage of NBD fluorescence quenched above the phase transition was significantly different in NBD PE and NBD PC. This trend was consistent with location of NBD moiety. The NBD of NBD PC is located in the fatty acyl chain of lipid. Here, the bilayer is more perturbed as a result of locating a more polar group in a non-polar hydrophobic environment. The effect is more aggravated at the phase transition region. As explained elsewhere in this chapter, this can be attributed to the disorder in the lipid bilayer. The differences observed in NBD PC and NBD PE can also be explained based on the looping back of NBD PC as reported by Raghuraman [22]. The NBD PE and NBD PC orientation change with the changes in temperature. This becomes more random with the increase in temperature as shown by the steady-

state anisotropy data of DMPC bilayer. Steady-state anisotropy was monitored as a function of the temperature passing through the phase transition of the DMPC lipid bilayer (Figure 4.11). The Figure shows that both NBD PE and NBD PC orientation becomes more random with increasing temperature. Differences in the NBD PE and NBD PC become more apparent above the phase transition temperature of DMPC.

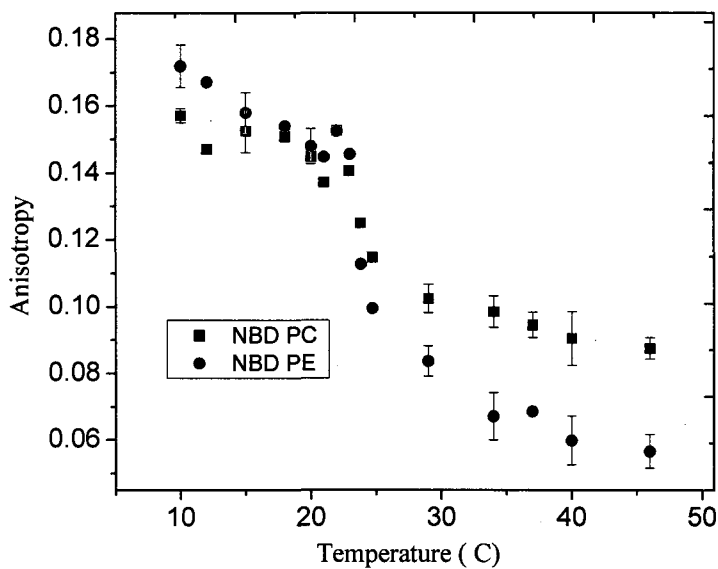


**Figure 4.10** Percentage of NBD quenched in the DMPC (14:0) lipid bilayer as a function of temperature.

The steady-state anisotropy was determined using Equation 1.4 in Section 1.9. The bilayer region of DMPC was investigated by varying the temperature from 10 to 49°C. The decrease in fluorescence anisotropy in NBD PE in the temperature range



between 10 and 45°C was larger (0.1). The NBD PC fluorescent probe had a smaller value (0.06) at the same temperature range. This value indicates that the NBD in the NBD PE has a greater rotational degree of freedom compared to the NBD PC. This degree of freedom leads to change of almost a factor of two in its anisotropy with increasing temperature compared to the NBD PC. The sudden drop in anisotropy at the phase transition could be attributed to the sudden changes in membrane polarity as a result of the gel to fluid transition as previously reported [33].

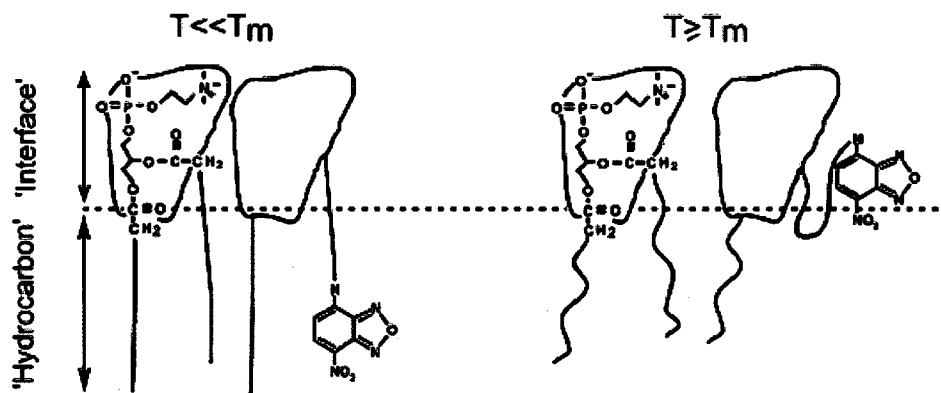


**Figure 4.11** Temperature-dependence steady-state anisotropy of NBD in DMPC (14:0) bilayer.

## 4.6 Conclusion

In recapitulation, we examined bilayer properties using behavior of NBD PE and NBD PC. Understanding these properties requires an experimental examination of the changes in relation to the temperature. The behavior of NBD PE (16:0) and NBD PC (16:0-12:0) probes were examined by studying dithionite quenching and the excited state lifetime in a saturated hydrocarbon of varying chain length from the DLPC to 20:0 PC.

The two fluorescent probes NBD PE and NBD PC were employed to investigate further dynamics of the DMPC liposomes. DMPC form liposomes that display a phase transition close to room temperature. We sought to explain the differences displayed by the two lipid analogs. The quenching kinetics for the NBD PE and NBD PC were investigated. The rate of quenching was found to decrease with the increasing acyl-chain length. The fluorescence intensity measurements of the NBD PE and NBD PC were found to decrease with the increase in the acyl-chain length. Even though it was not possible to evaluate the water concentration within our system, it can be pointed out that the influx of water in the hydrophobic region of the lipid bilayer could partly explain the quenching of NBD fluorescence. It was also noted that the NBD moiety in the NBD PC is constrained in the hydrophobic region. It can potentially loops back to the interface as shown in Figure 4.12. This behavior was recently been reported by studies using red edge excitation shift measurements conducted in extruded liposomes [22, 34].



**Figure 4.12** Looping back of the NBD of NBD PC as a function of the phase state of the host lipid [22].

Differences in orientation can influence the rate of quenching, lipid packing and excited lifetime dynamics. Using a polydisperse liposome system, we obtained excited state lifetime of NBD PE and NBD PC comparable to existing literature values. Here, it was found out that the NBD PE probe has a longer excited state lifetime than the NBD PC. Changes in membrane polarity, thickness and hydration shell in the hydrocarbon chain of varying lengths can possibly influence the excited state lifetimes of the probes embedded. The NBD moiety of NBD PE resides in a more rigid environment in the headgroup regions of the bilayer. This was demonstrated by the steady state anisotropy measurements obtained in the gel phase of DMPC lipid bilayer. On increasing temperature beyond phase transition, the degree of freedom for the movement of NBD PE became more random. This could possibly have a profound influence on the results obtained from dithionite quenching, the lifetime and fluorescence intensity measurements. Perhaps a relatively lower rate

of dithionite quenching in the NBD PE was due to negatively charged phosphate group that impedes dithionite approach to NBD moiety in the water-lipid interface as previously observed by Alakoskela [15].

#### 4.7 References

- 1 Huster, D., Muller, P., Arnold, K., Hermann, A. (2001) Dynamics of membrane penetration of the fluorescent 7-nitrobenz-2-oxa-1,3-diazol-4-yl (NBD) group attached to an acyl chain of phosphatidylcholine. *Biophys J* **80**, 822-831
- 2 Langer, M., Hui, S. W. (1993) Dithionite penetration through phospholipid bilayers as a measure of defects in lipid molecular packing. *Chem Phys Lipids* **65**, 23-30
- 3 Mukherjee, S., Chattopadhyay, A. (1996) Membrane Organization at Low Cholesterols: A study Using 7-Nitrobenz-2-oxa-1,3-diazol-4-yl-Labeled Cholesterol. *Biochemistry* **35**, 1311-1322
- 4 Chattopadhyay, A., Mukherjee, S. (1999) Red Edge Excitation Shift of a Deeply Embedded Membrane Probe: Implication in Water Penetration in the Bilayer. *J Phys Chem B* **103**, 8180-8185
- 5 Connor, J. and Schroit, A. J. (1987) Determination of lipid asymmetry in human red cells by resonance energy transfer. *Biochemistry* **26**, 5099-50105
- 6 Romsicki, Y. and Sharom, F. J. (2001) Phospholipid flippase activity of the reconstituted P-glycoprotein multidrug transporter. *Biochemistry* **40**, 6937-6947
- 7 Nichols, W. J., Angeletti, C. (1998) Dithionite Quenching Rate Measurement of Inside- Outside Membrane Bilayer Distribution of 7-Nitrobenz-2-oxa-,3-diazol-4-yl-Labeled Phospholipids. *Biochemistry* **37**, 15114-15119
- 8 McIntyre, J. C., Sleight, R. G. (1991) Fluorescent Assay for Phospholipid Membrane Assymetry. *Biochemistry* **30**, 11819-11827
- 9 Wolf, D. E., Winiski, A. P., Ting, A. E., Bocian, K. M. and Pagano, R. E. (1992) Determination of the transbilayer distribution of fluorescent lipid

analogues by nonradiative fluorescence resonance energy transfer. *Biochemistry* **31**, 2865-2873

- 10 Malatesta, F. (2005) The study of bimolecular reactions under non-pseudo-first order conditions. *Biophys Chem* **116**, 251-256
- 11 Hui, S. W., Mason, J. T. and Huang, C. (1984) Acyl chain interdigitation in saturated mixed-chain phosphatidylcholine bilayer dispersions. *Biochemistry* **23**, 5570-5577
- 12 Huang, C., Wang, Z. Q., Lin, H. N. and Brumbaugh, E. E. (1993) Calorimetric studies of fully hydrated phosphatidylcholines with highly asymmetric acyl chains. *Biochim Biophys Acta* **1145**, 298-310
- 13 Schram, V. and Thompson, T. E. (1995) Interdigitation does not affect translational diffusion of lipids in liquid crystalline bilayers. *Biophys J* **69**, 2517-2520
- 14 Mazeres, S., Schram, V., Tocanne, J. F. and Lopez, A. (1996) 7-nitrobenz-2-oxa-1,3-diazole-4-yl-labeled phospholipids in lipid membranes: differences in fluorescence behavior. *Biophys J* **71**, 327-335
- 15 Alakoskela, J. M. I., Kinnunen, P. K. J. (2001) Probing phospholipid main phase transition by fluorescence and a surface redox reaction. *J Phys Chem B* **105**, 11294-11301
- 16 Pressl, K., Jorgensen, K. and Laggner, P. (1997) Characterization of the sub-main-transition in distearoylphosphatidylcholine studied by simultaneous small- and wide-angle X-ray diffraction. *Biochim Biophys Acta* **1325**, 1-7
- 17 Milhaud, J. (2004) New insights into water-phospholipid model membrane interactions. *Biochim Biophys Acta* **1663**, 19-51
- 18 Nielsen, M., Miao, L., Ipsen, J. H., Jorgensen, K., Zuckermann, M. J. and Mouritsen, O. G. (1996) Model of a sub-main transition in phospholipid bilayers. *Biochim Biophys Acta* **1283**, 170-176

- 19 Heimburg, T. (2000) A model for the lipid pretransition: coupling of ripple formation with the chain-melting transition. *Biophys J* **78**, 1154-1165
- 20 Trandum, C., Westh, P. and Jorgensen, K. (1999) Slow relaxation of the sub-main transition in multilamellar phosphatidylcholine vesicles. *Biochim Biophys Acta* **1421**, 207-212
- 21 Soderlund, T., Julita, A., Kinnunen, P. K. (1999) Binding of adriamycin to liposomes as a probe for membrane lateral organization. *Biophys J.* **76**, 896-907
- 22 Raghuraman, H., Shrivastava, S., Chattopadhyay, A. (2007) Monitoring the looping up of acyl chain labeled NBD lipids in membranes as a function of membrane phase state. *Biochim. Biophys. Acta.* **1768**, 1258-1267
- 23 Lewis, B. A. and Engelman, D. M. (1983) Lipid bilayer thickness varies linearly with acyl chain length in fluid phosphatidylcholine vesicles. *J Mol Biol* **166**, 211-217
- 24 Ipsen, J. H., Joergensen, K., Mouritsen, O. G. (1990) Density fluctuations in saturated phospholipid bilayers increase as acyl-chain length decreases. *Biophys J.* **58**, 1099-1107
- 25 Newman, G. C. and Huang, C. (1975) Structural studies on phosphatidylcholine-cholesterol mixed vesicles. *Biochemistry* **14**, 3363-3370
- 26 Ladbrooke, B. D. and Chapman, D. (1969) Thermal analysis of lipids, proteins and biological membranes. A review and summary of some recent studies. *Chem Phys Lipids* **3**, 304-356
- 27 Perochon, E., Lopez, A. and Tocanne, J. F. (1992) Polarity of lipid bilayers. A fluorescence investigation. *Biochemistry* **31**, 7672-7682
- 28 Alakoskela, J.-M. I., Kinnunen, P. K. J. (2001) Control of a redox reaction on lipid bilayer surfaces by membrane dipole potential. *Biophys J* **80**, 294-304

- 29 Rawat, S. S., Chattopadhyay, A. (1999) Structural transition in the micellar assembly. A fluorescence study. *Journal of Fluorescence* **9**, 233-244
- 30 Chattopadhyay, A., Mukherjee, S. (1993) Fluorophore environments in membrane-bound probes: A red edge excitation shift study. *Biochemistry* **32**, 3804-3811
- 31 Yeagle, P. H. (1978) Phospholipid headgroup behavior in biological assemblies. *Acc Chem Res* **11**, 321-326
- 32 Koynova, R., Caffrey, M. (1998) Phases and phase transitions of the phosphatidylcholines. *Biochim Biophys Acta* **1376**, 91-145
- 33 Klymchenko, A. S., Mely, Y., Demchenko, A. P., Duportail, G. (2004) Simultaneous probing of hydration and polarity of lipid bilayers with 3-hydroxyflavone fluorescent dyes. *Biochim Biophys Acta* **1665**, 6-19
- 34 Mukherjee, S., Raghuraman, H., Dasgupta, S., Chattopadhyay, A. (2004) Organization and dynamics of N-(7-nitrobenz-2-oxa-1,3-diazol-4-yl)-labeled lipids: a fluorescence approach. *Chem Phys Lipids* **127**, 91-101



## CHAPTER 5

### TIME-RESOLVED MEASUREMENTS IN SINGLE LIPOSOME

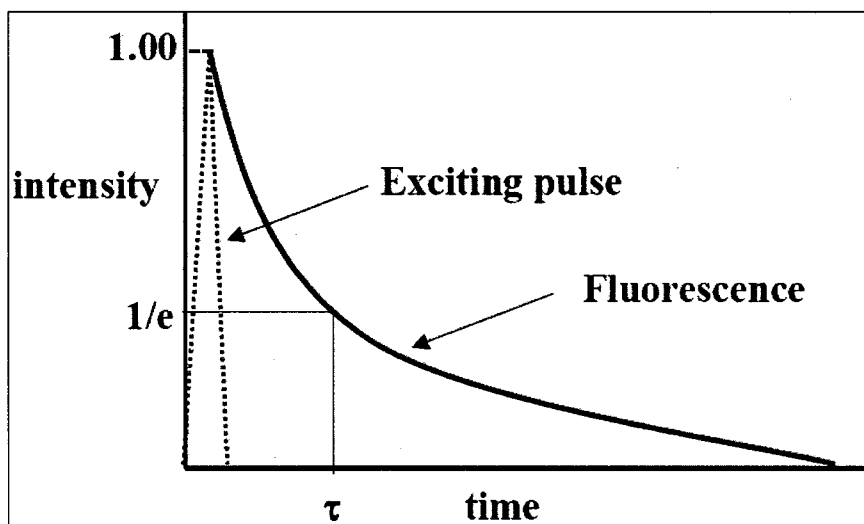
#### 5.1 Introduction

Time-resolved measurements have become very useful in understanding biochemistry and biophysics. This is because of the recent developments that have occurred in the instrumentation and the development of fluorescent probes. Numerous studies have evolved recently geared towards discerning the structure and motions of biological molecules. Fluorescence lifetime and anisotropy have proved useful in discerning dynamics of lipid membranes.

Fluorescence anisotropy was originally designed to study microviscosity of micelles and membranes [1]. The anisotropy measurement is attributed to the rate of rotational diffusion of the biological molecules. The rate of rotational diffusion of biological molecules is comparable to their decay times. Therefore, it is possible to study many of the activities of these molecules [2]. Fluorescence anisotropy measurements have been useful in discerning the location of probe in a lipid bilayer [2-5]. The anisotropy measurements have been used widely in quantifying protein properties such as denaturation, association and dynamics [6-8].

It is well established that fluorescence lifetime is sensitive to the pH, ion concentration, temperature and many other conditions in the microenvironment of a fluorophore in a biological system. Time-resolved lifetime is the average amount of

time that a fluorophore spends in the excited state, after absorption of a photon, before returning to the ground state [2]. It is defined as the time it takes for a number of excited population of a fluorophore to decay to  $1/e$  (36.8 %) of the original population (see Equation 1.1 Section 1.7). The fluorescence intensity decay exponentially as displayed by Figure 5.1.



**Figure 5.1** Fluorescence intensity decay signal after the excitation with a pulsed light. Lifetime  $\tau$  is obtained by the fraction that decays to  $1/e$  of the original population as indicated in the diagram [9].

The fluorescence lifetime has become very useful in revealing the information on quenching processes, rates of energy transfer, and time-resolved anisotropy.

Furthermore, multiple decay constants are useful in discerning the heterogeneity existing in the environments of a fluorophore. In time-resolved fluorescence, the individual photons can be detected with spatial resolution in the microscopy and time resolution [10]. It is a powerful tool for studying excited transient species in the time domain mode. These species are produced via electronic excitation of molecules created by the short pulses from either the UV or the VIS radiation. Time resolution in nanosecond is very useful in the characterization of processes such as the photochemical reactions, triplet electronic states, radical species diffusion-controlled bimolecular processes and energy transfer among others. In time resolved measurements, one can deduce temporal dynamics and kinetics of photophysical processes.

Time-resolved fluorescence can be detected by a number of detection methods that includes time-correlated single-photon counting (TCSPC) [2]. In TCSPC, a high probability exists in detecting one photon at time  $t$  after an excitation with a pulse source at time zero. This probability can yield fluorescence intensity at a particular time.

The intensity of fluorescence emission from a fluorophore can be measured as a function of the emission or excitation polarization. This can result in very useful information about the rotational freedom or rates of rotation of the fluorophores or molecules to which they are attached [2]. In order to obtain the information, measurements are usually made by exciting the fluorophore with a linearly polarized light and then monitoring the emission at orthogonal polarizations. For a fluorophore

excited with a linearly polarized light the emission is also polarized. Only molecules oriented in the direction parallel to the electric dipoles of the exciting light will be excited, as shown in Figure 5.2. If there is no rotational motion of the fluorophore in its excited state, the fluorescence emission will have same polarization as the exciting light. However, when angular movement occurs, due to thermal energy in solution, fluorescence emission assumes a new polarization. Steady-state anisotropy therefore, is a measure of the degree of depolarization of the emission with respect to the excitation as predicted in Equation 1.2 in Section 1.7.



**Figure 5.2** Photo-selection of the fluorophores oriented parallel to the electric vector of the exciting light [9]. The dark circles are not parallel to the exciting light and not excited whereas the fluorescent circles are parallel and are excited by light.

A number of sources of depolarization events can occur especially in anisotropy conducted under the steady-state mode as discussed in Section 4.5. In steady-state anisotropy, it is not easy to resolve between the global molecular dynamics and local rotational freedom of a fluorophore when attached to a larger molecule such as a protein [2]. In that case, time-resolved anisotropy can be useful in resolving some of this hidden information since the depolarization can occur at different time scales. Time-resolved anisotropy is calculated based on the parallel and perpendicular polarized emissions as shown in Equation 5.1. The time-resolved anisotropy is normally acquired by adding the polarization sensitivity to the time-resolved fluorescence measurements.

$$r = \frac{I_{\parallel}(t) - I_{\perp}(t)}{I_{\parallel}(t) + 2I_{\perp}(t)} \quad [5.1]$$

In this case  $r$  is a measure of a time-dependent steady-state anisotropy calculated by polarized fluorescence signal oriented in the in the parallel position,  $I_{\parallel}(t)$  and perpendicular,  $I_{\perp}(t)$  to the linear polarized laser excitation.

In this chapter, time-resolved measurements and anisotropy of the NBD moiety in the DMPC lipid bilayer are presented. We characterized the bilayer region of liposomes made from the egg PC phospholipids. The DMPC phospholipids have a

defined phase transition region. The egg PC phospholipids do not show a gel-fluid phase transition at ambient temperatures.

The DMPC lipid bilayer was systematically investigated as a function of temperature using the TCSPC technique. The fluorescence lifetime of the NBD moiety in the DMPC vesicle were analyzed with both NBD PE and NBD PC fluorescent probes. The results obtained were used to examine behavioral differences that possibly exist in the DMPC lipid bilayer. Single photon counting method was used in isolated vesicle system. The optical pulses generated by a laser were focused under high numerical aperture conditions on a single vesicle under a microscope. The lipid bilayer of the DMPC was also investigated in the bulk solution using an Edinburgh Fluorimeter. The results from the microscope and Edinburgh instruments were compared. We measured fluorescence lifetime in a variety of solvents to vary the dielectric constant. The results were obtained and discussed in each section as detailed below.

## **5.2 Fluorescence Lifetime of NBD Moiety**

### **5.2.1 Microscope Slide**

The fluorescence intensity of NBD is known to depend on the polarity of media in which the probe is located. The intensity decreases in a reduced polarity of environment [11]. The lifetime and intensity of NBD increases significantly from aqueous solvent of high dielectric constant to the hydrophobic core of the bilayer. The lifetime of NBD PE were measured in solvents of varying dielectric constants. This

was investigated by a time-correlated single-photon counting technique as described in the experimental section. In short, 26  $\mu\text{L}$  of 1 mg/ml NBD PE was dispersed in 1 mL of chloroform, methanol or a dioxane-water mixture. 50  $\mu\text{L}$  of each were transferred onto a depression microscope slide. A pulse laser was initiated with an excitation at 470 nm at a 20 MHz repetition rate. The emission was monitored at 540 nm. Time-domain fluorescence lifetime measurements were carried as described in section 2.2.3. Fluorescence decay can be reported by a sum of exponentials as indicated by equation 5.2.

$$I(t) = \sum_i \alpha_i e^{-t/\tau_i} \quad [5.2]$$

In this equation  $\tau_i$  and  $\alpha_i$  are the time constants and the corresponding amplitude respectively. The fluorescence intensity at a time  $t$  is given by  $I(t)$ . The bi-exponential decays in our case were calculated from the decay times and pre-exponential factors. This resulted in  $\tau_1$  and  $\tau_2$  for the long and short lifetime components respectively. The corresponding amplitudes were noted as  $\alpha_1$  and  $\alpha_2$  for  $\tau_1$  and  $\tau_2$  respectively. The goodness of the fit was evaluated from the residual and the reduced  $\chi^2$  ratio. This is a ratio of the minimum error-weighted sum of the squared deviations between measured and predicted values. A good fit is one that has  $\chi^2$  close to one. The fluorescence intensity decays fitted well to a bi-exponential with the least

chi-square below 1.3. All measurements were taken at 298 K except in temperature dependence cases.

Dioxane-water mixture is a useful solvent that allows a continuously changing dielectric constant value. Dioxane is completely miscible with the highly polar compounds such as water. It has a low dielectric constant [12]. The dielectric constant of the dioxane-water system at different temperatures between 20 and 35°C has been reported [13]. The dielectric constants reported at 298 K are shown in Table 5.1. The fluorescence lifetime measurements of the NBD PE in dioxane and water mixture showed an inverse relationship with the dielectric constant. This was expected. The lifetimes of NBD PE was found to be 9.7 ns at 100% dioxane and 3.1 ns for a 10% dioxane. The 100% dioxane had a dielectric constant of 2.21 while the 10% had 70.33 as displayed in Table 5.1 [13]. Methanol solvent with a dielectric constant of 33 resulted in a longer lifetime reported of 6.5 ns. The time-resolved and steady-state lifetime measurements of the NBD had earlier been shown to exhibit strong solvatochromic properties [14-16]. The results in Table 5.1 are rationalized on the basis of an environment polarity.



**Table 5.1** Fluorescence lifetime of NBD PE in solvents of varying polarity.

Solvent	Dielectric constant (298 K)	$\tau_1$	$\alpha_1$	$\tau_2$	$\alpha_2$	$\chi^2$
chloroform	4.8 (293K)[17]	1.76	11	0.36	89	1.3
methanol	33.0	6.51	65	0.81	35	0.9
100% dioxane	2.2	9.75	74	1.59	26	1.0
80% dioxane	11.9	6.31	0.1	0.00	100	1.3
50% dioxane	35.8	3.53	18	0.42	82	1.0
20% dioxane	61.9	2.13	42	0.28	58	0.93
10% dioxane	70.3	3.13	45	0.67	55	0.97

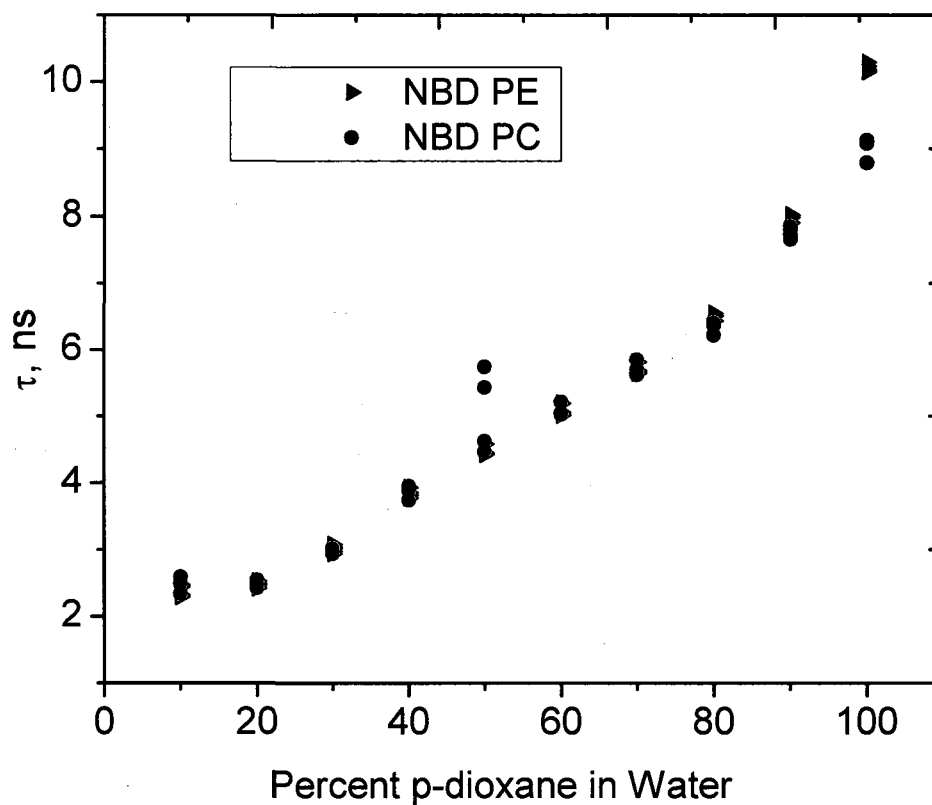
In this table,  $\tau_1$  and  $\tau_2$  are the fluorescence lifetimes for long and short lifetime components of biexponential fit.  $\alpha_1$  and  $\alpha_2$  are the corresponding contributions for the long and short lifetimes respectively.  $\chi^2$  is the reduced chi-square.

### 5.2.2 Edinburgh Fluorimeter

The fluorescence lifetime of the NBD PE and NBD PC was measured in a bulk solution in a quartz cuvette in the Edinburgh instrument. A 1 mL dioxane and variable percent mixtures in water in a quartz cuvette containing 26  $\mu\text{L}$  of 1 mg/ml NBD PE were used. The NBD PE probe in the solvent was excited at 470 nm and the emission studied at 540 nm. Fluorescence decays were fitted to a bi-exponential. A full description of Edinburgh instrument experimental set up is found in Chapter 2,

Section 2.3.6. The fluorescence lifetimes values obtained in solution bulk were compared to the microscope measurements shown in Table 5.2 and displayed by Figure 5.3.

It appeared from the table and the figure that the fluorescence lifetimes obtained by exciting NBD PE in solution in a cuvette and on a microscope slide were relatively similar. Dioxane and water mixtures provided a range of varying dielectric constants that could be compared to the region of a lipid bilayer. In lipid bilayers, the permittivity (or dielectric constant ) was shown by neutron and x-ray studies to vary from 78.5 in water to 2 in the hydrocarbon core of the lipid [18].



**Figure 5.3** Fluorescence lifetimes of the NBD PE and NBD PC dissolved in a mixture of dioxane and water (% w/w). The measurements were obtained using Edinburgh fluorimeter.

**Table 5.2** Long component lifetime for NBD PE in dioxane.

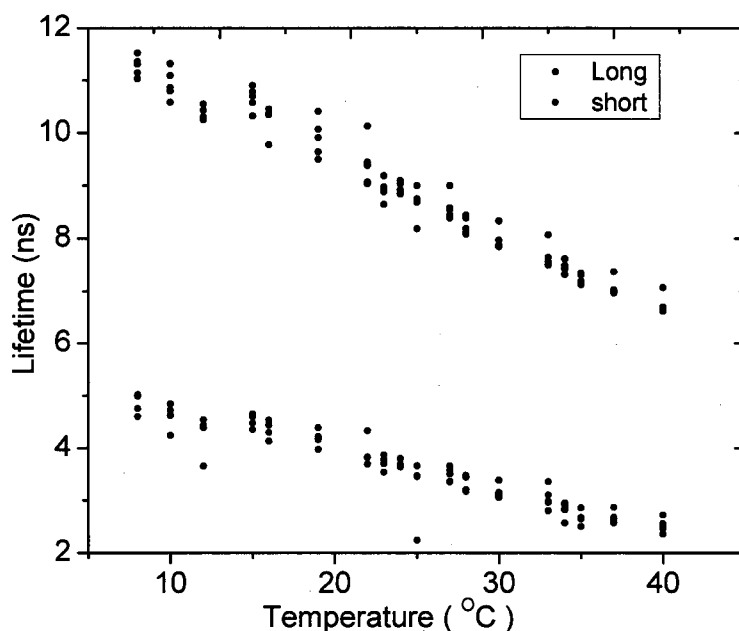
Percent dioxane in water	Long component Lifetime (ns)	
	Microscope slide	Edinburgh instrument
10	3.1	2.4
20	2.1	2.5
50	3.5	4.5
80	6.3	6.5
100	9.7	10.2

### **5.3 Time-Resolved Measurements on a Single Liposome**

#### **5.3.1 Egg PC**

The fluorescence lifetime of NBD PE and NBD PC were measured in an isolated single liposome made from egg PC and in DMPC phospholipids. The measurements were conducted by focusing a laser on the liposome as shown using Figure 2.6 in Chapter 2. The egg PC lipids do not exhibit phase transition at room temperature while the DMPC has phase transition at 23°C. Single liposome measurements were conducted following the method detailed in Section 2.3.5. The fluorescence lifetimes measured as a function of temperature for the NBD PE in egg PC is displayed in Figure 5.4. A number of measurements were taken at different times and plotted as a function of temperature as shown in Figure 5.4. The figure shows a continuous decrease in the lifetime of the NBD PE with increasing temperature. The mean lifetime for the long component decrease was from 11.5 to 6.7 ns when the temperature was increased from 8 to 40°C. This resulted in a 41%

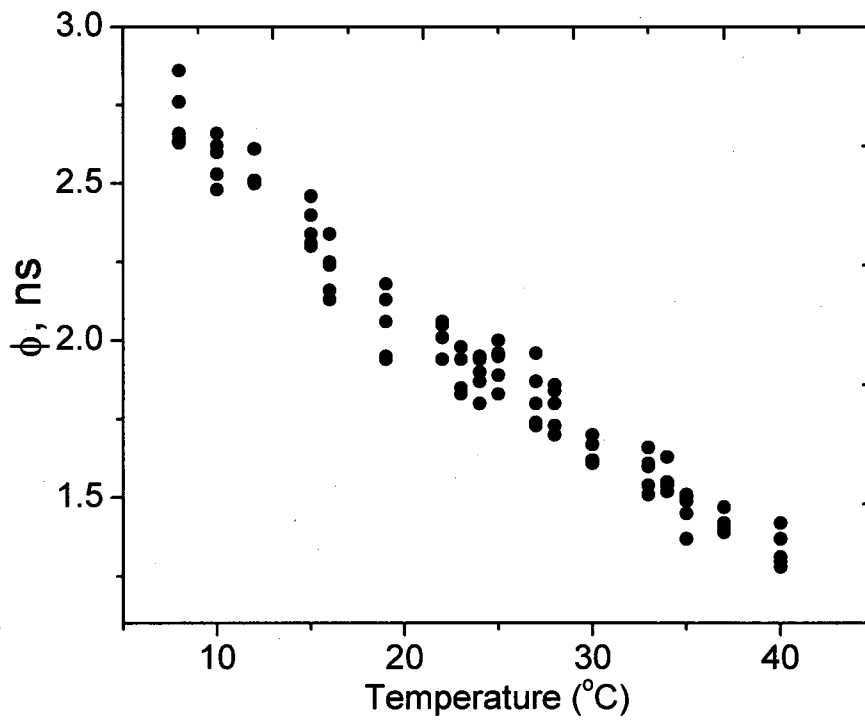
decrease in mean lifetimes. The short component lifetime of NBD PE decreased from 5.0 to 2.6 ns in the same temperature range as the long lifetime. This was approximately 54% decrease in lifetime.



**Figure 5.4** Fluorescence lifetime of NBD PE in egg PC liposome. This was measured as a function of temperature.

Time-resolved anisotropy of NBD PE in egg PC liposome was also reported as a function of temperature from 8 to 40°C. A detailed measurement is found in Section 2.3.5. A considerable decrease in the rotational times was observed from 2.8 to 1.4 when the temperature was increased from 8 to 40°C as shown in Figure 5.5.

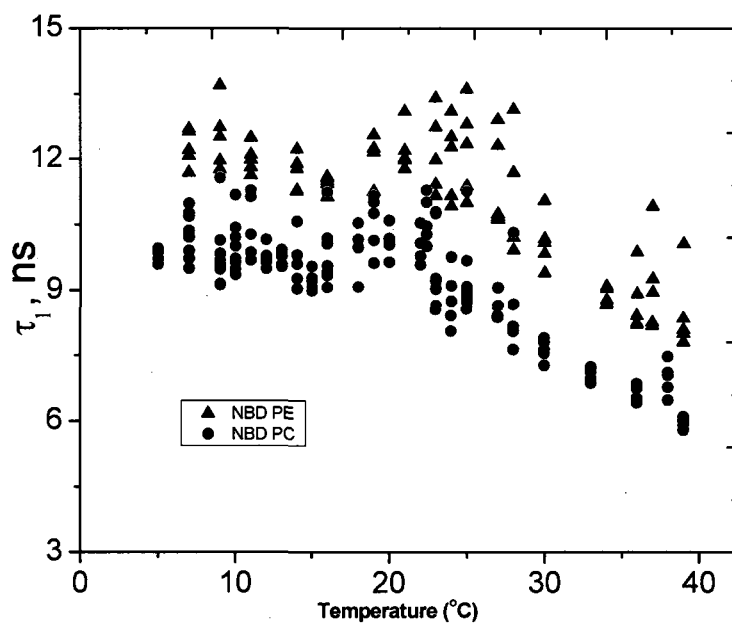
This was a 50% decrease in rotational times. This suggests that the entity rotates faster as the temperature increases.



**Figure 5.5** Time-resolved anisotropy of NBD PE in egg PC liposomes.

### 5.3.2 DMPC (14:0)

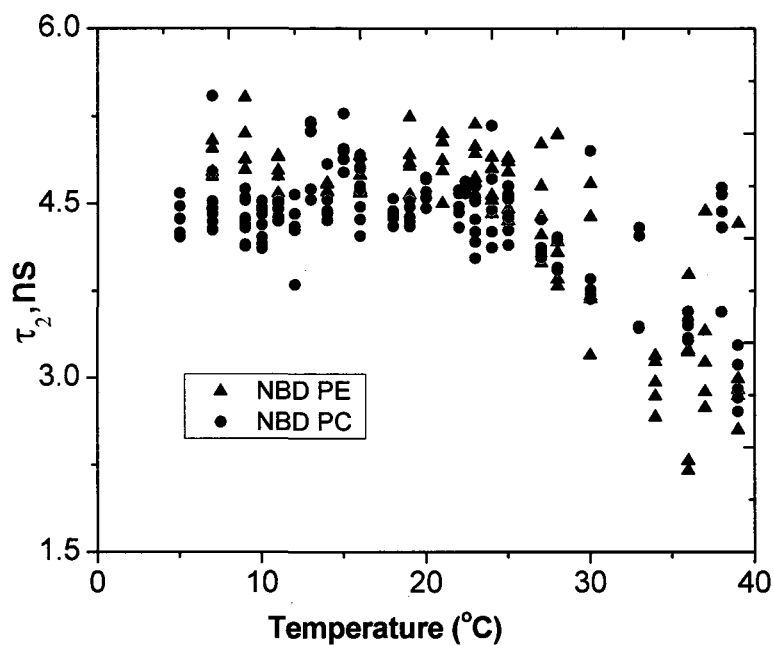
The fluorescence lifetime of NBD PE and NBD PC in a single isolated DMPC liposome was reported as a function of temperature from 7 to 39°C. The lifetimes for both cases were described by a two component function: the short and the long lifetime components. The lifetimes of the NBD PE and NBD PC were well separated due to the expected different locations in the DMPC bilayer region. It was observed that the fluorescence lifetime decreased with the temperature increase. The mean long lifetimes for the NBD PE decrease from  $12.2 \pm 0.4$  to  $8.4 \pm 0.9$  ns when the temperature was varied between 7 and 39°C as shown in Figure 5.6. In the same figure, the fluorescence lifetime for the long component in NBD PC decreased from  $10.3 \pm 0.5$  to  $5.9 \pm 0.1$  at the same temperature range as the NBD PE. The percent decrease in the NBD PE and NBD PC was approximately 31% and 42% respectively.



**Figure 5.6** Long component lifetime of NBD group in DMPC liposomes.

The mean fluorescence lifetime for the NBD PE for the short component varied between  $4.8 \pm 0.2$  to  $3.1 \pm 0.7$  ns when the temperature was increased from 7 to 39°C as displayed in Figure 5.7. Similarly, in the same figure, fluorescence lifetime for the short component in the NBD PC at the same temperature range decreased from  $4.5 \pm 0.3$  to  $3.0 \pm 0.2$  ns. This was a 35% decrease for both cases.



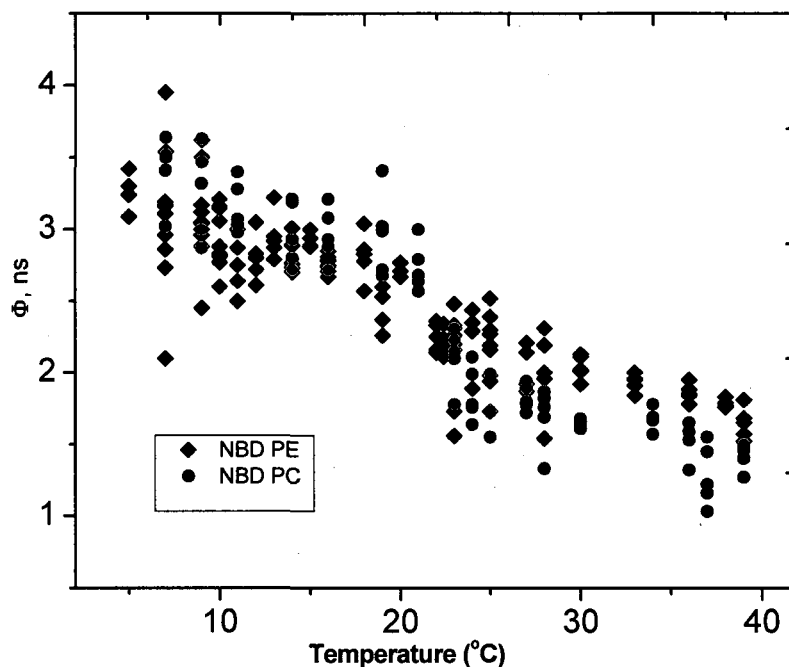


**Figure 5.7** Short component lifetime of NBD group in DMPC liposomes.

The long lifetime component for NBD PE and NBD PC in DMPC was strongly dependent on the temperature in the region of the lipid thermal phase transition ( $\sim 23^{\circ}\text{C}$ ). The short lifetime component was insensitive to either NBD PE or NBD PC in the bilayer region of DMPC.

Time-resolved anisotropy measurements were conducted as a function of the temperature from the gel to fluid across the phase transition of DMPC bilayer as shown in Figure 5.8. The results of the measurements showed that the value for the NBD PE in DMPC decreased from  $3.1 \pm 0.5$  to  $1.7 \pm 0.1$  ns for a temperature increased from 7 to  $39^{\circ}\text{C}$ . NBD PC showed a decrease from  $3.4 \pm 0.2$  to 1.4 ns when

the temperature was increased from 7 to 39 °C. The percent decrease for NBD PE and NBD PC was 46 and 58% respectively.



**Figure 5.8** Time-resolved anisotropy of NBD group in DMPC as a function of temperature.

The time-resolved fluorescence lifetime and anisotropy measurements were acquired simultaneously with the polarizer (perpendicular and parallel position) in place to obtain the anisotropy component. To investigate the influence of the polarizer on lifetime measured on a single liposome study, we proceeded with direct measurements of lifetimes with the polarizer out of the path of the laser signal.

Analysis for time-resolved anisotropy showed that NBD PE is more sensitive to the phase region of the DMPC liposome as shown in Figure 5.9. The results displayed in Figure 5.9 were obtained by fixing lifetimes in the fitting equation in the FluoroFit<sup>®</sup> (PicoQuant) software so that the software operated within a given boundary of the lifetime. The results showed that the NBD PE displayed a sudden and sharp decrease in time-resolved anisotropy around the phase region of the DMPC. But the NBD PC remained fairly linear in the same temperature range. The decrease for the NBD PE was from  $4.7 \pm 0.4$  to  $1.4 \pm 0.2$  ns when the temperature was dropped from 7 to 36°C. In the same temperature range, the NBD PC decreased from  $4.1 \pm 0.2$  to  $1.9 \pm 0.1$  ns. The percent decrease was higher in NBD PE (68%) than in NBD PC (55%).

The relationship between the steady-state anisotropy and the rotational correlation time is found in the Perrin equation [2]. The relationship between the rotational correlation time and the microviscosity,  $\eta_m$ , can be derived from the Debye-Stokes-Einstein equation 5.3 [19].

$$\eta_m = \frac{kT\tau_R}{v_h} \quad [5.3]$$

Where  $v_h$  is the hydrodynamic radius of the probe molecule and  $\tau_R$  is the rotational correlation of the fluorophore. From Perrin's equation shown by equation 5.4, it seems that when rotational correlation time,  $\theta$  is much larger than the lifetime,

then the measured anisotropy  $r$  is equal to the fundamental anisotropy  $r_o$ . If the correlation time is much shorter than the lifetime, then the anisotropy is zero.

$$r = \frac{r_o}{1 + \tau/\theta} \quad [5.4]$$

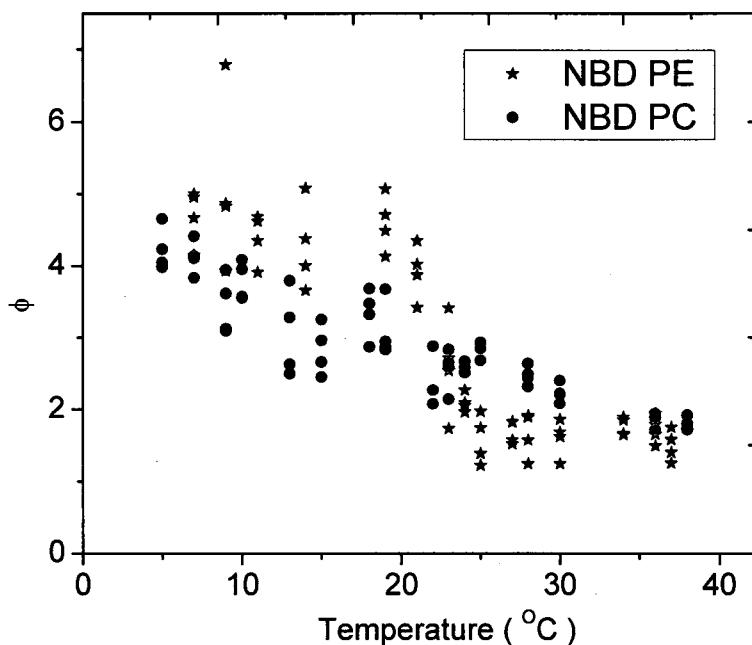
Where  $r$  is the measured steady-state anisotropy,  $\tau$  is the fluorescence lifetime,  $\theta$  is the rotational correlation time and  $r_o$  is the fundamental anisotropy measured in a highly viscous solvent. The fundamental anisotropy  $r_o$  is defined as the anisotropy in the absence of depolarization as shown by Equation 5.4.1 [2].

$$r_o = \frac{2}{5} \left( \frac{3 \cos^2 \beta - 1}{2} \right) \quad [5.4.1]$$

In this equation,  $\beta$  is the angle between absorption and emission transitions. The fundamental anisotropy  $r_o$  occurs between 0.4 and -0.20. The  $r_o$  value becomes zero when  $\beta$  is  $54.7^\circ$ , -0.20 when  $\beta$  is  $90^\circ$ , and 0.39 when  $\beta$  is  $7.4^\circ$ .

The time-resolved anisotropy, therefore, is a measure of the microviscosity of the environment of the NBD fluorophore in the lipid bilayer. It appears that the NBD in NBD PE experiences a stronger orientational constrain in the gel than fluid phase

of the DMPC lipid bilayer. This is demonstrated by the greater rotational correlation time of 4.7 ns compared to that for NBD PC (4.1 ns).

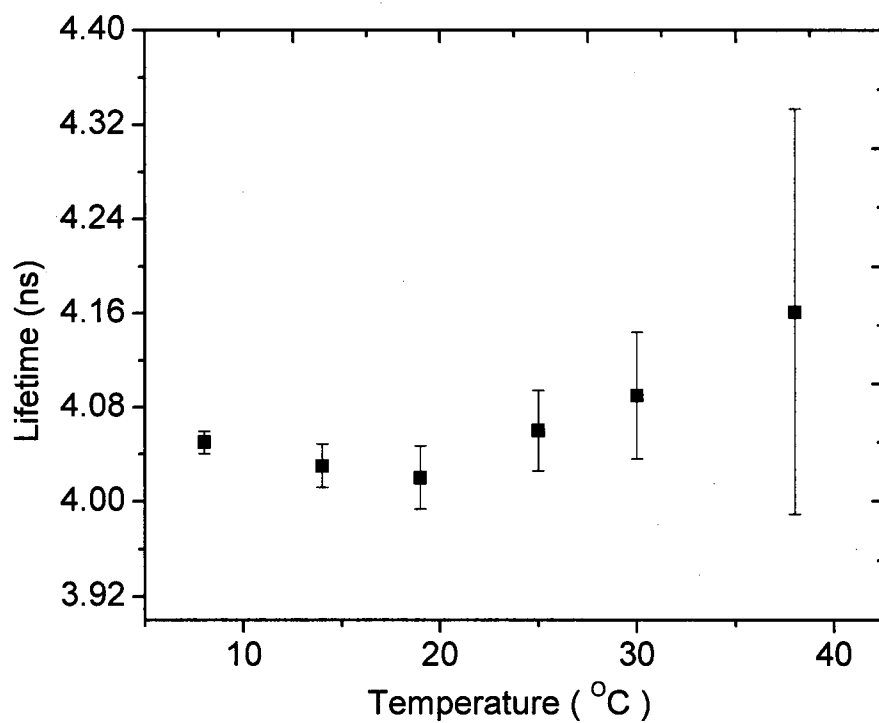


**Figure 5.9** Time-resolved anisotropy of the NBD group in the DMPC (14:0) with a fixed lifetime measured as a function of temperature.

### 5.3.3 Carboxyfluorescein

The lifetime of the 5-carboxyfluorescein (single isomer) standard was measured in a depression slide microscope similar to the procedure for the solvents as described in Section 5.2. The results showed a fairly constant lifetime with a mean value of  $4.1 \pm 0.05$  ns as displayed in Figure 5.10. Carboxyfluorescein was used as a

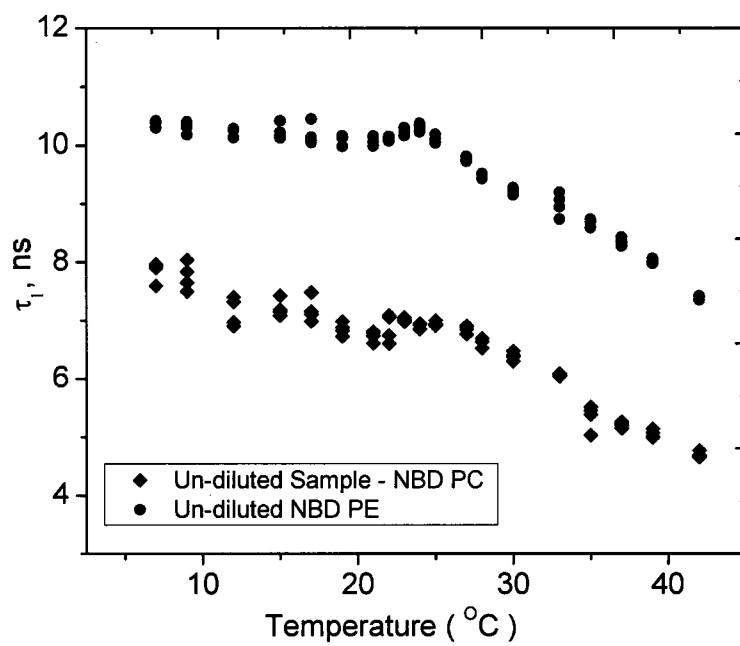
standard to ascertain that the results obtained with the slide in a microscope were not due to any instrument malfunction.



**Figure 5.10** Lifetime of 5-Carboxyfluorescein as a function of temperature.

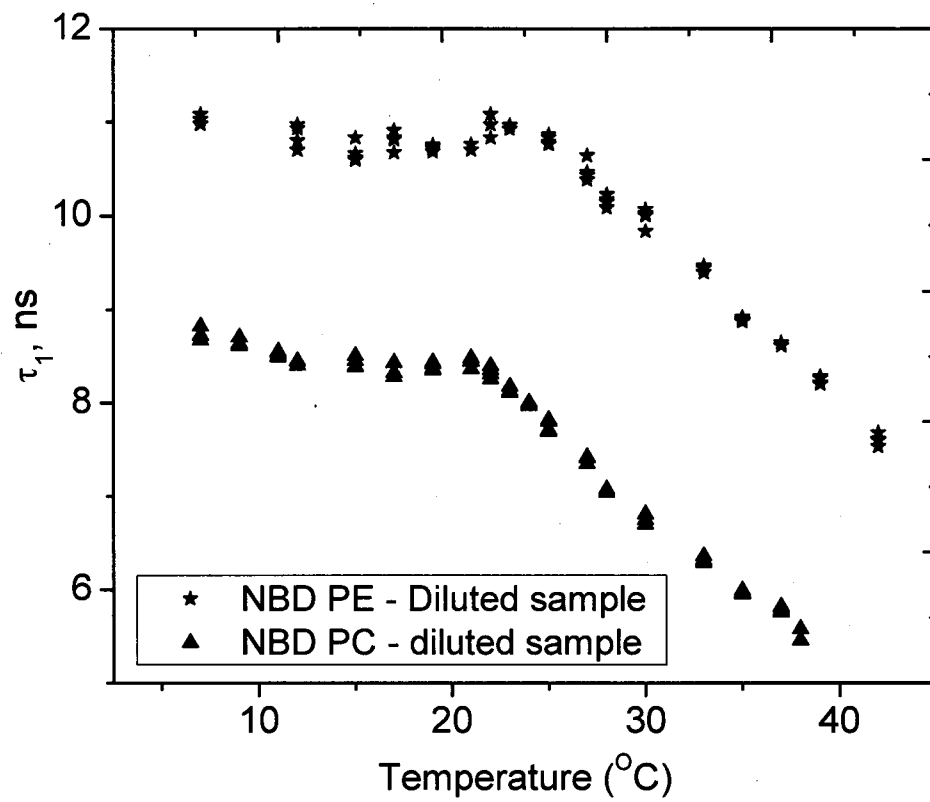
#### **5.4 Bulk Solution Measurements in Edinburgh Fluorimeter**

Lifetime measurements of NBD group in DMPC liposomes were carried out in a single-photon counting spectrophotometer (FLS900, Edinburgh instruments) as described in Section 2.3.6. The lifetime was determined at a 4 mg/mL total lipid concentration. 1 mL liposome suspension was used in a 1 cm quartz cuvette and the measurement was carried out as detailed earlier. The results are shown in Figure 5.11. A diluted liposome suspension was also examined. In this sample, 150  $\mu\text{L}$  of a 4 mg/mL was transferred to 850  $\mu\text{L}$  of 11 magnesium chloride solutions in a 1 cm quartz cuvette. The lifetime measurement fitted well to a biexponential with a reduced chi-square below 1.5 (Figure 5.12). The long component lifetime was displayed as a function of temperature in Figures 5.11 and 5.12.



**Figure 5.11** Edinburgh lifetime measurements of concentrated sample of DMPC (14:0).





**Figure 5.12** Edinburgh lifetime measurements of diluted DMPC (14:0) sample.

The Edinburgh method measurements were conducted in a bulk solution as opposed to a single vesicle measurement in a microscope slide as described in section 5.3. In Figure 5.1 and 5.1 the NBD PE and NBD PC lifetime were inversely correlated to the temperature. This was similar to the single vesicle measurement described in section 5.3. In the concentrated sample shown in Figure 5.11, the NBD PE lifetime decreased from  $10.4 \pm 0.1$  to  $7.4 \pm 0.1$  ns when the temperature was increased from 7 to 42°C. In the same figure, the NBD PC lifetime decreased from  $7.8 \pm 0.17$  to  $4.7 \pm 0.1$  ns in the same temperature range. The percent decrease was 29% for the NBD PE and 40% for NBD PC.

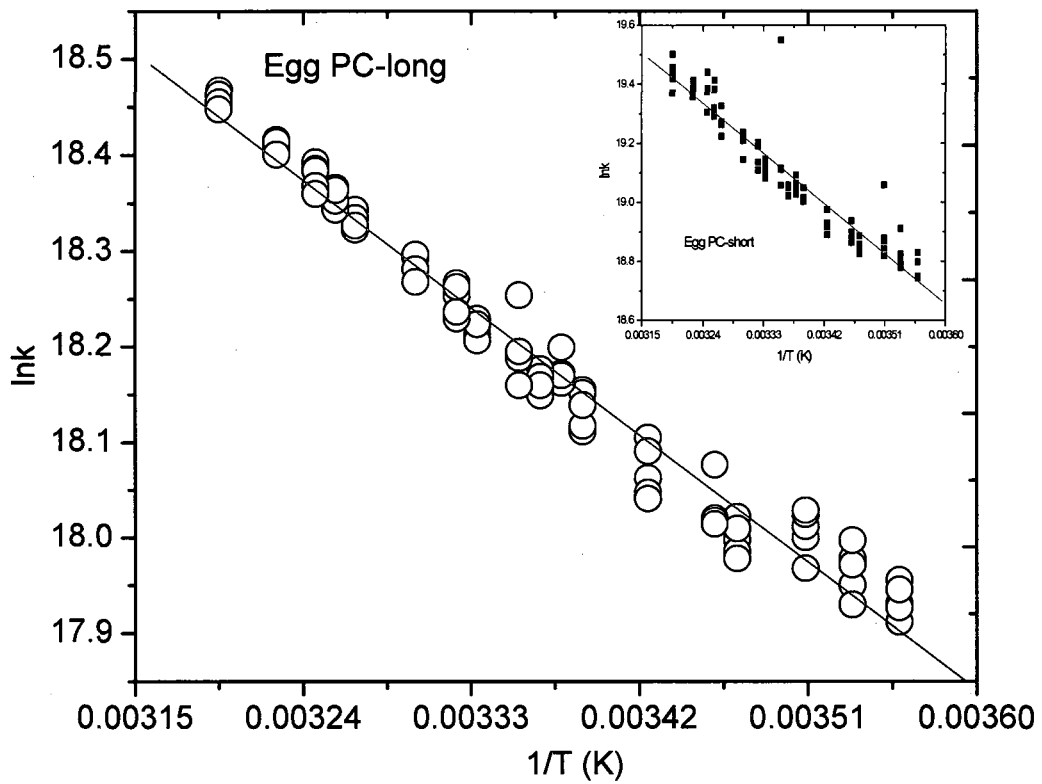
Similar analysis was carried out for the diluted samples displayed in Figure 5.12. The fluorescence lifetime for NBD PE decreased from  $11.1 \pm 0.1$  to  $8.6 \pm 0.1$  ns when the temperature was reduced from 7 to 37°C. In the same temperature range the fluorescence lifetime of NBD PC decreased from  $8.7 \pm 0.1$  to  $5.8 \pm 0.1$  ns. The percentage decrease was 22% for NBD PE and 34% for NBD PC in the DMPC bilayer. The percent change in the NBD PE was smaller than NBD PC. This was similar to the trend observed in the measurements of a single vesicle under microscope slide. The lifetimes in a concentrated liposome suspension in a bulk solution were relatively lower than the single vesicle measurements. The lifetime values for the diluted bulk liposome suspension were relatively higher than the undiluted component.

## 5.5 Activation Energy

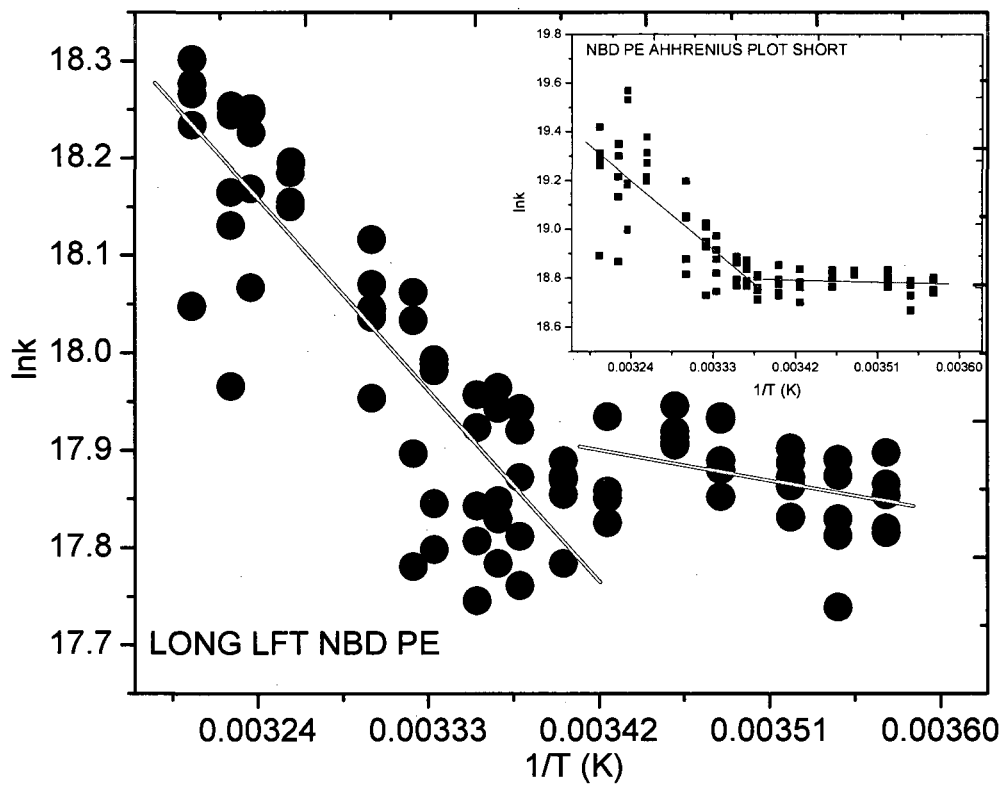
In order to distinguish between NBD PE and NBD PC in a more comprehensive characterization, the temperature dependent lifetimes obtained by single-photon counting techniques were analyzed using Arrhenius kinetic model. The lifetimes  $\tau$ , were converted to rate constant  $k$ , using the equation 5.5.

$$k = \frac{0.693}{\tau} \quad [5.5]$$

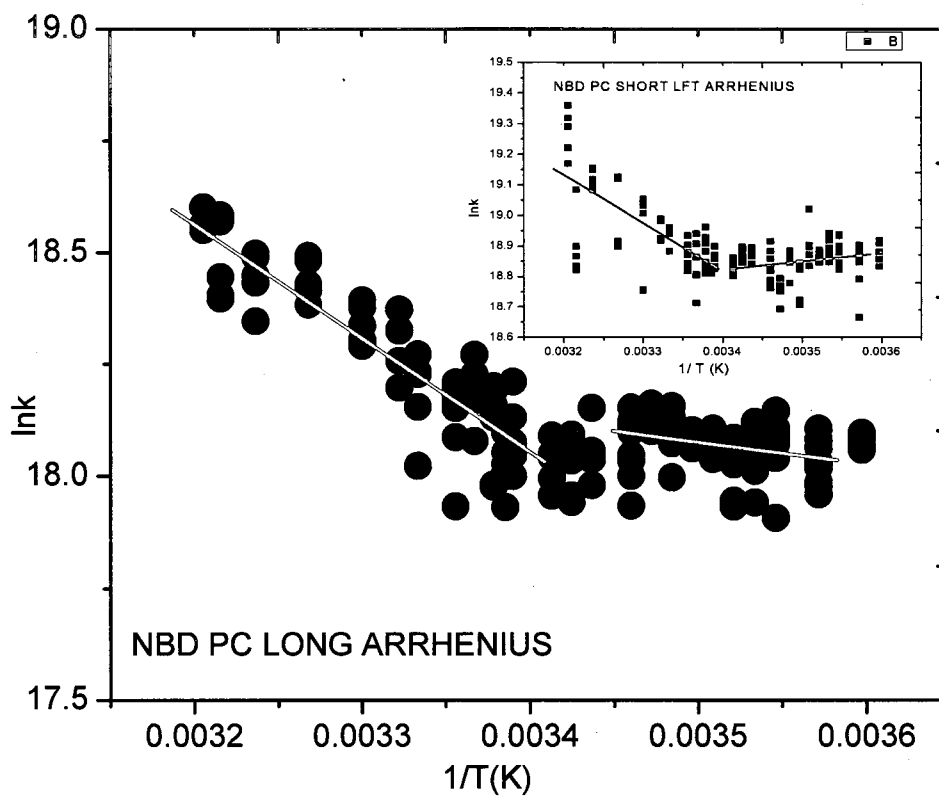
A plot of the natural logarithm of the rate constants as a function of temperature is displayed in Figures between 5.13 and 5.15. The slope was constantly linear for egg PC in Figure 5.13. In Arrhenius equation, the slope of a linear regression plot results in activation energy barrier. The intercept gives the pre-exponential factor.



**Figure 5.13** Arrhenius plot for the long component lifetime of the NBD PE in egg PC (see short lifetime insert).



**Figure 5.14** Arrhenius plot of long and short lifetime components for the NBD PE in DMPC (14:0) (see insert for short component).



**Figure 5.15** Arrhenius plot of long and short lifetime components for the NBD PC in DMPC (14:0) (see insert for short component).

The Arrhenius kinetic model was used in the analysis of the temperature dependent lifetime components in egg PC and DMPC liposome. We examined the long and short lifetime components. In the DMPC, both the NBD PE and NBD PC showed a region of discontinuity close to the phase transition of the DMPC lipid bilayer as seen in Figure 5.14 and 5.15. This suggests a change in the activation barrier for deactivation of the excited state of the NBD moiety in the bilayer. The activation barriers were calculated for the egg PC and DMPC in order to gain further insight into the fluorescence decay pathways in the gel and fluid lipid bilayer system. Egg PC phospholipids has a phase transition at  $-15^{\circ}\text{C}$  [20]. Therefore, it exhibits no discernible phase transition through the temperature range as seen in the Arrhenius plot in Figure 5.13. However, the DMPC shows a phase transition from gel to fluid phase via distinct phase transition temperature.

In Table 5.3 the short component lifetimes have activation energy barrier that is relatively lower than the long component lifetimes except in the fluid phase of DMPC-NBD PE ( $E_a$  is 6.21 kcal/mol). The short component lifetime of the fluorescence decay is related to the nonradiative deexcitation pathways as earlier reported [21]. In the gel phase of DMPC, the activation barriers are very low. This suggests that the nonradiative process involved in the deactivation pathway of the excited-state is either energy barrierless, or the gel phase is temperature independent. The energy of activation for the long lifetime for the fluid DMPC liposomes was reported as 4.32 and 5.05 Kcal/mol for the NBD PE and NBD PC respectively. The egg PC liposomes showed a relatively lower energy barrier in the reported the NBD

PE case yielding long component activation barrier of 2.9 Kcal/mol. Egg PC has several components of both saturated and unsaturated phospholipids as opposed to pure DMPC lipid. The combination of the different lipids in egg PC can create a more stable system that can lead to less activation energy barrier as seen in Table 5.3.

**Table 5.3** Arrhenius activation barriers for the long and short lifetime components in DMPC (14:0) and egg PC vesicles.

Lipid	Phase	Long ( $\tau_1$ )		Short ( $\tau_2$ )	
		$E_a$ Kcal/mol	A $s^{-1}$	$E_a$ Kcal/mol	A $s^{-1}$
Egg PC NBD PE		$2.9 \pm 0.1$	$1.14 \times 10^{10}$	$3.8 \pm 0.1$	$1.15 \times 10^{11}$
DMPC NBD PE	FLUID	$4.3 \pm 0.4$	$8.89 \times 10^{10}$	$6.2 \pm 0.8$	$5.51 \times 10^{12}$
DMPC NBD PE	GEL	$0.7 \pm 0.3$	$1.95 \times 10^8$	$0.2 \pm 0.2$	$1.927 \times 10^8$
DMPC NBD PC	FLUID	$5.1 \pm 0.3$	$3.91 \times 10^{11}$	$3.1 \pm 0.4$	$3.22 \times 10^{10}$
	GEL	$1.0 \pm 0.4$	$3.92 \times 10^8$	ND <sup>1</sup>	ND

<sup>1</sup> Not dependent on temperature



## 5.6 Discussion

In the past, studies of the fluorescence lifetime of the NBD PE in membranes have resulted in 7 ns for the long lifetime component. This decreases to about 1.5 ns in water. This was attributed to an increase in membrane polarity and due to hydrogen bonding between the fluorophores and the solvent [22, 23]. This increases the rate of nonradiative decay of fluorescence [16]. The decrease in lifetime in both egg PC and DMPC could be attributed to increase the solvent in the microenvironment of NBD group. This is also supported by data shown in Figure 5.3 and Table 5.2. An increase in the percent water in dioxane was followed by a decrease in lifetimes of the NBD PE. DMPC lipid has a well defined phase transition temperature of 23°C. This phase region was detected by a sharp decrease in the long lifetime component of the NBD PE and NBD PC in the DMPC. We did not observe such a sudden drop in egg PC phospholipids. The decrease in fluorescence lifetime for the long lifetime component in NBD PC (42%) was larger than NBD PE (31%). The difference in the short lifetime components of these fluorophores was found to insignificantly small. The percent decrease in the rotational correlation times for the NBD PC probe (58%) was also larger than for NBD PE (46%). This could be rationalized on the basis of the difference in the location of the NBD group in the bilayer.

The location of NBD moiety of NBD PE in the phospholipid bilayer has been investigated recently by Chattopadhyay [24]. It was shown that the NBD resides closer to the glycerol moiety of the phospholipid skeleton structure. Results obtained from this study showed that the NBD group of the NBD PE was located in a region of

more ordered environment that led to a smaller decrease in the fluorescence lifetimes. In DMPC (14:0) the liposomes undergo changes in the gel to fluid crystalline phase transition at about 23°C. The wobbling of the NBD moiety in the gel phase was restricted but not inhibited completely as shown by the time-resolved anisotropy measurements in the DMPC lipid bilayer. The wobbling cone angle appears to increase sharply at the phase transition. This increase in the angular range is consistent with the expansion of the area of the bilayer at the transition obtained from a comparison between the changes in volume and thickness. The volume of membrane increases by about 3-4% [25, 26] while the thickness decreases by 20-25% [27].

A number of studies has taken advantage of sensitive of the NBD fluorescence to the physical and chemical properties surrounding the NBD probe to study the dynamics of the lipid bilayer [22, 28, 29]. Measurements of the fluorescence decay of the NBD in the DMPC and egg PC bilayers under different conditions temperature reveal a heterogeneous decay as shown in Figures 5.4, 5.6 and 5.7. A double exponential decay for a lipid bilayer containing NBD probe has been reported [23]. The NBD PE has the NBD polar moiety located in the lipid bilayer surface and attached to the amino group of the NBD PE. However, the NBD PC has the NBD located in the tail and is expected to be buried in the hydrophobic tail. The heterogeneity of the fluorescence decays is related to the micro-heterogeneity of the environment surrounding a fluorophore [30-32]. For example, the use of the 1,6

diphenyl-1,3,5-hexatriene (DPH) in the study of the erythrocyte membrane structure showed two lifetimes: the long and the short lifetime components [30].

In this study, the long lifetime component was sensitive to changes in temperature in the liposomal preparations using phospholipids derived from the erythrocyte membranes. On the other hand, the excited-state of the tryptophan amino acid residue in proteins has shown different conformations of proteins [33, 34]. The double exponential fit of the fluorescence lifetime observed in the NBD PE and NBD PC can be associated with the heterogeneity in the membrane surrounding the NBD moiety. Each of the discrete regions where the probe is located in the lipid bilayer is affected by temperature. This is demonstrated by the temperature dependence of the fluorescence lifetimes as seen for both the NBD PE and NBD PC in the DMPC and egg PC. The increase in temperature shifted the average fluorescence lifetime to the lower values.

The temperature dependence of the rate of quenching of NBD fluorescence lifetime was analyzed by Arrhenius model for thermal quenching, yielding the activation energy barrier  $E_a$  and pre-exponential factor  $A$ . The pre-exponential factor is a measure of the collision frequency leading to a reaction. The gel phase of the DMPC had much lower activation barrier than the fluid phase for both the NBD PE and NBD PC probes as seen in Table 5.3. The shorter lifetime component of NBD PC showed lower activation barriers than the long lifetime component. The short lifetime of the NBD PE also reported a relatively lower activation energy barrier in the gel phase of the DMPC. The short component is probably temperature-independent.

The activation energy barriers obtained for the quenching of the NBD is close to the electron transfer quenching mechanism common for the indole group of tryptophan in proteins ( $E_a$  from 5.23 to 7.01 Kcal/mol) [21]. The gel-fluid phase transition in DMPC (14:0) lipid bilayer can lead the NBD to reside in region of varying viscosity of the medium. This is expected to change the height of the energy barriers between gel and fluid phases as indicated in Table 5.3. These may affect the fluorescence decay of the NBD at different viscosities and reflect the changes in the dynamics of the DMPC matrix as displayed in the study using single liposome system.

## **5.7 Conclusion**

In short, there were significant differences in the NBD PE and NBD PC with respect to the lifetime and time-resolved anisotropy determined by single liposome study. Pure synthetic phospholipid and natural egg PC systems were used to as a control to examine the behavior of the two fluorescent probes in the lipid bilayer. The fluorescence lifetime and time-resolved anisotropy decreased with temperature increases. The DMPC (14:0) system showed regions of discontinuity in the value of lifetime and anisotropy. This was attributed to the existence of the phase transition that occurs at approximately 23°C. This was not displayed in the egg PC liposomes. The egg PC liposome does not exhibit phase transition in the temperature range investigated. The fluorescence lifetime of the NBD was found to be inversely related

to the solvent polarity index. This was expected. It provided an explanation for the presence of short and the long lifetimes in lipid bilayer region.

The longer lifetime could be attributed to the NBD existing in a more hydrophobic region of the bilayer. The short lifetime is due to NBD residing in a more hydrophilic region of the lipid bilayer. The NBD of the NBD PC had relatively smaller lifetime in both the short and long component than the NBD PE probe. It could possibly reside in a more hydrophilic region closer to the water-lipid interface of the bilayer. The NBD has a higher affinity for polar environment of a lipid bilayer. It can loop back to the interfacial region of the bilayer. Consequently, the NBD PC perturbs the lipid bilayer. This could result in some degree of water penetration in the hydrocarbon region of the lipid bilayer. The NBD PE resides in a more restricted zone of the lipid bilayer. The water-lipid interface, where it resides, is expected to experience intermolecular interactions such as hydrogen bonding and the Van der Waal's interactions. In view of this, the rotational motions reported here are relatively slower than in the NBD PC probe in the DMPC and egg PC lipid bilayers.

Arrhenius activation energy barrier,  $E_a$  of the long lifetime component in the NBD PE and NBD PC were similar in the gel and fluid phase state of DMPC (14:0). The pre-exponential factor A differed by a factor of 5 and 2 in the fluid and gel phase state of the DMPC (14:0) respectively. The gel phase activation barrier was smaller than the fluid phase state of DMPC. This is perhaps a result of the temperature independent thermal quenching of the NBD in the DMPC. The short lifetime

component of the NBD PE and NBD PC in DMPC bilayer showed an activation energy barrier that was more temperature dependent.

## 5.8 References

- 1 Lakowicz, J. R., Cherek, H. and Maliwal, B. P. (1985) Time-resolved fluorescence anisotropies of diphenylhexatriene and perylene in solvents and lipid bilayers obtained from multifrequency phase-modulation fluorometry. *Biochemistry* **24**, 376-383
- 2 Lakowicz, R. L. (1999) *Principles of Fluorescence Spectroscopy*. Plenum Publishers, New York, N. Y.
- 3 Krishna, M. M. and Periasamy, N. (1999) Location and orientation of DODCI in lipid bilayer membranes: effects of lipid chain length and unsaturation. *Biochim Biophys Acta* **1461**, 58-68
- 4 Mely-Goubert, B., Freedman, M. H. (1980) Lipid fluidity and membrane protein monitoring using 1,6-diphenyl-1,3,5-hexatriene. *Biochim Biophys Acta* **601**, 315-327
- 5 Konopasek, I., Vecer, J., Strzalka, K. and Amler, E. (2004) Short-lived fluorescence component of DPH reports on lipid-water interface of biological membranes. *Chem Phys Lipids* **130**, 135-144
- 6 Michalet, X., Weiss, S. and Jager, M. (2006) Single-molecule fluorescence studies of protein folding and conformational dynamics. *Chem Rev* **106**, 1785-1813
- 7 Ferreira, S. T., Stella, L. and Gratton, E. (1994) Conformational dynamics of bovine Cu, Zn superoxide dismutase revealed by time-resolved fluorescence spectroscopy of the single tyrosine residue. *Biophys J* **66**, 1185-1196
- 8 Beechem, J. M., Sherman, M. A. and Mas, M. T. (1995) Sequential domain unfolding in phosphoglycerate kinase: fluorescence intensity and anisotropy stopped-flow kinetics of several tryptophan mutants. *Biochemistry* **34**, 13943-13948

- 9 Terpetschnig, E., Jameson D. M. (2009) Technical Notes Fluorescence Lifetime. In Principles of Fluorescence Techniques 2009, ISS, IBD NanoBiology Facility, The University of Chicago, Gordon Center for Intergrative Science, Chicago, IL
- 10 Periasamy, N., Koti, R. S. A. (2003) Time Resolved Fluorescence Spectroscopy: TRES and TRANES. Proc Indian Natn Sci Acad **69**, 41-48
- 11 Lin, S., Struve, S. W. (1991) Time-Resolved Fluorescence of Nitrobenzoxadiazole-Aminohexnoic acid: Effect of Intermolecular Hydrogen-Bodning on Non-Radiative Decay. J Photochem Photobiol **54**, 361-365
- 12 Gosta, A., Oliver, A. S. (1936) The Dielectric Constant of Dioxane-Water Mixtures between 0 and 80 °C. J. Am. Chem. Soc. **58**, 1241-1243
- 13 Critchfield, F. E., Gibson, Jr. J. A., Hall, J. L. (1953) Dielectric constant of dioxane-water system from 20 °C and 35 °C. J Am Chem Soc **75**
- 14 Fery-Forgues, S., Fayet, P. J., Lopez, A. (1993) Drastic changes in the fluorescence properties of NBD probes with polarity of the medium: involvement of TICT state? J Photochem Photobiol A Chem **70**, 229-243
- 15 Mukherjee, S., Chattopadhyay, A., Samata, A., Soujanya, T. (1994) Dipole moment changes of NBD group upon excitation studied using solvatochromic and quantum chemical approaches; implications in membrane research. J Phys Chem **98**, 2809-2812
- 16 Mazeris, S., Schram, V., Tocanne, J. F. and Lopez, A. (1996) 7-nitrobenz-2-oxa-1,3-diazole-4-yl-labeled phospholipids in lipid membranes: differences in fluorescence behavior. Biophys J **71**, 327-335
- 17 Norberg, J. and Nilsson, L. (1998) Solvent influence on base stacking. Biophys J **74**, 394-402



- 18 Wiener, M. C., White, H. S. (1992) Structure of a fluid dioleoylphosphatidylcholine bilayer determined by joint refinement of x-ray and neutron diffraction data III. Complete structure. *Biophys J* **61**, 434-447
- 19 Sumita, R., Ashok, M., Joykrishna, D. (2005) Microviscosity of lipid bilayer membranes of N-acylamino acid surfactants determined by fluorescence probe method. *Chemical Phys Lett* **414**, 23-27
- 20 Midhat, H. A., Vincent, T. M. (2007) Atomic Force Microscope Studies of the Fusion of Floating Lipid Bilayers. *Biophys J* **92**, 4369-4378
- 21 Ababou, A. and Bombarda, E. (2001) On the involvement of electron transfer reactions in the fluorescence decay kinetics heterogeneity of proteins. *Protein Sci* **10**, 2102-2113
- 22 Raghuraman, H., Pradhan, K. S., Chattopadhyay, A. (2004) Effect of Urea on the organization and Dynamics of Triton X-100 Micelles: A Fluorescence Approach. *J Phys Chem B* **108**, 2489-2496
- 23 Chattopadhyay, A., Mukherjee, S. (1993) Fluorophore environments in membrane-bound probes: A red edge excitation shift study. *Biochemistry* **32**, 3804-3811
- 24 Chattopadhyay, A., London, E. (1987) Parallax method for direct measurement of membrane penetration depth utilizing fluorescence quenching by spin-labeled phospholipids. *Biochemistry* **26**, 39-45
- 25 Nagle, J. F., Wilkinson, D. A. (1978) Lecithin bilayers. Density measurements and molecular interactions. *Biophys J* **23**, 159-175
- 26 Sheetz, M. P., Chan, S. I. (1972) Effect of sonication on the structure of lecithin bilayers. *Biochemistry* **11**, 4573-4581
- 27 Janiak, M. J., Small, D. M., Shipley, G. G. (1976) Nature of the thermal pretransition of synthetic phospholipids: dimyristoyl- and dipalmitoylecithin. *Biochemistry* **15**, 4575

- 28 Alakoskela, J. M. I., Kinnunen, P. K. J. (2001) Probing phospholipid main phase transition by fluorescence and a surface redox reaction. *J Phys Chem B* **105**, 11294-11301
- 29 Chattopadhyay, A., Mukherjee, S., Raghuraman, H. (2002) Reverse micellar organization and dynamics: A wavelength-selective fluorescence approach. *J Phys Chem B* **106**, 13002-13009
- 30 Fiorini, R. M., Valentino, M., Glaser, M., Gratton, E. and Curatola, G. (1988) Fluorescence lifetime distributions of 1,6-diphenyl-1,3,5-hexatriene reveal the effect of cholesterol on the microheterogeneity of erythrocyte membrane. *Biochim Biophys Acta* **939**, 485-492
- 31 Fiorini, R., Valentino, M., Wang, S., Glaser, M. and Gratton, E. (1987) Fluorescence lifetime distributions of 1,6-diphenyl-1,3,5-hexatriene in phospholipid vesicles. *Biochemistry* **26**, 3864-3870
- 32 Vanounou, S., Pines, D., Pines, E., Parola, A. H. and Fishov, I. (2002) Coexistence of domains with distinct order and polarity in fluid bacterial membranes. *Photochem Photobiol* **76**, 1-11
- 33 Alcalá, J. R., Gratton, E. and Prendergast, F. G. (1987) Interpretation of fluorescence decays in proteins using continuous lifetime distributions. *Biophys J* **51**, 925-936
- 34 Alcalá, J. R., Gratton, E. and Prendergast, F. G. (1987) Fluorescence lifetime distributions in proteins. *Biophys J* **51**, 597-604

## CHAPTER 6

### LINE TENSION FORCE AND PORE FORMATION DYNAMICS

#### 6.1 Introduction

The lipid bilayer of biological membrane controls transport of molecules to and from the cell. This is one of the remarkable physical properties that allow the cell to exchange with its environment. This exchange can occur when the lipid bilayer ruptures with the input of energy. The rupture leads to the formation of transient pores that allow transport across the bilayer to take place. The energy can come from applied electrical shock [1-4] or it can occur through peptide mediated processes [5].

Much experimental and theoretical work has been carried out to study pore opening and closure in lipid membranes. But there is still no clear understanding of the mechanism involved in these two processes in the lipid membrane [6]. Understanding dynamics of pore opening and closing in a biological membrane has recently been desired in drug delivery, gene therapy and immunization with liposomes [7, 8]. It is known that membrane tension regulates many biological processes such as endocytosis, exocytosis, fusion and budding processes [9, 10]. The tension has been investigated by the dynamics of tube extrusion on giant vesicles [11].

To begin with, membrane tension arises from the surface tension. This was first described by de Gennes in 1969 [12] and was further described by Brochard-

Wyart [13]. They described membrane of vesicles and cells having zero surface tension, as a result of minimal free energy with respect to the membrane surface tension and which was further confirmed by Tanford [14]. When a membrane is exposed to some mechanical stress or electrical pulses, pores may form and then widen [15, 16]. Such pores have been generated using unilamellar vesicles under different conditions [17, 18]. The pores generated can be transient or may continue to grow, leading to rupture of the membrane surface [6, 19]. The existence of the transient pores has been previously confirmed by a number of reports [18, 20].

It is important to understand the physical and the chemical basis of a transient pore formation in order to understanding the dynamics in biological systems. This has a wide implication in the formulation the free energy cost involved in forming and maintaining the pore size. It provides knowledge of the mechanisms of mechanical and electrical forces involved in forming a pore in the membrane [21]. Transient pores and line tension force have been investigated in model giant liposomes and natural cells [6, 18, 19]. Line tension force is a one dimensional force. It is force per unit length of the exposed edge that operates opposite to surface tension force which occurs per unit area. It facilitates the closure of transient pores. Line tension has been determined experimentally with values ranging between 5 and 30 pico-Newtons (pN) [21]. The cell membranes have a high line tension and never spontaneously form holes [22].

Recent development in the measurements of line tension has been made difficult by the extremely small value of the force which is in the range of pN. This

value has been obtained from transient pores created by optical illumination in the presence of a fluorescent probe [23, 24]. In this case, the transient pores are created by increasing membrane tension beyond a certain threshold limit by the constant flux of light on the membrane. Studies have shown that the line tension lifetime can be controlled by the rate of the leak-out of the internal fluid in the lumen of the membrane. This is possible with application of viscous fluid like glycerol to allow for the observation by video microscopy [6, 7]. The molecular mechanism of light induced pore formation is not clear but has been reported by several studies [25, 26]. On the other hand, the result of a micropipette method has shown that membrane tension leads to unstable holes formed by a kinetically controlled process [27]. This method has yielded line tension force [28]. Other techniques that have resulted in transient pores include solubilization using detergents as reported by Rodriguez [29], electroporation [1, 30], mechanical forces [31] and pore forming proteins and peptides [32]. The hydrodynamic model for pore opening and closure dynamics has been reported [7].

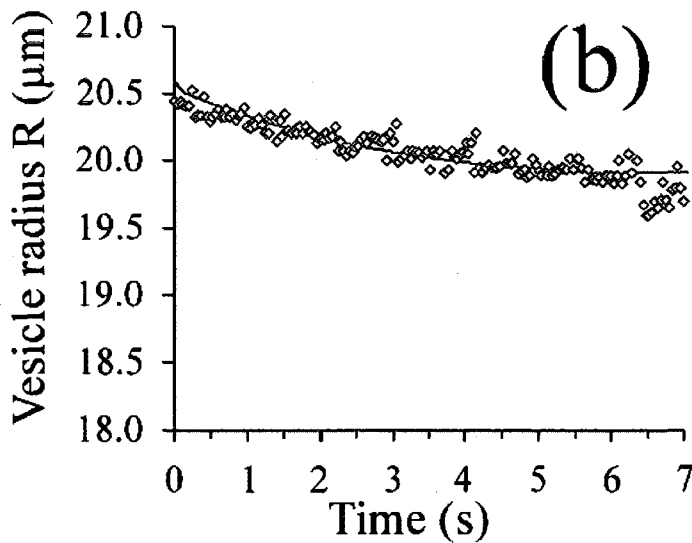
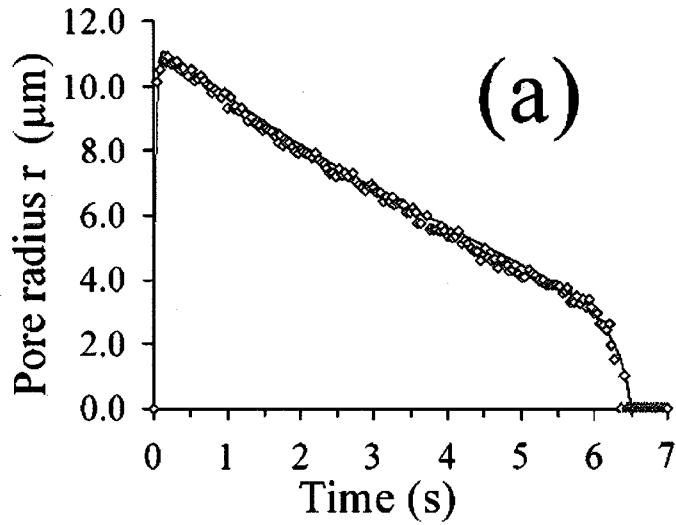
## **6.2 Line Tension**

In general, the pores generated from surface of a fluid membrane reseals rapidly without ever growing to an optically observable size. But, recent studies have shown that pores generated from giant vesicles can be as large as 10  $\mu\text{m}$  in a 100  $\mu\text{m}$  diameter vesicle [24, 33]. This can take several seconds. Brochard-Wyart showed that

the pores opened for several minutes and closed in several seconds upon continuous irradiation with UV light [24]. Therefore it allows line tension measurements to take place. It was reported that the radius of the vesicle was maintained constant throughout the pore opening and closure by glycerol medium. The line tension calculated from the method with glycerol was 6.9 pN [24]. The radius of the pores was seen to decrease with time while the vesicle radius remained constant through the measurements as shown in Figure 6.1.

Line tension can be determined in either the presence or the absence of glycerol. Rodriguez determined line tension force in giant liposomes made from DOPC (18:1) vesicles with an average value of 2 pN without glycerol [29]. The giant liposomes were generated by the electroformation method. The DOPC (18:1) lipids were labeled with NBD PC probe. Here, the pores were generated by optical illumination method that resulted in transient pores that lived from a few seconds to minutes.

Line tension measurement is obtained from the membrane edge in the outer leaflet and at the interface between the vesicle and the bulk medium. However, in some cases, the measurements have been taken in lipid mixtures. This has been done to mimic natural cell membranes that exhibit domains. These domains vary in size that can reach the order of microns [34] and have shown line tension of 1pN [35, 36].



**Figure 6.1** Time evolution of pore and vesicle radius. Pore radius is (a) and the vesicle radius (b) [19]. The vesicles were derived from DOPC (18:0) phospholipids from Sigma. The sizes were approximately  $10 \mu\text{m}$ .

A major achievement of this thesis is the determination of the pore formation dynamics in the giant liposome by the laser ablation method. Pore formation was investigated in the giant liposomes from a homologous series of the acyl-chain of synthetic lipids and in a more complex natural egg PC system. The structures of the lipids used are outlined in Section 2.1.1. Measurements were conducted without glycerol and in the absence of dye molecules in the lipid bilayer.

### **6.3 Pore Size and Vesicle Radius**

The formation of transient holes in giant vesicles have showed that holes start from a certain critical radius then grow to a certain larger radius and then close [18]. The rate of the closing of the pore is driven by a competition between the line tension  $\tau$  and the surface tension  $\sigma$  [29]. This is schematically illustrated by Figure 6.2. The surface tension stretches the lipid membrane leading to membrane rapture due to pore formation. As a result, the membrane lipids reorganize due to the interfacial force between the hydrophobic regions and the solvent medium. This reorganization leads to the line tension force which closes the pores in the bilayer.



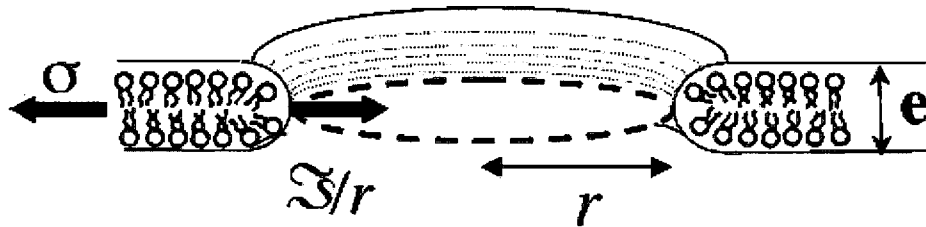


Figure 6.2 Traverse view of a pore with radius  $r$  [24].

The kinetics of the pore radius resulting from the competition between line tension and surface tension is described by Rodriguez [29]. This is illustrated by Equation 6.1 that describes the competition between the surface tension and line tension.

$$\frac{dr_{pore}}{dt} = \frac{r_{pore}(t)}{2\eta_{mb}} \left[ \sigma(t) - \frac{\tau}{r_{pore}(t)} \right] \quad [6.1]$$

In this equation  $\eta$  is the viscosity of the medium. In aqueous medium, the viscosity remains 1 cP. Equation 6.1 shows that for a long-lived pore, the value of  $\tau$  should be low and that of  $\sigma$  high. As noted in the introduction, a long lived hole in a membrane requires a highly viscous medium. This medium slows down the rate of the leak-out resulting in the hole reaching an equilibrium size. It is expected that the

pore size in water to be small as a result of the high rate of leak-out created by less viscous water.

In many occasions it is assumed that the pore radius  $r$  and the vesicle radius  $R$ , has an of area of  $(\pi r^2)$  and  $(4\pi R^2)$  respectively [6, 7]. The radius of the pore is much smaller than the vesicle radius. It is also assumed that radius of the vesicle remains constant during the closing of the pore. Therefore, the surface tension remains constant and Equation 6.1 reduces to Equation 6.2 which is used to calculate line tension force.

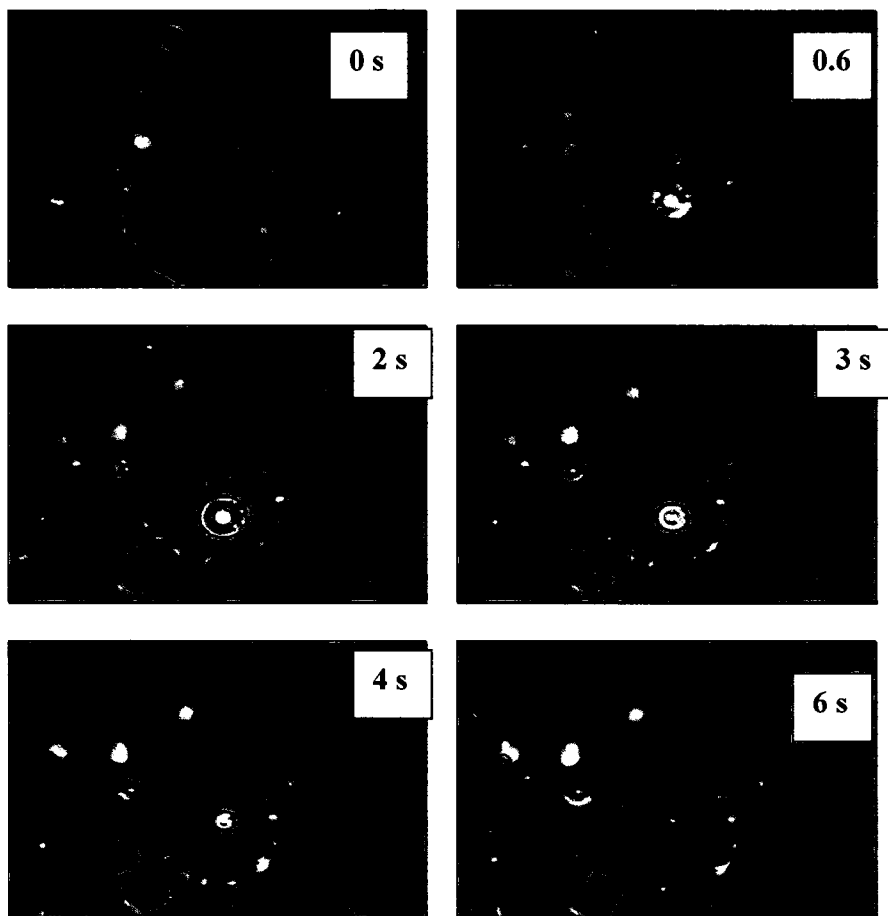
$$R^2 \ln r_{pore} \approx \frac{-2\tau}{3\pi\eta_{mb}} t \quad [6.2]$$

In this equation determining the pore radius a function of time,  $t$  at a constant vesicle radius,  $R$  results in the line tension  $\tau$ . A plot of  $R^2 \ln r_{pore}$  as a function time  $t$ , gives a straight line with a slope that yield line tension.

## **6.4 Pore Formation in Giant Vesicle by Laser Ablation**

### **6.4.1 Protocol**

The laser media used in this study was obtained from coumarin dye as discussed in Section 2.2.6. The dye laser produced a 440 nm wavelength used for laser ablation experiments. The vesicles were prepared by rapid evaporation method in 11 mM magnesium chloride. The viscosity of the medium is expected to be close to water at about 1 cP [37]. 1 centipoise is equivalent to  $10^{-2}$  Pascal. Therefore, the pressure difference between the inner and outer media of the giant vesicle is expected to be zero. The vesicles were observed by brightfield optical microscopy on an inverted microscope in (60X, 1.4 NA, oil immersion) as shown in Figure 2.4. In these experiments nitrogen laser, wavelength 337 nm was used as a pump laser. The nitrogen laser was employed to excite coumarin 440 nm dyes in a dispersive cavity yielding laser peak energy of 100  $\mu$ J. Pore formation, closure and deformation were video recorded using a fast digital Sentech STC630 CCD camera mounted on to the microscope and connected to a personal computer. This camera was capable of capturing video images at 30 frames/s.



**Figure 6.3** Time course event for coumarin laser ablation of a giant vesicle. The vesicle size was 20  $\mu\text{m}$  in diameter.

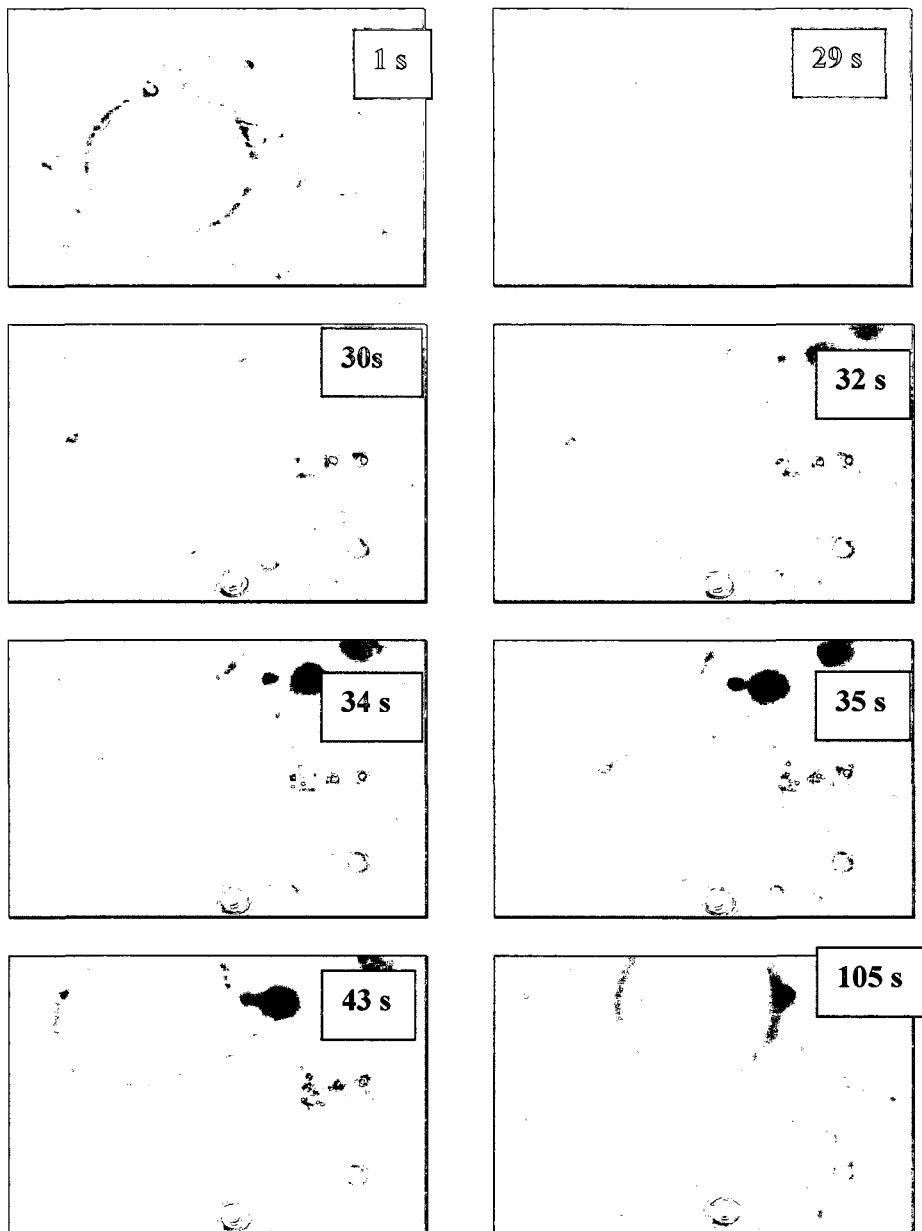


Figure 6.4 Time course event (video frames from 1-105 sec) of a 20 μm diameter egg PC liposome undergoing deformation without laser ablation.

#### **6.4.2 Membrane Deformation in Giant Vesicles**

The 440 nm laser was used to excite Rhodamine 610 dye that emitted laser of 626 nm emission wavelength. This wavelength was used to deform giant liposomes. A time course event of the deformation of an egg PC with 10% cholesterol liposome is shown in Figure 6.4. The deformation of the liposome occurred without laser ablation. The pore formation and deformation was video recorded using Sentech STC 630 CCD camera. The measurements of line tension and deformation time course events were analyzed by Videomach 4.0.4 download software. In the beginning (Figure 6.4) the vesicle appeared spherical ( $t = 1$  sec). Upon impact of laser focus, the vesicle was completely deformed from its original shape (frames 30 to 34 sec). The vesicle returned to its original shape as displayed by frames 43 to 105 sec in Figure 6.4.

### **6.5. Results**

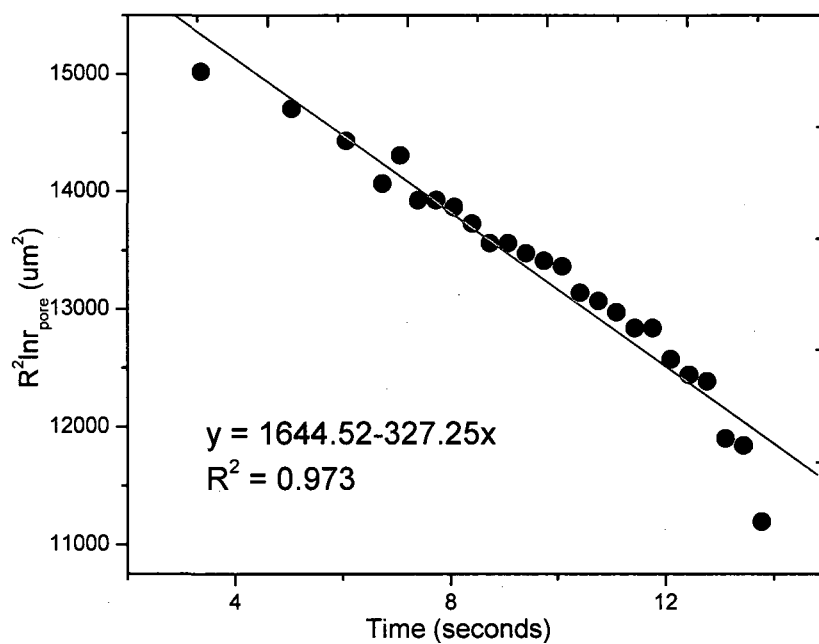
#### **6.5.1 Line Tension**

A time course event for laser ablation of a 20  $\mu\text{m}$  size liposome is displayed in Figure 6.3. The holes were generated from a vesicle with a radius 10  $\mu\text{m}$  that did not change significantly during the formation and closing of the pore. Since the radius of the pore is constant during the closing and opening of the pore, the surface tension remains constant. The line tension is determined by a plot of  $r_{\text{pore}}$  as a function of time at constant vesicle radius  $R$ . The line tension is obtained from the slope of the plot as displayed by Figure 6.5. Here, the laser ablation allowed the pore formation with

long-lived pore lifetimes. The pores appeared as a cylindrical rim as shown in Figure 6.3. All the measurements were conducted at room temperature (24°C).

The line tension was calculated from the acyl-chain of different lengths. The line tension in egg PC and egg PC with dihydrocholesterol was also investigated. Dihydrocholesterol is a saturated form of cholesterol. All lipids were purchased from Avanti Polar Lipids (Alabaster, AL, USA). The vesicles were prepared by modified evaporation method in 11 mM magnesium chloride aqueous medium.

The radius of the pore was calculated from the video time frames generated by Videomach 4.0.4 software. The radius of the pore was calculated for each time frame. The pore formation and closing were obtained in a few seconds. Figure 6.5 below is a typical plot of  $R^2 \ln r_{\text{pore}}$  as a function of time  $t$  generated using Origin 7.5 software. The diameter of the pore size and the vesicle was 1  $\mu\text{m}$  and 20  $\mu\text{m}$  respectively. The graph was linear throughout the time with a slope that allowed measurements of line tension force. The linearity of the curve supports the assumption that the radius  $R$  is constant throughout the opening and closing of the pore and very little of the vesicle fluid leaked out.



**Figure 6.5** A plot of  $R^2 \ln r_{\text{pore}}$  as a function of time  $t$  for egg PC with 10% dihydrocholesterol.

The typical line tension force values obtained for the first time with dye laser ablation are found tabulated in Table 6.1. The study revealed line tension for the homologous series of saturated phospholipids and in a natural system of egg PC. Addition of dihydrocholesterol to egg PC also revealed line tension force in a mixed lipid system with dihydrocholesterol. Line tension is obtained from the slope of the plot of  $R^2 \ln r_{\text{pore}}$  and time in seconds. The slope is given by  $-2\tau/3\pi\eta$ . The slope obtained from Figure 6.5 is  $-1289.81 \mu\text{m/s}$ . The line tension from the slope is  $61 \pm 8 \text{ pN}$ . The size of the vesicle is  $20 \mu\text{m}$ . We repeated the data analysis for vesicles of the



same size and calculated line tension for each vesicle. The average is line tension for egg PC with dihydrocholesterol was  $50 \pm 20$  pN as indicated in the Table 6.1. The viscosity of the medium was assumed equivalent to aqueous medium (1 cP).

The slope obtained in the egg PC with a 10% dihydrocholesterol was not consistent as expected for slopes from vesicles of same sizes as earlier reported [6]. Perhaps adding dihydrocholesterol modifies lipid bilayer of the egg PC liposome. It is known that such impurities as dihydrocholesterol can insert into the pore's edges and affect the line tension [6]. Pure lipid systems have a definite phase transition temperature as shown in Table 6.1. The DLPC and DOPC lipids have a phase transition temperature that is below zero degrees. Therefore, liposomes obtained from these lipids exist in the fluid phase at room temperature.

The DPPC and DSPC have phase transition above room temperature and exist in gel phase at room temperature. Egg PC has a negative phase region resulting in liposomes that are in fluid phase at room temperature. The study has reported the dynamics of pore formation and closing as a function of the phase state of the lipids. The DSPC and DOPC differ only in the level of the acyl-chain saturation. DSPC has saturated acyl-chain with 18 carbon atoms. DOPC has only one level of unsaturation in the acyl-chain with 18 carbons atoms in the structure. The egg PC liposomes showed line tension force slightly higher than the synthetic pure lipid system. The line tension force of  $32 \pm 2$  pN was almost three times higher than the fluid phase of the DOPC lipid. The egg PC with dihydrocholesterol showed line tension nearly double the value of the pure egg PC. The line tension measured in the DPPC was

higher than the DLPC. DSPC vesicles showed the least line tension value. Addition of dihydrocholesterol to egg PC resulted in a significantly elevated line tension force as shown in Table 6.1.

**Table 6.1** Line tension force in homologous series and in egg PC liposomes [38] at 24 °C.

<b>Lipid</b>	<b>Acyl-chain length</b>	<b>Phase transition ( °C )</b>	<b>Line tension ( pN )</b>
DLPC	12:0	-1 (fluid)	2.5 ± 0.3
DPPC	16:0	41 ( gel )	9.5 ± 1.0
DSPC	18:0	55 ( gel )	NR <sup>1</sup>
DOPC	18:1	-20 ( fluid )	11 ± 1
Egg PC	variable	No specific phase	32.3 ± 2.0
Egg PC and 10% Dihydrocholesterol	variable	No specific phase	(5 ± 2) x10

---

<sup>1</sup> NR-not reproducible

## 6.6 Discussion

The existence of a membrane is a condition for pore formation in lipid bilayers. Once the bilayer is exposed to the aqueous environment, it is natural tendency for the hydrophobic chains of the lipids to re-orient to minimize their contact with water. Line tension is the energy per unit edge length required to close the pore that is formed as a result of the re-orientation of the hydrocarbons.

Line tension was determined from the acyl-chains that varied in lengths and level of saturation in simple lipid system. In addition, the line tension force is calculated for a more complex system in the egg PC and that with 10% dihydrocholesterol. Brochard-Wyart estimated line tension force of DOPC vesicles and obtained  $6.9 \pm 0.4$  pN [24]. The DOPC lipid was purchased from Sigma and the liposomes were prepared using the electroformation method. This group found out that DOPC lipids purchased from Avanti Lipids gave a higher line tension value of  $21 \pm 4$  pN. The line tension calculated from pores generated by the dye laser gave value of  $11 \pm 1$  pN for the DOPC lipids from Avanti lipids. The different numbers of the line tension is attributed to effect of the impurities possibly from the source that can inserted in the pore's edge as earlier noted to affect line tension [6].

Line tension was calculated for homologous series of phospholipids. Depending on the phase transition temperature, the lipids were either in gel or fluid phase regions of the bilayer. The DOPC, DLPC and egg PC phospholipids have low phase transition and exist in the fluid phase at room temperature. The DPPC and DSPC have phase transition above room temperature. These lipids exist in gel phase

at room temperature. The DOPC and DSPC differ only in one degree of saturation in DOPC. Both have eighteen carbons forming acyl-chain.

Line tension was positively correlated with the number of carbons in the acyl-chain without considering the degree of unsaturation of lipids. Considering the DLPC, DPPC and DOPC, it was observed that the line tension increased linearly with  $0.7 \pm 0.2$  for each methylene group in acyl-chain of the lipids. The relationship of the methylene groups with bending modulus was earlier reported by Evans [39]. There is a relationship between line tension and the bending modulus [6, 37].

Considering the free energy existing at the membrane edge, a relationship exists between the line tension and the repulsive interactions in the headgroup region calculated by the headgroup parameter B [40]. The parameter B is a measure of the headgroup interaction of lipids. Line tension is a return to the equilibrium after pore formation. Therefore, this force should be dependent on headgroup parameter B. This value is  $0.8 \text{ \AA}$  and  $13.9 \text{ \AA}$  in DLPC and DPPC respectively as reported by May [40].

The difference in the line tension in DLPC and DPPC is rationalized on the basis of the differences existing in the phases. The DLPC and DPPC have phase transition temperature of  $-1$  and  $41^\circ\text{C}$  respectively. At room temperature it is expected that the DPPC to be in the gel phase while DLPC to be in the fluid phase state. The elastic area compressibility modulus of the lipids in gel and in fluid phases will be different as demonstrated by DMPC lipids [41].

The line tension from DSPC was difficult to reproduce and cannot fit the trend observed for the series. The pore formation of the DMPC lipid was not possible with

the laser ablation. The lipid exhibits gel fluid phase coexistence at room temperature that could result in difficulty in pore formation in the bilayer. The egg PC phospholipid is made of several combinations of phospholipids. It is a composition of both the saturated and unsaturated lipid hydrocarbon chains. The following are the main components of egg PC: 34% 16:0, 2% 16:1, 12% 18:0, 32% 18:1, 20% 18:2 and 4% 20:4 [42]. The value of the line tension reported for the egg PC was greater than in the homologous series. The egg PC liposomes appear more robust and capable of resisting pore formation by laser ablation. The line tension for the egg PC with 10% dihydrocholesterol is even much greater than pure egg PC giving  $50 \pm 20$  pN. As expected, the addition of cholesterol to the phospholipid bilayer increases the line tension [6]. Cholesterol increases the rigidity of membrane bilayer, straighten the hydrocarbon chains and thicken the bilayer. Therefore, cholesterol increases the membrane fluidity [43] and increases the bending modulus. Moreover, studies have showed a coexisting liquid-ordered and liquid disordered phases in cholesterol and phospholipid mixture [44]. These regions could possibly contribute to the fluctuation in line tension as observed by the magnitude of the deviations in the result of line tension in the egg PC with 10% dihydrocholesterol.

The characterization of a lipid membrane is important to understand its properties and functions. Imaging of a giant vesicle in an optical microscope can provide some important information on a lipid membrane response to a laser perturbation. A laser perturbation can be useful in determining mechanical properties of a lipid membrane. A lipid membrane maybe curved, compressed, dilated or

sheared in response to laser deformation. In Figure 6.4, egg PC response to focused laser radiation shows the different shapes of the lipid membrane. These shapes can be used to estimate the bending rigidity, bending modulus, area compressibility and shear elasticity modulus of the bilayer. These properties can be useful in defining both the simple and complex lipid bilayer system. Pure egg PC was not possible to ablate as result of tough nature of this lipid membrane. Figure 6.14 demonstrates that microscopy observation of a giant vesicle such as an egg PC can reveal events and shapes induced by laser deformation. These observations can reveal complex behavior of membranes and help provide answers to membrane composition and further improves our understanding of biomembranes.

## **6.7 Conclusion**

The line tension force of pores in giant liposomes made from a homologous series of saturated phospholipids was reported. The line tension was determined by laser ablation. Line tension determination from laser ablation was reported for the first time. It has been shown that this value is directly related to acyl-chain length, except in DSPC lipids which were found irreproducible.

The line tension in the homologous series has been explained on the basis of the existing models. The differences in the area compressibility modulus in the chains of variable length appear to influence the line tension. It was observed that the line tension increases with acyl-chain length increase. Line tension in the DMPC was not reported here since it was not possible to reliably form holes in the liposome from this

lipid using laser ablation. This was attributed to the existence of the gel and fluid phase regions at room temperature for the DMPC lipids.

The line tension in natural egg PC lipid was found higher than in the pure homologous lipid system. The egg PC phospholipids are composed of several lipids with the varying degree of saturation and acyl-chain length. Therefore, it is a complex system and robust to withstand pore formation by laser ablation. Addition of dihydrocholesterol to egg PC lipids at a concentration of 10% (mol/mol) was found to increase the line tension. The line tension was found to vary remarkably with dihydrocholesterol.

## 6.8 References

- 1 Akinlaja, J. and Sachs, F. (1998) The breakdown of cell membranes by electrical and mechanical stress. *Biophys J* **75**, 247-254
- 2 Freeman, S. A., Wang, M. A. and Weaver, J. C. (1994) Theory of electroporation of planar bilayer membranes: predictions of the aqueous area, change in capacitance, and pore-pore separation. *Biophys J* **67**, 42-56
- 3 Chizmadzhev, Y. A., Zarnitsin, V. G., Weaver, J. C. and Potts, R. O. (1995) Mechanism of electroinduced ionic species transport through a multilamellar lipid system. *Biophys J* **68**, 749-765
- 4 Schwarzott, M., Lasch, P., Baurecht, D., Naumann, D. and Fringeli, U. P. (2004) Electric field-induced changes in lipids investigated by modulated excitation FTIR spectroscopy. *Biophys J* **86**, 285-295
- 5 Wieprecht, T., Dathe, M., Epanand, R. M., Beyermann, M., Krause, E., Maloy, W. L., MacDonald, D. L. and Bienert, M. (1997) Influence of the angle subtended by the positively charged helix face on the membrane activity of amphipathic, antibacterial peptides. *Biochemistry* **36**, 12869-12880
- 6 Karatekin, E., Sandre, O., Guitouni, H., Borghi, N., Puech, P. H., Brochard-Wyart, F. (2003) Cascades of transient pores in giant vesicles: line tension and transport. *Biophys J* **84**, 1734-1749
- 7 Brochard-Wyart, F., Gennes de, G. P., Sandre, O. (2000) Transient pores in stretched vesicles: role of leak-out. *Physica A* **278**, 32-51
- 8 Ulrich, A. S. (2002) Biophysical Aspects of Using Liposomes as Delivery Vehicles. *Biosciences Reports* **22**, 129-150
- 9 Dai, J., Ting-Beall, H. P. and Sheetz, M. P. (1997) The secretion-coupled endocytosis correlates with membrane tension changes in RBL 2H3 cells. *J Gen Physiol* **110**, 1-10



- 10 Jackson, M. B. and Chapman, E. R. (2006) Fusion pores and fusion machines in Ca<sup>2+</sup>-triggered exocytosis. *Annu Rev Biophys Biomol Struct* **35**, 135-160
- 11 Borghi, N., Kremer, S., Askovic, V., Brochard-Wyart, F. (2006) Tube extrusion from permeabilized giant vesicles. *Europhys. Lett* **75**, 666-672
- 12 Brochard-Wyart, F., Gennes, G., Pfeuty, P. (1976) Surface Tension and Deformations of Membrane Structures: Relation to Two-Dimensional Phase Transitions. *Journal de Physique* **37**, 1099
- 13 Jahnig, F. (1996) What is the surface tension of a lipid bilayer membrane? *Biophys J* **71**, 1348-1349
- 14 Tanford, C. (1979) Hydrostatic pressure in small phospholipid vesicles. *Proc Natl Acad Sci U S A* **76**, 3318-3319
- 15 Wilhelm, C., Winterhalter, M., Zimmermann, U. and Benz, R. (1993) Kinetics of pore size during irreversible electrical breakdown of lipid bilayer membranes. *Biophys J* **64**, 121-128
- 16 Kroeger, J. H., Vernon, D. and Grant, M. (2009) Curvature-driven pore growth in charged membranes during charge-pulse and voltage-clamp experiments. *Biophys J* **96**, 907-916
- 17 Saitoh, A., Takiguchi, K., Tanaka, Y. and Hotani, H. (1998) Opening-up of liposomal membranes by talin. *Proc Natl Acad Sci U S A* **95**, 1026-1031
- 18 Sandre, O., Moreaux, L., Brochard-Wyart, F. (1999) Dynamics of transient pores in stretched vesicles. *Proc Natl Acad Sci U S A* **96**, 10591-10596
- 19 Karatekin, E., Sandre, O., Brochard-Wyart, F. (2003) Transient pores in vesicles. *Polym Int* **52**, 486-493

- 20 Rodriguez, N., Heuvingh, J., Pincet, F., Cribier, S. (2005) Indirect evidence of submicroscopic pores in giant unilamellar [correction of unilamellar] vesicles. *Biochim Biophys Acta* **1724**, 281-287
- 21 Wohlerlert, J., den Otter, W. K., Edholm, O. and Briels, W. J. (2006) Free energy of a trans-membrane pore calculated from atomistic molecular dynamics simulations. *J Chem Phys* **124**, 154905
- 22 Betterton, M. D., Brenner, M. P. (1999) Electrostatic edge instability of lipid membranes. *Phys Rev Lett* **82**, 1598-1601
- 23 Bar-Ziv, R., Frisch, T. and Moses, E. (1995) Entropic expulsion in vesicles. *Phys Rev Lett* **75**, 3481-3484
- 24 Karatekin, E., Sandre, O., Guitouni, H., Borghi, N., Puech, P. H. and Brochard-Wyart, F. (2003) Cascades of transient pores in giant vesicles: line tension and transport. *Biophys J* **84**, 1734-1749
- 25 Bar-Ziv, R., Moses, E., Nelson, P. (1998) Dynamic excitations in membranes induced by optical tweezers. *Biophys J* **75**, 294-320
- 26 Bar-Ziv, R., Frisch, T., Moses, E. (1995) Entropic expulsion in vesicles. *Phys Rev Lett* **75**, 3481-3484
- 27 Evans, E., Heinrich, V., Ludwig, F., Rawicz, W. (2003) Dynamic tension spectroscopy and strength of biomembranes. *Biophys J* **85**, 2342-2350
- 28 Ly, H. V. and Longo, M. L. (2004) The influence of short-chain alcohols on interfacial tension, mechanical properties, area/molecule, and permeability of fluid lipid bilayers. *Biophys J* **87**, 1013-1033
- 29 Rodriguez, N., Cribier, S. and Pincet, F. (2006) Transition from long- to short-lived transient pores in giant vesicles in an aqueous medium. *Phys Rev E Stat Nonlin Soft Matter Phys* **74**, 061902

- 30 Genco, I., Gliozzi, A., Relini, A., Robello, M. and Scalas, E. (1993) Electroporation in symmetric and asymmetric membranes. *Biochim Biophys Acta* **1149**, 10-18
- 31 Opsahl, L. R. and Webb, W. W. (1994) Transduction of membrane tension by the ion channel alamethicin. *Biophys J* **66**, 71-74
- 32 Abrunhosa, F., Faria, S., Gomes, P., Tomaz, I., Pessoa, J. C., Andreu, D. and Bastos, M. (2005) Interaction and lipid-induced conformation of two cecropin-melittin hybrid peptides depend on peptide and membrane composition. *J Phys Chem B* **109**, 17311-17319
- 33 Puech, P. H., Borghi, N., Karatekin, E. and Brochard-Wyart, F. (2003) Line thermodynamics: adsorption at a membrane edge. *Phys Rev Lett* **90**, 128304
- 34 Samsonov, A. V., Mihalyov, I. and Cohen, F. S. (2001) Characterization of cholesterol-sphingomyelin domains and their dynamics in bilayer membranes. *Biophys J* **81**, 1486-1500
- 35 Baumgart, T., Hess, S. T., Webb, W. W. (2003) Imaging coexisting fluid domains in biomembrane models coupling curvature and line tension. *Nature* **425**, 821-824
- 36 Baumgart, T., Das, S., Webb, W. W., Jenkins, J. T. (2005) Membrane elasticity in giant vesicles with fluid phase coexistence. *Biophys J* **89**, 1067-1080
- 37 Rodriguez, N., Cribier, S., Pincet, F. (2006) Transition from long- to short-lived transient pores in giant vesicles in an aqueous medium. *Phys Rev E Stat Nonlin Soft Matter Phys* **74**, 061902
- 38 Srividya, N., Muralidharan, S., Okumu, W. and Tripp, B. (2008) Determination of the line tension of giant vesicles from pore-closing dynamics. *J Phys Chem B* **112**, 7147-7152

- 39 Rawicz, W., Olbrich, K. C., McIntosh, T., Needham, D., Evans, E. (2000) Effect of chain length and unsaturation on elasticity of lipid bilayers. *Biophys J* **79**, 328-339
- 40 May, S. (2000) A molecular model for the line tension of lipid membranes. *Eur Phys J E* **3**, 37-44
- 41 Needham, D., McIntosh, T. J. and Evans, E. (1988) Thermomechanical and transition properties of dimyristoylphosphatidylcholine/cholesterol bilayers. *Biochemistry* **27**, 4668-4673
- 42 Avanti, P. L. (2009) Phosphatidylcholines. *Avanti Polar Lipids Retrieved on September 25, 2009 from <http://www.avantilipids.com/>*
- 43 Israelachvili, J. N., Marcelja, S. and Horn, R. G. (1980) Physical principles of membrane organization. *Q Rev Biophys* **13**, 121-200
- 44 Ipsen, J. H., Mouritsen, O. G. and Zuckermann, M. J. (1989) Theory of thermal anomalies in the specific heat of lipid bilayers containing cholesterol. *Biophys J* **56**, 661-667

## CHAPTER 7

### CHARACTERIZATION OF THE N-TERMINAL HUMAN WILSON PROTEIN DOMAIN 4

#### 7.1 Introduction

##### 7.1.1 Importance of Copper and Wilson Disease

Cells acquire variety of transition elements and use them as cofactors in enzymatic reactions. Copper is an example of such a transition metal. The daily copper intake from variety of food sources is between 0.6 and 1.6 mg copper per day [1]. Copper is a redox heavy metal that is essential in trace amounts to all living organisms [2]. It exists in the cells in the concentrations ranging between 10 and 100  $\mu\text{M}$  [3]. Copper is found as a cofactor in a large number of proteins and enzymes such as cytochrome c oxidase [4], catechol oxidase [5], Cu / Zn superoxide dismutase, oxidoreductases and monooxygenases.

Copper ions do not exist freely in the cytoplasm of eukaryotic cells. copper forms a variety of metal complexes with small molecules in blood and cell cytoplasm [3, 6]. In most reactions copper participates in the oxidation and reduction processes involving the electron transfer reactions. It exists in two oxidation states, Cu(I) and oxidized Cu(II) form. An excess of copper is toxic. Therefore, the concentration of copper ions is tightly controlled in the cell cytoplasm using copper ion pumps [7]. Copper toxicity is based on its reactivity with cellular macromolecules and inorganic

compounds found in the cell. The transition between Cu(I) and Cu(II) can generate reactive oxygen species via the Fenton pathway that can damage cellular components [8]. It can also form chelates with organic molecules including DNA and proteins.

Because of the adverse effects of copper ions in the cell, living organisms have developed tight control mechanisms to transport or sequester copper within the cell cytoplasm [9, 10]. Genes for a copper-responsive regulatory system have recently been identified. This has recently been discovered in the genes involved in human disorder of copper transport Menkes disease (MK) [11], familial amyotrophic lateral sclerosis (FALS) [12], Alzheimer's disease [13, 14] and Wilson disease (WD) [15-17]. These are some of the known inherited disorders of copper metabolism found in humans. The coordination chemistry and control mechanism involving copper ions is well studied in yeast cells [18].

### **7.1.2 Wilson Disease**

Wilson Disease, or sometimes hepatolenticular degeneration disease, is an autosomal recessive disorder of copper metabolism in liver and brain cells. The liver and brain of the Wilson disease patients have abnormally large amount of copper [19]. It was first described in detail in 1912 by Wilson Kinnier as a familial, lethal neurodegenerative disease accompanied by a chronic liver failure if not treated in time [19, 20]. The biliary excretion of metal ion is defective in the Wilson disease patient, thus leading to the ion build up in the hepatocytes and extra-hepatic tissues such as the central nervous system and cornea of the eye. The build up in the cornea

of the eye is manifested in Kayser-Fleischer rings [21, 22]. Wilson disease incidence in the population is of one in 30000 to 100000 [22, 23].

In 1952, Scheinberg and Gitlin reported deficiency of ceruloplasmin in the serum of Wilson disease patients [24]. Ceruloplasmin is an oxidase that can carry 95% of plasma copper and transport it to the peripheral tissues. To date, a test for serum ceruloplasmin is still the most applicable clinical method for detecting Wilson disease [25]. In WD patients, a defective or dysfunctional Wilson disease protein (ATP7B) cannot incorporate copper ions into ceruloplasmin. Therefore, ceruloplasmin exists in the apo form and it is rapidly degraded, leading to a reduced circulating level of serum ceruloplasmin in WD patients [26]. ATP7B is a P-type ATPase that is primarily expressed in the liver. Zinc acetate, penicillamine and trientine are drugs currently safe for the treatment of WD [22].

### **7.1.3 P-Type ATPases**

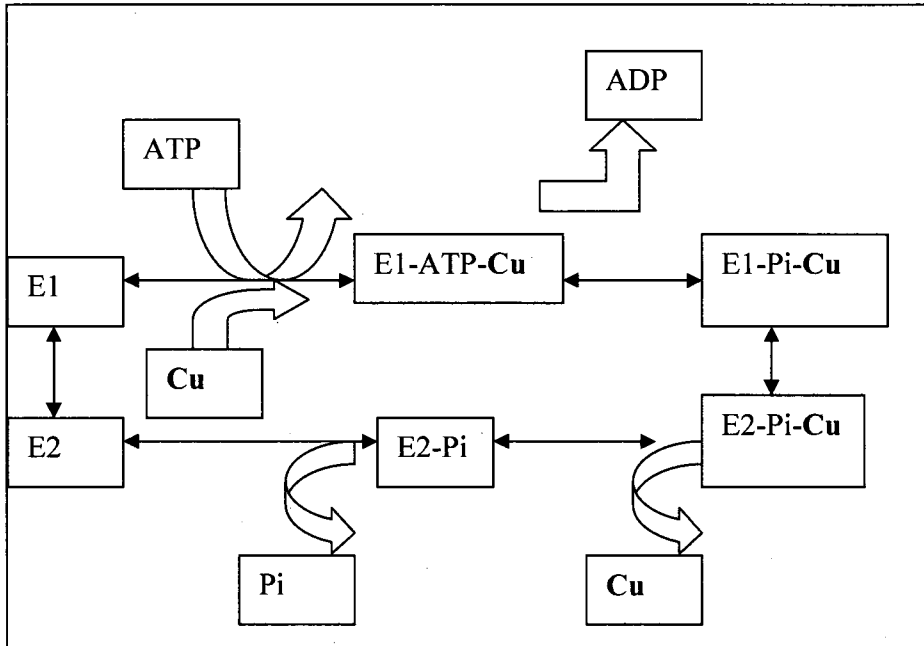
The P-type ATPases are polytopic membrane proteins involved in the uphill transport of cations coupled to the energy of hydrolysis of ATP [27]. These ATPases are selective for soft transition metals. The designation of the P-type comes from the mechanism that involves the transient transfer of the terminal phosphate of ATP to a conserved aspartate residue in the active site [28-30]. The key regulators of copper metabolism in the cell are the copper transporting P-type ATPase ATP7A and ATP7B [31]. Mutations in ATP7A and ATP7B affect the copper cellular balance, resulting in copper deficiency (Menkes Disease) and copper overload (Wilson Disease),

respectively [32, 33]. Overexpression of these two proteins has been associated with cancer resistance to chemotherapeutic drugs [34].

The Menkes protein (ATP7A) is expressed in many tissues except in the liver cells while ATP7B is mostly abundantly expressed in the liver [35]. The role of ATP7B is to hydrolyze ATP upon stimulation by copper binding. The energy released as a result of the hydrolysis causes conformational changes in the structure of the proteins which lead to the release of copper bound at the other opposite side of the membrane [36].

A cartoon to illustrate the process of hydrolysis of the ATP upon copper binding and subsequent release of copper after hydrolytic reaction is displayed in Figure 7.1. Hydrolysis occurs by transient acyl-phosphorylated intermediates of ATP hydrolysis. In this process Asp1027 found in the ATP binding domain is phosphorylated [37]. This amino acid is a family of DKTG sequence motifs that is typical of P-type ATPase.



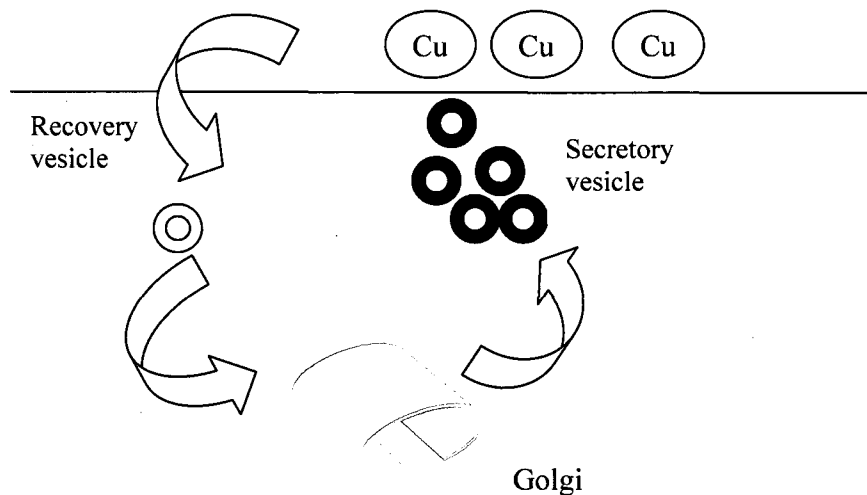


**Figure 7.1** Hydrolysis of ATP upon copper binding to Cu-ATPase. E1 is the initial step in catalytic cycle involving binding of ATP to the N-terminal domain and metal to the transmembrane region. E1-Pi-Cu is a phosphorylated intermediate formed by transfer of  $\gamma$ -phosphate from ATP to invariant Asp residue of DKTG sequence motif in P-domain. E2-Pi-Cu state is a conformational change that allow release of metal to one side of the membrane. E2- state is dephosphorylation reaction step in the catalytic pathway.

The sequence homology of the Menkes and Wilson disease proteins shows amino acid identity of 56% [38]. WD is caused by mutation in the ATP7B gene [39-41]. ATP7B is localized in the *trans*-Golgi network of hepatocytes [35, 41, 42]. It transports copper into the secretory pathway for incorporation into ceruloplasmin *and* into the bile [16, 43].

ATP7B activity is controlled by the level of copper ions present in the cytoplasm of the cell. The ATP7B protein not only transports copper to the *trans*-Golgi network for further incorporation into ceruloplasmin but also sequesters copper ions into the endocytotic vesicles for export out of the cell. An increase in the copper level in the hepatocytes signals the ATPase to shift from the *trans*-Golgi network to the cytoplasmic vesicular compartment near the canalicular membrane [44-47].

Copper accumulates in the vesicular compartment and decreases from the cell cytoplasm. The decrease in the cytoplasmic copper concentrations results in the redistribution of the ATPase back to the *trans*-Golgi network and excretion of copper to the bile. This provides a rapid mechanism to maintain intracellular copper balance. The movement of ATP7A in response to copper concentration in the cytoplasm is illustrated by Figure 7.2.



**Figure 7.2** Cycling of Menkes protein between trans-Golgi network and plasma membrane in excess of copper.

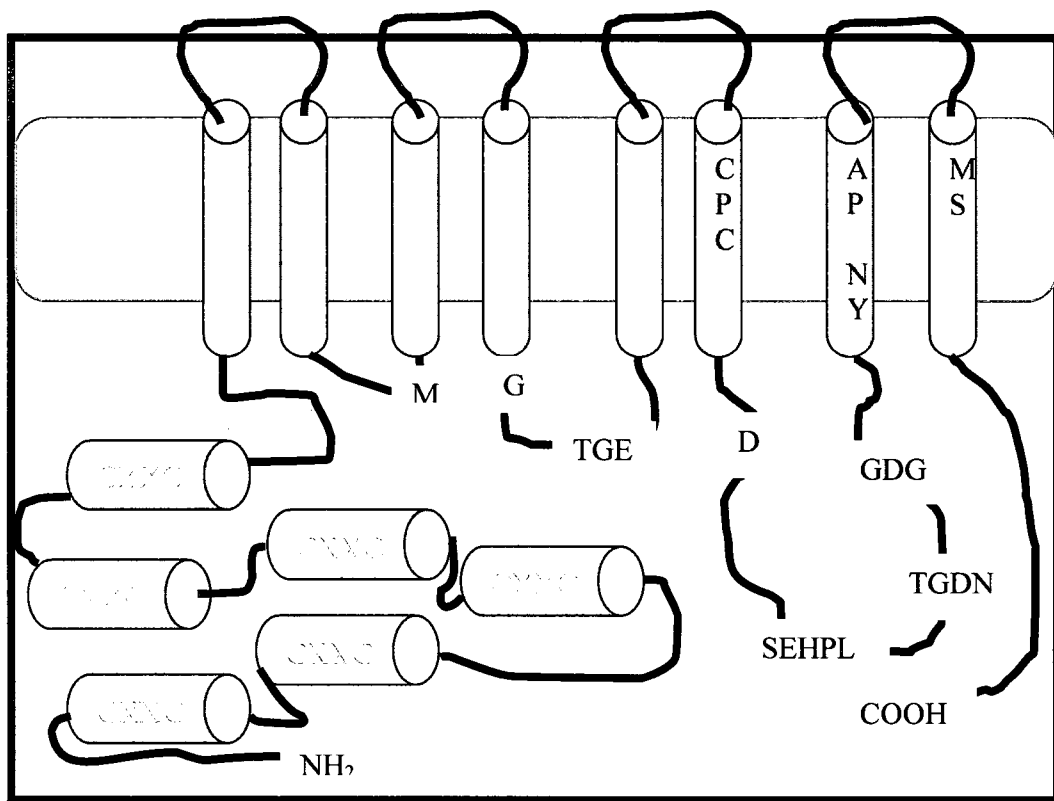
#### 7.1.4 Structure of ATP7B

The ATP7B gene encodes a 165 kDa membrane protein [16]. Both the wild-type and mutants of the entire protein sequence has been expressed in large amounts *in vivo* [48]. The protein in addition to the C-terminal domain has four main distinct domains: the N-terminal metal-binding domain, the functional region of the P-type ATPase domain, transmembrane helices and the phosphatase domain [49]. This protein has approximately 630 amino acid residues. It has cytosolic N-terminus six metal binding domains (MBD) which are connected by peptide linkers. The longest linker occurs between the fourth (MBD4) and fifth domain (MBD5). Each MBD

contains approximately 70 amino acids [50]. The longest linker subdivides the N-terminal domain into two parts: MBD1-4 and MBD5, 6.

The structures of the metal binding domains are similar to each other and to the human copper chaperone Atox1. The similarity between MBDs to the Atox1 does not confer similar roles in the transfer of copper ions in the cells [51]. Each domain has a  $\beta\alpha\beta\beta\alpha\beta$  ferredoxin-like fold and solvent exposed loops with a conserved CXXC motif (where C is cysteine and X is any other amino acid). These motifs bind copper ions in form of Cu(I) with high affinity [52].

The structure of the ATP7A with all the domains is displayed in Figure 8.3. Both ATP7A and the ATP7B have eight transmembrane domains. The sixth transmembrane domain has a conserved CPC motif which is postulated to bind metal ions. The ATP-binding domain is composed of 350 amino acid residues. It has two domains: a P-domain with an invariant aspartic acid in the sequence motif DKTG that is phosphorylated and the N-domains that is responsible for the binding of nucleotides. The P-and N-domains are connected by a short peptide linker [53]. The ATP-binding domain is the center of most mutations with the H1069Q found in WD patients [54, 55].



**Figure 7.3** The structure of Wilson disease protein.

### 7.1.5 Copper Trafficking in Cells

Copper ions have to be shuttled within and between compartments of the cells to target sites in the cell cytoplasm. Movement of copper ions between organelles and between cell membranes is conducted by small target proteins working in tandem with the ATP-driven mechanisms as described in Section 8.1.3. Most of the cellular components engaged in the transport of copper are well conserved throughout the course of evolution. The majority of copper in serum is bound to a multi-copper

oxidase ceruloplasmin protein having three distinct copper sites [26, 56]. The highly reducing cytosolic environments and presence of plasma membrane reductase enzyme ensures the conversion of Cu(II) to Cu(I) before uptake by transport to the cell membrane. Cu(I) is taken to the cell by a plasma membrane spanning high affinity copper transport protein 1 (Ctr1) [57]. This protein is specific for transporting Cu (I) and not Cu (II) or any other metal ion in the cell [56].

Our current knowledge in copper trafficking in mammalian cells is made possible by many studies in two proteins involved in copper trafficking in yeast cells [58]. These are Atx1 and Ccc2 [18, 58]. Atx1 is 73 amino acids protein. It binds copper in form of Cu(I) oxidation state [10]. It was discovered in 1995 in yeast as a protective protein against oxidative damage to the yeast cells and delivers copper to transport ATPase Ccc2 [59, 60]. Once in the cell, copper is transported to different locations that include metalloenzymes in the secretory pathway, cytoplasm and mitochondria as shown in Figure 7.4.

In humans copper is transported by human homologue Atox1 or HAH1. This protein was isolated by Gitlin and co-workers and was found to be ubiquitously expressed in the cell to transport copper [61, 62]. Copper is transported to the secretory pathways that depend on the activity of ATP7A or ATP7B [61]. In humans, copper is shuttled by Ctr1 and then transported by HAH1 [61, 63]. Copper is pumped to the lumen of the *trans*-Golgi by copper transporters for insertion into copper enzymes destined for the cell surface or extracellular environment.

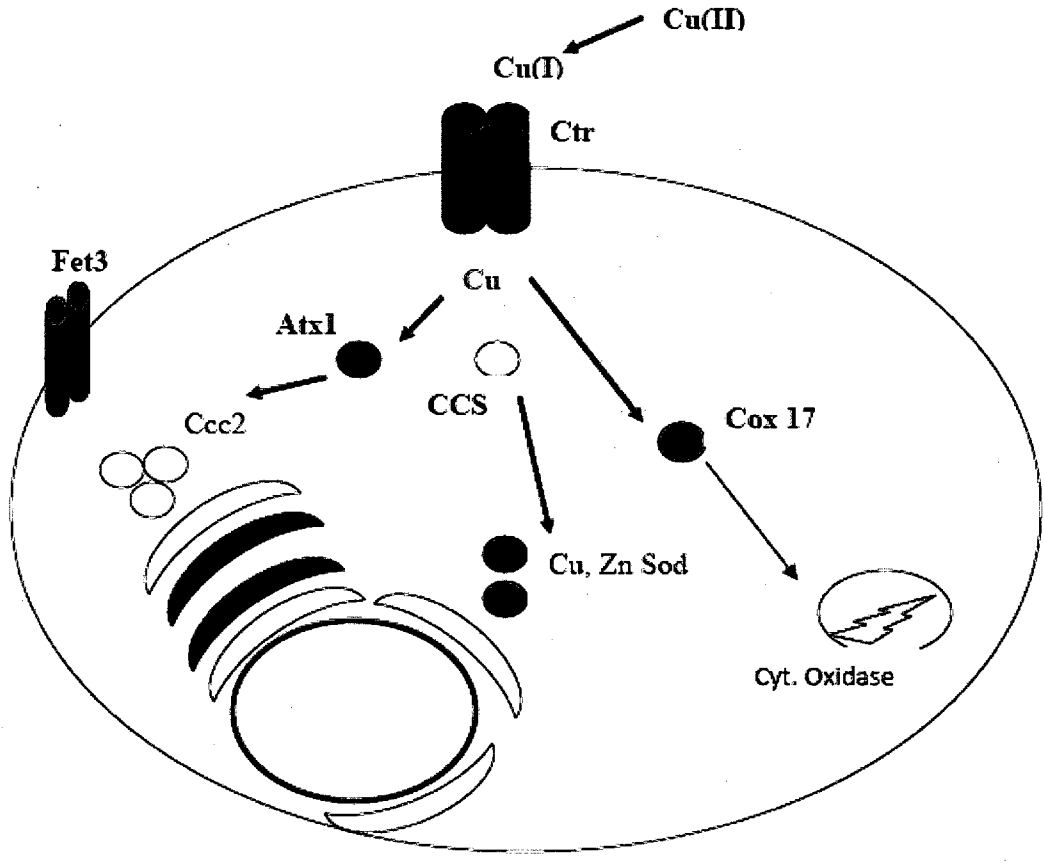


Figure 7.4 Copper trafficking pathways in a cell.

### 7.1.6 Metallochaperone and Copper Transport in Cells

Metallochaperones are soluble cytosolic proteins that potentially bind and deliver copper ions to target proteins in the cell [3, 9, 64]. They possess an invariant CXXC metal binding motif common in the N-terminal region similar to MBDs of Cu-ATPase in humans and Ccc2 in yeast. This domain binds and transports metal ions via protein-protein interaction to their target protein sites [59]. Copper chaperones, for example, forms a transient complex with Cu(I) and target proteins. In humans, Atox1, also originally known as HAH1, binds copper through two cysteines in the CXXC motif in the exposed loop. Atox1 targets the N-terminal region of ATP7B in a copper-dependent fashion and regulates activity of this protein [9, 37].

The transfer of Cu(I) to Atox1 takes place rapidly and is controlled by thermodynamics of the system [9]. There are three main classifications of copper chaperones: Atox1-like chaperones, the chaperones for copper superoxide dismutase (CCS) and copper chaperones for cytochrome c oxidase. Other bacterial systems include mercury chaperone, a small mercury binding protein also known as MerP that is regulated by mercury-responsive gene (MerR) [65]. The protein transports highly toxic  $\text{Hg}^{2+}$  that is converted to a less toxic  $\text{Hg}^0$  by the membrane protein mercuric reductase. The MerP is regulated by dimeric MerR in response to the levels of the mercury ions. The mechanisms involved in the recognition of certain specific proteins, binding to metal ions and delivery of these ions to these targets by metallochaperones is currently a subject of many studies in chemistry [59].



### 7.1.7 Metal Coordination Chemistry

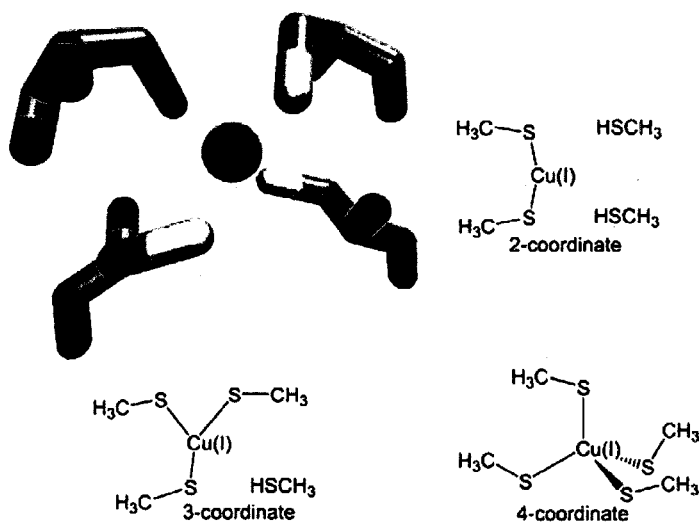
The interaction of the Cu(I) ions with copper chaperones and the Cu(I)-ATPase in living organisms are of fundamental interests in understanding the chemistry of metal coordination in bioinorganic chemistry. The Atx1 and Atox1 are similar to the fourth domain of Menkes protein in the overall fold and metal binding site [66, 67]. Atx1 is also similar to the MerP protein. The X-ray structure of the Hg(II) form of Atx1 and the NMR structure of the Ag(I) form of the fourth domain of the Menkes protein have been elucidated [10, 68].

The details of copper coordination still are not clear [68], possibly due to loss of copper during crystallization or aggregation and the loss of signal data [67, 69]. This is also attributed to the uncertainty in the Cu-S distance at a resolution of 1.8 Å [70]. The X-ray structure of the Hg(II) form bound to Atx1 shows Hg(II) is coordinated to two cysteine sulfur atoms (2.33 Å for Cys15 and 2.34 Å Cys18) in a linear fashion and an S-Hg-S bond angle of 167° [10, 66]. The Hg(II) bound to HAH1 has a three coordinate geometry [67].

The cysteines involved in metal binding are found in the conserved CXXC motif in both the chaperone and in the target protein. Using NMR spectroscopy, the Ag(I) is modeled with a linear coordination to the two cysteines in the conserved region motif in Menkes domain four. Atx1 can transfer Hg(II) as well as Cu(I) to Ccc2 [10, 67]. It was therefore postulated that the metal coordination chemistry in both Hg(II) and Cu(I) are similar [71]. Recent studies with HAH1 show that this is not the case [70]. In addition to two similar bond lengths of 2.25 Å each involved in

the coordination, there is a third bond of 2.40 Å that is suggested to be either a third or fourth ligand involved in the coordination as shown in Figure 7.5.

Using quantum mechanics and molecular simulations it was reported that the fourth coordination in Cu(I) and Atox1 is not energetically possible [71]. There is still a great need to elucidate copper coordination and transfer. This could provide insights into copper chaperone function and the copper complex found in the Wilson disease protein.



**Figure 7.5** Coordination chemistry for the Cu(I) ions in metal binding sites showing possible 2, 3 and 4 coordination sites in HAH1 [71].

### 7.1.8 Copper Transfer from HAH1 to ATPase

Copper transfer from chaperones to a target protein involves docking between the donor and the acceptor by electrostatic interaction and hydrogen bond formation [9, 72]. The copper chaperone and target protein have similar protein folds. However, the surface residues seem to be different. The target protein and chaperone both have the conserved sequence motif CXXC coming in close proximity to one another. This motif is common in both chaperone and the metal binding domains, which lead to the hypothesis that the copper transfer occurs by a docking mechanism and via ligand exchange. Subsequent docking occurs via formation of two and three-coordinate intermediates in which the metal ion remains ligated simultaneously to the chaperone and target enzyme.

Spectroscopic studies of Atx1 in yeast cells have given profound insight into the mechanism involved in copper transfer from the chaperone to its target partner Ccc2. In the docking mechanism proposed by Huffman and colleagues [9], Cu(I)-Atx1 docks transiently with the apoCcc2a and causes a specific orientation to occur between the chaperone and the target partner that allows strategic positioning of the Cu(I) center for nucleophilic attack by the adjacent protein forming an intermediate Cu-(S-Cys) 3. In this way, copper partitions between two metal binding sites in the protein-protein complex, following the formation of two and three-coordinate copper thiolate intermediates. The complex finally dissociates to form the apoAtx1 and Cu-Ccc2a.

Recent studies using HAH1 confer with the Atx1 copper transfer mechanism. The crystal structure of HAH1 that was elucidated in the presence of Cu(I), Hg(II) and Cd(II) shows a metal-bridged homodimer by three to four cysteine ligands from two monomers [70]. The intermonomer bonding is stabilized by both the hydrogen bonding network and other metal ion holding the HAH1 monomers intact.

#### **7.1.9 HAH1 and Human Wilson Protein Domain 4 (WLN4)**

The role of metal binding domains, especially how the domains interact with each other and with the metal ion, is becoming a subject of intense study. The Ccc2 ATPase in yeast possesses two metal binding sites which interact with Atx1. However, in humans the Menkes and Wilson Protein ATPases display six metal binding domains which are similar to that of the HAH1 metallochaperone [9].

ATPases have similar role in pumping copper to the *trans*-Golgi network and further incorporation into the target enzymes. The Ccc2 is a cation ATPase that pumps copper into vesicles to be incorporated into the multicopper oxidase Fet3 that is involved in iron uptake. The N-terminus (Met1-Ser258) encloses two copper-binding domains. Experiments with yeast two-hybrid assays show that Atx1 interacts with each of the domains in the presence of copper [58, 73]. Studies *in vitro* have shown that the first domain of Ccc2 can exchange copper independently with Atx1 [74]. Since only two metal binding sites in Ccc2 play a similar significant role in Menkes and Wilson proteins, it means that the additional metal binding sites in the

latter protein are either redundant or are involved in some other function in the copper transfer mechanism.

The Menkes second domain (MNK2) provided an insight into the structure of individual domains and copper transfer in humans.  $^1\text{H}$  and  $^{15}\text{N}$  heteronuclear NMR spectroscopy of the reduced form of the MNK2 showed that the metal binding sites are found within an exposed loop and that binding of copper causes structural changes in the conserved residues near the binding sites [75, 76]. It was recently reported that HAH1 and first domain of Menkes protein (MNK1) formed Cu(I) metal complex with a stoichiometry of 1:1:1 [77]. This complex was in fast exchange with the free proteins in solution. MK1 and MNK4 are the primary targets for HAH1 in a study with all the size domains of ATP7A [78].

The second domain of the Wilson disease protein (WLN2) was cited as the domain that accepts copper from Atox1 and subsequently, activation the catalytic activity of the protein [79, 80]. The HAH1 protein domain can exchange copper with both WLN2 and WLN4 of Wilson disease protein [81]. Studies on the metal binding domains 1-4 and 5-6 gave insight into the roles of individual domains in ATP7B in human cells [82]. Here, copper binding to the Wilson disease protein stimulated the catalytic activity of this protein as earlier observed with the yeast system. Both the fifth (WLN5) and sixth (WLN6) domains of Wilson disease protein are critical in regulating the affinity of the intramembrane binding sites. The study showed that domains 1-4 in the normal, mutated and deleted forms do not affect the catalytic

activity of Wilson disease protein and they seem to be redundant in copper stimulation or in catalytic phosphorylation of Cu-ATPase.

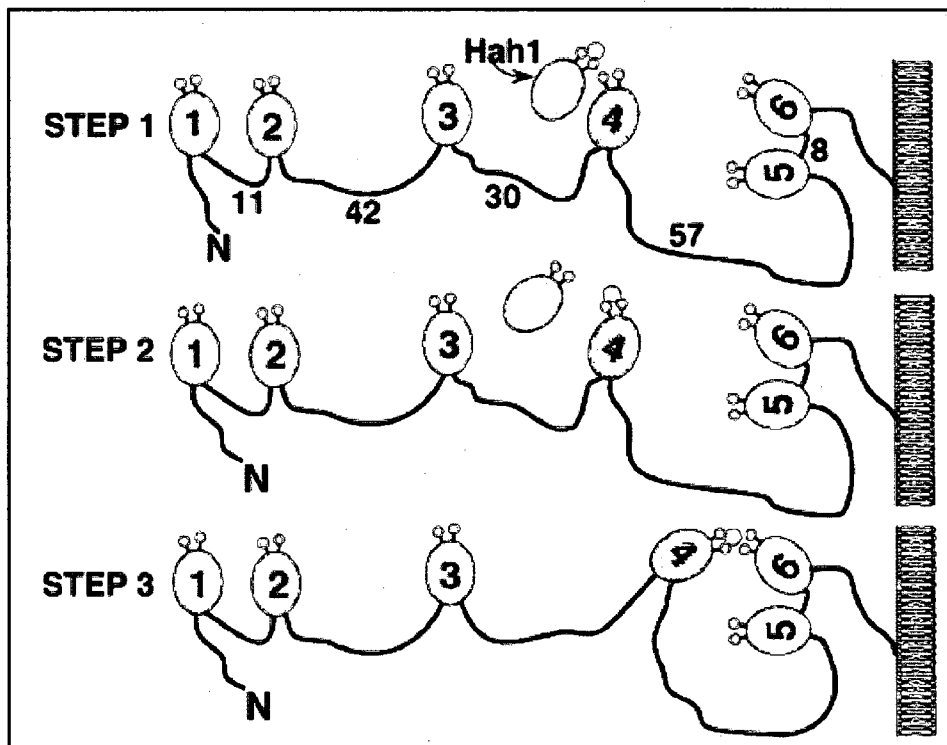
#### **7.1.10 Domain–Domain Interaction and Copper Transfer**

Achila and colleagues presented a model for copper transfer from the HAH1 to the N-terminal domain of the Wilson disease protein and finally to the *trans*-Golgi network in the cell [81]. The model proposed, based on the NMR spectroscopy and copper titration data, depicts the fourth domain, WLN4, playing a central role in the transfer of copper from HAH1 to the sixth domain and finally to the fifth metal binding domain of the Wilson disease protein. The study demonstrated that the strength of the interaction between WLN4 and HAH1 is stronger than other domains of the Wilson disease protein. The WLN4 domain was the first to be characterized in the presence of Cu(I) and Ag I in Menkes disease [67].

WLN4 has the lowest isoelectric point of 3.85 [83]. This domain was capable of exchanging Cu(I) with WLN1, which has highest isoelectric point of 6.77 in the N-terminal domains [83]. This further demonstrated that individual N-terminal domains of WNDP can communicate with another to transfer copper to the lumen of the *trans*-Golgi network. WLN5 and WLN6 are attached together through a short peptide linker. These two domains were expressed together as WLN5-6 [81].

The WLN5-6 domain is the closest to the membrane and was found in most studies to have a high degree of sequence conservation, from yeast to human. It could be involved in copper(I) transfer to the lumen of the membrane. A model proposed

involving copper exchange from HAH1 and the domains of Wilson disease protein is shown in Figure 7.6. Here, the length of the peptide linker in the adjacent domains surrounding WLN4 is longer than those furthest from the same domain, which can possibly allow for efficient copper transfer.



**Figure 7.6** Proposed model of copper transfer from Atox1 to ATPase [81].

The interactions between the metallochaperones and their target ATPase are critical in maintaining the levels of cations in the cell. These proteins sense and respond to copper concentrations in the cytoplasm. The metal binding sites are conserved in both the chaperone and the ATPase. This is significant in the transfer of copper ions from the donor (chaperone) to the acceptor target protein. In humans, the interaction between the holo-HAH1 chaperone and the apo-WLN4 in the transport of Cu(I) shows specificity and affinity required in this process. It also opens up a wide array of studies to understand protein-protein interactions and metal coordination in biology.

Recently, titration of the Cu(I)-HAH1 with apo-WLN4 showed a complex formation between HAH1 and WLN4 in fast exchange equilibrium [84]. Two hybrid assays with domains from 1 to 4 of Wilson protein confer with these studies [73, 85]. The distal domain binding sites WLN1-4 regulate the binding of copper to WLN5 and WLN6 and thus alter the affinity of the intramembrane sites and catalytic activity of the ATP7B. The WLN1-4 domains of Wilson disease protein interact with each other and the ATP-binding domains in the absence of copper and decrease the protein activity. Binding of copper or deletion of the domains relieves the interaction and thus accelerates catalysis [37, 82].

The structures of both apo and Cu(I) loaded WLN3-4 forms were resolved by NMR spectroscopy [86]. These domains were found independent of one another and have flexible loops. They can be loaded with Cu(I) either from solvent acetonitrile or from Cu(I)-HAH1 and were found to bind two Cu(I) ions with similar affinities. The



copper binding sites are found located far from each other and copper binding does not affect protein structure [67, 81, 86]. It is also established that, upon copper binding to the N-terminal ATPase, the linkers between the WLN3-4 and WLN2-3 regions are exposed, while those between the WLN1-2 and WLN4-5 are protected. The flexible loops connecting WLN3 and WLN4 are targets for kinase phosphorylation [67, 87]. Recent data and experimental conditions have shown that in the presence of Cu(I)-HAH1 domains 1, 2 and 4 are different from domains 3, 5 and 6 [88]. This suggests that these domains have different mechanistic behavior in the transfer of copper(I) from the metallochaperone HAH1 to the Wilson protein.

Put together, each domain of the Wilson disease protein is involved either directly or indirectly in the transfer of Cu(I) from the Atox1 to the ATPase. This mechanism could be of fundamental interest in understanding Wilson disease.

#### **7.1.11 Significance of this Study**

This study is designed to gain insight into transient interactions between WLN4 and the Atox1 chaperone. The data obtained could be useful in understanding in greater detail the role of the Wilson disease protein in copper transport. Various studies have been conducted with WLN1-4, WLN3-4 and WLN5-6. These studies have already established distinct functional roles of the N-terminal Wilson disease protein in Cu(I) transfer.

The interaction between Cu(I)-Atox1 and WLN4 in copper transfer presents a good model and good opportunity to study transient protein-protein interactions and

metal coordination chemistry connected to metal ion metabolism in humans. Furthermore, these studies will provide a platform to understand behavior of molecules at a single molecule level.

Proof of concept was recently demonstrated by single molecule studies involving fluorescence resonance energy transfer and nanovesicle trapping of the interaction between Atox1 and WLN4 [89]. Metal complexation with the WLN4 that is possible with other metals apart from copper can be elucidated by different techniques such as gel filtration chromatography-light scattering. The data provided will advance our current knowledge, not only in metal coordination chemistry, but will also help in understanding Wilson disease and Menkes disease that is affecting a great number of human populations.

#### **7.1.12 Objectives of the Study**

The general objectives of the study presented here were to understand the mechanism behind copper transfer by the Wilson disease protein (ATP7B) and the metallochaperones involved in the process. The study was specifically meant to understand the role played by the fourth domain (WLN4) that is widely implicated in accepting copper(I) ions from the Atox1 metallochaperone and transfers the same copper to other domains of the ATP7B. To achieve these objectives, the WLN4 protein was over-expressed in bacteria cells. This protein was characterized by biochemical and biophysical techniques. The results will be presented in this thesis in Chapter 9.

## 7.2 References

- 1 Linder, M. C. and Hazegh-Azam, M. (1996) Copper biochemistry and molecular biology. *Am J Clin Nutr* **63**, 797S-811S
- 2 Pena, M. M., Lee, J. and Thiele, D. J. (1999) A delicate balance: homeostatic control of copper uptake and distribution. *J Nutr* **129**, 1251-1260
- 3 Finney, L. A. and O'Halloran, T. V. (2003) Transition metal speciation in the cell: insights from the chemistry of metal ion receptors. *Science* **300**, 931-936
- 4 Hamza, I. and Gitlin, J. D. (2002) Copper chaperones for cytochrome c oxidase and human disease. *J Bioenerg Biomembr* **34**, 381-388
- 5 Eicken, C., Krebs, B. and Sacchettini, J. C. (1999) Catechol oxidase - structure and activity. *Curr Opin Struct Biol* **9**, 677-683
- 6 Rae, T. D., Schmidt, P. J., Pufahl, R. A., Culotta, V. C. and O'Halloran, T. V. (1999) Undetectable intracellular free copper: the requirement of a copper chaperone for superoxide dismutase. *Science* **284**, 805-808
- 7 Vulpe, C. D. and Packman, S. (1995) Cellular copper transport. *Annu Rev Nutr* **15**, 293-322
- 8 Stohs, S. J. and Bagchi, D. (1995) Oxidative mechanisms in the toxicity of metal ions. *Free Radic Biol Med* **18**, 321-336
- 9 Huffman, D. L. and O'Halloran, T. V. (2001) Function, structure, and mechanism of intracellular copper trafficking proteins. *Annu Rev Biochem* **70**, 677-701
- 10 Rosenzweig, A. C. (2001) Copper delivery by metallochaperone proteins. *Acc Chem Res* **34**, 119-128

- 11 Tumer, Z. and Horn, N. (1997) Menkes disease: recent advances and new aspects. *J Med Genet* **34**, 265-274
- 12 Cao, X., Antonyuk, S. V., Seetharaman, S. V., Whitson, L. J., Taylor, A. B., Holloway, S. P., Strange, R. W., Doucette, P. A., Valentine, J. S., Tiwari, A., Hayward, L. J., Padua, S., Cohlberg, J. A., Hasnain, S. S. and Hart, P. J. (2008) Structures of the G85R variant of SOD1 in familial amyotrophic lateral sclerosis. *J Biol Chem* **283**, 16169-16177
- 13 Macreadie, I. G. (2008) Copper transport and Alzheimer's disease. *Eur Biophys J* **37**, 295-300
- 14 Klevay, L. M. (2008) Alzheimer's disease as copper deficiency. *Med Hypotheses* **70**, 802-807
- 15 Cox, D. W. (1997) Review: molecular approaches to inherited liver disease. Focus on Wilson disease. *J Gastroenterol Hepatol* **12**, S251-255
- 16 Schaefer, M., Hopkins, R. G., Failla, M. L. and Gitlin, J. D. (1999) Hepatocyte-specific localization and copper-dependent trafficking of the Wilson's disease protein in the liver. *Am J Physiol* **276**, G639-646
- 17 Sarkar, B. (2000) Copper transport and its defect in Wilson disease: characterization of the copper-binding domain of Wilson disease ATPase. *J Inorg Biochem* **79**, 187-191
- 18 O'Halloran, T. V. and Culotta, V. C. (2000) Metallochaperones, an intracellular shuttle service for metal ions. *J Biol Chem* **275**, 25057-25060
- 19 Compston, A. (2009) Progressive lenticular degeneration: a familial nervous disease associated with cirrhosis of the liver, by S. A. Kinnier Wilson, (From the National Hospital, and the Laboratory of the National Hospital, Queen Square, London) *Brain* 1912: 34; 295-509. *Brain* **132**, 1997-2001
- 20 Wilson, S. A. K. (1912) Progressive lenticular degeneration: A familial nervous disease associated with cirrhosis of the liver. *Brain* **34**, 295-509

- 21 Liu, M., Cohen, E. J., Brewer, G. J. and Laibson, P. R. (2002) Kayser-Fleischer ring as the presenting sign of Wilson disease. *Am J Ophthalmol* **133**, 832-834
- 22 Mak, C. M. and Lam, C. W. (2008) Diagnosis of Wilson's disease: a comprehensive review. *Crit Rev Clin Lab Sci* **45**, 263-290
- 23 Wan, L., Tsai, C. H., Tsai, Y., Hsu, C. M., Lee, C. C. and Tsai, F. J. (2006) Mutation analysis of Taiwanese Wilson disease patients. *Biochem Biophys Res Commun* **345**, 734-738
- 24 Scheinberg, I. H. and Gitlin, D. (1952) Deficiency of ceruloplasmin in patients with hepatolenticular degeneration (Wilson's disease). *Science* **116**, 484-485
- 25 Scheinberg, I. (1963) Ceruloplasmin test for Wilson's disease. *Pediatrics* **31(1) Pt 1**, 160-161
- 26 Hellman, N. E. and Gitlin, J. D. (2002) Ceruloplasmin metabolism and function. *Annu Rev Nutr* **22**, 439-458
- 27 Palmgren, M. G. and Axelsen, K. B. (1998) Evolution of P-type ATPases. *Biochim Biophys Acta* **1365**, 37-45
- 28 Sweadner, K. J. and Donnet, C. (2001) Structural similarities of Na,K-ATPase and SERCA, the Ca(2+)-ATPase of the sarcoplasmic reticulum. *Biochem J* **356**, 685-704
- 29 Moller, J. V., Juul, B. and le Maire, M. (1996) Structural organization, ion transport, and energy transduction of P-type ATPases. *Biochim Biophys Acta* **1286**, 1-51
- 30 Lutsenko, S. and Kaplan, J. H. (1995) Organization of P-type ATPases: significance of structural diversity. *Biochemistry* **34**, 15607-15613

- 31 La Fontaine, S. and Mercer, J. F. (2007) Trafficking of the copper-ATPases, ATP7A and ATP7B: role in copper homeostasis. *Arch Biochem Biophys* **463**, 149-167
- 32 de Bie, P., Muller, P., Wijmenga, C. and Klomp, L. W. (2007) Molecular pathogenesis of Wilson and Menkes disease: correlation of mutations with molecular defects and disease phenotypes. *J Med Genet* **44**, 673-688
- 33 Voskoboinik, I., Mar, J. and Camakaris, J. (2003) Mutational analysis of the Menkes copper P-type ATPase (ATP7A). *Biochem Biophys Res Commun* **301**, 488-494
- 34 Dmitriev, O., Tsivkovskii, R., Abildgaard, F., Morgan, C. T., Markley, J. L. and Lutsenko, S. (2006) Solution structure of the N-domain of Wilson disease protein: distinct nucleotide-binding environment and effects of disease mutations. *Proc Natl Acad Sci U S A* **103**, 5302-5307
- 35 Suzuki, M. and Gitlin, J. D. (1999) Intracellular localization of the Menkes and Wilson's disease proteins and their role in intracellular copper transport. *Pediatr Int* **41**, 436-442
- 36 Tsivkovskii, R., MacArthur, B. C. and Lutsenko, S. (2001) The Lys1010-Lys1325 fragment of the Wilson's disease protein binds nucleotides and interacts with the N-terminal domain of this protein in a copper-dependent manner. *J Biol Chem* **276**, 2234-2242
- 37 Tsivkovskii, R., Eisses, J. F., Kaplan, J. H. and Lutsenko, S. (2002) Functional properties of the copper-transporting ATPase ATP7B (the Wilson's disease protein) expressed in insect cells. *J Biol Chem* **277**, 976-983
- 38 Hsi, G. and Cox, D. W. (2004) A comparison of the mutation spectra of Menkes disease and Wilson disease. *Hum Genet* **114**, 165-172
- 39 Okada, T., Morise, T., Takeda, Y. and Mabuchi, H. (2000) A new variant deletion of a copper-transporting P-type ATPase gene found in patients with Wilson's disease presenting with fulminant hepatic failure. *J Gastroenterol* **35**, 278-283

- 40 Barnes, N., Tsivkovskii, R., Tsivkovskaia, N. and Lutsenko, S. (2005) The copper-transporting ATPases, menkes and wilson disease proteins, have distinct roles in adult and developing cerebellum. *J Biol Chem* **280**, 9640-9645
- 41 Payne, A. S., Kelly, E. J. and Gitlin, J. D. (1998) Functional expression of the Wilson disease protein reveals mislocalization and impaired copper-dependent trafficking of the common H1069Q mutation. *Proc Natl Acad Sci U S A* **95**, 10854-10859
- 42 Hung, I. H., Suzuki, M., Yamaguchi, Y., Yuan, D. S., Klausner, R. D. and Gitlin, J. D. (1997) Biochemical characterization of the Wilson disease protein and functional expression in the yeast *Saccharomyces cerevisiae*. *J Biol Chem* **272**, 21461-21466
- 43 Terada, K., Nakako, T., Yang, X. L., Iida, M., Aiba, N., Minamiya, Y., Nakai, M., Sakaki, T., Miura, N. and Sugiyama, T. (1998) Restoration of holoceruloplasmin synthesis in LEC rat after infusion of recombinant adenovirus bearing WND cDNA. *J Biol Chem* **273**, 1815-1820
- 44 Cater, M. A., Forbes, J., La Fontaine, S., Cox, D. and Mercer, J. F. (2004) Intracellular trafficking of the human Wilson protein: the role of the six N-terminal metal-binding sites. *Biochem J* **380**, 805-813
- 45 Klomp, A. E., Juijn, J. A., van der Gun, L. T., van den Berg, I. E., Berger, R. and Klomp, L. W. (2003) The N-terminus of the human copper transporter 1 (hCTR1) is localized extracellularly, and interacts with itself. *Biochem J* **370**, 881-889
- 46 Solioz, M. (2002) Role of proteolysis in copper homeostasis. *Biochem Soc Trans* **30**, 688-691
- 47 Weiss, K. H., Lozoya, J. C., Tuma, S., Gotthardt, D., Reichert, J., Eehalt, R., Stremmel, W. and Fullekrug, J. (2008) Copper-induced translocation of the Wilson disease protein ATP7B independent of Murr1/COMMD1 and Rab7. *Am J Pathol* **173**, 1783-1794

- 48 Pilankatta, R., Lewis, D., Adams, C. M. and Inesi, G. (2009) High yield heterologous expression of wild-type and mutant Cu<sup>+</sup>-ATPase (ATP7B, Wilson disease protein) for functional characterization of catalytic activity and serine residues undergoing copper-dependent phosphorylation. *J Biol Chem* **284**, 21307-21316
- 49 Fan, Y., Yu, L., Han, Y., Ren, M., Yang, R. and Zhao, S. (2004) Identification of three novel insertion/deletion mutations in Wilson disease's gene. *Biochem Genet* **42**, 377-384
- 50 Lutsenko, S., Efremov, R. G., Tsivkovskii, R. and Walker, J. M. (2002) Human copper-transporting ATPase ATP7B (the Wilson's disease protein): biochemical properties and regulation. *J Bioenerg Biomembr* **34**, 351-362
- 51 Rodriguez-Granillo, A., Crespo, A. and Wittung-Stafshede, P. (2009) Conformational dynamics of metal-binding domains in Wilson disease protein: molecular insights into selective copper transfer. *Biochemistry* **48**, 5849-5863
- 52 Yatsunyk, L. A. and Rosenzweig, A. C. (2007) Cu(I) binding and transfer by the N terminus of the Wilson disease protein. *J Biol Chem* **282**, 8622-8631
- 53 Efremov, R. G., Kosinsky, Y. A., Nolde, D. E., Tsivkovskii, R., Arseniev, A. S. and Lutsenko, S. (2004) Molecular modelling of the nucleotide-binding domain of Wilson's disease protein: location of the ATP-binding site, domain dynamics and potential effects of the major disease mutations. *Biochem J* **382**, 293-305
- 54 Forbes, J. R. and Cox, D. W. (1998) Functional characterization of missense mutations in ATP7B: Wilson disease mutation or normal variant? *Am J Hum Genet* **63**, 1663-1674
- 55 Thomas, G. R., Roberts, E. A., Walshe, J. M. and Cox, D. W. (1995) Haplotypes and mutations in Wilson disease. *Am J Hum Genet* **56**, 1315-1319
- 56 Harris, E. D. (2000) Cellular copper transport and metabolism. *Annu Rev Nutr* **20**, 291-310



- 57 Dancis, A., Haile, D., Yuan, D. S. and Klausner, R. D. (1994) The *Saccharomyces cerevisiae* copper transport protein (Ctr1p). Biochemical characterization, regulation by copper, and physiologic role in copper uptake. *J Biol Chem* **269**, 25660-25667
- 58 Lin, S. J., Pufahl, R. A., Dancis, A., O'Halloran, T. V. and Culotta, V. C. (1997) A role for the *Saccharomyces cerevisiae* ATX1 gene in copper trafficking and iron transport. *J Biol Chem* **272**, 9215-9220
- 59 Rosenzweig, A. C. (2002) Metallochaperones: bind and deliver. *Chem Biol* **9**, 673-677
- 60 Lin, S. J. and Culotta, V. C. (1995) The ATX1 gene of *Saccharomyces cerevisiae* encodes a small metal homeostasis factor that protects cells against reactive oxygen toxicity. *Proc Natl Acad Sci U S A* **92**, 3784-3788
- 61 Klomp, L. W., Lin, S. J., Yuan, D. S., Klausner, R. D., Culotta, V. C. and Gitlin, J. D. (1997) Identification and functional expression of HAH1, a novel human gene involved in copper homeostasis. *J Biol Chem* **272**, 9221-9226
- 62 Hung, I. H., Casareno, R. L., Labesse, G., Mathews, F. S. and Gitlin, J. D. (1998) HAH1 is a copper-binding protein with distinct amino acid residues mediating copper homeostasis and antioxidant defense. *J Biol Chem* **273**, 1749-1754
- 63 Zhou, B. and Gitschier, J. (1997) hCTR1: a human gene for copper uptake identified by complementation in yeast. *Proc Natl Acad Sci U S A* **94**, 7481-7486
- 64 Pufahl, R. A., Singer, C. P., Peariso, K. L., Lin, S. J., Schmidt, P. J., Fahrni, C. J., Culotta, V. C., Penner-Hahn, J. E. and O'Halloran, T. V. (1997) Metal ion chaperone function of the soluble Cu(I) receptor Atx1. *Science* **278**, 853-856
- 65 Huffman, D. L., Utschig, L. M. and O'Halloran, T. V. (1997) Mercury-responsive gene regulation and mercury-199 as a probe of protein structure. *Met Ions Biol Syst* **34**, 503-526

- 66 Rosenzweig, A. C., Huffman, D. L., Hou, M. Y., Wernimont, A. K., Pufahl, R. A. and O'Halloran, T. V. (1999) Crystal structure of the Atx1 metallochaperone protein at 1.02 Å resolution. *Structure* **7**, 605-617
- 67 Gitschier, J., Moffat, B., Reilly, D., Wood, W. I. and Fairbrother, W. J. (1998) Solution structure of the fourth metal-binding domain from the Menkes copper-transporting ATPase. *Nat Struct Biol* **5**, 47-54
- 68 Wernimont, A. K., Yatsunyk, L. A. and Rosenzweig, A. C. (2004) Binding of copper(I) by the Wilson disease protein and its copper chaperone. *J Biol Chem* **279**, 12269-12276
- 69 Wimmer, R., Herrmann, T., Solioz, M. and Wuthrich, K. (1999) NMR structure and metal interactions of the CopZ copper chaperone. *J Biol Chem* **274**, 22597-22603
- 70 Wernimont, A. K., Huffman, D. L., Lamb, A. L., O'Halloran, T. V. and Rosenzweig, A. C. (2000) Structural basis for copper transfer by the metallochaperone for the Menkes/Wilson disease proteins. *Nat Struct Biol* **7**, 766-771
- 71 Op't Holt, B. T. and Merz, K. M., Jr. (2007) Insights into Cu(I) exchange in HAH1 using quantum mechanical and molecular simulations. *Biochemistry* **46**, 8816-8826
- 72 Arnesano, F., Banci, L., Bertini, I. and Bonvin, A. M. (2004) A docking approach to the study of copper trafficking proteins; interaction between metallochaperones and soluble domains of copper ATPases. *Structure* **12**, 669-676
- 73 van Dongen, E. M., Klomp, L. W. and Merckx, M. (2004) Copper-dependent protein-protein interactions studied by yeast two-hybrid analysis. *Biochem Biophys Res Commun* **323**, 789-795
- 74 Huffman, D. L. and O'Halloran, T. V. (2000) Energetics of copper trafficking between the Atx1 metallochaperone and the intracellular copper transporter, Ccc2. *J Biol Chem* **275**, 18611-18614

- 75 Jones, C. E., Daly, N. L., Cobine, P. A., Craik, D. J. and Dameron, C. T. (2003) Structure and metal binding studies of the second copper binding domain of the Menkes ATPase. *J Struct Biol* **143**, 209-218
- 76 Banci, L., Bertini, I., Del Conte, R., D'Onofrio, M. and Rosato, A. (2004) Solution structure and backbone dynamics of the Cu(I) and apo forms of the second metal-binding domain of the Menkes protein ATP7A. *Biochemistry* **43**, 3396-3403
- 77 Banci, L., Bertini, I., Calderone, V., Della-Malva, N., Felli, I. C., Neri, S., Pavelkova, A. and Rosato, A. (2009) Copper(I)-mediated protein-protein interactions result from suboptimal interaction surfaces. *Biochem J* **422**, 37-42
- 78 Banci, L., Bertini, I., Cantini, F., Ciofi-Baffoni, S., Cavet, J. S., Dennison, C., Graham, A. I., Harvie, D. R. and Robinson, N. J. (2007) NMR structural analysis of cadmium sensing by winged helix repressor CmtR. *J Biol Chem* **282**, 30181-30188
- 79 Walker, J. M., Huster, D., Ralle, M., Morgan, C. T., Blackburn, N. J. and Lutsenko, S. (2004) The N-terminal metal-binding site 2 of the Wilson's Disease Protein plays a key role in the transfer of copper from Atox1. *J Biol Chem* **279**, 15376-15384
- 80 Yatsunyk, L. A. and Rosenzweig, A. C. (2007) Cu(I) binding and transfer by the N terminus of the Wilson disease protein. *J Biol Chem* **282**, 8622-8631
- 81 Achila, D., Banci, L., Bertini, I., Bunce, J., Ciofi-Baffoni, S. and Huffman, D. L. (2006) Structure of human Wilson protein domains 5 and 6 and their interplay with domain 4 and the copper chaperone HAH1 in copper uptake. *Proc Natl Acad Sci U S A* **103**, 5729-5734
- 82 Huster, D. and Lutsenko, S. (2003) The distinct roles of the N-terminal copper-binding sites in regulation of catalytic activity of the Wilson's disease protein. *J Biol Chem* **278**, 32212-32218

- 83 Bunce, J., Achila, D., Hetrick, E., Lesley, L. and Huffman, D. L. (2006) Copper transfer studies between the N-terminal copper binding domains one and four of human Wilson protein. *Biochim Biophys Acta* **1760**, 907-912
- 84 Achila, D., Banci, L., Bertini, I., Bunce, J., Ciofi-Baffoni, S. and Huffman, D. L. (2006) Structure of human Wilson protein domains 5 and 6 and their interplay with domain 4 and the copper chaperone HAH1 in copper uptake. *Proc Natl Acad Sci U S A* **103**, 5729-5734
- 85 Larin, D., Mekios, C., Das, K., Ross, B., Yang, A. S. and Gilliam, T. C. (1999) Characterization of the interaction between the Wilson and Menkes disease proteins and the cytoplasmic copper chaperone, HAH1p. *J Biol Chem* **274**, 28497-28504
- 86 Banci, L., Bertini, I., Cantini, F., Rosenzweig, A. C. and Yatsunyk, L. A. (2008) Metal binding domains 3 and 4 of the Wilson disease protein: solution structure and interaction with the copper(I) chaperone HAH1. *Biochemistry* **47**, 7423-7429
- 87 Bartee, M. Y., Ralle, M. and Lutsenko, S. (2009) The loop connecting metal-binding domains 3 and 4 of ATP7B is a target of a kinase-mediated phosphorylation. *Biochemistry* **48**, 5573-5581
- 88 Banci, L., Bertini, I., Cantini, F., Massagni, C., Migliardi, M. and Rosato, A. (2009) An NMR study of the interaction of the N-terminal cytoplasmic tail of the Wilson disease protein with copper(I)-HAH1. *J Biol Chem* **284**, 9354-9360
- 89 Benitez, J. J., Keller, A. M., Ochieng, P., Yatsunyk, L. A., Huffman, D. L., Rosenzweig, A. C. and Chen, P. (2008) Probing Transient Copper Chaperone-Wilson Disease Protein Interactions at the Single-Molecule Level with Nanovesicle Trapping. *J Am Chem Soc*

## CHAPTER 8

### EXPERIMENTAL METHODS AND PROCEDURES

#### 8.1 Reagents

##### 8.1.1 Plasmid Vector and Bacterial Cells

A plasmid construct pET-32Xa/LIC expression vector that encoded the fourth domain of the Wilson disease protein gene (WLN4) was available in the laboratory of Dr. David Huffman in the Chemistry Department at Western Michigan University. The pET expression system was originally designed by Studier and his group as efficient for mass production of proteins from host *Escherichia coli* (*E. coli*) bacteria [1]. This pET system was used for protein expression of WLN4.

The plasmid vector pET-32Xa/LIC/WLN4 was propagated in sufficient quantity for use in the subsequent studies. The bacterial strains and DNA plasmids were all purchased from Novagen®. NovaBlue GigaSingle™ competent cells (Cat. No. 71227) were used for plasmid DNA storage while Rosetta (DE3) strains (Cat. No. 70954) were used in the protein expression of WLN4. QIAGEN plasmid DNA isolation and purification kits (Cat. No. 12162) were purchased from QIAGEN Inc.

### 8.1.2 Chemicals and Apparatus

Dimethyl sulfoxide (DMSO) solvent (# 7033), mono (# 0307) and dibasic (# 0305) sodium phosphate salts were purchased from the J.T. Baker Chemical company. Isopropyl-s-D-thiogalactopyranoside (IPTG) for protein induction was obtained from Inalco Pharmaceuticals (#1758-1400). Agarose powder (#15510-019) was purchased from Invitrogen. BugBuster<sup>®</sup> protein extraction reagent (#70584-4) was from Novagen<sup>®</sup>. Tryptone was from MO BIO Laboratories Inc. (#12111-1), sodium chloride (#BP330-1), yeast extract (#7264672), dextrose (#BP350-1) and MES (2-(4-morpholino)-ethane sulphonic acid, (#BP300-100) were purchased from Fischer Scientific. Ampicillin antibiotic (#A-9518) and Bacto-Agar (#214010) were from Difco Laboratories. Bio-Rad dye (#500-0006) used for the Bradford assay was obtained from Bio-Rad Laboratories (Hercules, CA). Coomassie blue reagent dye (#B-0149) for SDS-PAGE analysis was obtained from Pierce Protein Research Products. HiLoad<sup>™</sup> Superdex<sup>™</sup> 75 26/60 gel filtration column (Code # 17-1070-01) (Pharmacia Biotech) was used in gel filtration. HisPrep<sup>™</sup> FF 16/10 (#17-5256-01) (GE Healthcare) was used for affinity based gel filtration. Filtration membranes for concentrating protein used with the Amicon ultra filtration device all were purchased from Millipore Corporation (Billerica, MA, USA).

### 8.1.3 Components of pET-32Xa/LIC Plasmid Vector

The arrangement of the various components of the pET-32Xa/LIC is shown in Figure 8.1. This plasmid is designed for the expression of recombinant proteins as fusions with thioredoxin and a His-tag<sup>TM</sup> for purification.

The plasmid has the Ampicillin resistance gene (Amp<sup>®</sup> gene) that confers resistance to the ampicillin antibiotic. The DNA coding sequence for WLN4 was inserted behind the His-tag sequence.

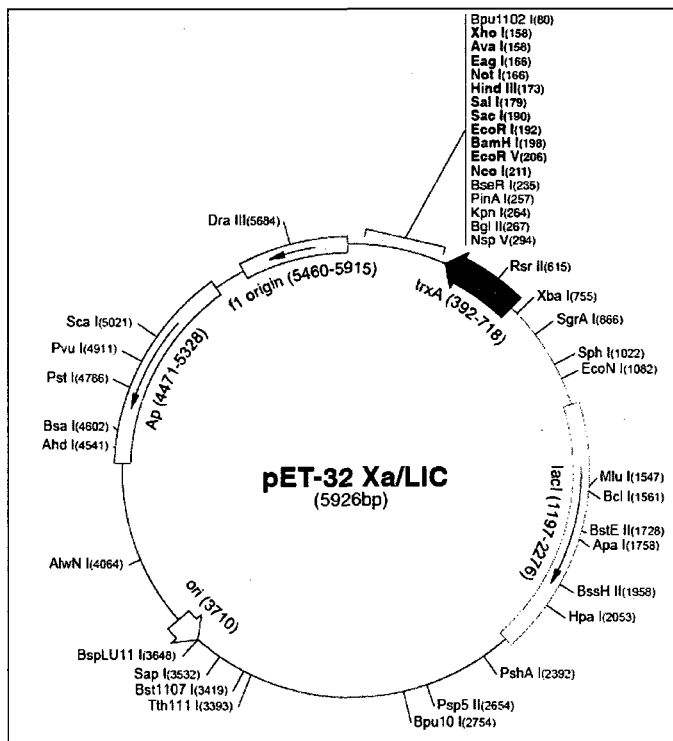


Figure 8.1 Map of plasmid vector pET32XaLIC [2].

## 8.2 Transformation of pET-32Xa/LIC/WLN4

Plasmid vector pET-32Xa/LIC/WLN4 containing the gene coding for WLN4 was transformed into NovaBlue GigaSingle *E. coli* competent cells. 200  $\mu$ L aliquots of these cells normally stored in a  $-80^{\circ}\text{C}$  freezer were retrieved and thawed on ice for approximately 5 min. The cells were gently mixed after thawing using a pipette tip to ensure they were evenly suspended. 1  $\mu$ L of 90 ng of pET32Xa/LIC/WLN4 was added to the cells above and mixed. 3  $\mu$ L of DMSO was added to the mix and cells were left on ice for a further 15 min.

The cells were heat shocked at  $42^{\circ}\text{C}$  for 45 sec and cooled on ice for additional 2 min. 1 mL of SOC media was added to the cells and incubated for 1 hr at  $37^{\circ}\text{C}$ . The incubated cells were subjected to centrifugation force in a desktop centrifuge at 14000g for 60 sec. 1 mL of supernatant was discarded while the remainder was used to suspend the bacterial cells. These cells were plated on Luria Bertini broth (LB) agar plates. The plates were prepared with a 100  $\mu\text{g}/\text{mL}$  ampicillin antibiotic for bacterial cell selection. The plates were kept at  $4^{\circ}\text{C}$ . These plates were equilibrated before use at  $37^{\circ}\text{C}$  in the oven for 30 min. 20  $\mu$ L of the cell suspensions spread on the LB media using a sterilized bent glass rod spreader. The bench top was earlier cleaned thoroughly and wiped with 20% ethanol solution. The plates were placed in a  $37^{\circ}\text{C}$  oven upside down exposed for 5 min and then closed and flipped to incubate overnight.

The plates with bacterial colonies were retrieved from the oven the following day. A few colonies were selected and put in a 10 mL starter autoclaved LB culture



(10.0 g tryptone, 10.0 g NaCl, 5.0 g yeast extract, 1 L of RO 18 M $\Omega$ /cm water) in 37°C incubator rotating at 250 rpm for 1 hr. The cells were used for plasmid DNA recovery using a QIAGEN QIAprep Spin miniprep Kit as described by the supplier. The plasmid was obtained in large quantity. Plasmid recovery was tested using agarose gel electrophoresis as described in Section 8.2.1.

### **8.2.1 Agarose Gel Electrophoresis**

A 0.8% (w/v) agarose gel was prepared for plasmid DNA separation. 0.32 grams of agarose powder was weighed in a 250 mL Erlenmeyer flask and mixed and swirled with 40 mL 1x Tris- Borate –EDTA (TBE) buffer, pH 8.0. The container was heated in a microwave for 1 min until all the agarose was dissolved in the buffer. The molten agarose was cooled to 60°C before being poured in agarose gel slab containing a sample comb. The gel was allowed to solidify at room temperature for 30 min. The gel was immersed in the TAE buffer such that the side with the comb was facing on the cathode.

The DNA samples were prepared as follows: 1  $\mu$ L of pET-32Xa/LIC/WLN4 plasmid was mixed with 3  $\mu$ L of sample loading buffer and 4  $\mu$ L of RO water 18 M $\Omega$  / cm. A 1 kilo base pair DNA ladder (part # N3232, NEB) was prepared in a similar manner. The sample was transferred to the well u and run alongside the DNA ladder. The gel was allowed to run for 1 hr and 15 min at 94 V. The gel was stained with 0.5  $\mu$ g/mL ethidium bromide solution for 15 min.

## **8.3 WLN4 Protein Expression**

### **8.3.1 Transformation**

The pET32-Xa/LIC/WLN4 plasmid obtained in Section 8.2 was used to express Wilson disease protein domain 4 (WLN4). The protein was expressed in Rosetta (DE3) bacterial *E. coli* cells. The plasmid was transformed in Rosetta (DE3) cells and plated on a LB media similar to the description in section 8.2. The plates contained 100 µg/ mL ampicillin. The antibiotic was used to select for the bacteria containing the plasmid of interest since the plasmid possess the Amp gene.

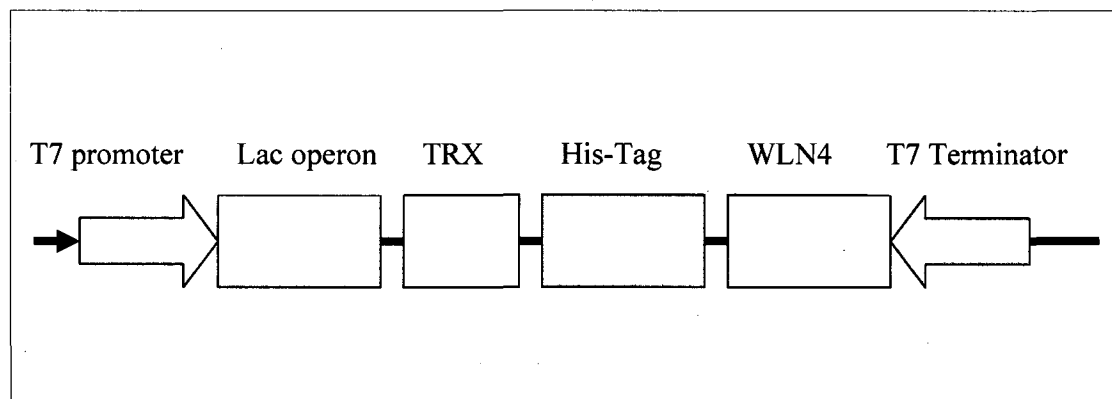
### **8.3.2 Induction and Expression WLN4 Protein**

Fresh colonies obtained in Section 8.3.1 were selected and cultured under a sterilized environment in 5 and 10 mL LB starter culture tubes containing ampicillin (100 µg/mL). The cells were grown in an incubator at 37°C at 250 rpm for 1 hr or until an optical density (OD) of approximately 0.6 was achieved. The solution was then transferred to 100 mL LB culture Erlenmeyer flask containing ampicillin (100 µg/mL). The cells were incubated at the same temperature and shaking speed until the OD was deemed sufficient to transfer to 1 L of growth culture. The 100 mL culture was transferred to 1 L of LB culture containing 1 mM ampicillin. This culture was set in an incubator at 37°C and 250 rpm. The OD was measured using a Beckman DU 7400 UV-Vis spectrophotometer at a wavelength of 600 nm. When the bacterial cells had grown to an OD of 0.6 or above, IPTG to a final concentration of 1 mM was

added to the cell suspension to induce protein expression in the bacteria using the bacteria transcription machinery. This took an average of 3 hrs.

Rosetta (DE3) cells have T7 polymerase in the lambda lysogen (DE3). This is under the control of Lac-UV5 operon. When the lactose analog, IPTG, is added to the LB media containing these cells, it binds to the lac repressor and induces its dissociation from the operator in the lac operon. This leads to transcription from the promoter region.

A cartoon representation of the transcription machinery of the T7 promoter of the vector is shown in Figure 8.2.



**Figure 8.2** A cartoon drawing showing the various parts of a vector.

After induction, a 1 mL sample was taken immediately and after every 1 hr to monitor progress of induction and protein expression. These samples were stored at -20°C for further sodium dodecyl sulphate polyacrylamide gel electrophoresis (SDS-PAGE) analysis. In SDS-PAGE, the proteins are separated based on size. The samples were analyzed in a 15% TRICINE SDS-PAGE. After 3 hr the 1 L cell culture was subjected to a Sorvall RC5B at 9000 rpm, for 20 min at 4°C to harvest the bacterial cells. The cell pellets were kept at -20°C for SDS-PAGE analysis and protein extraction by BugBuster<sup>®</sup> extraction reagent.

### **8.3.3 Extraction of Protein WLN4**

A number of protein extraction methods are currently available [3]. The expressed WLN4 protein was extracted from the bacterial cells by BugBuster<sup>®</sup> protein extraction reagent from Novagen. BugBuster<sup>®</sup> reagent is formulated to gently disrupt and break the bacterial cell wall and release target protein into the solution for further purification. This reagent was used as prescribed by the supplier. A 45 mL solution was obtained after the BugBuster<sup>®</sup> extraction procedure. It was filtered using a 0.22 µm nylon membrane filter before further subjecting to protein purification using His-tag column.

#### 8.4 Protein Purification

The plasmid vector pET-32Xa/LIC has a sequence encoding a six histidine residue peptide upstream of the target protein. This is expressed together with WLN4 as Trx- 6 His-WLN4 fusion protein.

Nickel-loaded Chelating Sepharose 200 (Pharmacia Biotech) column was rinsed with RO 18 M $\Omega$ /cm water and equilibrated with Buffer A (20 mM sodium phosphate, 20 mM imidazole, 500 mM NaCl, buffer pH 7.4). 15 ml of BugBuster<sup>®</sup> reagent cell extract was injected into the column and then the column was washed with Buffer A. WLN4-thioredoxin fusion protein was eluted from the column with an isocratic elution of 5 column volumes of Buffer B (20 mM sodium phosphate, 500 mM NaCl, 500 mM imidazole and pH 7.4). The fractions with the target protein were isolated and concentrated to a volume of 1.5 mL using 10,000 MW cutoff membrane filter fitted to an Amicon Ultra filtration Device from Millipore Corporation Inc. (Billerica, MA). A volume of 3 mL of the concentrated protein was injected into a desalting column connected to AKTA fast performance liquid chromatography (FPLC). This system is controlled by UNICORN software.

The desalting column was rinsed with RO 18 M $\Omega$ /cm water and equilibrated with Factor Xa buffer prepared in autoclaved RO 18 M $\Omega$ /cm water (0.1 M NaCl, 50 mM Tris, 5 mM CaCl<sub>2</sub>, buffer pH adjusted with HCl to pH 8.0). The protein was eluted with the same Factor Xa buffer. The fractions containing the WLN4 fusion tag protein were analyzed using the chromatogram and the purity by the SDS-PAGE. The

positive samples were pooled together to yield a volume of approximately 45 mL. This solution was subjected to Factor Xa cleavage as described in Section 8.4.1.

#### **8.4.1 Factor Xa Protease Cleavage**

The Factor Xa protease is a site specific endoprotease that cleaves a C-terminal peptide bond with a recognition sequence Ile-Glu-Gly-Arg [4, 5]. The pET-32Xa/LIC plasmid vector encodes a 6X His-tag followed by this recognition sequence. Therefore, it is possible to cleave the WLN4 protein by treating a purified 6X His-tagged protein with Factor Xa protease in Factor Xa buffer. Here, 45 ml of purified Trx-6 His- WLN4 fusion protein with a concentration of 4.7  $\mu\text{g}/\mu\text{L}$  was incubated at room temperature with a 50  $\mu\text{L}$  of 100 U of Factor Xa for 16 hours.

The protease was deactivated at room temperature by the addition of phenylmethanesulphonylfluoride (PMSF) in isopropanol to a final concentration 1 mM. A sample product was analyzed by SDS-PAGE and confirmed a successful cleavage. The samples containing the cleavage protein were concentrated in the presence of 0.5 mM EDTA and passed through Superdex 75 26/60 gel filtration column (Pharmacia Biotech)). The target protein WLN4 was eluted from the column with 20 mM sodium phosphate and 150 mM NaCl. The protein fractions were analyzed by the SDS-PAGE. The positive fractions were concentrated to about 2 mL using 10,000 MW cutoff membranes in an Amicon ultra centrifugation device. The purified WLN4 protein samples were transferred to 200  $\mu\text{L}$  aliquots and stored at -20°C.

#### **8.4.2 Protein Concentration**

The Bradford assay is based on the principle that the absorbance maximum for an acidic solution of Coomassie Brilliant Blue G-250 dye changes from 465 to 595 nm when it binds to a protein [6]. It forms a stable complex with a blue color change. The extinction coefficient of the complex is linear over a 10-fold concentration range.

The concentration of WLN4 purified samples were determined based on Bradford assay. A series of standards of BSA derived from a stock solution of 1.47 mL/mg BSA were prepared in a 96-well micro-plate. 10  $\mu$ L of each standard was transferred to each well and 100  $\mu$ L of dye reagent (a 1: 4 dilution of concentrate to water) was added to each aliquot and mixed using a pipette tip. WLN4 was prepared in the same manner. The plate was incubated in an oven at 37°C for 15 min. The absorbance was measured at 595 nm in a 96-well Benchmark Plus microplate reader (BIO-RAD).

#### **8.5 Static and Dynamic Light Scattering**

The molar mass and hydrodynamic radius of WLN4 was determined using both static and dynamic light scattering instruments at the W.M. Keck Facility at Yale University. WLN4 protein was characterized by gel filtration chromatography coupled in series to a multi-angle DAWN HELEOS laser light (658 nm) scattering instrument from Wyatt, Technology (Santa Barbara, CA). 100  $\mu$ L volume of 21 mg/mL of purified WLN4 in 20 mM sodium phosphate pH 7.4, 150 mM NaCl was sent to the W. M. Keck Facility at Yale University.

The column was pre-equilibrated with the sodium phosphate buffer pH 7.4 with a refractive index of 1.340 and viscosity of  $8.945 \times 10^{-3} \text{ gcm}^{-1}\text{sec}^{-1}$ . The protein was eluted from the column at a flow rate of 1.0 mL/min. The column was connected downstream to a multi-angle laser light scattering instrument and the concentration was determined using an Optilab rEx refractive index detector arranged in series. A value of 0.175 for the refractive index  $dn/dc$  was used. Molecular weights were determined using a Debye plot approximation model. Data were analyzed using Astra software (Wyatt Technology). A standard protein Bovine Serum Albumin (BSA) was analyzed alongside WLN4.

## 8.6 Circular Dichroism Measurements

Conformation stability, structure and unfolding characteristics of WLN4 were obtained using circular dichroism (CD) spectroscopy. Here, asymmetric molecules can absorb differently left and right circular polarized light. This has been used to estimate protein conformation [7, 8]. Different secondary structures ( $\alpha$ -helix,  $\beta$ -sheets and  $\beta$ -turns) have unique CD spectra [9]. The spectra in the far UV region are dominated by electronic transitions of the amide group [10]. It is influenced by the geometries of the polypeptide backbone of the protein. Therefore, the spectra are reflective of the secondary structures that are determined by the  $\Phi$  and  $\psi$  angles. The CD measurements were performed on a Jasco J-815 Spectrophotometer at Western Michigan University. This instrument was equipped with a peltier thermoelectric device and water circulating bath to cool the peltier. A rectangular quartz cuvette with



a 10 mm path length was used. Molar mean residue ellipticity values  $\theta$ , for all the wavelength scans, were expressed in degrees centimeter squared per decimeter according to Equation 8.0.

$$\theta = \frac{\theta_{obs} * 107}{10 * d * c} \quad [8.0]$$

In this equation,  $\theta_{obs}$  is observed ellipticity in degrees, 107 is the mean residue molar mass of WLN4 (72 amino acids, molar mass 7720 Daltons),  $c$  is the concentration of WLN4 (0.2 mM), and  $d$  is the path length in cm. Purified 2 mM WLN4 protein in 50 mM sodium phosphate, pH 7.4 was used in this experiment.

### 8.6.1 Chemical and Thermal Denaturation

Guanidine hydrochloride (GnHCl) was employed as a chemical denaturant. An 8M solution in sodium phosphate buffer, pH 7.4, was prepared and diluted accordingly. A series of guanidine hydrochloride concentrations from 1-6 M were used to determine stability and conformation of WLN4.

WLN4 was incubated with GnHCl at least 1 hr before spectral measurement. There were four measurements for every wavelength scan at 25°C. Thermal unfolding experiments were performed to monitor WLN4 thermal denaturation characteristics.

A denaturation transition curve was constructed from  $\theta$  at 222 nm versus the molar concentration of GnHCl. The free energy for unfolding of WLN4 was calculated assuming a two-state kinetic model following Equation 8.1.



In this equation, FF and FU are the fractions in the fully folded and denatured states. K is the equilibrium constant. The fraction FU of the WLN4 that was denatured was calculated assuming a two-state model following Equation 8.2. In a two state model, the sum of FF and FU equals 1 [11].

$$FU = \left( \frac{YF - Y}{YF - YU} \right) \quad [8.2]$$

In this equation, Y is the measured mean residue ellipticity at particular GnHCl concentration and temperature. YF and YU are the mean residue ellipticity of WLN4 in the native and fully unfolded states, respectively, under the same conditions. The fraction of WLN4 in the native state under similar conditions was calculated according to Equation 8.3.

$$FF = \left( \frac{Y - YU}{FY - YU} \right) \quad [8.3]$$

### 8.6.2 Free Energy of Unfolding

The free energy of unfolding of WLN4 protein was calculated based on Equation 8.4.

$$\Delta G = -RT \ln K = -8.314 * 298 K * \ln(FU / FF) \quad [8.4]$$

In this equation, R is the gas constants, K is the equilibrium constant,  $\Delta G$ , free energy change between folded and unfolded states of the protein and T is the temperature measured in Kelvin. The enthalpy change can be obtained from Equation 8.5.

$$\Delta G = \Delta H - T\Delta S \quad [8.5]$$

The enthalpy change is denoted by  $\Delta H$  and the change in entropy by  $\Delta S$ . The enthalpy change is a measure of the binding energy that largely contributed by the dispersion forces, van der Waals potential and hydrogen bonding. The entropic value given by  $\Delta S$  describes the hydrophobic interactions.

## 8.7 References

- 1 Studier, F. W. and Moffatt, B. A. (1986) Use of bacteriophage T7 RNA polymerase to direct selective high-level expression of cloned genes. *J Mol Biol* **189**, 113-130
- 2 LaVallie, E. R., DiBlasio, E. A., Kovacic, S., Grant, K. L., Schendel, P. F. and McCoy, J. M. (1993) A thioredoxin gene fusion expression system that circumvents inclusion body formation in the *E. coli* cytoplasm. *Biotechnology (N Y)* **11**, 187-193
- 3 De Mey, M., Lequeux, G. J., Maertens, J., De Muynck, C. I., Soetaert, W. K. and Vandamme, E. J. (2008) Comparison of protein quantification and extraction methods suitable for *E. coli* cultures. *Biologicals* **36**, 198-202
- 4 Nagai, K., Perutz, M. F. and Poyart, C. (1985) Oxygen binding properties of human mutant hemoglobins synthesized in *Escherichia coli*. *Proc Natl Acad Sci U S A* **82**, 7252-7255
- 5 Owen, W. G., Esmon, C. T. and Jackson, C. M. (1974) The conversion of prothrombin to thrombin. I. Characterization of the reaction products formed during the activation of bovine prothrombin. *J Biol Chem* **249**, 594-605
- 6 Bradford, M. M. (1976) A rapid and sensitive method for the quantitation of microgram quantities of protein utilizing the principle of protein-dye binding. *Anal Biochem* **72**, 248-254
- 7 Schneider, A. S., Schneider, M. J. and Rosenheck, K. (1970) Optical activity of biological membranes: scattering effects and protein conformation. *Proc Natl Acad Sci U S A* **66**, 793-798
- 8 Greenfield, N. and Fasman, G. D. (1969) Computed circular dichroism spectra for the evaluation of protein conformation. *Biochemistry* **8**, 4108-4116

- 9 Bazzi, M. D. and Woody, R. W. (1985) Oriented secondary structure in integral membrane proteins. I. Circular dichroism and infrared spectroscopy of cytochrome oxidase in multilamellar films. *Biophys J* **48**, 957-966
- 10 Whitmore, L. and Wallace, B. A. (2008) Protein secondary structure analyses from circular dichroism spectroscopy: methods and reference databases. *Biopolymers* **89**, 392-400
- 11 Jackson, S. E. and Fersht, A. R. (1991) Folding of chymotrypsin inhibitor 2. 1. Evidence for a two-state transition. *Biochemistry* **30**, 10428-10435

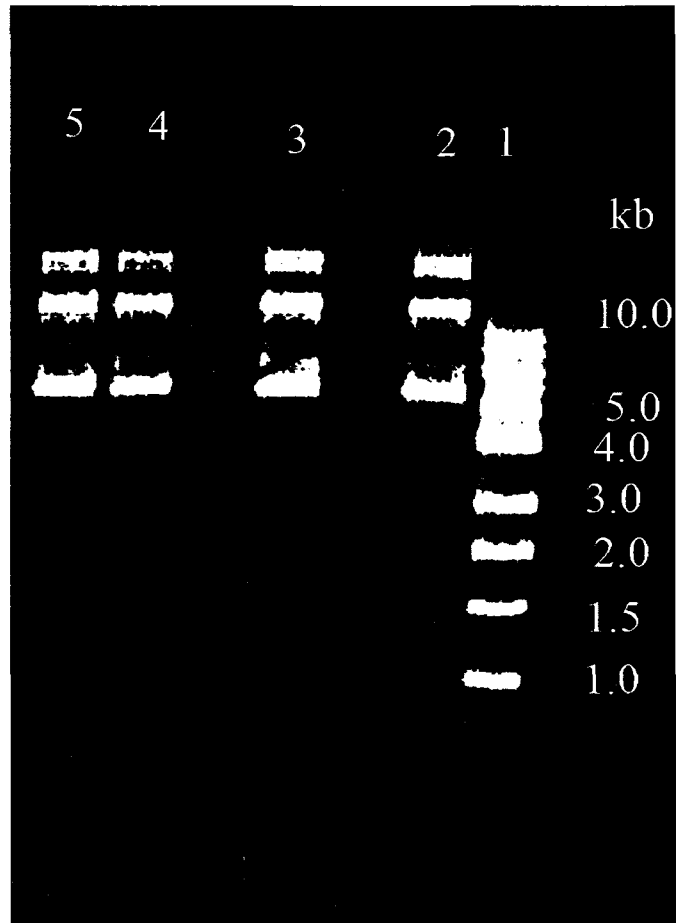
## CHAPTER 9

### RESULTS AND DISCUSSIONS

#### 9.1 Recovery of the Plasmid Vector

A construct containing the fourth domain of the Human Wilson protein was overexpressed in Rosetta (DE3) bacterial cells. The pET-32Xa/LIC/WLN4 vector was used in expressing the WLN4. The vector encodes an N-terminal thioredoxin tag that is followed by six histidines and a Factor Xa cleavage site. This vector was transformed to NovaBlue *E. Coli* cells, propagated in LB, then recovered. The plasmid vector was loaded alongside 1 kb standard DNA ladder in agarose gel electrophoresis.

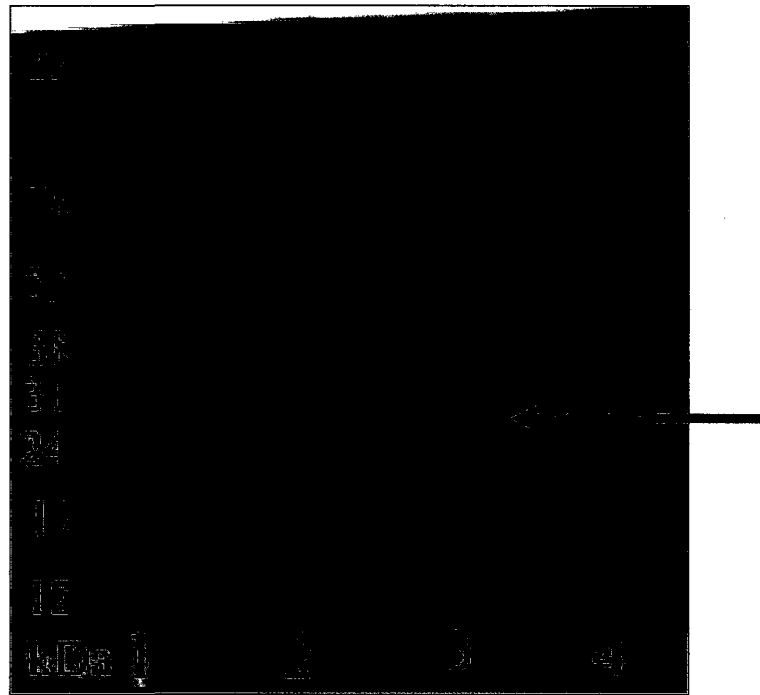
The gel displayed in Figure 9.1 shows an uncut plasmid DNA run alongside a standard 1kb standard. Three distinct bands that correspond to different migration rates are observed in agarose gel displayed in Figure 9.1. These bands are due to the different migration rates of DNA conformers: nicked, linear and supercoiled DNA. The latter occurred at a approximately 6 kb that is consistent with the size expected for a pET-32Xa/LIC plasmid and sequence encoding for the WLN4 as shown previously in Figure 8.1. The vector was sequenced previously in our laboratory.



**Figure 9.1** Agarose gel of plasmid vector pET-32Xa/LIC/WLN4. Standards are in lane 1. Lanes 2,3,4,5 are uncut plasmid DNA from different preps.

## 9.2 Protein Induction and Expression

WLN4 is a small protein approximately 70 amino acid residues in size [1]. IPTG, an analog of lactose, was used to induce protein expression in Rosetta (DE3) *E. coli* cells. Induction tests to monitor progress in the course of 3 hr are shown in the SDS-PAGE in Figure 9.2.



**Figure 9.2** SDS-PAGE analysis of protein induction and expression of WLN4. Expression of this protein was monitored after induction at zero (lane 2), one (lane 3) and 3 hr (lane 4) as shown in the gel. Lane 1 is the full range rainbow marker (GE Healthcare). The arrow points to the position of the protein of interest.



At time zero of induction and immediately after adding IPTG, there was no observable protein band expressed in the cells. However, after 1 and 3 hr a distinct protein band appeared at 24 kDa that corresponds to the size of domain 4 fused with thioredoxin protein. A high level of protein expression of WLN4 was achieved by adopting a thioredoxin fusion strategy.

The gene for WLN4 protein was linked to the gene encoding a thioredoxin carrier protein. Thioredoxin protein improves translation efficiency [2] and has the capacity to accumulate cellular protein and still remain soluble in the matrix [3-6]. Thioredoxin has a molecular mass of approximately 12 kDa [7, 8]. Thioredoxin stabilize most proteins in solution [8]. As a result, a high level of WLN4 fusion protein was expressed in bacterial cells in solution.

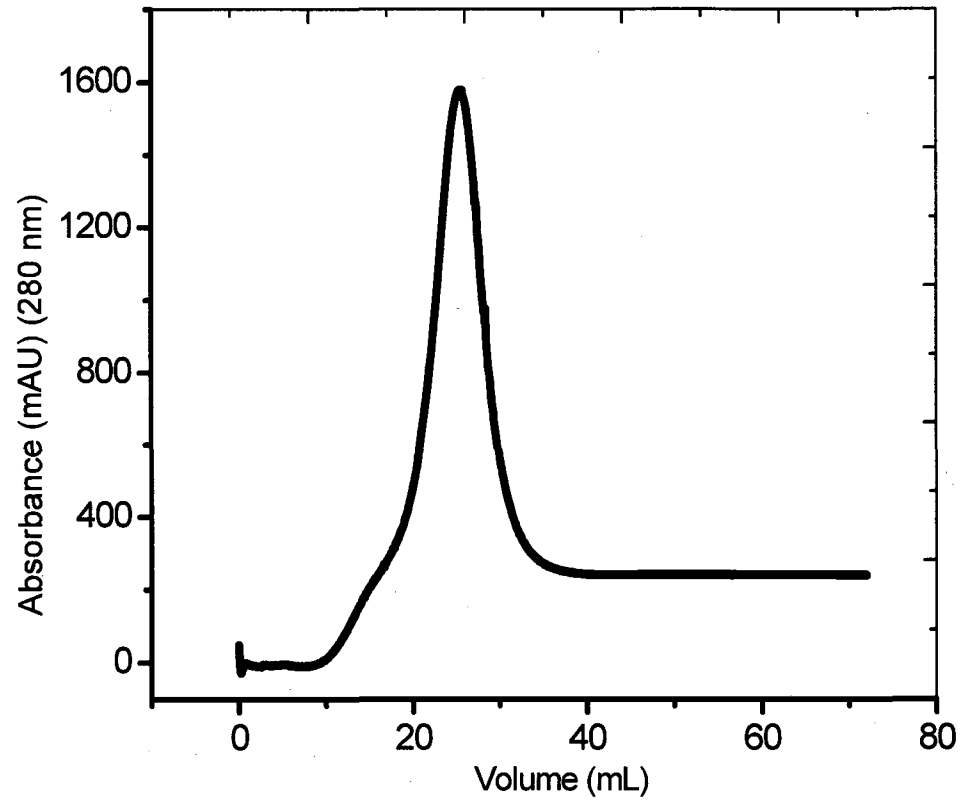
The SDS-PAGE band in Figure 9.2 shows an intense protein band 1 hr after IPTG induction of the WLN4-thioredoxin fusion protein. The increased band intensity with increasing time indicates the progress of expression of WLN4 fusion in bacteria cells.

### **9.3 Purification of WLN4 Fusion Protein**

#### **9.3.1 HisPrep Purification**

WLN4 fusion protein was successfully extracted from the bacterial cells using BugBuster<sup>®</sup> reagent. The cell-free BugBuster<sup>®</sup> reagent extract was decanted into a 50 mL falcon tube for purification in a nickel chelating sepharose HisPrep FF 16/10 column (GE Healthcare). The AKTA FPLC purification system was used together

with the HisPrep FF 16/10 column. The column was cleaned with 5 column volumes (CV) of water and then equilibrated with similar volume of HisPrep binding buffer (20 mM sodium phosphate, pH 7.4, 500 mM NaCl, 20mM imidazole). A 15 mL cell-free extract was loaded into the column at a flow rate of 2 mL/min. The protein was eluted isocratically through the column using 1 CV of elution buffer (20 mM sodium phosphate, 500 mM NaCl, and 500 mM imidazole). The column was rinsed with HisPrep binding buffer. The elution maximum peak is displayed in Figure 9.3. The major fractions with the protein were determined by SDS-PAGE on a 15 % gel. These fractions were pooled together, concentrated with Amicon ultrafiltration device and kept in a -20 °C.



**Figure 9.3** The WLN4 fusion protein elution from HisPrep FF 16/10 Ni Sepharose column.

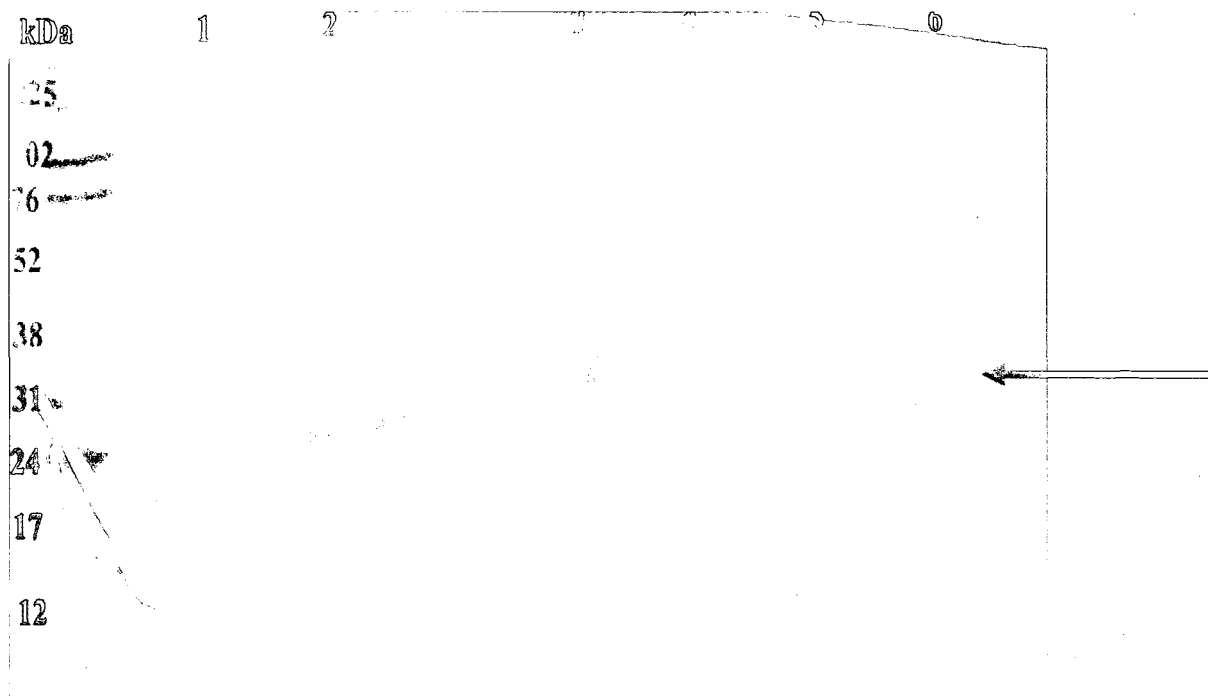


Figure 9.4 SDS-PAGE gel showing progress of Factor Xa cleavage of WLN4-Trx-His-tag protein. Lanes 1 and 2 are samples without Factor Xa. Lanes 3-6 are samples with Factor Xa 6 hr after adding Factor Xa. The arrow shows protein band before Factor Xa cleavage.

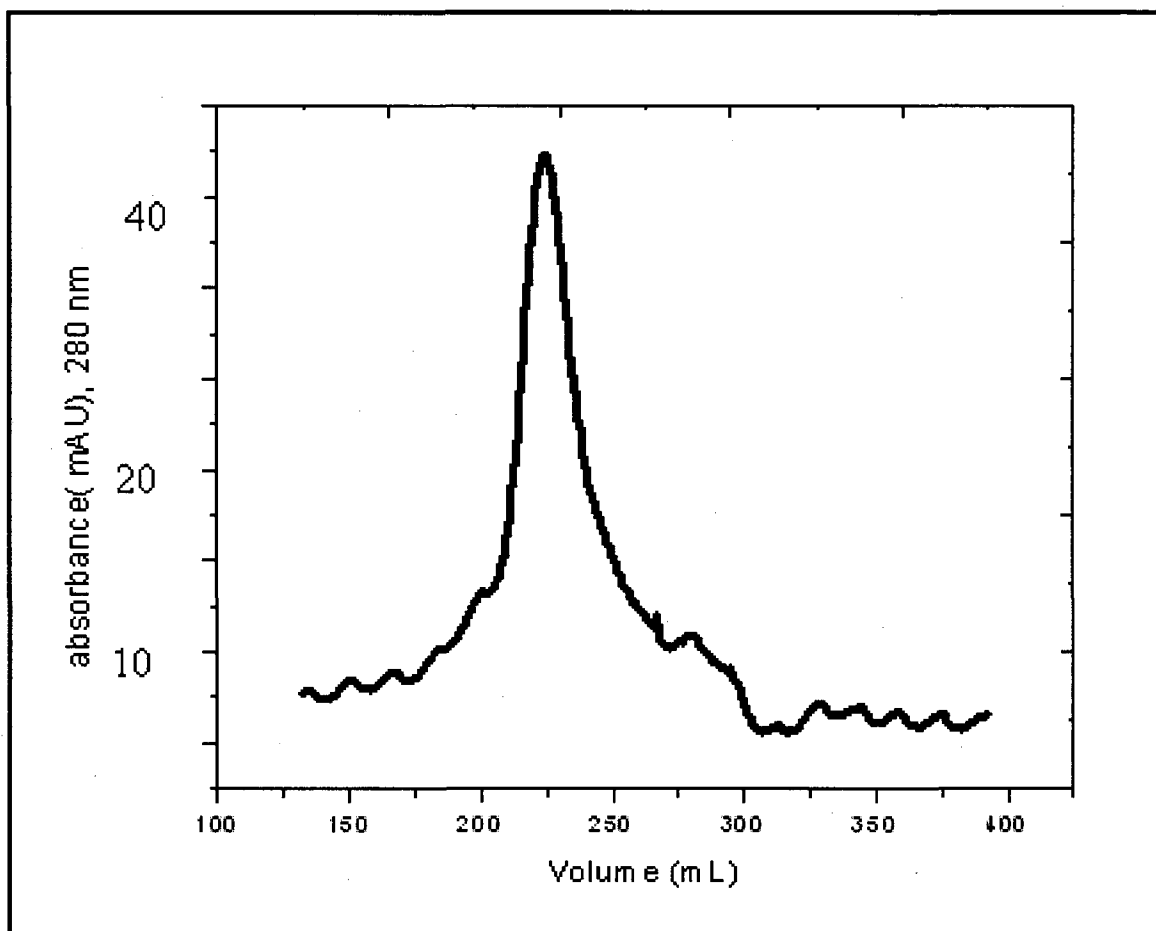
### 9.3.2 Factor Xa Protease Cleavage

The WLN4-Trx-6-His fusion protein was exchanged into Factor Xa cleavage buffer pH 8.0 (50 mM Tris/Cl, 100 mM NaCl, 5 mM CaCl<sub>2</sub>). It was subjected to a Factor Xa serine protease (Enzyme research Laboratories, IN USA) cleavage 16 hrs at 25°C. The concentration of the enzyme used was to a final concentration of 1.4 µg/ml. The protease is specific in its recognition sequence and should not exhibit internal cleavage of the target protein [9, 10]. The sample from the Factor Xa cleavage was analyzed by an SDS-PAGE electrophoresis and the results are shown in Figure 9.4.

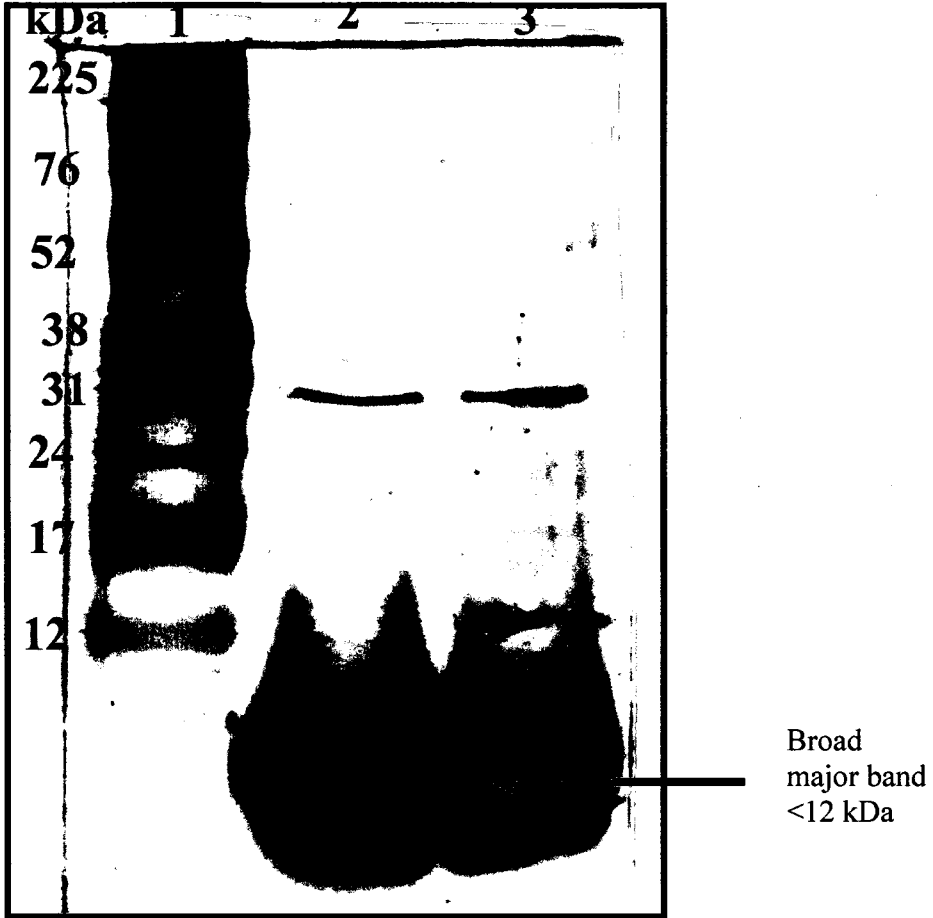
The SDS-PAGE in Figure 9.4 showed the progress of Factor Xa cleavage with increasing time. The cleavage product was passed through affinity-based capture to remove Factor Xa. The cleavage was successful after 16 hr at room temperature and further subjected to HisPrep chelating resin and gel filtration purification to obtain pure WLN4. A Superdex 75 26/60 gel filtration column (Biotech Pharmacia) was used. A chromatogram of an elution profile is displayed in Figure 9.5. The elution volume of the WLN4 protein at a flow rate of 2.6 mL/min was 224.1 mL.

Figure 9.6 shows the SDS-PAGE gel of the HisPrep<sup>TM</sup> elution products. Lane 1 in Figure 9.6 is a migration profile for protein standards. Lanes 2 and 3 are two different samples from HisPrep<sup>TM</sup> gel filtration column. The migration of the protein showed two distinct protein bands: a sharp minor and broad major protein band. A sharp minor band at 31 kDa is as a result of an overloaded SDS-PAGE gel. A major

broad band appearing at position  $< 12$  kDa is due to the presence of the WLN4 protein [11].



**Figure 9.5** HiLoad Superdex 75 26/60 gel filtration chromatogram. Final stage after cleavage demonstrating purity of WLN4.



**Figure 9.6** SDS-PAGE analysis of purified WLN4. Lane 1 is the full range rainbow marker (GE Healthcare) and lanes 1-2 are products from gel filtration for two different batch samples.

### **9.3.3 Protein Concentration**

The protein concentration of the purified WLN4 protein was measured by the Bradford assay using bovine serum albumin protein as the standard. The protein content of the WLN4 was calculated from a linear regression line from BSA standard curve. The Bradford assay is stable for determining protein concentration [12, 13]. The concentration of purified WLN4 was calculated as 21 mg/mL. The protein yield from a 1 L induction was 42 mg.

## **9.4 Determination of Protein Size by Light Scattering**

### **9.4.1 Static Light Scattering (MALS-SEC)**

Laser light scattering is a non-invasive technique that can provide information on the size and shape of proteins or protein aggregates in solution [14]. Gel filtration chromatography (SEC), connected to a multi-angle laser light scattering detector (MALS), analysis of WLN4 showed protein peaks.

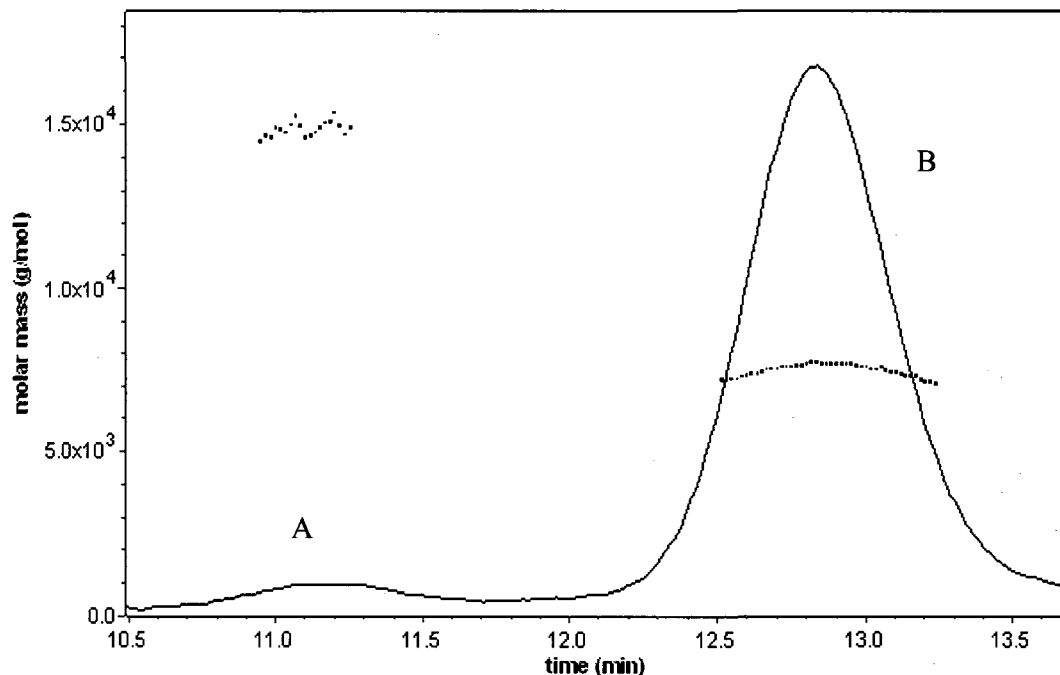
For effective determination of molar mass, scattering intensity, concentration and specific refractive index increment must be known. The molecular mass at low concentrations was accurately determined by the specific refractive index increment with molecular weight  $dn/dc$ . Where  $dn$  and  $dc$  are change in refractive index and concentration respectively. This value is a measure of polarizability of the material and hence amount of light it will scatter. Isotropic bovine serum albumin (66 kDa) was used as a reference protein to normalize the light scattering intensity of the photodiode array around the scattering cell to the 90° detector. The relative scattering



intensity of laser light was determined as the difference in intensity of the sample and the solvent intensity at 25°C.

The relative intensity in dilute solutions is a measure of weight average molar mass and structure factor [15, 16]. The structure factor is a mathematical measure of how a material scatters incident radiation at different angles. This is a function of a particle size. In dilute solutions where protein interactions are weak, the weight average molar mass, the radius of gyration and the second virial coefficient can be obtained using the Rayleigh-Debye approximation [17-19]. The radius of gyration is a measure of the average square distance to the center of gravity of a particle.

A gel filtration chromatography profile of WLN4 protein in response to 90° LS detector is shown in Figure 9.7. In Figure 9.7, two molar mass distributions in WLN4 protein sample were detected in MALS. A large protein mass eluted close to 13 mL and a small one at 11 mL. Analysis of the data using ASTRA 5.3.4.10 version software showed aggregated materials that yielded molar mass of 14.9 kDa as shown in Table 9.1. This value is almost twice the measured mass of WLN4 of 7.5 kDa (Table 9.1).

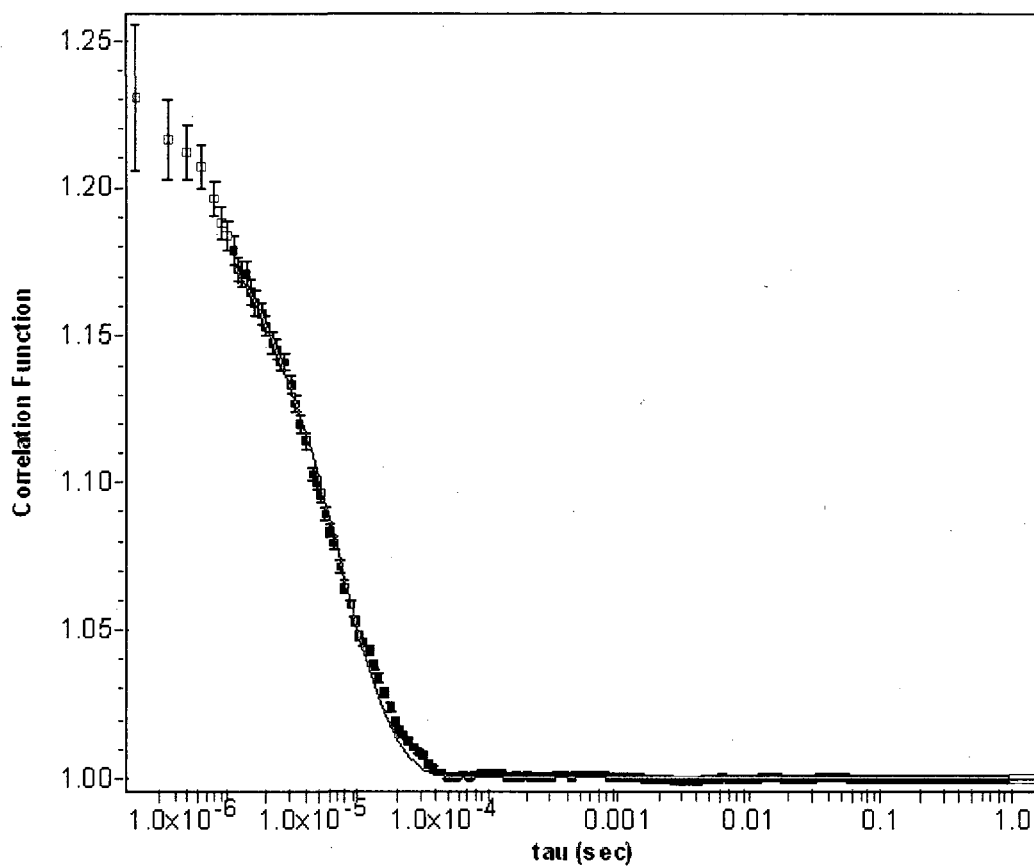


**Figure 9.7** Molar mass versus time for the WLN4 protein. Molar mass of 14.9 kDa is A and B corresponds to 7.5 kDa. The solid line is the UV (280 nm) trace for WLN4. The dotted line corresponds to the molar mass of WLN4.

#### 9.4.2 Dynamic Light Scattering

Dynamic light scattering was also used to characterize the size and hydrodynamic radius of the WLN4 protein. In this method, time dependent fluctuations in the intensity of scattered light that occur due to Brownian motion are measured in a small volume. Analysis of the intensity fluctuations can be used to determine the translation diffusion coefficients. The diffusion coefficient can then be converted to size distribution. The diffusion coefficient is calculated from auto

correlation function. The angle dependence scattering intensity of light depends on the root mean square radius of the particle. An autocorrelation function plot obtained for WLN4 is shown in Figure 9.8.



**Figure 9.8** Autocorrelation function.

For a sample containing a single species undergoing Brownian diffusion the autocorrelation function can be deduced from Equation 9.1. It defines how quickly on average the light intensity changes with time. It shows how probable that at some time  $\tau$  later the same intensity of light will be seen by the detector.

$$g(\tau) = 1 + \alpha e^{-\tau/\kappa} \quad [9.1]$$

In this equation,  $g(\tau)$  is the autocorrelation function and a  $\kappa$  time constant, a measure of how quickly the light intensity changes.  $\kappa$  is defined by Equation 9.2

$$q = \frac{4\pi}{\lambda} \sin\left(\frac{\theta}{2}\right), \quad [9.2]$$

$$\kappa = \frac{1}{2D_T q^2} = R_H \frac{3\eta\lambda^2}{16\pi k_B T \sin^2(\theta/2)}$$

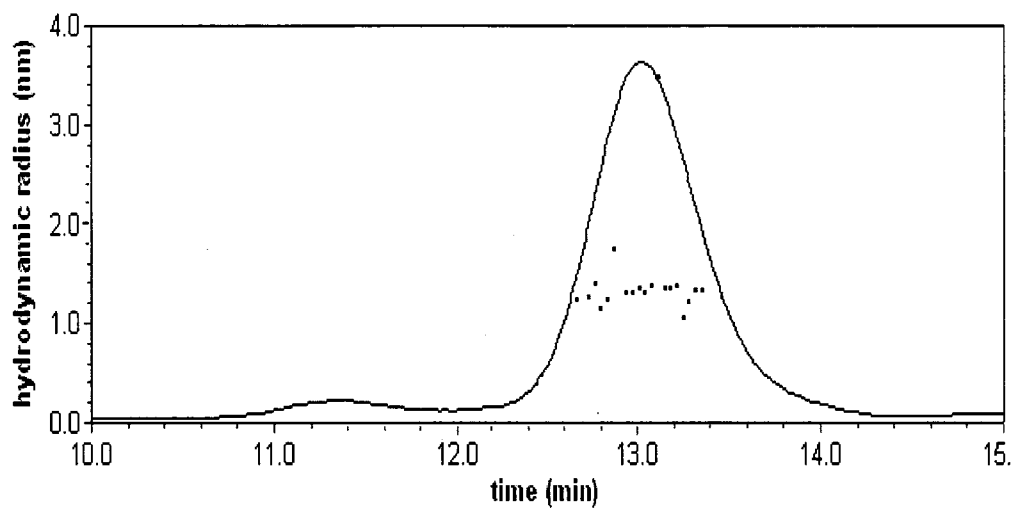
In this equation,  $R_H$  is the hydrodynamic radius of particle undergoing diffusion,  $\lambda$  is the wavelength of light, and  $\eta$  dynamic viscosity at temperature  $T$  (Kelvin),  $k_B$  is the Boltzmann's constant,  $\theta$  is the angle of detector normally  $90^\circ$  but  $100^\circ$  was used in the experiment. The exponential time constant of the autocorrelation function is directly related to the hydrodynamic radius of the particle in solution.

The hydrodynamic radius is also related to the translation diffusion coefficient assuming a perfect hard sphere. This relationship is based on Stokes-Einstein relationship of a particle based on Equation 9.3. The distribution of translational diffusion constants can be used to determine size distribution of the particles analyzed.

$$R_H = \frac{k_B T}{6\pi\eta D} \quad [9.3]$$

Here,  $R_H$  is the hydrodynamic radius of the particle undergoing diffusion with a diffusion coefficient  $D$ ,  $k_B$  is the Boltzmann constant,  $\eta$  is the solvent viscosity.

The average hydrodynamic radius for WLN4 protein calculated based on this equation was  $13.3 \pm 0.7 \text{ \AA}$  and diffusion coefficient,  $D$  of  $(1.84 \pm 0.09) \times 10^{-6} \text{ cm}^2\text{sec}^{-1}$  as shown in Table 9.1. A typical plot of hydrodynamic radius as a function of elution time using MALS is shown in Figure 9.9.



**Figure 9.9** Hydrodynamic radius distributions. The solid line is the UV (280 nm) trace for WLN4. The dotted line is the trace for hydrodynamic radius.

**Table 9.1** Summary HPLC-Gel filtration and light scattering.

Properties	MALS <sup>1</sup>	DLS <sup>2</sup>
Light scattering	<b>Peak 2</b> 7.5 ± 0.0	7.64 ± 0.06
Molar mass X 10 <sup>3</sup> (g/mol)	<b>Peak 1</b> 14.9 ± 0.0	
Hydrodynamic radius (nm)	-	1.33 ± 0.07
Frictional ratio	-	1.02

<sup>1</sup> Multi-angle laser light scattering

<sup>2</sup> Dynamic laser light scattering

In addition to hydrodynamic radius, the dynamic light scattering yielded an average mass of 7.64 kDa for the WLN4 protein, comparable to the MALS result. A perfect spherical conformation shape was deduced from the frictional ratio of 1.02, assuming a partial specific volume inverse of density of 0.734 mL/g. A frictional ratio is a ratio between hydrated and non-hydrated sphere. It can be deduced from the ratio between a root mean square radius ( $R_G$ ) obtained from static light scattering and hydrodynamic radius ( $R_H$ ) from dynamic scattering. For a solid sphere or a compact molecule this ratio should be one or less. For an extended object the  $R_G$  is strongly influenced by the outlying masses but  $R_H$  is not influenced. Therefore, the ratio increases as the object becomes less compact.

A radius of a perfect sphere can also be determined from the shape and dimensions. An equivalent sphere radius of the WLN4 protein can be obtained from its molecular volume  $v_m$  and density according to Equation 9.4 [20].

$$v_m = \frac{M}{\rho_p A_v} \quad [9.4]$$

In this equation,  $M$  is the molecular mass obtained from MALS of the WLN4 protein,  $\rho_p$  is the protein density, and  $A_v$  is the Avogadro's number. The density of protein is  $1.36 \text{ g cm}^{-3}$ . It can be calculated from Equation 9.4 that  $v_m$  for WLN4 equals  $9.16 \text{ nm}^3$ . Therefore, an equivalent sphere radius  $R_s = (3v_m/4\pi)^{1/3}$  is 1.30 nm. The

experimental value is 1.33 nm. This suggests that the shape of the WLN4 protein deviates insignificantly from that of a perfect spherical shape.

The hydrodynamic radius is highly affected by the shape of the protein and the solvent that forms the hydration sphere around the protein itself. Accurate shape analysis can be obtained from the sedimentation coefficient. This technique can give the correct shape of a given protein.

### **9.5 Circular Dichroism**

A variety of optical methods are widely used to estimate the protein structure and stability. These methods include absorbance spectroscopy, circular dichroism, fluorescence spectroscopy, Fourier transform infrared spectroscopy and nuclear magnetic resonance [21-25]. The conformation stability of WLN4 was analyzed using circular dichroism (CD) in a JASCO J-815 spectrometer. The CD was chosen because WLN4 sequence has limited chromophores suitable for UV or fluorescence spectroscopy.

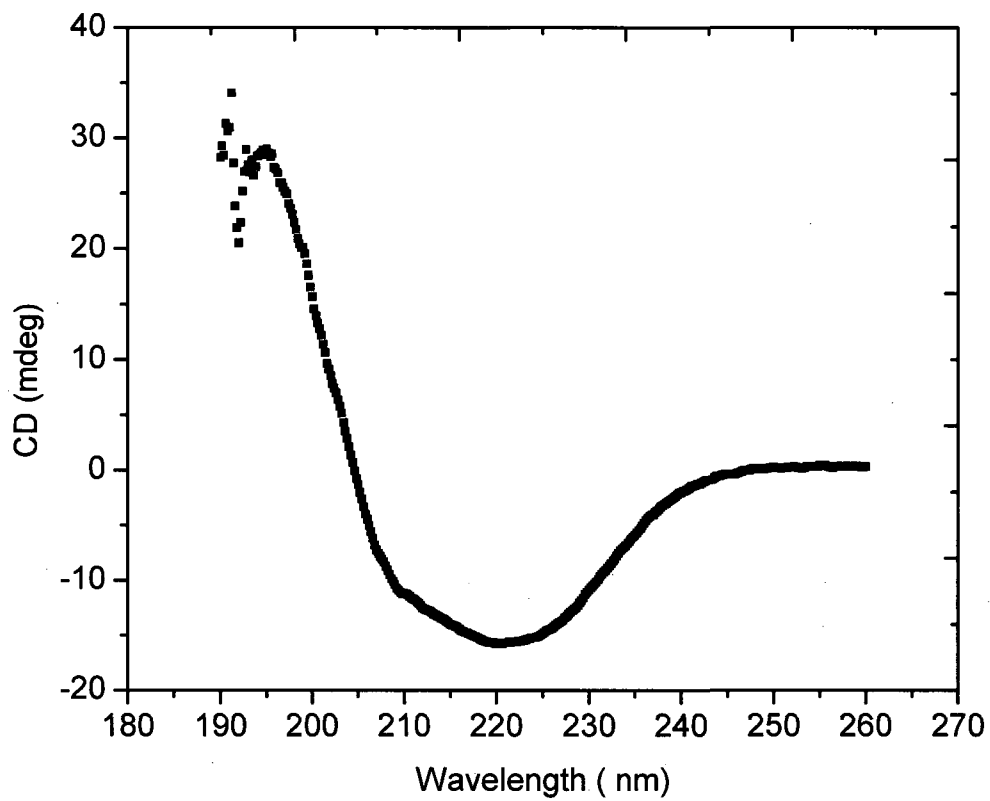
A CD spectrum of WLN4 measured in sodium phosphate buffer pH 7.4 and 25°C is displayed in Figure 9.10. The spectrum was obtained by wavelength scan in the far UV from 190 to 260 nm. The scan for the buffer alone was subtracted from the average scans for each sample measured either at a particular temperature or concentration of the denaturant. The concentration of WLN4 protein was 0.2 mM based on Bradford assay. The CD spectrum shows ellipticity minimum at 222 nm. A



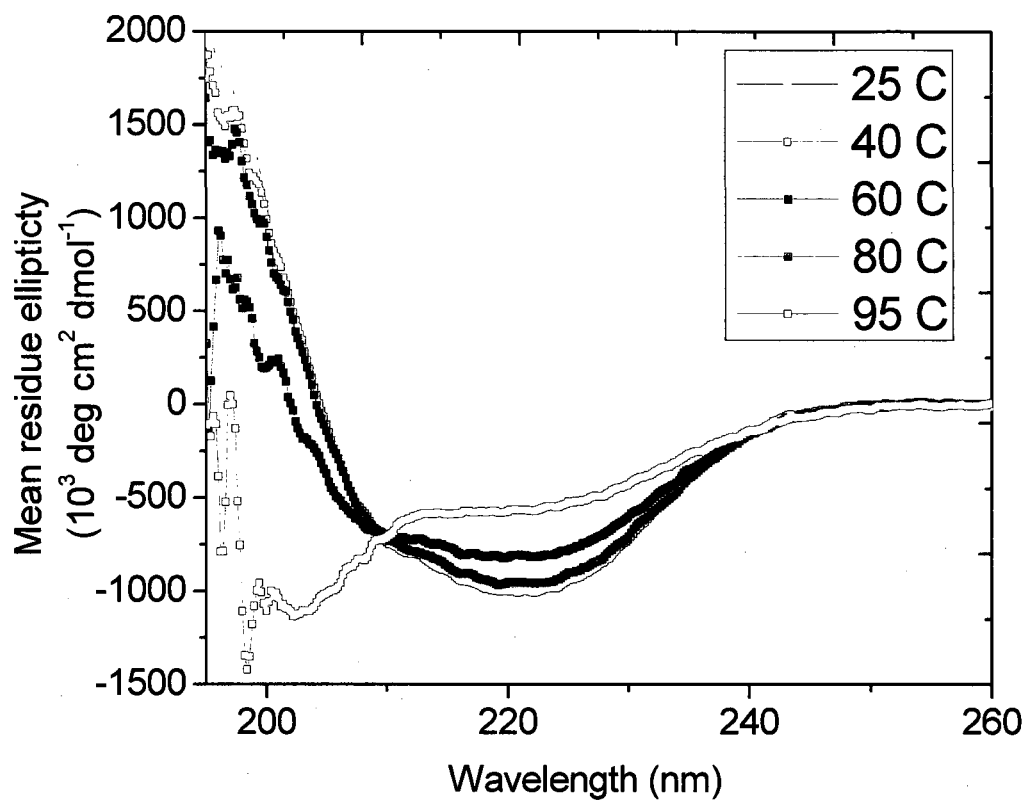
typical  $\alpha$ -helix secondary structure has two deep minima at 222, 208 and an intense peak at 193 nm [26, 27].

The solution structure of WLN4 was previously determined using solution NMR. The structure data shown in Figure 9.16 for the WLN3-4 protein showed a structure organized into two domains composed of 6  $\alpha$ -helices and 9  $\beta$ -sheets [1]. In this study, the WLN3-4 showed 20%  $\alpha$ -helicity and 23%  $\beta$ -sheets based on the secondary structure prediction.

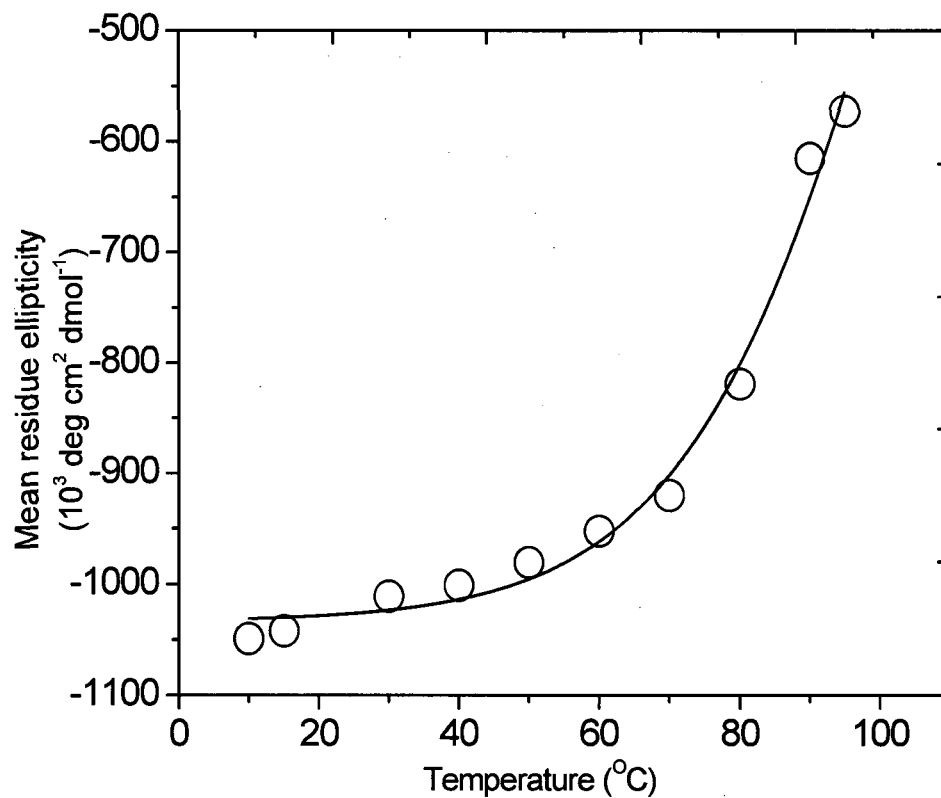
A spectra recorded in millidegrees of ellipticity was converted to a mean molar ellipticity to study the effect of temperature and chemical denaturant on the unfolding of the WLN4 protein. A plot of mean molar ellipticity at a wavelength of 222 nm against temperature is displayed in Figures 9.11 and 9.12. In Figure 9.11, a smooth transition curve was observed for the thermal denaturation. When WLN4 was thermally denatured, a minimal change occurred in the CD spectrum of WLN4. It appeared that the helical structure was maintained prior to denaturation above 80°C.



**Figure 9.10** CD spectrum of WLN4. The units are in ellipticity in millidegrees. The measurements were carried out at 25°C in a 50 mM sodium phosphate pH 7.4



**Figure 9.11** Thermal unfolding of WLN4 measured between 190 and 260 nm.

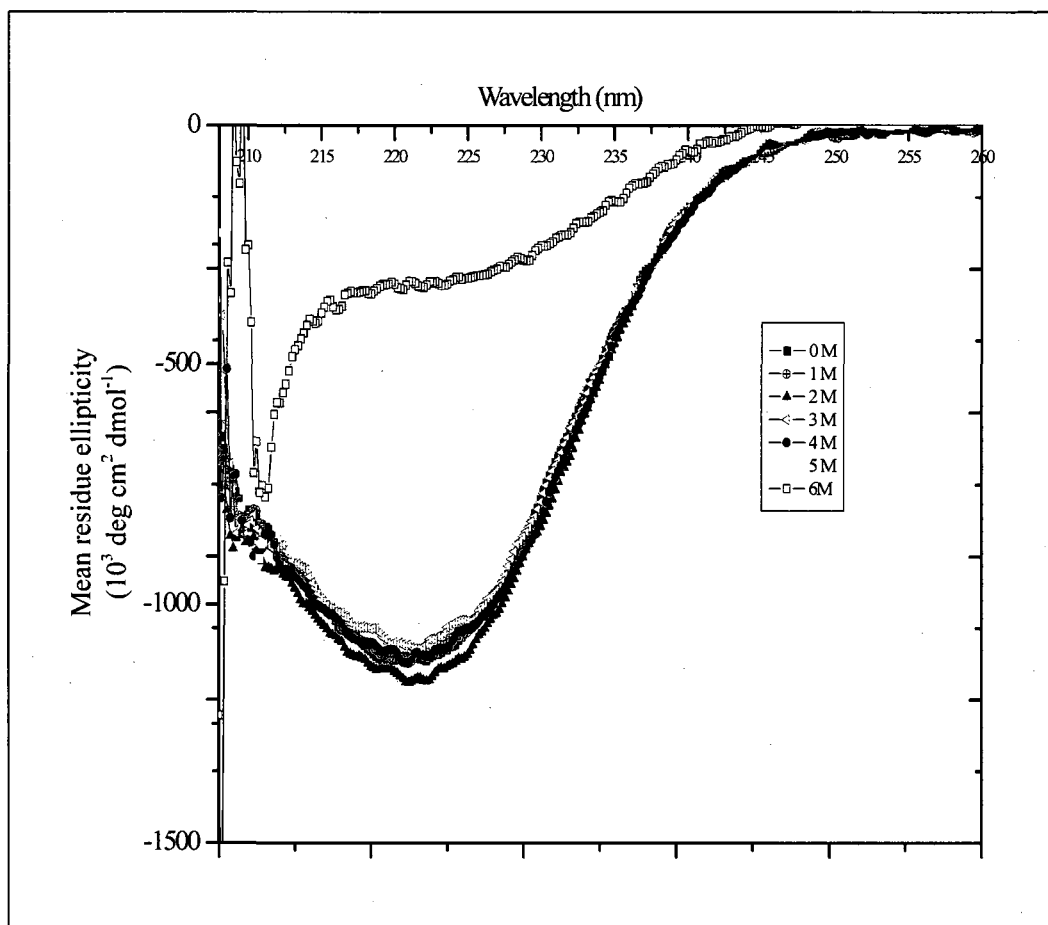


**Figure 9.12** A two-state model of thermal unfolding of WLN4 taken at 222 nm.

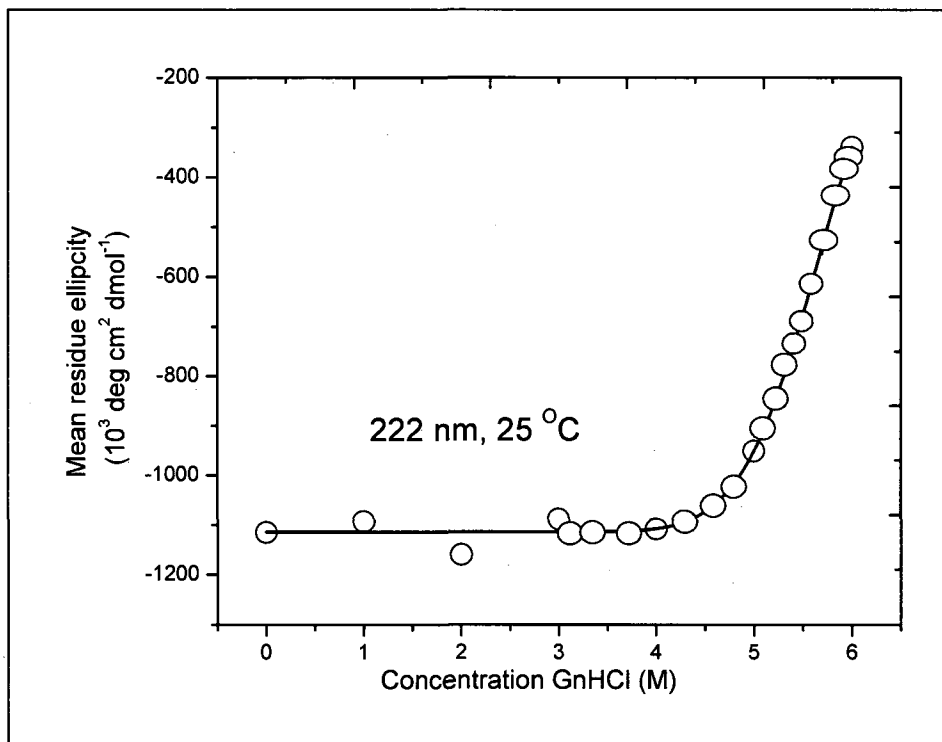
The aforementioned observation possibly suggests that the helical structure of WLN4 is remarkably stable with the observed transition ( $T_m$ ) values occurring above 90°C.  $T_m$  is the temperature at which 50% of the protein is in an unfolded state. Gel filtration of the protein after heat denaturation was not done to ascertain any presence of protein aggregates that could possibly contribute to the high thermal stability of WLN4.

Guanidine hydrochloride (GnHCl) is believed to cause a complete unfolding of most proteins. The chemical unfolding process exhibits a two-state behavior. The denaturation curve of the WLN4 protein was monitored At 25°C as a function of GnHCl concentration and wavelength scan. The unfolding of the WLN4 protein is shown in Figure 9.13.

The WLN4 protein retains its folded structure in the presence of up to 5 M GnHCl as indicated in Figure 9.14. Both the thermal and chemical unfolding data presented here indicate an extreme stability of the N-terminal domain WLN4 of Wilson protein. The standard free energy of unfolding of WLN4 obtained by linearly extrapolating to zero denaturant concentration (Figure 9.15) is shown in Table 9.2. The value of  $10.1 \pm 0.1$  kcal/mol measured at 25°C is comparable to small copper binding proteins and other metal binding proteins [28, 29]. The data used to calculate the free energy change is shown in Table 9.4. In Table 9.4, the fraction of folded and unfolded protein was measured at different concentrations of guanidine hydrochloride. In Figure 9.14 the concentrations of the denaturant between 1 and 4 M showed almost a completely folded WLN4 protein.



**Figure 9.13** Chemical unfolding with GdnHCl. Measurements were taken at 25°C.

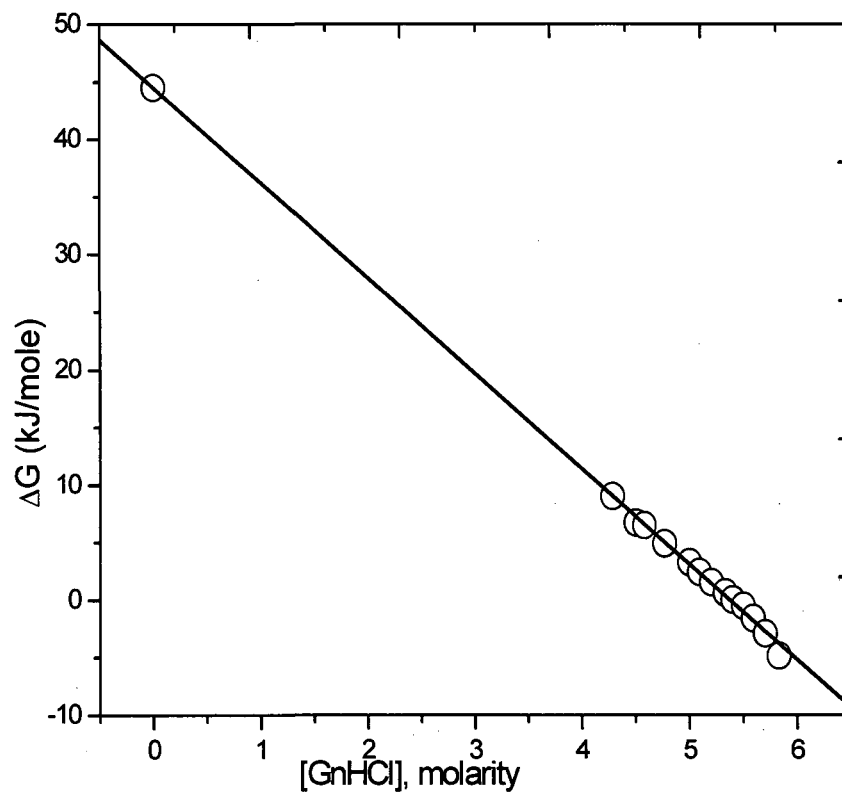


**Figure 9.14** Equilibrium curves for chemical unfolding. Measurements were taken at 25°C. Open circles are the data points obtained from the instrument. The closed circles are points generated within the curve to estimate fractions unfolded and folded at every concentration of GnHCl using a two-state model.

A number of potential interactions could lead to such high thermal stability. These include an increase in hydrogen bond formation, presence of increased electrostatic interactions and salt bridges, hydrophobic interactions and stronger binding to metal ions [30-36].

The  $m$  value in Table 9.2 is strongly correlated to the surface area of protein exposed to solvent upon unfolding [37]. A lower value of  $m$  in WLN4 protein can be attributed to the presence of more than one equilibrium states. This is not addressed by the two-state model employed in the above mentioned analysis for WLN4. The presence of disulfide linkages in the unfolded state of WLN4 may result in a more compact structure that reduces the accessibility of the unfolded polypeptide chain to solvent. The free energy change extrapolated to zero denaturant concentration for the WLN4 protein is comparable to that observed for several water soluble globular proteins as shown in Table 9.4. A value 6.24 kcal/mol was calculated at ambient conditions for ferric enterobactin protein (FeA), an integral outer membrane protein responsible for the uptake of iron in gram negative bacterial cells [38].





**Figure 9.15** Concentration dependence of the chemical unfolding and change in free energy. This graph was obtained using points from a curve generated in Fig. 9.14.

**Table 9.2** Summary free energy of unfolding of WLN4.

Property	WLN4
$\Delta G_U^{H_2O}$ kcal mol <sup>-1</sup>	10.6 ± 0.1
m kcal mol <sup>-1</sup> M <sup>-1</sup>	-2.0 ± 0.0
[GnHCl], M	5.4

**Legend;**  $\Delta G_U^{H_2O}$  is Gibb's free energy in the absence of denaturant estimated by extrapolating the curves to zero concentration.

$[GnHCl]$  is the molar concentration of denaturant chemical guanidine hydrochloride  
 $M$  is the concentration of guanidine hydrochloride at equilibrium.

**Table 9.3** Free energy of unfolding extrapolated to zero denaturant concentration. The denaturant used in all cases is guanidine hydrochloride [39].

Globular Protein	$\Delta G_U^{H_2O}$ (kcal/mol)	pH
Myoglobin	10.1	6.0
Lysozyme	10.7	2.9
$\alpha$ -chymotripsin	13.7	4.3
Ribonuclease	18.9	6.6
$\beta$ -Lactoglobulin	26.0	3.2

**Table 9.4** Chemical unfolding parameters for WLN4 protein.

YF <sup>3</sup>	Y <sup>4</sup>	FF <sup>5</sup>	K <sup>6</sup>	FU <sup>7</sup>	YU <sup>8</sup>	$\Delta G^9$	[GnHCl] <sup>10</sup>
-1114	692.15	0.45234	1.21073	0.54766	-343.51	-473.776	5.5
-1114	527	0.23807	3.2005	0.76193	-343.51	-2882.18	5.7
-1114	953.27	0.79113	0.26402	0.20887	-343.51	3299.44	5
-1114	1066.74	0.93835	0.06571	0.06165	-343.51	6745.38	4.5
-1114	1113.64	0.9992	8.05E-04	8.04E-04	-343.51	17651.7	4
-1114	846.3	0.65234	0.53295	0.34766	-343.51	1559.222	5.2
-1114	1062.36	0.93266	0.0722	0.06734	-343.51	6511.887	4.58
-1114	1021.71	0.87992	0.13646	0.12008	-343.51	4934.563	4.77
-1114	1113.64	0.9992	8.05E-04	8.04E-04	-343.51	17651.7	3.71
-1114	1094.57	0.97445	0.02622	0.02555	-343.51	9021.768	4.28
-1114	1113.64	0.9992	8.05E-04	8.04E-04	-343.51	17651.7	3.34
-1114	906.02	0.72982	0.3702	0.27018	-343.51	2462.007	5.09
-1114	780.01	0.56633	0.76575	0.43367	-343.51	661.2619	5.33
-1114	734.99	0.50792	0.96881	0.49208	-343.51	78.50453	5.4
-1114	613.04	0.3497	1.85961	0.6503	-343.51	-1537	5.59
-1114	439.51	0.12455	7.02865	0.87545	-343.51	-4831.25	5.83
-1114	384.16	0.05274	17.96064	0.94726	-343.51	-7155.68	5.91
-1114	1113.64	0.9992	8.05E-04	8.04E-04	-343.51	17651.7	3.097
-1114	1111.45	0.99635	0.00366	0.00365	-343.51	13900.48	3.547
-1114	354.15	0.0138	71.43891	0.9862	-343.51	-10576.4	5.97

<sup>3</sup> Mean residue ellipticity of the folded state

<sup>4</sup> Measured mean ellipticity at a particular [GnHCl]

<sup>5</sup> Fraction folded

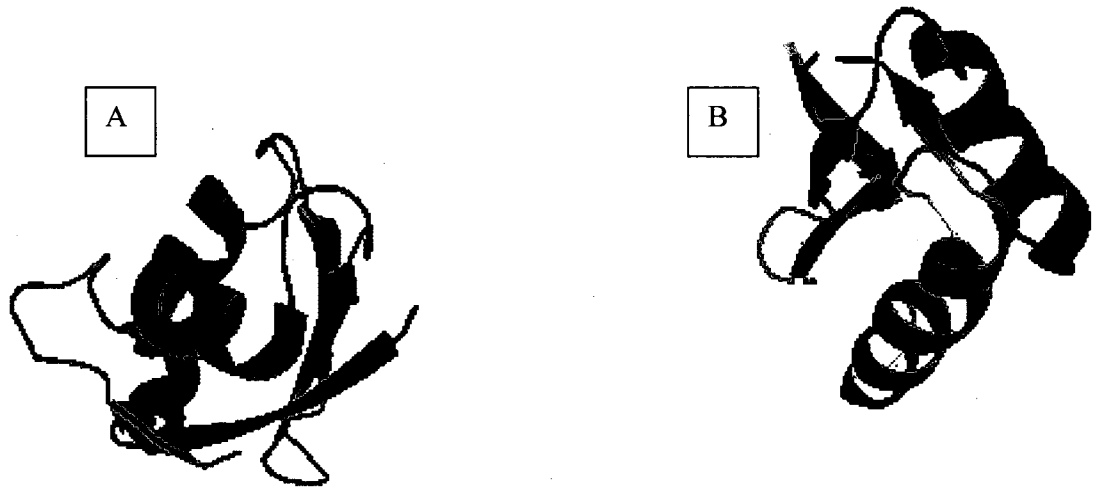
<sup>6</sup> Equilibrium constant

<sup>7</sup> Fraction unfolded

<sup>8</sup> Measured mean residue ellipticity of unfolded state

<sup>9</sup> Gibbs free energy change

<sup>10</sup> Guanidine hydrochloride concentration



**Figure 9.16** Structure of WLN4 (B) and Third domain of Wilson protein (A). WLN4 protein shows two  $\alpha$ -helices (RED) and three  $\beta$ -sheets (GREEN). The structure was obtained from Protein Data Bank (PDB 2ROP).

## 9.6 References

- 1 Banci, L., Bertini, I., Cantini, F., Rosenzweig, A. C. and Yatsunyk, L. A. (2008) Metal binding domains 3 and 4 of the Wilson disease protein: solution structure and interaction with the copper(I) chaperone HAH1. *Biochemistry* **47**, 7423-7429
- 2 Jun, K. O., Song, C. H., Kim, Y. B., An, J., Oh, J. H. and Choi, S. K. (2009) Activation of translation via reduction by thioredoxin-thioredoxin reductase in *Saccharomyces cerevisiae*. *FEBS Lett* **583**, 2804-2810
- 3 Ems-McClung, S. C. and Hainline, B. E. (1998) Expression of maize gamma zein C-terminus in *Escherichia coli*. *Protein Expr Purif* **13**, 1-8
- 4 LaVallie, E. R., Lu, Z., DiBlasio-Smith, E. A., Collins-Racie, L. A. and McCoy, J. M. (2000) Thioredoxin as a fusion partner for production of soluble recombinant proteins in *Escherichia coli*. *Methods Enzymol* **326**, 322-340
- 5 LaVallie, E. R., DiBlasio, E. A., Kovacic, S., Grant, K. L., Schendel, P. F. and McCoy, J. M. (1993) A thioredoxin gene fusion expression system that circumvents inclusion body formation in the *E. coli* cytoplasm. *Biotechnology (N Y)* **11**, 187-193
- 6 McCoy, J. and Lavallie, E. (2001) Expression and purification of thioredoxin fusion proteins. *Curr Protoc Mol Biol* **Chapter 16**, Unit16 18
- 7 Gleason, F. K., Lim, C. J., Gerami-Nejad, M. and Fuchs, J. A. (1990) Characterization of *Escherichia coli* thioredoxins with altered active site residues. *Biochemistry* **29**, 3701-3709
- 8 McEvoy, M., Lantz, C., Lunn, C. A. and Pigiet, V. (1981) Isolation and characterization of a protease-nicked thioredoxin. *J Biol Chem* **256**, 6646-6650

- 9 Nagai, K., Perutz, M. F. and Poyart, C. (1985) Oxygen binding properties of human mutant hemoglobins synthesized in *Escherichia coli*. *Proc Natl Acad Sci U S A* **82**, 7252-7255
- 10 Kuhnel, B., Alcantara, J., Boothe, J., van Rooijen, G. and Moloney, M. (2003) Precise and efficient cleavage of recombinant fusion proteins using mammalian aspartic proteases. *Protein Eng* **16**, 777-783
- 11 Bunce, J. (2004) Copper Exchange Studies Between the First and Fourth N-Terminal Metal-Binding Domains of Wilson Protease ATPase. In M S Thesis WMU
- 12 Bradford, M. M. (1976) A rapid and sensitive method for the quantitation of microgram quantities of protein utilizing the principle of protein-dye binding. *Anal Biochem* **72**, 248-254
- 13 Seevaratnam, R., Patel, B. P. and Hamadeh, M. J. (2009) Comparison of total protein concentration in skeletal muscle as measured by the Bradford and Lowry assays. *J Biochem* **145**, 791-797
- 14 Philip, J. W. (1993) Light scattering and the absolute characterization of macromolecules. *Analytica Chimica Acta* **272**, 1-40
- 15 Carr, C. I. J., Zimm, B. H. (1950) Absolute intensity of light scattering from pure liquids and solutions. *J Chem Phys* **18**, 1616-1626
- 16 Philip, J. W. (1993) Light scattering and the absolute characterization of macromolecules. *Analytical Chimica Acta* **272**, 1-40
- 17 Olaof, G. O. (1970) Scattering by two rayleigh-debye spheres. *Appl Opt* **9**, 429-437
- 18 Bishop, M. F. (1989) Calculations of scattered light from rigid polymers by Shifrin and Rayleigh-Debye approximations. *Biophys J* **56**, 911-925

- 19 Wyatt, P. J. (1968) Differential light scattering: a physical method for identifying living bacterial cells. *Appl Opt* **7**, 1879-1896
- 20 Jachimska, B., Wasilewska, M. and Adamczyk, Z. (2008) Characterization of globular protein solutions by dynamic light scattering, electrophoretic mobility, and viscosity measurements. *Langmuir* **24**, 6866-6872
- 21 Blancuzzi, Y., Padilla, A., Parello, J. and Cave, A. (1993) Symmetrical rearrangement of the cation-binding sites of parvalbumin upon  $\text{Ca}^{2+}/\text{Mg}^{2+}$  exchange. A study by  $^1\text{H}$   $2\text{D}$  NMR. *Biochemistry* **32**, 1302-1309
- 22 Bauer, H. H., Muller, M., Goette, J., Merkle, H. P. and Fringeli, U. P. (1994) Interfacial adsorption and aggregation associated changes in secondary structure of human calcitonin monitored by ATR-FTIR spectroscopy. *Biochemistry* **33**, 12276-12282
- 23 Gahn, L. G. and Roskoski, R., Jr. (1995) Thermal stability and CD analysis of rat tyrosine hydroxylase. *Biochemistry* **34**, 252-256
- 24 Eftink, M. R. and Shastry, M. C. (1997) Fluorescence methods for studying kinetics of protein-folding reactions. *Methods Enzymol* **278**, 258-286
- 25 Eftink, M. R. (1994) The use of fluorescence methods to monitor unfolding transitions in proteins. *Biophys J* **66**, 482-501
- 26 Whitmore, L. and Wallace, B. A. (2008) Protein secondary structure analyses from circular dichroism spectroscopy: methods and reference databases. *Biopolymers* **89**, 392-400
- 27 Bruch, M. D., Dhingra, M. M. and Gierasch, L. M. (1991) Side chain-backbone hydrogen bonding contributes to helix stability in peptides derived from an alpha-helical region of carboxypeptidase A. *Proteins* **10**, 130-139
- 28 Wisz, M. S., Garrett, C. Z. and Hellinga, H. W. (1998) Construction of a family of Cys2His2 zinc binding sites in the hydrophobic core of thioredoxin by structure-based design. *Biochemistry* **37**, 8269-8277

- 29 Melo, E. P., Fernandes, A. T., Durao, P. and Martins, L. O. (2007) Insight into stability of CotA laccase from the spore coat of *Bacillus subtilis*. *Biochem Soc Trans* **35**, 1579-1582
- 30 Sujak, A., Sanghamitra, N. J., Maneg, O., Ludwig, B. and Mazumdar, S. (2007) Thermostability of proteins: role of metal binding and pH on the stability of the dinuclear CuA site of *Thermus thermophilus*. *Biophys J* **93**, 2845-2851
- 31 Vogt, G., Woell, S. and Argos, P. (1997) Protein thermal stability, hydrogen bonds, and ion pairs. *J Mol Biol* **269**, 631-643
- 32 Cho, Y., Sagle, L. B., Iimura, S., Zhang, Y., Kherb, J., Chilkoti, A., Scholtz, J. M. and Cremer, P. S. (2009) Hydrogen bonding of beta-turn structure is stabilized in D(2)O. *J Am Chem Soc* **131**, 15188-15193
- 33 Razvi, A. and Scholtz, J. M. (2006) Lessons in stability from thermophilic proteins. *Protein Sci* **15**, 1569-1578
- 34 Trefethen, J. M., Pace, C. N., Scholtz, J. M. and Brems, D. N. (2005) Charge-charge interactions in the denatured state influence the folding kinetics of ribonuclease Sa. *Protein Sci* **14**, 1934-1938
- 35 Pace, C. N., Shirley, B. A., McNutt, M. and Gajiwala, K. (1996) Forces contributing to the conformational stability of proteins. *Faseb J* **10**, 75-83
- 36 Shirley, B. A., Stanssens, P., Hahn, U. and Pace, C. N. (1992) Contribution of hydrogen bonding to the conformational stability of ribonuclease T1. *Biochemistry* **31**, 725-732
- 37 Myers, J. K., Pace, C. N. and Scholtz, J. M. (1995) Denaturant m values and heat capacity changes: relation to changes in accessible surface areas of protein unfolding. *Protein Sci* **4**, 2138-2148



- 38 Klug, C. S., Su, W., Liu, J., Klebba, P. E. and Feix, J. B. (1995) Denaturant unfolding of the ferric enterobactin receptor and ligand-induced stabilization studied by site-directed spin labeling. *Biochemistry* **34**, 14230-14236
- 39 Pace, C. N. and Vanderburg, K. E. (1979) Determining globular protein stability: guanidine hydrochloride denaturation of myoglobin. *Biochemistry* **18**, 288-292

## CHAPTER 10

### CONCLUSIONS AND FUTURE DIRECTIONS

#### 10.1 Success in Giant Liposomes

Significant achievements have been made in the development of phospholipid vesicles. There is emergence of new and exciting applications of liposomes in biology and chemistry. Giant liposomes can be visualized by optical microscopy. Phospholipids are the major lipids in the cell membranes. Phosphatidylcholines and phosphatidylethanolamine are the majority of the phospholipids found in eukaryotic cell membranes. Studies on the physical and chemical properties of liposomes systems can be followed systematically and controlled by the lipid and its environment. Lipid composition can be varied to help mimic certain features normally displayed by the cell membranes.

Here, we have explored fluorescence properties of the NBD moiety in a lipid bilayer to discern lipid dynamics of the lipid bilayer region. These properties are fluorescence intensity, quenching, lifetime and anisotropy. We studied both the ensemble and a single isolated liposome system. Line tension force in a series of

phospholipid bilayers was quantified by laser ablation. Taken together the research findings obtained herein offer insight into the dynamics of natural cell membranes.

Assessing future directions of this project is important. We begin by observing our limitations. We were not able to measure the line tension in the DMPC and DSPC giant unilamellar liposomes. We were unable to continue dithionite quenching on a single liposome system suspended in solution in a microscope slide as a result of dithionite quenching by oxygen. One major goal of this project was to study isolated systems such as single isolated liposome. Measurements on single vesicles will be useful in discerning the pore closing dynamics of a single cell entity. Improving on these limitations will aid evaluating the feasibility of liposomes in applications that might have practical utility.

Time-resolved measurement is a great tool that can provide significant increase in knowledge of molecules and environments. Fluorescence lifetime imaging microscopy should give even higher resolution compared to the current mode we have used. The excited state lifetime of molecules is typically in the region of nanoseconds. This nanosecond excited state of the probe is independent of the probe concentration but depend on the excited state reactions such as quenching reactions. These excited reactions can allow exploration of the molecular environment that can improve our knowledge of how molecules operate.

## 10.2 Single Molecule Fluorescence Studies of Wilson Protein and HAH1

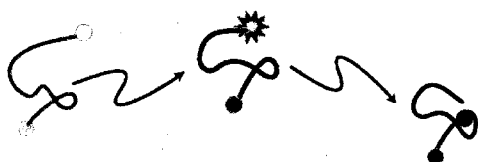
Wilson disease protein located in the *trans* Golgi network is responsible for the cellular transportation [1] of copper in the liver and brain cells [2]. The N-terminal domains interact with HAH1 metallochaperone to transfer copper to the Golgi network.

Several mechanisms have been proposed, suggesting metal binding sites in the N-terminal of Wilson disease protein is responsible for the transfer of copper [3, 4]. The transfer of copper from the chaperone to the N-terminal domain of Wilson disease protein occurs by direct transient protein-protein interaction.

Cysteine ligands within binding sites are implicated in the exchange of copper. The HAH1 chaperone and Wilson disease protein share a conserved CXXC (single letter amino acid code where X is any amino acid) sequence motif [5]. The spatial separation and orientation of the N-terminal copper-binding domains in the chaperone and target protein, leading to copper exchange is the key point in determining copper trafficking in the Golgi network.

Single molecule fluorescence studies can help unravel transient interactions involving the domains of Wilson disease protein and HAH1 [6, 7]. HAH1 can be trapped in a liposome and any of the metal binding domains of the Wilson disease protein.

Single molecule measurements can occur either by monitoring diffusing fluorescent or on an immobilized single fluorescent molecule. These are commonly used in single molecule applications. Diffusing single molecules in a focused laser beam is shown in Figure 10.1.



**Figure 10.1** Single molecule diffusing in a focused laser beam [8].

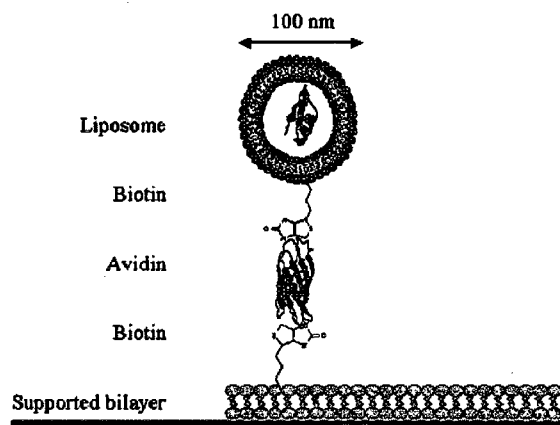
Fluorescence resonance energy transfer (FRET) is a great tool to observe single molecule behavior in diffusing in solutions. In FRET, a donor (D) fluorophore and a complementary single acceptor (A) are used to monitor the conformation dynamics in biomolecules at single-molecule resolution. A critical component of FRET experiment is the ability to label a protein such as Wilson disease protein chain with a unique D/A-pair in a site-specific way. A tightly focused laser beam

concentrated on a small and defined volume of the liposomes of 100 nm diameter can be used to trap one domain molecule of Wilson disease protein and HAH1. Dilute buffer solutions of these proteins can be prepared and added to liposomes during preparing stages. The vesicles can be extruded to produce 100 nm size using 100 nm polycarbonate membrane sizes

Vesicles can be immobilized onto a surface by avidin biotin conjugation. Liposome immobilized on a surface is displayed in Figure 10.2. A laser beam with an excitation wavelength appropriate for the donor can be used to excite the donor vesicles immobilized on the surface. The donor transfer energy to the acceptor by dipole-dipole overlaps when the distance between the donor and acceptor is within 10 nm [9]. It is possible to monitor fluorescence intensity signals from the donor and acceptor. The efficiency of energy transfer between the donor and the acceptor is measured by the ratio of the fluorescence intensity between the A and the total intensity from both the A and D. One can evaluate the signals from a two channel system provided by the instrument. The efficiency  $E$  of energy transfer depends on the inverse of the sixth power of the distance between the D and A as shown in Equation 10.1.

$$E = \frac{1}{1 + (R/R_0)^6} \quad [10.1]$$

In this equation E is the FRET efficiency, R is the distance between the donor and acceptor.  $R_0$  is the Förster distance or distance when the probability of energy transfer is 0.5.



**Figure 10.2** Immobilization of liposome on a surface by avidin biotin conjugation.

### 10.3 Significance and Conclusion

Developing molecular approaches at single cell and molecule level will help unravel the mechanisms involved in the cell transformation and differentiation especially leading to cancer. Liposomes can provide a good model that can be studied systematically. This can help provide information in the cell morphology and transformation. Target delivery by liposome can reduce drug toxicity and increase potency.

The development of the optical microscopy and fluorescence probes has laid a good foundation for tracking molecules at a single molecular level. We propose that transient protein-protein interaction between HAH1 and domains of Wilson protein can be studied at a single molecule level. The FRET signals can be monitored in the presence or absence of copper or other cations like Ag(I), Hg(I) and Cd(II). This could help advance knowledge in metal coordination chemistry and metal-proteins interactions. This is an important step in understanding human diseases at molecular level.



## 10.4 References

- 1 Huffman, D. L. and O'Halloran, T. V. (2001) Function, structure, and mechanism of intracellular copper trafficking proteins. *Annu Rev Biochem* **70**, 677-701
- 2 Lutsenko, S. and Petris, M. J. (2003) Function and regulation of the mammalian copper-transporting ATPases: insights from biochemical and cell biological approaches. *J Membr Biol* **191**, 1-12
- 3 Achila, D.; Banci, L.; Bertini, I.; Bunce, J.; Ciofi-Baffoni, S.; Huffman, D. L. (2006) Structure of human Wilson protein domains 5 and 6 and their interplay with domain 4 and the copper chaperone HAH1 in copper uptake. *Proc Natl Acad Sci U S A* **103**, 5729-5734
- 4 Bunce, J.; Achila, D.; Hetrick, E.; Lesley, L.; Huffman, D. L. (2006) Copper transfer studies between the N-terminal copper binding domains one and four of human Wilson protein. *Biochim Biophys Acta* **1760**, 907-912
- 5 Bull, P. C., Thomas, G. R., Rommens, J. M., Forbes, J. R. and Cox, D. W. (1993) The Wilson disease gene is a putative copper transporting P-type ATPase similar to the Menkes gene. *Nat Genet* **5**, 327-337
- 6 Benitez, J. J., Keller, A. M., Ochieng, P., Yatsunyk, L. A., Huffman, D. L., Rosenzweig, A. C. and Chen, P. (2008) Probing Transient Copper Chaperone-Wilson Disease Protein Interactions at the Single-Molecule Level with Nanovesicle Trapping. *J Am Chem Soc*
- 7 Benitez, J. J., Keller, A. M., Ochieng, P., Yatsunyk, L. A., Huffman, D. L., Rosenzweig, A. C. and Chen, P. (2008) Probing transient copper chaperone-Wilson disease protein interactions at the single-molecule level with nanovesicle trapping. *J Am Chem Soc* **130**, 2446-2447
- 8 Joo, C., Balci, H., Ishitsuka, Y., Buranachai, C. and Ha, T. (2008) Advances in single-molecule fluorescence methods for molecular biology. *Annu Rev Biochem* **77**, 51-76

- 9 Thomas, D. D., Carlsen, W. F. and Stryer, L. (1978) Fluorescence energy transfer in the rapid-diffusion limit. *Proc Natl Acad Sci U S A* **75**, 5746-5750